

# THIS WEEK



## EDITORIALS

**SPACEFLIGHT** Virgin Galactic sets optimistic countdown for trip beyond Earth **p.408**

**WORLD VIEW** How the BBC still gets climate change badly wrong **p.409**

**ZOOLOGY** Cold comfort farmland for rare kestrels **p.411**

## Fish have feelings too

*Our obligation to keep the suffering of laboratory animals to a minimum — both in life and in death — does not apply only to mammals.*

Former US President George W. Bush once cryptically remarked that he was sure that “the human being and fish can coexist peacefully”. Fish might beg to differ. Humans continue to deplete ocean stocks for food and to stalk rivers in the name of sport. And then there are the millions of fish that die in scientific laboratories every year.

Much of the debate about the use of animals in research focuses on what happens while they are alive: the degree of pain and suffering inflicted on them, how this can be kept to a minimum, and the balance between this discomfort and the greater benefit it can and does bring to both people and animals. Less talked about — perhaps fortuitously, given the way emotion can drive such debates — is the fact that most of the animals lose more than their freedom and their comfort. The majority of laboratory animals are killed at the end of the work. Killing animals is an unpleasant thing to have to do, but unfortunately in some areas of science it is unavoidable. So it is important that the regulations scientists follow for animal euthanasia reflect the most humane options available. New research suggests that this might not always be the case for zebrafish.

A native of the southeastern Himalayas, zebrafish are one of the most commonly used model organisms in research. One reason for their popularity is that zebrafish embryos are transparent, making them an ideal organism in which to track development, as well as the influence that genes and other factors have on this process. As tools to exploit this unusual embryonic feature have grown, so has the use of zebrafish. Exact numbers are hard to find, but the total number of fish used in UK laboratories is second only to the number of mice.

Another factor that makes zebrafish attractive is that the creatures are relatively cheap to house. They need less space, less dedicated staff time and there are fewer regulations than for rodents on, say, habitat enrichment.

In the hierarchy of living things, fish are viewed by many as a lesser life form than mammals, but not everyone agrees. A small but committed number of animal-rights campaigners, for example, extend their attention to fish and related creatures. Certainly, whether hooked fish feel pain and what, if anything, lobsters experience when dropped live into boiling water are genuine scientific questions, and ones with the potential to stir feelings and change behaviour.

The questions raised this week concern the ways in which zebrafish used in laboratories are killed at the end of their useful lives. As we report on page 419, experimental work suggests that an approved anaesthetic commonly used in fish euthanasia causes the creatures distress.

Many researchers will rightly respond cautiously to calls to change regulations and long-standing experimental practice on the basis of just two papers, which are detailed in the News story. And it is not clear whether alternative options to the anaesthetic, MS-222, are more humane.

As animal-welfare researchers have probed the methods used in laboratory euthanasia, they have provoked sometimes fierce debate over which is the kindest option. The widespread use of carbon dioxide in rodent euthanasia has come under particular scrutiny, because

**“It is important that the regulations scientists follow for animal euthanasia reflect the most humane options available.”**

evidence is growing that this method is more unpleasant for rats and mice than alternatives such as anaesthesia.

At the very least, the work on the zebrafish should prompt reassessment of how much we know about some routine practices of animal research. Frequently, when researchers have probed the assumptions underpinning laboratory standards they have exposed flaws. And fixing these flaws — such as that revealed by the finding that rodents should not be picked up by their tails because this causes them stress, which could interfere with the results of some experiments — can produce better science.

Most laboratory animals are looked after by skilled and dedicated technicians and scientists who care deeply about the creatures' welfare. Their existence may not always be peaceful, but we can — and must — try to make it so, especially at the end. ■

## Parallel lines

*A collaborative online mathematics project holds lessons for other disciplines.*

Crowd-sourcing has reached mathematics, and at first glance it might seem as if this stereotypically solitary discipline is finally catching up with what other sciences have been doing for years. But, as we explore on page 422, the maths project Polymath, which invites participants to pitch in with ideas and results that might help to solve whatever problem the coordinator has set, is in some ways ahead of the curve. Not all of Polymath's challenges — nine so far — have produced a successful solution. But even ‘failures’ can be productive, and all of these efforts represent genuine collaborations at the highest technical level.

It is in these respects that Polymath differs from the many other crowd-sourcing enterprises. Most commercial ventures are competitive: entrants vie to ‘win’ the challenge, and often to receive a financial prize as a result. As one researcher who has used these resources comments, this isn't necessarily the way to secure a truly useful solution: an extended period of post-competition development is often needed

to turn a winning entry into a practical approach. Entrants may not have the motivation or the time for that.

Other established crowd-sourcing efforts, such as Galaxy Zoo and Foldit, are all about weight of numbers, not expertise: they enlist lay volunteers to conduct repetitive tasks — such as classifying galaxy morphologies or predicting protein structures — for which human judgement still out-performs automated solutions. This is useful, but is not going to lead to the kind of conceptual novelty that drives science forwards.

So although all the various approaches to harnessing the ‘wisdom’ (or perhaps just the labour) of the crowd have a part to play, there are surely lessons that other disciplines could learn from Polymath. One is the value of openness. The system is fully democratic: anyone can propose and coordinate a project, and if it is deemed to be worth the effort, anyone can pitch in with answers or suggestions, however small, which are judged purely on merit. “Anybody who had anything whatsoever to say about the problem could chip in,” Polymath’s creator Timothy Gowers explains. “You would contribute ideas even if they were undeveloped and/or likely to be wrong.” Although it is perhaps not surprising that the challenges so far have been instigated by senior researchers, an ethos of this sort means that, in principle, the barrier to participation of younger, less experienced people is low.

And the process is a conversation, not a competition. It’s not just, or even primarily, about cracking a problem, but about sharing ideas. “One strength is in gathering literature and connections with other fields that a traditional small collaboration might not be aware of without a fortuitous conversation with the right colleague,” says Terence Tao, another of Polymath’s coordinators. And participants are learning the effort’s limits. “Projects that seem to require a genuinely new idea have so far not been terribly successful,” says Gil Kalai of the Hebrew University of Jerusalem in Israel. That’s one reason why he feels “it will

be nice to have a Polymath devoted to theory-building rather than to specific problem-solving”.

Preconceptions aside, it is perhaps not surprising that mathematicians are the first to approach crowd-sourcing in this way. Their field is relatively small and well connected, and not nearly as competitive as some might think. It has an active blogging community. And it faces problems that can be tackled online with digital pen and paper. It is less obvious

**“Sometimes it is not market forces that achieve efficiencies, but cooperatives.”**

how, say, a chemistry challenge that demands lab work could be solved in this manner.

But is that really the case? Some of the successful Polymath problems have been those that could be broken down into smaller parts that individuals could work on independently. An organic chemical synthesis is rather like that: a series of distinct steps between intermediates. The total synthesis of quinine was famously — and controversially — claimed in 1944 on that basis, when, rather than making the compound itself, Robert Woodward and William Doering bridged the last gap in a multi-stage process that had been largely completed by others. Might not these feats of synthesis be more systematically apportioned between several groups, swapping ideas, tips and techniques along the way? That could be much more efficient than the herculean efforts often doggedly pursued in single labs today, not least because there is less chance of going down blind alleys when many minds are involved. But it would require a change in the prevailing mentality of competition and victory that was evident, for example, in the total synthesis of taxol that was reported in 1994.

This is just one way in which crowd-sourcing need not be about letting a thousand flowers bloom and then throwing away all but the most fragrant, nor putting all hands to the pump. Sometimes it is not market forces that achieve efficiencies, but cooperatives. ■

# Virgin territory

*Putting a private craft into space requires vision, hard work and a big dose of optimism.*

Last week, *Nature* painted a pessimistic picture of the Google Lunar X Prize challenge in space exploration — which asks firms to land a robot explorer on the Moon by the end of next year. The technical hurdles are too high, critics say, and the financial incentives too low. A halfway house has been announced to offer encouragement: US\$6 million for groups that can demonstrate that their lander works on Earth by September this year (see *Nature* 506, 278; 2014).

By then, the X Prize model to encourage scientific progress could have launched its most successful venture yet. The word ‘could’ is pertinent, for the man talking up the chances of the venture is Richard Branson, the business tycoon with an ear for a catchy and ambitious sound bite. This is a man who does not do pessimism.

Branson said in the British newspaper *The Guardian* last week that the maiden flight of his private suborbital space-plane will blast off later this year — and that he and his family will be on board. We have been here before. Branson first promised that his company Virgin Galactic would start its space rides for paying customers in 2007, and it has been selling tickets for a decade.

He now says that work to launch the vehicle, *SpaceShipTwo*, is almost done. It is the successor to *SpaceShipOne*, which won the \$10-million Ansari X Prize for repeatable space flight with a manned craft in 2004, and for which Virgin bought the rights. And Branson is typically bullish about the craft’s prospects. The re-entry technology, always the most risky part, is foolproof, he claims: “The pilot could be sound asleep on re-entry.” Branson wants *SpaceShipTwo* to fly to the

edge of space “100 times, maybe 1,000 times”, he said.

*SpaceShipOne* hangs from the ceiling of the Smithsonian National Air and Space Museum in Washington DC, alongside the *Spirit of St. Louis* monoplane. *SpaceShipTwo* will have large windows, and white and silver seats. Engineers will customize those seats to the rears of the wealthy guests, to minimize the effects of *g* force and to allow them to get the most of their estimated five minutes of weightlessness.

*The Guardian* spoke to astronaut Chris Hadfield, veteran of the NASA space shuttle and former commander of the International Space Station, who was sceptical of Branson’s guarantees that nothing could go wrong. “To come into any programme with any vehicle and think you’re somehow immune from what everybody else has always experienced with every machine in history is unrealistic,” he said. “They don’t know everything yet.”

One thing that Branson does know (almost) everything about is how to keep a jumbo jet flying. As we report on page 420, that is more difficult than it sounds, particularly when the jet has a 2.5-metre infrared telescope sticking out of a hole in its fuselage. More than \$1 billion has so far gone into the modified Boeing 747, formally called the Stratospheric Observatory for Infrared Astronomy. After years of delays (sound familiar?) it is now fully operational, and could do some valuable science. And with annual running costs of \$78 million, it needs to.

There is something brilliantly simple about sticking a telescope on an aircraft as a way to beat atmospheric interference. But in 2014, doesn’t such a solution seem a bit, well, twentieth century?

Back in the mid-1980s, Branson was invited by then Soviet leader Mikhail Gorbachev to become the first civilian in space. The ticket would have cost \$50 million. “I thought,” Branson said, “wouldn’t it be better to spend that \$50 million building a spaceship company instead?” Optimism is not for everyone, but it has its benefits. ■

➔ **NATURE.COM**  
To comment online,  
click on Editorials at:  
[go.nature.com/xhunq](http://go.nature.com/xhunq)



## Scientist-versus-activist debates mislead the public

*The UK floods show the need to address the risks of climate change, but news teams still insist on pitching experts against sceptics, says Simon L. Lewis.*

The British are famous for conversations about the weather, and this winter there has been much to talk about. The United Kingdom's December–February rainfall was the highest since records began in 1910. Tracts of southern England have been flooded for weeks. The army has been deployed to build flood defences. Once again, climate change has floated to the top of the UK political agenda.

Extreme weather tends to do that — a similar dynamic has been seen across the world. After Hurricane Sandy hit the United States in 2012, climate change became a presidential election issue. In Australia, floods, droughts and heatwaves have pushed the topic in a way that reports from climate scientists could not.

As a scientist who has been on the wrong end of climate change misreporting (see *Nature* **468**, 7; 2010), this surge of interest begs the question: has the often dysfunctional relationship between science and the media improved this time around?

Certainly, the question posed by journalists in response to an extreme weather event — “Is this caused by climate change?” — is sensible and good news. Such questioning implicitly accepts the basic science that the climate is changing and that human activity has a central role. It moves the discussion on to the severity of the impacts, rather than the existence of a problem.

It is a promising question, but too often we hear that no single weather event can be attributed to climate change. Although that used to be the case, research has moved on. Last September, the *Bulletin of the American Meteorological Society* published analyses from 18 research groups examining 12 extreme weather events from 2012 (hurricanes, droughts, severe cold, floods and heatwaves) and concluded that anthropogenic climate change was a contributing factor to half of the extremes examined. The answer to “Is it caused by climate change?” is now: “I’ll tell you after the analyses are complete and the results have been published.”

Yet the people directly affected — the public — have a different question for scientists: “Will this happen to me again?” In other words, is the current event in line with what we expect to be happening? Will this type of event occur with increased frequency or magnitude in the future? For the UK floods, the answer is an uncontroversial “yes”. A 2004 report by the then government chief scientist David King identified flooding as a serious impact of climate change for the United Kingdom.

By approaching questions about extreme weather and climate change in this way, scientists can avoid a common trap set by ‘climate sceptics’ and the media: drawing us into a refusal to say definitively whether a given event is caused by climate change. Furthermore, this approach separates scientists from such sceptics because focusing on past predictions and model

projections — even if uncertain — highlights that climate contrarians have not produced alternative predictive models, and therefore have little to contribute.

Some things have not improved this time around, however. The reporting on the UK floods again shows that scientists must be more vocal if the public are to receive more-accurate information from the media. Extreme events that are consistent with climate-change projections should open public debate about risk and societal responses. Images of flooded homes illustrate the danger to long-term investments that really matter to people. The demand is there for a valuable discussion, first on the science — the past projections and the results of attribution studies — and then on the possible political responses. Instead, the United Kingdom was again treated to a series of scientist-versus-climate-contrarian debates that conflate the two.

Most controversially, BBC Radio 4’s news programme *Today* broadcast a debate between leading climatologist Brian Hoskins of Imperial College London and Britain’s most influential climate contrarian, and former Chancellor of the Exchequer, Nigel Lawson. Unsurprisingly, Lawson mangled the science, incorrectly stating that there had been no recent global increase in air temperature and that measurements of ocean temperature were “pure speculation”. BBC editorial guidelines state: “The BBC must not knowingly and materially mislead its audiences. We should not distort known facts.” Clearly, the BBC failed.

Why does this happen? In short, producers do not want an inbox of complaints, and climate sceptics complain if they are not represented. And executives might feel they need to ‘be fair’ by

bringing in sceptics. Of course, accuracy is in conflict with this notion of balance. So scientists should debate science with other scientists — there is enough disagreement about the details of climate change to give the BBC their desired conflict. If Lawson is to be wheeled out to debate climate change, then let him argue on policy responses with another activist who promotes a different plan of action. Lawson leads a policy-advocate organization, so put him up against the head of Greenpeace. It would be a lively debate. Separating the science from the policy response in this way is crucial to avoid mismatching interviewees as the BBC has done, with inevitably misleading consequences.

When this separation does not happen, scientists of all stripes should kick up a fuss. As a starting point, here is Lawson’s BBC interview transcript: [go.nature.com/nvrhar](http://go.nature.com/nvrhar). And here is the complaint form: [go.nature.com/boofqk](http://go.nature.com/boofqk). ■

**Simon L. Lewis** is reader in global change science at University College London and at the University of Leeds, UK.  
e-mail: [s.l.lewis@leeds.ac.uk](mailto:s.l.lewis@leeds.ac.uk)

**SCIENTISTS MUST BE  
MORE VOCAL  
IF THE PUBLIC ARE TO  
RECEIVE MORE-  
ACCURATE  
INFORMATION  
FROM THE MEDIA.**

➔ **NATURE.COM**  
Discuss this article  
online at:  
[go.nature.com/i8oy2e](http://go.nature.com/i8oy2e)



# RESEARCH HIGHLIGHTS

Selections from the  
scientific literature

## NEUROSCIENCE

### Carbon dating spots new neurons

Human cells renew themselves in the striatum, a brain region involved in cognition and coordinating body movements.

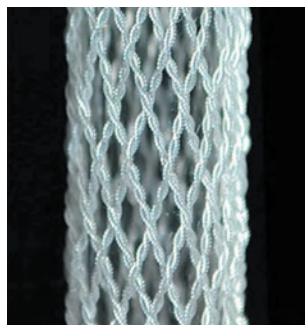
Neurons are known to regenerate in the human adult hippocampus. To find out whether regeneration occurs in other areas, Jonas Frisén at the Karolinska Institute in Stockholm and his colleagues developed a carbon-14 dating technique. They compared levels of the isotope in DNA extracted from different areas of post-mortem brains with levels of atmospheric carbon-14 during the birth year and lifetime of the donors. The team found that the carbon-14 levels in the striatum matched atmospheric levels present after the birth of the donors, suggesting that new neurons in this brain region were generated post-natally.

Only a type of neuron called an interneuron seems to regenerate in the striatum.  
**Cell** <http://dx.doi.org/10.1016/j.cell.2014.01.044> (2014)

## MATERIALS

### Muscles made from thread

Twisting strong fibres such as sewing thread and fishing line produces artificial 'muscles' that are stronger than their



human counterparts.

People have long made yarn by twisting fibres. But Ray Baughman at the University of Texas at Dallas in Richardson and his team twisted low-cost nylon or polyethylene fibres so tightly, while applying just the right amount of weight, that the fibres became extremely coiled muscles. The researchers could then weave the muscles into braids (**pictured**) or textiles. A bundle of polyethylene muscle fibres generated mechanical work that was more than 100 times greater than that produced from the same weight of human muscle.

The artificial muscles could one day be used in robotics,

prosthetic devices, and even in clothing with pores that open and close in response to temperature changes.

**Science** 343, 868–872 (2014)

## ARCHAEOLOGY

### Ancient artists' gender is a mystery

Efforts to infer the sex of ancient hand-painting artists by comparing their prints with those of modern humans could be flawed, according to a team in the Czech Republic.

Patrik Galeta and his colleagues at the University of West Bohemia in Pilsen studied the handprints of 50 modern

*americanus*) that used 20 animal crossings along a 45-kilometre stretch of highway bisecting the park. The researchers snared fur samples from passing bears, using barbed wire and other devices, for DNA analysis.

Genetic data from bears using the crossings and those in the greater park area revealed a healthy amount of genetic exchange between populations on either side of the road.

**Proc. R. Soc. B** 281, 20131705 (2014)



## CONSERVATION BIOLOGY

### Bears use animal bridges to breed

Animal crossings in Canada's Banff National Park allow bears to cross a major highway to breed, preventing genetic isolation.

Roads can fragment animal populations, increasing the risk of inbreeding and extinction. Bridges (pictured) and underpasses could help, but it has not been clear how well they work. Michael Sawaya and his colleagues at Montana State University in Bozeman studied grizzly bears (*Ursus arctos*) and black bears (*Ursus*

men and 50 modern women from France. An analysis of data, including the length of the hand and fingers, correctly identified the sex to which the print belonged in 92% of cases, but only 54% could be classified with 95% certainty. When the authors used a method previously developed using US handprints, 100% of French female prints were successfully classified, compared with only 58% of those belonging to French males; this discrepancy is mainly due to differences in hand size between the US and French populations.

Modern measurements cannot be generalized across populations, casting doubt

BANFF WILDLIFE CROSSINGS PROJECT

SCIENCE/AAAS



on the ability of these methods to accurately assign sex to handprints made by long deceased humans, the authors say. *J. Arch. Sci.* <http://doi.org/rmr> (2014)

## ZOOLOGY

## Farming shifts bird reproduction

Exposure to agricultural habitat early in life seems to speed up the reproductive schedule of a tropical bird species.

Samantha Cartwright at the University of Reading, UK, and her colleagues looked at 79 female Mauritius kestrels (*Falco punctatus*; pictured), a threatened, forest-dwelling bird. The authors found that birds born in nests near agricultural areas had lower survival rates as young adults, but also bred earlier in life, compared with birds born in forested habitats.

This reproductive shift could be an adaptive response to nutritional stress in early life that foreshadows a harsh or unpredictable adult life, the authors suggest.

*Curr. Biol.* <http://doi.org/rnc> (2014)

## REGENERATIVE BIOLOGY

## Altered proteins boost healing

Adding a protein 'tail' to molecules that drive cell replication and tissue repair could improve wound-healing treatments.

Most growth factors used in the clinic do not stimulate healing well in humans, possibly because they do not bind tightly to the proteins that make up the matrix between cells. Jeffrey Hubbell at the Swiss Federal Institute of Technology in Lausanne and his colleagues discovered that one growth factor, PlGF-2, has an amino-acid tail that lets the protein bind to the extracellular matrix. The team added this tail to other growth factors, including BMP-2,

which stimulates bone growth. When the team used these modified molecules to treat mice with skin wounds or bone defects, the injuries healed much more quickly than those treated with unmodified growth factors. *Science* 343, 885–888 (2014)

## VISION

## Molecule makes blind mice see light

A chemical injected into the eyes of blind mice restores the animals' sensitivity to daylight.

Richard Kramer at the University of California, Berkeley, and his colleagues tested a small synthetic molecule called DENAQ, which interacts with retinal ganglion cells and changes shape when exposed to white light of moderate intensity. In mice missing the light-sensing rod and cone cells in the retina and treated with DENAQ, light altered the interaction between the chemical and retinal ganglion cells so that the cells, which normally do not respond to light, became responsive. These animals were also more active when exposed to light.

The chemical works for several days, and only in retinas with degenerated rods and cones. DENAQ could be a possible drug candidate for the treatment of blinding diseases such as age-related macular degeneration, the authors say. *Neuron* 81, 800–813 (2014)

## CLIMATE CHANGE

## Permafrost grows thanks to plants

Despite rising temperatures in the Arctic, permafrost has been expanding around some lakes, probably because of vegetation springing up nearby.

Twelvemile Lake in Alaska has been shrinking, causing permafrost and willow-shrub growth to expand along its shores. A team led by Martin Briggs of the US Geological Survey in Storrs, Connecticut, modelled the response of ground ice to shading and

## COMMUNITY CHOICE

The most viewed papers in science

## GEOLOGY

## Plate tectonics got an early start

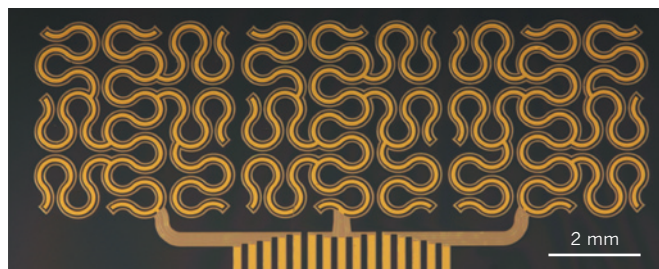
**HIGHLY READ**  
on [geology.gsa-pubs.org](http://geology.gsa-pubs.org) in January

Plates of Earth's crust could have been sliding beneath one another (or subducting) as far back as 4.4 billion years ago — soon after the planet's crust formed.

Previous studies have estimated that subduction started anywhere between roughly 1 billion and 4 billion years ago. Simon Turner at Macquarie University in Sydney, Australia, and his colleagues studied rocks in northern Quebec, Canada, that are up to 4.4 billion years old. Trace elements in the rocks and the sequence in which the rocks are layered strongly resemble those formed along a modern-day subduction zone south of Japan, called the Izu-Bonin-Mariana arc.

The geochemical similarities suggest that the Canadian rocks were formed in a subduction environment, the authors say. They add that chemical reactions in deep-diving crustal slabs could have generated the organic molecules that fuelled the development of early organisms.

*Geology* 42, 139–142 (2014)



transpiration by plants. The simulations show that, thanks to the effects of vegetation (for example, by cooling and drying the surface), shallow permafrost can persist and even expand in warmer temperatures.

However, the team calculates that, within 70 years, rising air temperatures will win out and cause this permafrost to thaw. *Geophys. Res. Lett.* <http://doi.org/rmp> (2014)

## MATERIALS

## Patterns make circuits stretchy

Laying wires in fractal patterns could improve stretchable electronics.

Devices such as wearable sensors require circuits that can withstand stretching. A

team led by John Rogers at the University of Illinois at Urbana-Champaign bonded wires in fractal motifs to elastic materials (pictured). Fractals are complex patterns that, when divided into smaller parts, look the same as they do when whole. The authors showed that their devices were more stretchable than those that had repeating loop and S-shaped patterns, with certain fractal designs allowing for stretching in specific directions.

The authors say that such structures could be used in sensors worn on the skin or radio antennas that can be mechanically tuned.

*Nature Commun.* 5, 3266 (2014)

**NATURE.COM**

For the latest research published by Nature visit:

[www.nature.com/latestresearch](http://www.nature.com/latestresearch)

# SEVEN DAYS

The news in brief

## EVENTS

### Nuclear leak

The US Department of Energy confirmed on 20 February that radiation has escaped from a facility storing nuclear waste. The department closed the Waste Isolation Pilot Plant (WIPP) near Carlsbad, New Mexico, after an underground air-monitoring system detected radiation on 14 February. Five days after the closure, the Carlsbad Environmental Monitoring and Research Center at New Mexico State University announced that it had found elevated levels of radioactive plutonium and americium at an independent air-sampling station nearly 1 kilometre from the site. Energy-department officials say radiation levels have now dropped and they expect plant staff to be able to re-enter the WIPP within two weeks.

## POLICY

### Health-data delay

England's National Health Service has postponed the creation of a database of medical records that would eventually be accessible to researchers. Data collection was scheduled to begin in April, but on 19 February the organization announced a six-month delay after members of the public complained that they were ill-informed about the project and how to opt out. See [go.nature.com/97zxcx](http://go.nature.com/97zxcx) for more.

### Patent reform

US President Barack Obama's administration announced on 20 February several initiatives to bolster the nation's troubled patent system. These include three executive actions: to improve training for patent examiners; to expand free legal assistance for independent inventors and small businesses;

and to facilitate crowd-sourcing to help patent examiners to determine whether a claimed invention is new. The actions are part of Obama's ongoing push to restrict opportunities for 'patent trolls' that aggregate patents and then profit from them by threatening other businesses with lawsuits, rather than commercializing the invention.

### Pollution curbs

On 23 February, Colorado lawmakers adopted the first regulations in the United States for reducing methane emissions from the oil and gas sector. The rules require producers in Colorado to retrofit facilities with low-emission equipment and to monitor emissions using site inspections and aerial surveys.

The regulations were first announced in November 2013, and must now be approved by the state legislature.

## FACILITIES

### Synchrotron to shut

A light source at the University of Wisconsin–Madison will close on 7 March, following a US National Science Foundation (NSF) decision to cut off its funding. The Synchrotron Radiation Center has provided researchers with infrared, ultraviolet and X-ray photons for experiments including semiconductor research and biological imaging since 1986. The NSF cut support in 2011 because of budget constraints (see *Nature* **471**, 278; 2011). The centre was unable to raise alternative

funding to save itself from closure; the synchrotron costs US\$5 million per year to run.

## BUSINESS

### Drug buyout

The biggest pharmaceutical deal since 2009 was announced on 18 February with the US\$25-billion purchase of Forest Laboratories in New York. Forest is being acquired by Actavis, which is headquartered in Dublin and is known for producing generic pharmaceuticals. The buyout will create a company with annual sales of \$15 billion from drugs targeting disorders of the heart, digestive system and central nervous system, among other areas. The expanded company will have a



GEORGIA POWER/PNEWSFOTO

## Reactor construction gets funding boost

The US Department of Energy has approved US\$6.5 billion in loan guarantees to build two nuclear reactors at the \$14-billion Vogtle Electric Generating Plant (pictured) near Waynesboro, Georgia, it said on 19 February. The reactors are the first new nuclear facilities

to be constructed in the United States in nearly 30 years. Competition from natural gas and renewable energy as well as safety concerns have prompted several US nuclear plants to shut in the past year. See [go.nature.com/pmauru](http://go.nature.com/pmauru) for more.

ESA combined investment in new drug development of \$1 billion per year.

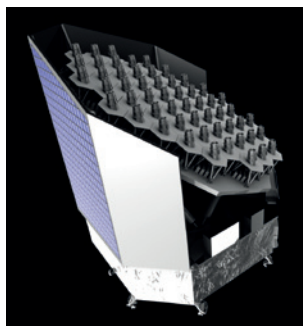
## RESEARCH

## Military psychology

Many mental-health programmes designed for the military and their families are not based on good science, finds the US Institute of Medicine in a report released on 20 February. The US Department of Defense needs to evaluate the psychological help it provides to veterans to ensure that its services are effective, it says. The defence department sponsored the report to help to address the prevalence of psychological problems, such as depression and anxiety, plaguing veterans who served in Iraq and Afghanistan.

## Planet hunter

The European Space Agency announced on 19 February that it will launch a space-based observatory to hunt for planets around nearly one million stars outside the Solar System. The Plato (Planetary Transits and Oscillations of stars) mission (pictured) will launch in 2024. It will use an array of 34 telescopes and cameras to search for Earth-sized planets and super-Earths at distances from their parent star that would allow them to be



habitable. The aim is to study possible conditions for planet formation and the emergence of life. See [go.nature.com/ufeafl](http://go.nature.com/ufeafl) for more.

## Sea sickness

Europe's seas are in poor health. This is the conclusion of two reports published on 20 February detailing the state of the continent's marine ecosystems. One of the reports, from the European Commission, says that the European Union is failing to meet a pledge to clean up its seas by 2020. According to the other report, from the European Environment Agency, 88% of the assessed fish stocks in the Mediterranean Sea and Black Sea were overfished in 2013. See [go.nature.com/qcetra](http://go.nature.com/qcetra) for more.

## Tracking forests

A tool enabling the public to track deforestation around the globe was launched on

19 February by the World Resources Institute (WRI), a think tank based in Washington DC. The Global Forest Watch monitoring system integrates several data sources — including satellite imagery and publicly available statistics — to track forest cover, loss and use. The WRI developed the tool with more than 40 partners, including Google.

## PEOPLE

## Holt retires

Physicist and congressman Rush Holt (Democrat, New Jersey) announced on 18 February that he will retire from the House of Representatives at the end of this year. Holt was a former assistant director of the Princeton Plasma Physics Laboratory in New Jersey. During his eight terms representing the state's 12th district, he campaigned for better use of science in policy-making (see *Nature* **489**, 493–494; 2012). Holt did not give a reason for his decision, but did not rule out a return to politics in future.

## Italy research head

Linguist Stefania Giannini was appointed minister for education, universities and research in Italy's new government on 21 February. Giannini's first task will be to

## COMING UP

### 4 MARCH

US President Barack Obama unveils his proposed 2015 budget. It is expected to include a request for a US\$1-billion fund to fight climate change.

### 5–7 MARCH

The Wellcome Trust biomedical charity hosts the Genomic Disorders 2014 conference in Cambridge, UK. Researchers will look at the latest findings on the genomic basis of rare disorders and discuss how genome analysis can aid clinical practice and patient care. [go.nature.com/dqzhpa](http://go.nature.com/dqzhpa)

enact a seven-year national research programme that was approved by the outgoing government last month. Funding for the programme has not yet been approved, but it has an anticipated €6.3-billion (US\$8.7-billion) budget that includes funding for hundreds of extra academic posts. Giannini is a former rector of the University for Foreigners of Perugia.

## New medical chief

Cardiologist Victor Dzau will be the next president of the US Institute of Medicine, it was announced on 19 February. The institute, based in Washington DC, provides the government and the public with health advice. Dzau will start on 1 July, taking over from Harvey Fineberg, who has led the institute for 12 years. Dzau is president and chief executive of the Duke University Health System. His research contributed to the development of enzyme inhibitors used to treat heart disease.

➔ [NATURE.COM](http://NATURE.COM)

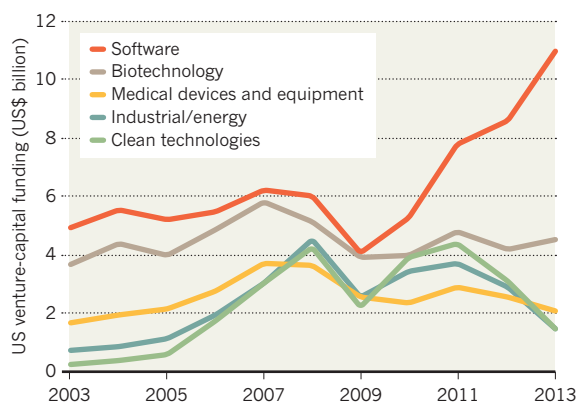
For daily news updates see: [www.nature.com/news](http://www.nature.com/news)

## TREND WATCH

US venture-capital investment rose to US\$29.4 billion in 2013, a 7% increase on the year before. According to a report by PriceWaterhouseCoopers and the US National Venture Capital Association based on Thomson Reuters data, the jump was aided by a 27% rise in money ploughed into software firms compared with 2012. By contrast, investment in companies working on medical devices, energy or clean technologies all fell in 2013, with biotechnology rising slightly (see chart).

## SOFTWARE SUPPORT

Investment in software firms by US venture capitalists continues rising; biotech funding holds steady but cash for other industries falls.





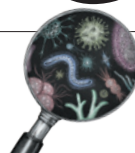
# NEWS IN FOCUS

**NEUROSCIENCE** Monkey dilemma test sheds light on decision making **p.416**

**COSMOLOGY** Lost Einstein paper describes his Big Bang alternative **p.418**

**ANIMAL RESEARCH** Studies question zebrafish euthanasia method **p.419**

**FORENSICS** How to tell who infected whom — and when **p.424**



LU JIAN/FEATURECHINA/NEWS.COM



H7N9 avian flu spreads silently in poultry, making surveillance difficult and hindering efforts to control it.

## EPIDEMIOLOGY

# Vietnam on high alert over flu risk

*H7N9 avian influenza may spread from China for first time.*

BY DECLAN BUTLER

The H7N9 avian-influenza virus that has killed more than 100 people in China in the past year has for the first time been detected in a province bordering Vietnam, raising the prospect that the disease may take hold across Asia and beyond. It was found in poultry in the live-bird markets of southern China's Guangxi province in late January, and has caused three known human cases in the region.

The news comes as a surge in human H7N9

flu cases in China since the start of the year shows signs of abating, possibly because of the reintroduction of control measures. Vietnam, which had already prepared response plans for such an H7N9 outbreak, has placed itself on high alert. "There is a very high likelihood of H7N9 entering the poultry sector in Vietnam," says Peter Horby, a researcher at the Oxford University Clinical Research Unit in Hanoi.

H7N9 flu was first detected in China in March last year, and almost all of the human cases were reported the following month.

They subsequently dropped off sharply after the prompt, temporary closure of live-bird markets, which were quickly identified as the places where most human infections occurred. Researchers say that the surge in cases since the start of the year is probably due to the arrival of winter and the intense poultry trading at live markets in the run-up to the Chinese New Year on 31 January.

So far, more than 200 human cases of H7N9 flu have been registered in China this year, compared with around 160 recorded in 2013 (see 'Ups and downs'). This year's outbreak has been centred in many of the same eastern provinces as last year's, although with a coastal and southerly shift (see [go.nature.com/dog4da](http://go.nature.com/dog4da)). Zhejiang and Guangdong provinces are the worst affected. Last week, the first human case of H7N9 flu was detected in Jilin province in the far north of the country, raising a further risk of spread to North Korea and Russia, which border the province.

Vietnam, at least, is well prepared. The country was hit hard by another avian-flu virus, H5N1, a decade ago, and suffered enormous economic losses and more than 60 human deaths. Learning from that experience, it has since introduced measures to prevent and mitigate avian-flu outbreaks, including boosting the number of veterinary surgeons and improving diagnostic facilities.

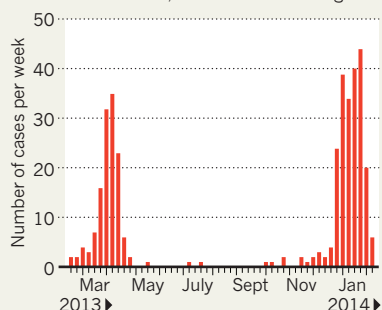
To specifically address the risk of H7N9 flu, Vietnam has banned the importation of poultry from China. It has also introduced twice-weekly monitoring for H7N9 in markets in the north of the country, and ordered their weekly disinfection.

In addition, the country's health and agriculture ministries have developed contingency plans should H7N9 arrive, including closing markets and shutting down trade routes. "Vietnam's preparedness and response actions should be seen as a model for the region," says Scott Newman, senior technical coordinator at the Vietnam branch of the Emergency Centre for Transboundary Animal Diseases, part of the Food and Agriculture Organization of the United Nations.

Some researchers are surprised that Chinese cities did not begin to close markets as soon as cases started rising in late December. Zhejiang province began closing markets in cities only at the end of January, for example, and extended this to the rest of the province only on 15 February. The heavily populated city ►

## UPS AND DOWNS

The numbers of human cases of H7N9 avian flu diagnosed plummeted last year after live-bird markets were closed, but have since resurged.



► of Guangzhou in Guangdong province began closing its markets on that day too.

“Interventions were clearly less stringent this year,” says Ben Cowling, a flu epidemiologist at the University of Hong Kong. “My impression is that financial concerns had a greater influence this winter compared to last spring.” The Chinese poultry industry has vigorously protested against the policy of shutting down markets.

But the surge in H7N9 flu cases highlights the continuing public-health — and possibly pandemic — threat that it poses. The virus’s epidemiology remains largely unchanged from last year: it is still, essentially, an avian virus that is sporadically infecting humans from a reservoir in poultry, and there is no evidence of any continued human-to-human spread. But the virus is being sustained in unknown reservoirs in the poultry supply chain, making future outbreaks likely, and its geographical expansion is a reminder of the threat beyond China. Furthermore, although case numbers have shown signs of dropping in the past two weeks, it is too early to tell if this marks a clear trend.

One year on from the first outbreak, researchers are still struggling to understand the origins and dynamics of the virus’s reservoirs and spread. H7N9 surveillance is difficult, in part because the virus causes only mild disease in poultry and thus spreads silently, with human cases typically the first warning of a poultry outbreak. H5N1, by contrast, is lethal to birds, making outbreaks easier to spot and control. And despite extensive sampling of farms, wholesale markets and other parts of the poultry supply chain, the only strong link to H7N9 found so far is live-bird markets.

The difficulty of surveillance and of sampling China’s huge poultry industry — it produces 6 billion birds annually — means that this is unlikely to be the full picture, however. Such uncertainty is also hampering efforts to develop effective control measures that are less drastic than closing the markets, says Cowling. ■

## NEUROSCIENCE

# Monkey brains wired to share

*Game-theory test exposes circuits for social interaction.*

BY SARA REARDON

Two monkeys sit at computer screens, eyeing one another as they wait for a promised reward: apple juice. Each has a choice — it can either select a symbol that results in juice being shared equally, or pick one that delivers most of the juice to itself. But being selfish is risky. If its partner also chooses not to share, neither gets much juice.

This game, the ‘prisoner’s dilemma’, is a classic test of strategy that involves the simultaneous evaluation of an opponent’s thinking. Researchers have now discovered — and manipulated — specific brain circuits in rhesus macaques (*Macaca mulatta*) that seem to be involved in the animals’ choices, and in their assessments of their partners’ choices. Investigating the connections could shed light on how social context affects decision-making in humans, and how disorders that affect social skills, such as autism spectrum disorder, disrupt brain circuitry.

“Once we have identified that there are particular neural signals necessary to drive the processes, we can begin to tinker,” says Michael Platt, a neurobiologist at Duke University in Durham, North Carolina.

Neurobiologists Keren Haroush and Ziv Williams of Harvard Medical School in Boston, Massachusetts, zoomed in on neural circuits in rhesus macaques by implanting electrode arrays into a brain area called the dorsal anterior cingulate cortex (dACC), which is associated with rewards and decision-making. The arrays recorded the activity of hundreds of individual neurons. When the monkeys played the prisoner’s dilemma (see ‘A juicy experiment’) against

a computer program, they rarely chose to cooperate. But when they played with another monkey that they could see, they were several times more likely to choose to share the juice.

As the monkey made its decision, a specific set of dACC neurons tended to fire if the animal was choosing to cooperate, allowing the researchers to predict its decision two-thirds of the time. A different set often fired if the monkey thought its partner would cooperate, and the predictions were 80% accurate.

Researchers have long known about mirror neurons, which are involved in copying other individual’s actions, but this is the first discovery of neurons that predict another individual’s unknown actions. The researchers also found that when they interfered with the cooperation circuit by delivering an electric shock to the area, the monkeys became less likely to cooperate — suggesting that the circuits for social interaction normally override an inherent desire to self-indulge. Haroush and Williams will present their findings this week at the Computational and Systems Neuroscience meeting in Salt Lake City, Utah.

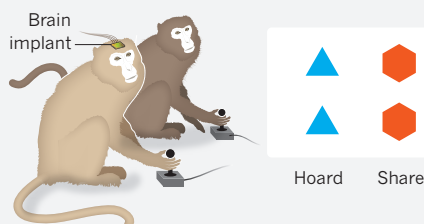
The ability to track individual circuits while monkeys assess one another is an important advance, says Robert Seyfarth, a psychologist at the University of Pennsylvania in Philadelphia, although he cautions that real social interactions are much more complex. Furthermore, he says, a monkey’s willingness to cooperate might depend on the other monkey — whether it is a dominant male, for instance, or a relative. “We really need to ask monkeys what they know about other monkeys,” says Seyfarth.

A closer look at the circuits could reveal

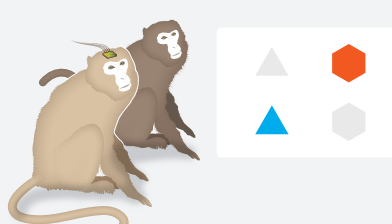
## A JUICY EXPERIMENT

Researchers have monitored the brains of monkeys playing the prisoner’s dilemma strategy game. If both monkeys pick the ‘share’ symbol, they split an apple-juice reward. If both pick ‘hoard’, neither gets much juice. If one hoards while the other shares, it gets most of the juice — but its partner may be less likely to share later.

### 1 Monkeys choose



### 2 Choices revealed





how they respond to hormones or drugs, says Steve Chang, a psychologist at Yale University in New Haven, Connecticut. The neurohormone oxytocin, in particular, has been touted as a potential treatment for autism, because it seems to aid the formation of social bonds. For example, men playing the prisoner's dilemma are more likely to cooperate if they have breathed in oxytocin<sup>1</sup>.

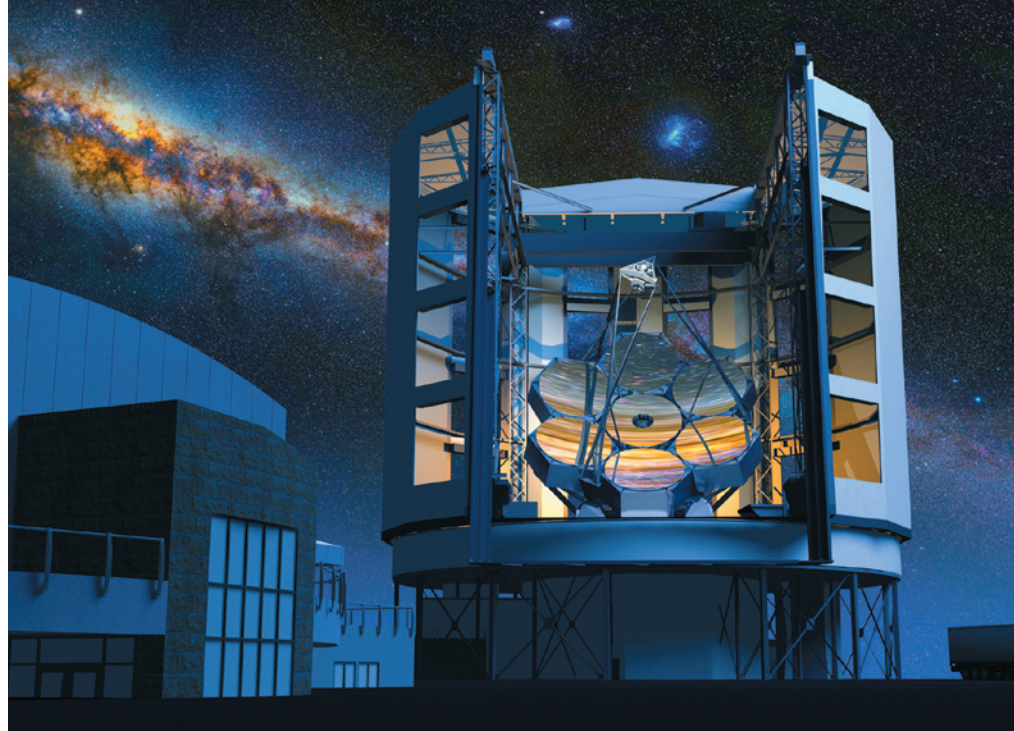
Chang and Platt have monitored the brains of monkeys playing a different game, in which they can choose to reward other monkeys without any sacrifice. Receiving a reward causes one set of neurons to fire, they found<sup>2</sup>; watching another monkey receive a reward triggers a different set. As in the prisoner's dilemma, the monkeys wanted to reward another monkey only if it was physically present, and were unlikely to reward a computer. Chang is now studying how oxytocin, which has been shown to increase monkeys' willingness to reward<sup>3</sup>, affects neural circuitry.

Besides drugs and neurohormones, electrical stimulation can also alter the brain. Platt's lab is trying to map neural circuits, and show how they respond to electromagnetic stimulation. Previous work has shown<sup>4</sup> that stimulating certain parts of the brain can increase people's ability to perform empathetic tasks, such as assessing what someone else knows or likes.

But Platt says that scientists are just beginning to understand how such methods work. He adds that watching the response of neural circuits in monkeys is a good way to work out how much stimulation or hormone should be applied, and where. "If you were a parent and considering oxytocin or brain stimulation for your child, you would want to know the answers to all those questions," he says. ■

1. Rilling, J. K. *et al. Psychoneuroendocrinology* **37**, 447–461 (2012).
2. Chang, S. W. C., Gariépy, J.-F. & Platt, M. L. *Nature Neurosci.* **16**, 243–250 (2013).
3. Chang, S. W. C., Barter, J. W., Ebitz, R. B., Watson, K. K. & Platt, M. L. *Proc. Natl Acad. Sci. USA* **109**, 959–964 (2012).
4. Santiesteban, I., Banissy, M. J., Catmur, C. & Bird, G. *Curr. Biol.* **22**, 2274–2277 (2012).

### 3 Rewards delivered



The proposed Giant Magellan Telescope in Chile is seeking to secure funding for its construction phase.

#### ASTRONOMY

## São Paulo poised to join megatelescope

*Brazilian state mulls support for Giant Magellan Telescope.*

BY ELIZABETH GIBNEY

Astronomers in Brazil's richest state are pushing for a stake in the Giant Magellan Telescope (GMT), one of three planned megatelescopes. The São Paulo Research Foundation (FAPESP) is evaluating a proposal that would see it invest US\$40 million in the 25-metre facility, to be built at the Carnegie Institution for Science's Las Campanas Observatory in Chile.

If Brazil finalizes joining the European Southern Observatory (ESO) as planned under a separate proposal, São Paulo state astronomers would have access to another megatelescope, the 39-metre European Extremely Large Telescope (E-ELT), which ESO also plans to build in Chile. Brazil's accession agreement to ESO, signed in 2010 by the then science minister Sergio Machado Rezende, would deliver €270 million (US\$371 million) to the organization over a decade — almost one-third of the E-ELT's cost. But Brazil's legislative committees are still hunting for funds and its Congress has not ratified the agreement (see *Nature* **501**, 13–14; 2013).

The strength of the astronomy department at the University of São Paulo alone helps to explain the state's move to join the GMT, says Gary Sanders, project manager of the Thirty Meter Telescope, the third megatelescope

in the pipeline, planned for Mauna Kea in Hawaii. "As an outsider, it does seem natural for me for the state of São Paulo to provide access to an extremely large telescope for that community," he says.

The GMT project is managed by a consortium of institutions in the United States, Australia and South Korea. The telescope will study the skies with about six times the collecting power of the largest existing observatories, probing deeply into how stars and galaxies formed in the early Universe. On 19 February, the GMT board announced that a major milestone had been cleared when a panel of experts approved its design. Now that the \$880-million telescope is technically ready for construction, it must secure its financial commitments. Cash is exactly what São Paulo could provide.

The state generates one-third of Brazil's gross domestic product, and more than half of its scientific output. São Paulo produces more scientific articles than any South American country, aside from Brazil as a whole. Funding for the GMT would bypass complicated federal mechanisms and come directly from FAPESP, which is supported by 1% of state taxes.

The proposal before FAPESP would secure a 4% stake in the GMT, guaranteeing São Paulo's researchers 4% of observation time each year, as well as representation on the consortium's decision-making board. This would be a ►



► huge advantage for astronomers in the state — particularly those at smaller institutions, says Cassio Leandro Barbosa, an astronomer at the University of Paraíba Valley in São Paulo state.

Wendy Freedman, chair of the GMT board and director of the Carnegie Observatories, thinks that São Paulo and the GMT are “a good match”. The decision to join will now come down to FAPESP’s review

**“Our reputation would drop off a cliff.”**

of a November 2013 workshop between Brazilian astronomers and the GMT leadership, along with an evaluation of benefits

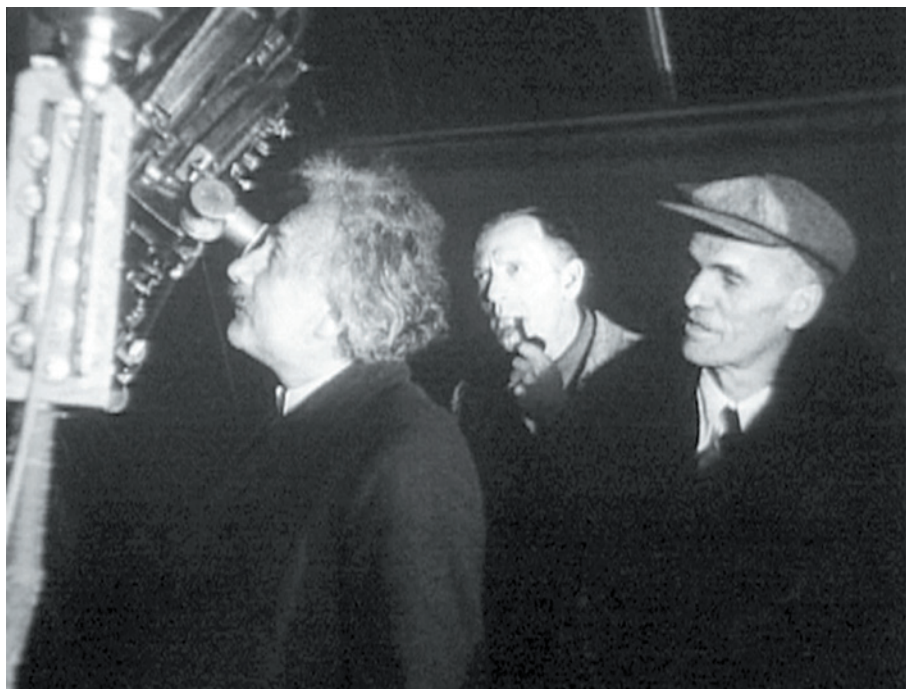
for local industry, says Hernan Chaimovich, special aide to the scientific department at FAPESP. A decision is likely to be made by April, he says.

According to Chaimovich, FAPESP is also in discussions with the Brazilian Ministry of Science and Technology about a federal contribution to the GMT, which would grant telescope access to investigators outside the state of São Paulo. If the ministry does contribute, ESO advocates could have cause for concern, because that might undercut interest in using the E-ELT, a major driver for Brazil to ratify its ESO membership.

For ESO director-general Tim de Zeeuw, one proposal does not necessarily exclude the other. FAPESP’s bid to join the GMT “is independent of the ratification of Brazil to ESO and is very different”, he says. Both megatelescopes are a decade or so away from completion, but being part of the ESO gives Brazilian astronomers access to existing observatories in Chile, such as the Atacama Large Millimeter/submillimeter Array and the Very Large Telescope, he adds. “They are cutting-edge facilities available to the Brazilian community here and now.”

The ratification process formally began in February last year, but has stalled in Congress. De Zeeuw expects Brazil to confirm the agreement in the first half of 2014, but those familiar with the Brazilian system are less willing to make firm predictions in an election year. Beatriz Barbuy, head of the Astronomical Society of Brazil’s ESO committee, is hopeful that the process will wrap up this year. “We will see,” she says. “The next step is to find the budget.”

Further delays could hurt both ESO and Brazil. Under present rules, major construction contracts for the E-ELT cannot be awarded until Brazil’s funds are secure. The country’s growing standing in international science would also take a nose dive, says Barbosa, just as it seeks to join other global organizations, such as CERN, Europe’s particle-physics laboratory near Geneva, Switzerland. “Our reputation would drop off a cliff,” he says. ■



Albert Einstein at Mount Wilson Observatory in 1931, with Edwin Hubble (centre) and Walter Adams.

#### COSMOLOGY

# Einstein’s lost theory uncovered

*Physicist explored the idea of a steady-state Universe in 1931.*

BY DAVIDE CASTELVECCHI

A manuscript that lay unnoticed by scientists for decades has revealed that Albert Einstein once dabbled with an alternative to what we now know as the Big Bang, proposing instead that the Universe expanded steadily and eternally. The recently uncovered work, written in 1931, is reminiscent of a theory championed by British astrophysicist Fred Hoyle nearly 20 years later. Einstein soon abandoned the idea, but the manuscript reveals his continued hesitance to accept that the Universe was created during a single explosive event.

Evidence for the Big Bang first emerged in the 1920s, when US astronomer Edwin Hubble and others discovered that distant galaxies are moving away and that space itself is expanding. This seemed to imply that, in the past, the contents of the observable Universe had been a very dense and hot ‘primordial broth’.

But, from the late 1940s, Hoyle argued that space could be expanding eternally and keeping a roughly constant density. It could do this by continually adding new matter, with elementary particles spontaneously popping up from

space, Hoyle said. Particles would then coalesce to form galaxies and stars, and these would appear at just the right rate to take up the extra room created by the expansion of space. Hoyle’s Universe was always infinite, so its size did not change as it expanded. It was in a ‘steady state’.

The newly uncovered document shows that Einstein had described essentially the same idea much earlier. “For the density to remain constant new particles of matter must be continually formed,” he writes. The manuscript is thought to have been produced during a trip to California in 1931 — in part because it was written on American note paper.

It had been stored in plain sight at the Albert Einstein Archives in Jerusalem — and is freely available to view on its website — but had been mistakenly classified as a first draft of another Einstein paper. Cormac O’Raifeartaigh, a physicist at the Waterford Institute of Technology in Ireland, says that he “almost fell out of his chair” when he realized what the manuscript was about. He and his collaborators have posted their findings, together with an English translation of Einstein’s original German manuscript, on the arXiv preprint server (C. O’Raifeartaigh *et al.* Preprint at <http://arxiv.org/abs/1402.0132>;

2014) and have submitted their paper to the *European Physical Journal*.

"This finding confirms that Hoyle was not a crank," says study co-author Simon Mitton, a science historian at the University of Cambridge, UK, who wrote the 2005 biography *Fred Hoyle: A Life in Science*. The mere fact that Einstein had toyed with a steady-state model could have lent Hoyle more credibility as he engaged the physics community in a debate on the subject. "If only Hoyle had known, he would certainly have used it to punch his opponents," O'Raifeartaigh says.

Although Hoyle's model was eventually ruled out by astronomical observations, it was at least mathematically consistent, tweaking the equations of Einstein's general theory of relativity to provide a possible mechanism for the spontaneous generation of matter. Einstein's unpublished manuscript suggests that, at first, he believed that such a mechanism could arise

$$\begin{aligned} & \text{Die Gleichungen (1) liefern} \\ & -\frac{3}{4} \alpha^2 + \lambda c^2 = 0 \\ & \frac{3}{4} \alpha^2 - \lambda c^2 = 8\pi c^2 \end{aligned}$$

Einstein's correction to his erroneous calculation.

from his original theory without modification. But then he realized that he had made a mistake in his calculations, O'Raifeartaigh and his team suggest. When he corrected it — crossing out a number with a pen of a different colour — he probably decided that the idea would not work and set it aside.

The manuscript was probably "a rough draft commenced with excitement over a neat idea and soon abandoned as the author realized he was fooling himself", says cosmologist James Peebles of Princeton University in New Jersey. There seems to be no record of Einstein ever mentioning these calculations again.

But the fact that Einstein experimented with the steady-state concept demonstrates his continued resistance to the idea of a Big Bang, which he at first found "abominable", even though other theoreticians had shown it to be a natural consequence of his general theory of relativity. (Other leading researchers, such as the eminent Cambridge astronomer Arthur Eddington, were also suspicious of the Big Bang idea, because it suggested a mystical moment of creation.) When astronomers found evidence for cosmic expansion, Einstein had to abandon his bias towards a static Universe, and a steady-state Universe was the next best thing, O'Raifeartaigh and his collaborators say.

Helge Kragh, a science historian at Aarhus University in Denmark, agrees. "What the manuscript shows is that although by then he accepted the expansion of space, [Einstein] was unhappy with a Universe changing in time," he says. ■

## ANIMAL RESEARCH

# Fish-kill method questioned

*Common anaesthetic not the most humane option for zebrafish euthanasia, say studies.*

BY DANIEL CRESSEY

Researchers have called for a common method of killing zebrafish used in laboratories to be abandoned amid growing evidence that it causes unnecessary suffering.

The anaesthetic MS-222, which can be added to tanks to cause overdose, seems to distress the fish, two separate studies have shown. The studies' authors propose that alternative anaesthetics or methods should be used instead.

"These two studies — carried out independently — use different methodologies to reach the same conclusion: zebrafish detect and avoid MS-222 in the water," says Stewart Owen, a senior environmental scientist at AstraZeneca's Brixham Environmental Laboratory in Brixham, UK, and a co-author of one of the studies. "As this is a clear aversive response, as a humane choice, one would no longer use this agent for routine zebrafish anaesthesia."

The use of zebrafish (*Danio rerio*) in research has skyrocketed in recent years as scientists have sought alternatives to more controversial animal models, such as mammals. The fish are cheap and easy to keep, and although no firm data on numbers have been collected, millions are known to be housed in laboratories around the world. Nearly all will eventually be killed.

MS-222 (ethyl 3-aminobenzoate methanesulphate, also known as TMS) is one of the agents most frequently used to kill the creatures.



A researcher checks zebrafish tanks in a cancer lab.

It is listed as an acceptable method of euthanasia by many institutions, and also by societies such as the American Veterinary Medical Association. But the study by Owen and his co-authors, published last year (G. D. Readman *et al.* *PLoS ONE* 8, e73773; 2013), and the second study, published earlier this month by Daniel Weary

and his colleagues at the University of British Columbia in Vancouver, Canada (D. Wong *et al.* *PLoS ONE* 9, e88030; 2014), show that zebrafish seem to find the chemical distressing. The research should fundamentally change the practice, say the authors of both papers.

Owen's study used video tracking to measure whether zebrafish avoided anaesthetics flowing through one side of a tank by moving to the other, untreated side. In the case of MS-222, the team found that zebrafish spent significantly more time in the untreated side than on the side containing the anaesthetic.

Weary's team allowed zebrafish to first spend time in either a light or a dark section of a tank, and then exposed them to MS-222 on their preferred side, the light side. After exposure to the anaesthetic, all but one of 17 fish in the study spent less time on the light side, and nine completely avoided it. This indicates that the fish would rather undergo discomfort — in this case, darkness — than be exposed to MS-222.

"There must be something unpleasant" about MS-222 to produce such a strong signal in the experiment, says Weary, because fish do not avoid many other harmful chemicals to such an extent. "The results are pretty clear," he adds. "We're at a stage where it is a matter of getting policy-makers and researchers to think about this and to rethink the procedures."

There is growing debate over the most humane methods of killing laboratory mammals, with rodent euthanasia coming ▶



► under increased scrutiny (see *Nature* **500**, 130–131; 2013). Fish euthanasia has so far attracted less attention. “I think of fish welfare as being 10 to 20 years behind mammal welfare,” says Lynne Sneddon, who studies welfare in fish and is director of bioveterinary science at the University of Liverpool, UK.

Sneddon says the two papers convincingly show that the use of MS-222 to kill zebrafish should probably be avoided. But she notes that there are significant differences between species — data on zebrafish should not be generalized to other laboratory fish, such as salmonids, for example — and therefore cautions against banning its use in the animals entirely.

Zoltan Varga, director of the Zebrafish International Resource Center at the University of Oregon in Eugene, also cautions against abandoning MS-222 because the optimal method of killing will depend heavily on the individual experiment and set-up. “A choice of anaesthetics is critical, as there is a range of reactions possible and we need to administer drugs that address any situation,” he says. In some cases, this could be MS-222.

There is not enough evidence to know which is the most humane method, and opinions differ. Owen suggests using the anaesthetic etomidate, which is cheaper than MS-222 (US\$0.15 per litre compared with \$0.23 per litre of working solution) and which seemed to be less aversive in his tests. Weary’s research suggests clove oil as another cheap alternative. Varga favours ‘hypothermal shock’ — in which the zebrafish, a tropical species, are rapidly cooled. (This method is illegal in the United Kingdom owing to concerns that ice may damage fish tissue while the animals are still conscious.)

As the number of fish experiments continues to rise — they are the second most popular research species in the United Kingdom — the question grows in importance. “We must have the patience to allow the zebrafish field research time to critically explore what the best — that is, most humane — standards are,” says Varga. “We can neither infer these standards from human experience nor from the guidelines and regulations already established for other laboratory organisms.” ■ **SEE EDITORIAL P.407**



The Stratospheric Observatory for Infrared Astronomy carries a 2.5-metre telescope to viewing hotspots.

#### ASTRONOMY

# SOFIA irons out technical kinks

*US–German airborne telescope slow to reach full capability.*

BY ALEXANDRA WITZE

Last October, Diane Wooden was chasing a comet — from the back of a jumbo jet. The aeroplane, known as the Stratospheric Observatory for Infrared Astronomy (SOFIA), is a Boeing 747 modified to hold a 2.5-metre telescope and fly to altitudes of up to 13.7 kilometres, where it escapes most of the atmospheric water vapour that obscures infrared light in the night sky. Wooden, an astrophysicist at the NASA Ames Research Center in Moffett Field, California, was on board in the hope of capturing images of warm dust spewing off Comet ISON (see *Nature* **506**, 281–283; 2014). But soon after she pointed the telescope at the comet, a circuit-breaker failed. It could not be replaced until the plane landed. Instead of nearly an hour observing the comet, Wooden got just a few minutes.

Wooden is still happy with the data she got: the only direct measurement of heat coming

off ISON’s larger dust grains. But the glitch was typical of those that have plagued the complex flying observatory, a joint project that has so far cost about US\$1.25 billion for NASA and the DLR, Germany’s aerospace centre.

After years of delays and cost overruns, and many flight hours lost to technical and other issues, SOFIA scientists say that they are finally on the verge of putting their predicaments in the past. On 21 February, a fourth telescope instrument was fully implemented, a long-awaited milestone that means SOFIA has reached full operational capability. “We’re entering a different phase now, where our real focus will be on operations and observing and gathering science,” says Erick Young, the science mission operations director for SOFIA at Ames. “We’ll hit our stride.”

Yet just as momentum starts to build, SOFIA will be grounded for a 5.5-month maintenance check mandated by the US government. That will limit the upcoming observing cycle to

NASA/JIM ROSS

**MORE ONLINE**

#### TOP STORY



Meningitis immunization campaign in West Africa delivers without ice boxes  
[go.nature.com/1ac7yl](http://go.nature.com/1ac7yl)

#### MORE NEWS

- Wings and fins share a universal geometry across taxa  
[go.nature.com/h2G6wg](http://go.nature.com/h2G6wg)
- Chemists call for boycott over lack of female speakers  
[go.nature.com/3dzkf9](http://go.nature.com/3dzkf9)
- Publishers withdraw more than 120 gibberish papers  
[go.nature.com/bbt9a](http://go.nature.com/bbt9a)

#### NATURE PODCAST



Cancer spread by UV; why Earth’s mantle flows; and Einstein’s forgotten manuscript  
[nature.com/nature/podcast](http://nature.com/nature/podcast)



## UP IN THE AIR

Technical troubles have kept SOFIA from meeting its observation goals.

Phase	Dates	Planned hours*	Completed hours	Oversubscription**
Early science	May 2011 to November 2011	139 hours	75 hours	3.7
Cycle 1	April 2013 to January 2014	240 hours	175 hours	6.0
Cycle 2	February 2014 to January 2015	222 hours		3.0

\*Planned hours are for general investigator observations. Additional science can be done with time given to instrument teams.

\*\*Ratio of time requested in applications to available telescope time. Source: SOFIA science office.

222 hours, or fewer than 32 nights (see ‘Up in the air’), and leave astronomers trying to grab what flight hours they can, when they can. SOFIA will not reach its goal of 960 research hours in a calendar year until 2016. “Things are moving in the right direction, but there is a ways to go,” says Paul Goldsmith, an astronomer at the Jet Propulsion Laboratory in Pasadena, California.

## ABOVE THE ATMOSPHERE

SOFIA was conceived in the early 1990s as a replacement for NASA’s Kuiper Airborne Observatory, a smaller telescope-on-a-plane that had been in use since 1975. The goal was to fly SOFIA from dusk until dawn several times a week so that astronomers could observe planets, stars and galaxies at the infrared wavelengths that are impossible to detect from the ground.

That goal is still far off. SOFIA saw its first light in 2010 (see *Nature* **466**, 428–431; 2010) and began limited science runs in 2011. Since then, mission scientists have been following a drawn-out schedule for ramping-up research while bringing the major instruments into use. “It was a strategy to get the most science out,” says Paul Hertz, head of NASA’s astrophysics division in Washington DC.

SOFIA has found itself scooped by the European Space Agency’s Herschel space telescope, an infrared instrument launched in 2009. SOFIA was meant to be a pathfinder for Herschel, but instead has been left to chase interesting targets identified by the space telescope, which ceased operations last year.

SOFIA is also spending much less time doing science than project managers would like: in 2013, it logged just 175 of 240 scheduled research hours. The biggest culprit was the two-week US government shutdown in October, triggered when legislators could not reach agreement on a budget bill. Nine SOFIA flights were lost to the shutdown, including planned observations of a bright exploding star in the constellation Delphinus. “We lost the nova!” says Robert Gehrz, an astronomer at the University of Minnesota in Minneapolis and chair of the SOFIA users advisory group.

Technical troubles were also to blame. One instrument sprang a helium leak. Another experienced problems with its power supply and the fasteners used to attach it in the telescope cavity. Some images are still less than

ideal because the telescope shakes during flight. But dealing with instrument issues is part of the normal teething process of bringing a complex observatory online, says Dan Lester, an astronomer at the University of Texas at Austin.

Keeping a modified jumbo jet flying night after night carries other challenges. Late last year, for example, a damaged turbine blade meant that an entire engine had to be replaced. The cost of employing pilots, technicians and mechanics adds up. The mission’s \$78-million annual operation budget is the second most expensive in NASA’s astrophysics division, after the \$93 million needed to keep the Hubble Space Telescope going.

For all its troubles, SOFIA has still racked up some scientific achievements, including the

**“Our real focus will be on operations and observing and gathering science.”**

best measurements yet of an occultation, in which Pluto passed in front of a distant star and revealed its thin atmosphere. Because SOFIA can fly to locations up to

10 hours away from its home base in Palmdale, California, it can travel to many of the geographical spots where occultations and other such rare astronomical events are visible. Hans Zinnecker, SOFIA’s deputy director for science mission operations, says that research flights are getting more regular. He points to a string of nine flights over the course of three weeks from New Zealand, where SOFIA was deployed to study southern-sky targets such as the Magellanic Clouds. “That was a smashing success,” says Zinnecker. “It surprised even ourselves.”

Lester, who served on a 2013 NASA oversight panel for the mission, feels much more positive about it than he did a few years ago. “In many respects, SOFIA has turned the corner,” he says. “The problems that we’re having today are problems that we won’t have tomorrow.” ■ [SEE EDITORIAL P.408](#)

## CORRECTION

The News story ‘Moon shots stuck on Earth’ (*Nature* **506**, 278; 2014) wrongly gave November instead of September 2013 as the date for when the Google Lunar X Prize dropped a penalty clause relating to government-sponsored missions.

# STRENGTH IN NUMBERS

*Researchers are finding that online, crowd-sourced collaboration can speed up their work — if they choose the right problem.*

BY PHILIP BALL

**A**t the end of January 2009, Timothy Gowers embarked on what he later called “one of the most exciting six weeks of my mathematical life”. Inspired by the online citizen-science movement, Gowers, a mathematician at the University of Cambridge, UK, posted an esoteric theorem on his blog and challenged his readers to prove it — together.

Crowd-source your expertise, he urged them: “If a large group of mathematicians could connect their brains efficiently, they could perhaps solve problems very efficiently as well.”

They could. Within hours of the problem being posted, Gowers’ blog was abuzz with back-and-forth brainstorming, as mathematicians chimed in with ideas and possible avenues of attack. Gowers had hoped for new insights, but even he was surprised that by March, after nearly 1,000 comments, he was able to declare the theorem proved. “The quite unexpected result — an actual solution to the problem — added an extra layer of excitement to the whole thing,” he says. The proof was published<sup>1</sup> under the collective pseudonym D. H. J. Polymath.

Gowers’ online challenge was a radical suggestion for mathematics — a field that is often viewed as the domain of lonely, secretive figures who work for years in isolation. And it went against the grain of the wider academic culture, which tends to encourage researchers to share their ideas only by publishing them.

Yet this open approach has taken root as an ongoing crowd-sourcing project called Polymath. Today, just past its fifth anniversary, Polymath has a dedicated website where people can post and debate suggestions for new challenges — and, if they agree that the challenge is worthwhile, circulate ideas for its solution.

Not every challenge has worked as well as the first, but other mathematicians offer

cautious praise for the project, both for providing solutions to problems and for helping to spark a much-needed shift towards greater openness in mathematical research. “The impact on the community is larger than the net scientific impact,” says Gil Kalai, a mathematician at the Hebrew University of Jerusalem, who coordinated one of the challenges.

Many of the Internet’s most popular crowd-sourced science projects require no expertise from their participants. One called Galaxy Zoo, for example, engaged more than 150,000 lay users during its first year, 2007, to sort images of galaxies by shape (see *Nature* **466**, 685–687; 2010). Problems on Polymath, by contrast, attract just a few dozen participants, but those users have real expertise. In that way, the project parallels commercial ventures that pose technological and data-analysis problems online, looking for responses from highly skilled people. Companies such as InnoCentive in Waltham, Massachusetts, offer cash rewards to encourage participation, but most of the entries come from individuals motivated by a deep love for solving problems — and the chance to win recognition.

As with Polymath, these companies are finding that some challenges work well, but others go nowhere.

“We’re still learning what works and what doesn’t,” says Terence Tao, a mathematician at the University of California, Los Angeles, and the coordinator of several Polymath challenges.

## A WINNING FORMULA

One key strength, says Tao, is Polymath’s responsiveness. “We can react rather quickly to hot events in mathematics,” he says.

Last April, for example, Yitang Zhang, a previously obscure mathematician at the University of New Hampshire in Durham, announced that he had taken a giant step

towards answering one of the great open questions in the theory of prime numbers: is there an infinite number of ‘twin primes’ that differ by 2, as in (11, 13) and (41, 43)?

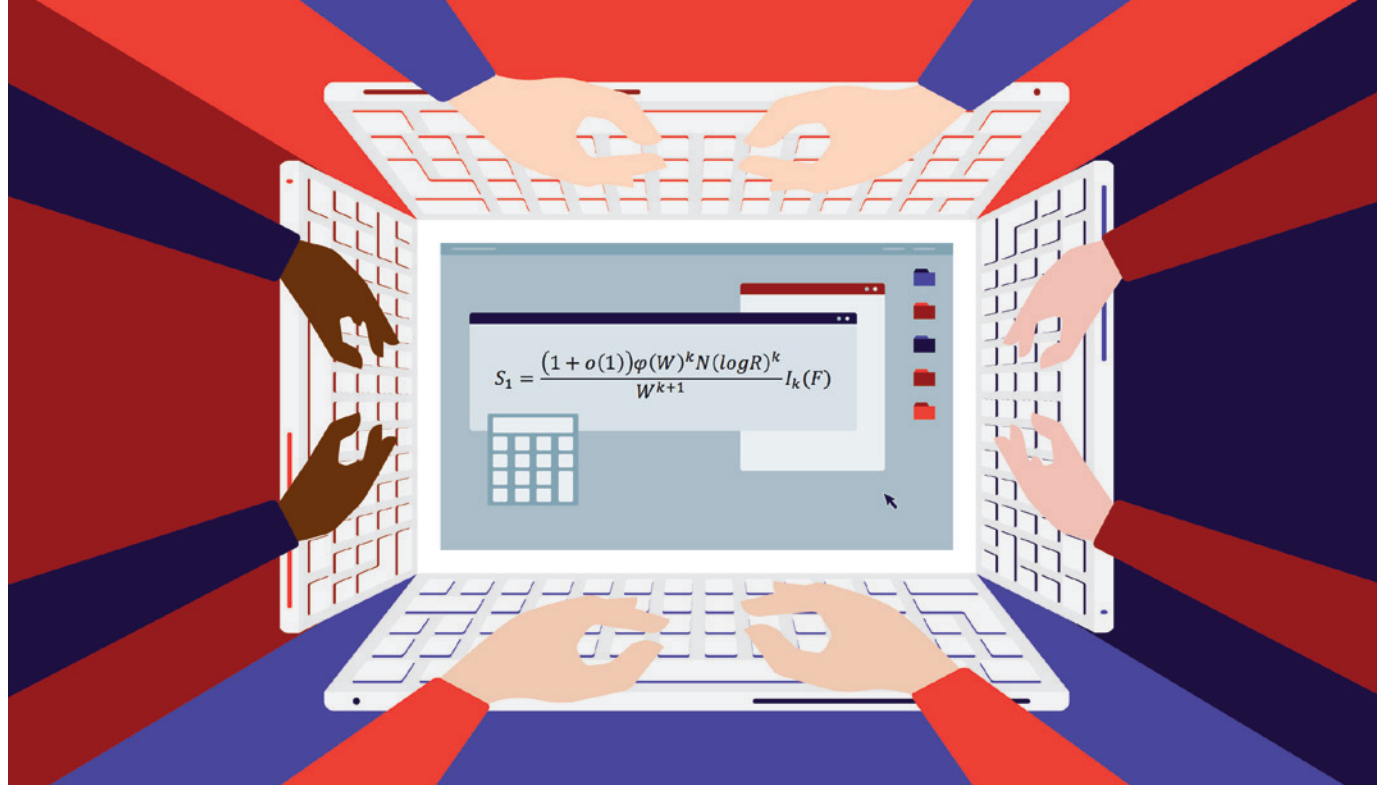
Zhang had not given the complete answer: he was able to show only that there is an infinite number of ‘near-twin’ primes that differ by no more than 70 million (ref. 2). But it was the first time that anyone had put any limit on such pairings. Polymath seemed like an ideal tool for whittling down that limit.

The project, dubbed Polymath 8, got under way last June with Tao as coordinator. Within months, mathematicians all around the world had pitched in with refinements to Zhang’s proof, using the Polymath website to discuss and answer one another’s questions. They swiftly reduced the separation between the primes from the millions to the thousands<sup>3</sup>. And by November, James Maynard, a mathematician at the University of Montreal in Canada, had drawn on that impetus to reduce the limit to 600 (ref. 4).

Polymath 8 was a triumph for the collaborative approach, says Tao. If mathematicians had been attacking the problem in the standard way, with what he describes as “a flood of mini-papers”, it might have taken years to get the bound down that far.

Polymath has not always worked so well, however: some of the challenges simply never got off the ground. But after five years of experience with it, users have begun to hone in on the features that determine success. For example, says Tao, “It helps if the problem is broadly accessible and of interest to a large number of mathematicians”. This tends to draw a wide range of participants with a rich mix of skills, but it works only if the problem can easily accommodate what they have to offer.

That was one of the virtues of the twin-primes challenge, says Maynard. “The proof



can be split into separate sections, with each section more-or-less independent of the others,” he says.

Perhaps the most important lesson is that setting up and sustaining a Polymath project is a big commitment. So far, Tao and Gowers have initiated all but two of the Polymath projects. “It’s quite difficult to get people interested,” Gowers admits. “It needs an active leader who is willing to spend a fair amount of effort to organize the discussion and keep it moving in productive directions,” says Tao. “Otherwise, the initial burst of activity can dissipate fairly quickly.”

## KEEP THEM COMING

Incentives can help with that. “In academia, people are willing to spend a lot of time for ‘kudos’ or for the sake of science — but only up to a point,” says Thomas Kitching, a cosmologist at University College London who has been involved in crowd-sourcing ventures. Beyond that point, he says, “monetary incentives or prizes seem to be required”.

That is the idea behind prize-based crowd-sourcing initiatives, which offer financial rewards to experts who provide solutions. Some of these initiatives are government-led, such as the NASA Tournament Lab and the US cross-agency Challenge.gov, which offers cash prizes for solutions to a whole range of engineering and technological problems.

Other efforts are completely commercial, and charge clients to post a problem online. Among the most prominent is InnoCentive, which will host any scientific or technological challenge. These range from the mundane but important — developing economical forms of “latrine lighting in emergencies”, for

**NATURE.COM**  
To learn more about crowd-sourced science, see:  
[go.nature.com/kjugsd](http://go.nature.com/kjugsd)

example, or “keeping hair clean for longer without washing” — to the esoteric: “seeking 4-hydroxy-1H-pyridin-2-one analogues”, or “stabilizing foamed emulsions”. It has more than 300,000 registered ‘solvers’, who stand to gain rewards of between US\$5,000 and \$1 million if their solution works.

Another commercial venture, Kaggle in San Francisco, California, specializes in data analysis, with applications ranging from oil and gas recovery to predicting drug targets. In 2012, a team of astronomers led by Kitching launched a Kaggle competition called Observing Dark Worlds. It offered \$20,000 — donated by London-based financial firm Winton Capital Management — for the three best algorithms to map the distribution of dark matter in galaxies using the matter’s gravitational-lensing effects on background objects. The competition was a success for all parties: the winning entries offered the astronomers about a 30% improvement over existing algorithms, and Winton recruited new analysts from the contestant list for a fraction of the usual advertising and interviewing costs.

The need for such projects might well increase, says David Harvey, an astronomer at the University of Edinburgh, UK, and a co-author of a study<sup>5</sup> that resulted from the competition. “With new telescopes such as the Square Kilometre Array, the Large Synoptic Survey Telescope and Euclid on the horizon, astronomers will be facing real problems of data processing, handling and analysing”.

But Harvey stresses that Observing Dark Worlds was not an unalloyed success. As interesting as the resulting algorithms were, none of them had been tested and developed to a point at which they could routinely be used on real data. “It’s vital that the winners of the competition work in collaboration — post-competition — on the problem and

develop the initial idea all the way through to a final package,” he says. That process will probably require a lot more time and compensation than the initial prize money.

## THE LOVE OF THE CHASE

On the surface, at least, Polymath differs from commercial ventures in several ways. Most importantly, its challenges seem to be genuinely collaborative, rather than competitive. People make possibly small contributions that others build on, or they each solve part of the puzzle, rather than vying to be the victor.

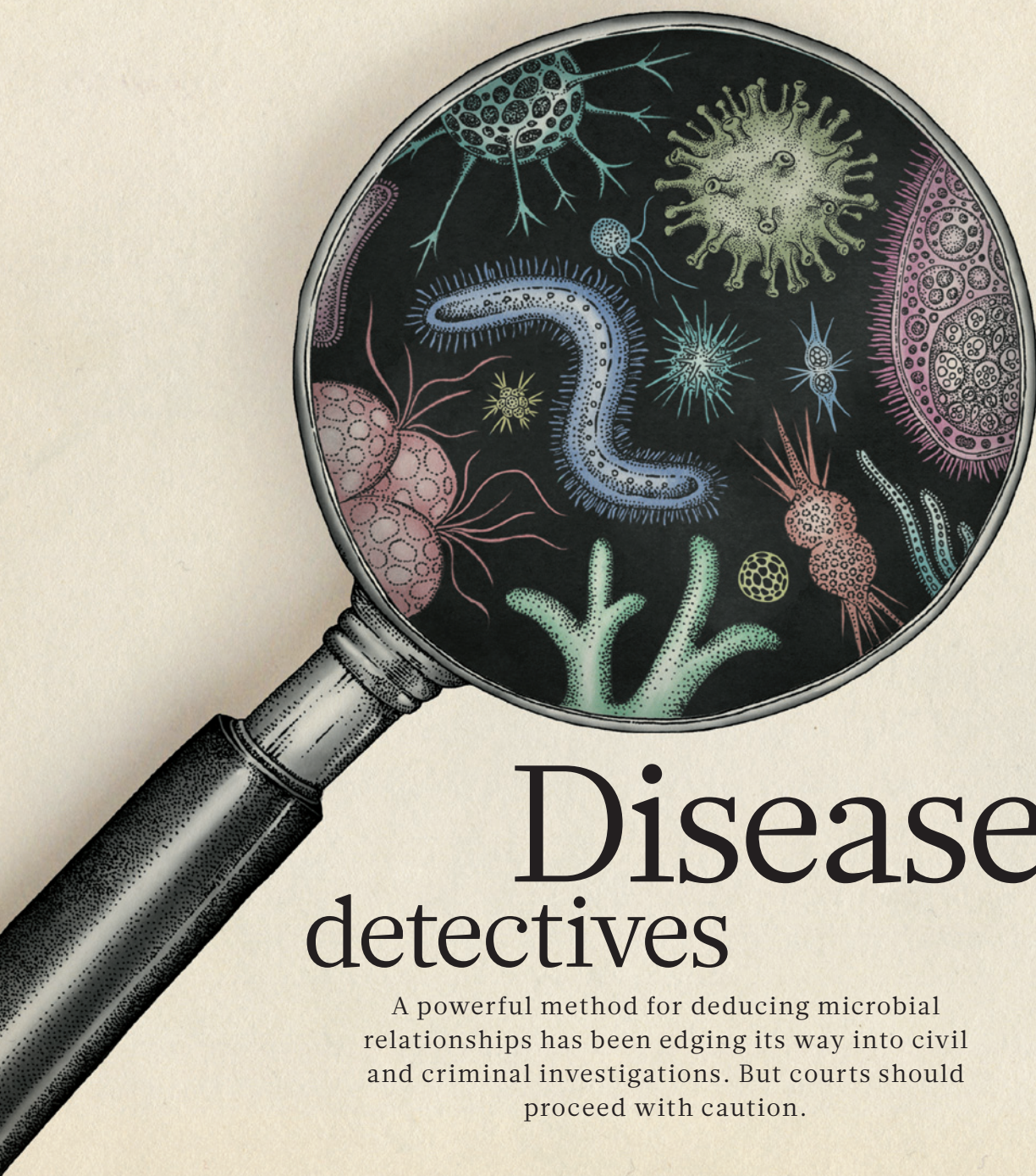
But Polymath and the commercial ventures also have some essential elements in common — starting with people’s fundamental reasons for participating. “Winning solvers rarely list the cash among their top motivations,” says InnoCentive founder Alph Bingham. “Their motivations are frequently more intrinsic, such as intellectual stimulation or curiosity to explore where an idea might lead.” InnoCentive aims to encourage this through non-cash incentives, such as prospects for further collaboration or joint press releases publicizing the winner. Kaggle invites participants to “compete as a data scientist for fortune, fame and fun”.

“Competition, if well posed, can help in science,” says Kitching. “But a poorly posed problem may just increase noise.” ■

**Philip Ball** is a freelance writer in London.

1. Polymath, D. H. J. Preprint at <http://arxiv.org/abs/0910.3926> (2009).
2. Zhang, Y. *Ann. Math.* (in the press).
3. Polymath, D. H. J. Preprint at <http://arxiv.org/abs/1402.0811> (2014).
4. Maynard, J. Preprint at <http://arxiv.org/abs/1311.4600> (2013).
5. Harvey, D., Kitching, T. D., Noah-Vanhoecke, J., Hamner, B. & Salimans, T. Preprint at <http://arxiv.org/abs/1311.0704> (2013).





# Disease detectives

A powerful method for deducing microbial relationships has been edging its way into civil and criminal investigations. But courts should proceed with caution.

By Shaoni Bhattacharya

**A**naesthetist Juan Maeso led a seemingly respectable life in the coastal Spanish town of Valencia. But he had a secret. Over the course of at least a decade, at two different hospitals, he regularly skimmed morphine from his patients, injecting himself just before using the same needle to administer their doses.

In 2007, Maeso was found guilty of infecting at least 275 people with hepatitis C, four of whom had died from complications related to the disease. He was sentenced to 1,933 years in prison, although he is expected to serve only 20 under Spanish law.

To this day, Maeso protests his innocence, saying that a patient must have infected him with the hepatitis C virus (HCV). But the

scientific evidence, which was published in full only last year<sup>1</sup>, overwhelmingly suggests otherwise. In that work, Fernando González-Candelas and his colleagues at the University of Valencia analysed and categorized almost 4,200 viral sequences in an effort to disentangle the path the infection followed, using a process known as phylogenetic forensics.

The method, which marries classic evolutionary-biology practices with modern sequencing technology, is increasingly being used in criminal and civil investigations, and for biodefence. A paper published this month<sup>2</sup>, for example, describes how the technique allowed scientists to trace the likely origin of an anthrax-laced batch of heroin that has been

killing users across Europe since 2009.

But the intersection of this science with the legal system makes many uneasy, says Anne-Mieke Vandamme, an evolutionary geneticist at the University of Leuven in Belgium, who has worked on 19 criminal cases since 2002, mostly for the defence. Unlike DNA evidence, which is routinely used in legal settings around the world, the results of phylogenetic forensics are rarely definitive. "You can never prove guilt," she says.

And there are social concerns. Many patient advocates feel that tracing the path of infection in civil and criminal cases may further stigmatize diseases such as AIDS. Now, as the field matures thanks to advanced sequencing

ILLUSTRATION BY KATIE SCOTT



and analytical tools, a team of experts led by Vandamme is trying to develop guidelines for best practice both on technical aspects of the work and on presenting the evidence in courts. She hopes, she says, “to make clear to lawyers, judges and prosecution officers the powers and limitations of these methods”.

### A common factor

Maeso's misdeeds started to come to light when doctors at Spanish utility companies noticed clusters of HCV among workers. While reviewing the workers' medical records, one doctor, Manuel Beltran, noticed that they had all had minor surgery at the Hospital Casa de Salud in Valencia some months before.

Beltran contacted the local public-health authority, sparking what turned out to be a massive investigation that scoured the records of more than 66,000 patients across two hospitals. Early on, it was clear that Maeso was a common factor in many of the cases. But prosecutors would need more evidence.

This is where phylogenetics came in. Some viruses, such as HCV, HIV and influenza, mutate incredibly quickly. By sequencing virus samples from different individuals — and then comparing tiny differences in their genomes — scientists can trace their evolution and place them on a family tree (see ‘Infectious forensics’). “What we are doing is a virus genealogy,” says Oliver Pybus, who studies evolution and infectious diseases at the University of Oxford, UK.

The process allows scientists to predict how likely it is that two or more infections are closely related and what their relationship is. And as the technology has steadily improved, such information has proved increasingly useful. Prosecutors have used it in cases of intentional infections, such as that of Richard Schmidt, who was in 1998 convicted by a Louisiana court of attempted second-degree murder. He injected his former girlfriend with HIV- and HCV-tainted blood, telling her that he was giving her a vitamin B12 jab. The method was used to help track the source of anthrax spores posted to several US politicians and media outlets in 2001. And it has been used to provide evidence in rape accusations and in investigations of child sexual abuse in which a disease was transmitted years earlier.

But phylogenetic evidence is very different in nature from the DNA matches that juries may be more familiar with, says Vandamme: the latter can often confirm or exclude a suspect's involvement in a crime with extremely high certainty. Phylogenetic analyses can offer supporting evidence — that a virus found in person A is very likely to have come from person B, say — but can never prove direct transmission on their own, she says. In the Maeso case, for example, prosecutors used viral phylogenies to corroborate evidence gained from epidemiological investigations.

González-Candelas and his colleagues

used patterns of changes in a highly variable region of the HCV genome to sort the viruses into clades, or branches of a tree that illustrate their evolutionary relationships. The scientists analysed, on average, 11 such viral sequences per person from 321 people believed to have been infected by Maeso and 42 controls — local HCV-infected patients with no known connection to the case. When printed out, the tree that the researchers developed was 11 metres long.

Using all the data, the team determined for each infected individual a ‘likelihood ratio’ — that is, the probability that the infection was related to Maeso's and others whom Maeso had presumably infected, versus the probability that it had come from a source unrelated to the outbreak. Because there were so many samples and a strong phylogenetic signal, the

“  
Just because we can  
test these relationships  
doesn't mean  
that it is always in society's  
best interest to do so.

”

likelihood ratios the scientists got were high. Most were higher than  $10^5$ , and the highest was  $6.6 \times 10^{95}$ , exceptionally strong support for this type of analysis.

The Valencia work was also notable in that it attempted to pinpoint when individuals had contracted the virus, using a ‘molecular clock’ technique. To do this, the researchers sampled the genetic diversity of viruses in each person, and then used the mutation rate of HCV in the outbreak to estimate when they had been infected. Almost two-thirds of the estimated dates of infection lined up with when the patients had visited the Valencia hospitals, adding to the evidence that Maeso was the source.

Presenting such data in court is challenging. González-Candelas and his colleague Andrés Moya had to lecture judges and attorneys for two days to familiarize them with evolutionary terms and concepts before launching into three weeks of scientific testimony.

One of the challenges was differentiating the process from conventional DNA testing in minds of the judges and lawyers. Court officials needed to understand that the analysis is inherently more messy: because HCV mutates so rapidly, the longer a person has an infection, the more viral diversity they are likely to have.

When that person infects another, any of the new variants could be passed on, and not all are necessarily sampled in the forensic process, meaning that a connection could be missed or the strength of the relationship distorted. “There is never a full match between strains

of linked individuals or even within a single individual,” says Vandamme. Even in cases in which the viruses from two or more individuals are clearly related, she says, “there are several possible trees, depending on when the samples are taken and how many variants were passed during transmission”.

In the Maeso case, the probabilities linking him to some of the patients were quite strong. But the method also helped to clear him of blame in 47 suspected cases. Those individuals were therefore not entitled to compensation. “Our analysis worked both ways,” says González-Candelas.

### Clear cut

Many scientists see the technique's ability to clear individuals of crimes as its greatest strength. In May 2004, five Bulgarian nurses and a Palestinian doctor were sentenced to death for allegedly infecting 426 children with HIV at the al-Fateh Hospital in Benghazi, Libya (see *Nature* **430**, 277; 2004). The ‘Benghazi Six’ had been detained and reportedly tortured since 1999.

A phylogenetic analysis had suggested that the particular strain of HIV involved had been circulating years before the arrival of the foreign health workers. *Nature* published the results online just before a retrial in 2006 (ref. 3), and although they did not sway the court from the death penalty at the time, the findings did seem to change diplomatic relations “quite considerably”, says Pybus, who was part of the research team. In 2007, the sentences were commuted to life imprisonment, and the health workers were extradited to Bulgaria, where they were pardoned by the Bulgarian president.

The field has developed since these watershed cases. In 2010, evolutionary biologist David Hillis of the University of Texas at Austin and his colleagues described methods that, for the first time, gave supportive evidence on the direction of viral transmission<sup>4</sup>.

To do this, investigators look closely at the populations of viruses in infected individuals. Because one person harbours many variants, only a subset is transmitted when they infect someone new. Once transmitted, this subset will multiply in number and continue to evolve rapidly. As a result, some viruses in the source may seem to be more closely related to the viruses in a recipient than to other viruses in the source, Hillis explains. Identifying these relationships can help to support a hypothesis of who infected whom.

New sequencing technologies are also increasing the power of what phylogenetics can do. “The more you sample, the better — the more you can fill in the gaps,” says Andrew Rambaut of the University of Edinburgh, UK, who worked with Pybus on the Benghazi case.

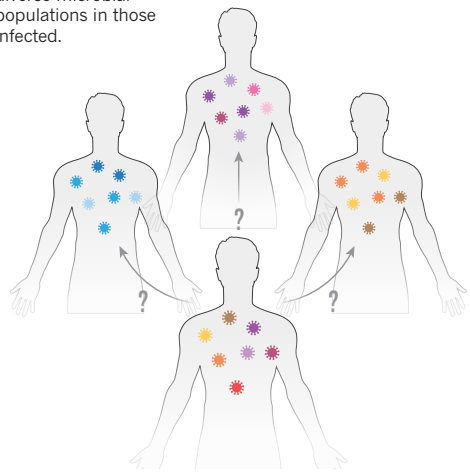
Rapid, automated sequencing can give a huge amount of information, says Bruce Budowle, who worked as a scientist for the



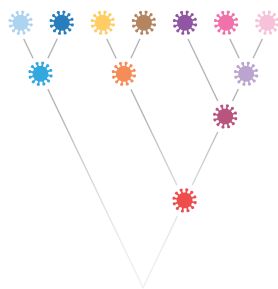
# Infectious forensics

Phylogenetics offers a way to establish relationships between microbes infecting several individuals and can be used as corroborating evidence when someone is suspected of infecting others with a disease.

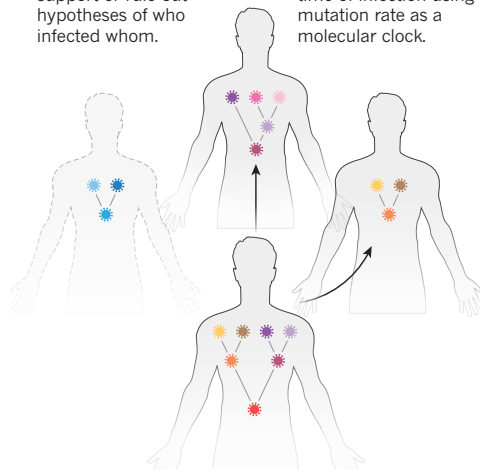
**1** Pathogen genomes can mutate quickly, creating diverse microbial populations in those infected.



**2** By sequencing highly variable regions of pathogen genomes scientists can build a phylogenetic tree that suggests how the microbes are related.



**3** The relatedness of the viral populations can support or rule out hypotheses of who infected whom.



**4** Pathogen diversity can also be used to corroborate time of infection using the mutation rate as a molecular clock.

US Federal Bureau of Investigation (FBI) for 26 years, and is now director of the Institute of Applied Genetics at the University of North Texas Health Science Center in Fort Worth.

But there is a catch. The masses of data generated have to be processed in a way that is useful for forensic purposes, he says: if software or methods for developing the phylogenies are not properly validated, findings could be challenged in court. Many useful applications developed in academia may not be subjected to such validation because it is not a priority until the methods are needed for forensics work. “We often get so enamoured with our science, and then something comes up and you have to use it,” Budowle says.

Budowle and his colleagues were in exactly this situation during the 2001 anthrax attacks. To piece together the bacterial phylogenies, they had to use an unvalidated method developed by an academic microbiologist — Paul Keim at Northern Arizona University in Flagstaff. “It gave us guidance on what may have occurred, and pointed to a laboratory strain rather than one found in nature,” says Budowle.

This helped investigators to track the microbe back to a laboratory strain called Ames. A variant of this strain was later linked to Bruce Ivins, a microbiologist at the US Army Medical Research Institute of Infectious Diseases at Fort Detrick in Maryland. It is impossible to say how important the phylogenetic data would have been because the case never went to court. After the FBI began to investigate Ivins in 2008, he committed suicide (see *Nature* **454**, 672; 2008).

The high stakes involved in many cases using phylogenetics has led to other concerns — notably, that the technique might contribute to the stigmatization of people infected with HIV, or to the criminalization of HIV transmission. In several countries, people have been charged and prosecuted for murder,

attempted murder or bodily harm for unwittingly transmitting the virus to a sexual partner or not disclosing that they have it — even if it was not transmitted. Some researchers think this dissuades people from coming forward for testing.

For this reason, some in the phylogenetics field have stopped working on criminal cases altogether or are extremely selective about the cases they take on. Andrew Leigh Brown, who studies HIV evolution at the University of Edinburgh, assisted in the first-ever investigations using phylogenetics for forensics in the early 1990s. But he no longer works on such cases.

Leigh Brown contributed to a policy document, published by the Joint United Nations Programme on HIV/AIDS last May, calling for an end to prosecution for HIV transmission other than in clearly intentional cases. Where intent is apparent, phylogenetic forensics should be used carefully and with other supporting evidence, the document advises: the burden of proof must be high.

## Promise and pitfalls

Vandamme laments the lack of guidance for researchers in phylogenetic forensics. She hopes the guidelines that she and other concerned specialists are currently drafting will help scientists to avoid misinterpretations. In addition to providing tools for presenting findings in court, Vandamme hopes to reach a consensus on technical issues such as how to find a control population and which genetic regions of a virus should be assessed. “This will help the increasing number of phylogenetic experts that are called by court to provide their expertise in a forensic context,” she says.

Moving forward, scientists say that they will continue to carefully pick which cases they agree to get involved in. “Just because we can test these relationships doesn’t mean that it is always in society’s best interest to do so,”

says Hillis. “My own choice is to work on such analyses only when they are used to test a clear crime that goes beyond accidental viral transmission, such as rape or attempted murder.”

Although the Valencia case is several years old, publication of the data has renewed discussion about phylogenetic forensics, its potential uses and its pitfalls, not just in legal proceedings, but also in biodefence. To that end, González-Candelas was invited to speak at a meeting in Zagreb, Croatia, last October to hammer out the main challenges that the field faces.

The workshop, hosted by the US National Academy of Sciences and the UK Royal Society, among others, has not yet published its findings. But Budowle says that there is a major conflict in the field over access to data, with members of the biosecurity and intelligence communities wishing to keep data confidential because of concerns about risk.

Where lives may hang in the balance, getting it right is crucial, says Budowle. The answers from phylogenetic forensics could mean sending an individual to prison or ostracizing a patient population. In cases involving bio-weapons, the conclusions could mean levying sanctions against a country or even going to war. Validating the tools and tests is all the more challenging in an area evolving nearly as fast as the microorganisms it traces. “It’s still an emerging field,” Budowle says. “We expect that what we are using today, we probably won’t be using two years from now.” ■

**Shaoni Bhattacharya** is a freelance science writer based in London.

1. González-Candelas, F., Bracho, M. A., Wróbel, B. & Moya, A. *BMC Biol.* **11**, 76 (2013).
2. Hanczaruk, M. et al. *Emerg. Infect. Dis.* **20**, 322–323 (2014).
3. de Oliveira, T. et al. *Nature* **444**, 836–837 (2006).
4. Scaduto, D. I. et al. *Proc. Natl Acad. Sci. USA* **107**, 21242–21247 (2010).



POLARIS/EYEVINE

Timothy Brown was cured of HIV after a bone-marrow transplant for leukaemia.

## VIROLOGY

# Vanquishing HIV

**Sharon Lewin** welcomes a book tracing how two men with HIV were functionally cured.

In the 30 years since HIV was identified as the cause of AIDS, antiretroviral treatment has changed the infection from a death sentence to a chronic, manageable disease. Now, treatment is lifelong but often consists of just a tablet a day; resistance to the drugs is rare; and side effects are infrequent. However, the virus integrates into the patient's DNA and becomes silenced, in what is known as latency, and no tools have yet been found to eliminate it. When the antiretrovirals are stopped, infectious virus re-emerges.

But since at least 2009, a cure for HIV has been widely accepted as possible, thanks to a handful of reported cases. Members of this select group are functionally cured, often in unusual circumstances: the virus is detectable at low levels, but is under control without antiretrovirals. Now, in *Cured*, Nathalia Holt — an immunologist who has done groundbreaking research on gene therapy as a cure strategy — traces the fascinating cases of two people who have effectively vanquished HIV.

The Berlin patients, both diagnosed in the city, are 'Christian' (not his real name), and Timothy Brown, an American. *Cured* covers their personal stories and the science that their cases inspired, as well as the scientific

and political history of HIV.

Christian, Holt tells us, was functionally cured after receiving antiretroviral treatment and a fairly toxic cancer drug, hydroxyurea, within days of infection. Brown was cured of HIV after a bone-marrow transplant for leukaemia; the donor lacked the CCR5 receptor, which normally ushers HIV into human cells, and so was naturally resistant to the virus. Both cases were reported in *The New England Journal of Medicine* (*NEJM*), in 1999 and 2009 respectively.

The cases are similar in many details, as Holt relates. Both men were diagnosed in the mid-1990s — when infection with HIV heralded a real prospect of early death. Both were cared for at some time by the same dedicated family doctor, Heiko Jessen. Both had access to life-saving antiretrovirals. Both their identities were initially hidden. And



**Cured: How the Berlin Patients Defeated HIV and Forever Changed Medical Science**  
NATHALIA HOLT  
Dutton: 2014.

both cases became the focus of media stories claiming that a cure had been found, even though the treating physicians had carefully avoided using that word in interviews.

The Berlin patients also highlight the often vicious and competitive nature of science — rife with big egos, high stakes and a reluctance to brook unexpected findings from outsiders. Much of the innovation in how they were managed came from two unknown German physicians: Jessen and Gero Hütter, Brown's haematologist, who tested unconventional treatments outside formal clinical trials. The big science, which demanded an analysis of how much virus was left and why it was under control, was driven largely by well-known US investigators. The tensions between the two cultures are telling.

Jessen, for example, ended up as fourth author of the 1999 *NEJM* paper on Christian's case; as Holt explains, he no longer works with any of his US-based collaborators. Hütter's initial submission to *NEJM* was rejected, and his presentation of Brown's case at the 2008 Conference on Retroviruses and Opportunistic Infections in Boston, Massachusetts — the premier meeting for HIV scientists — was largely ignored. In Holt's view, it was only



when the American Foundation for AIDS Research started to take an interest that Hütter engaged well-recognized names, and *NEJM* eventually accepted his paper.

More importantly, the Berlin patients' cases have inspired new scientific ideas. We still do not know what led to either cure. Many researchers think that Christian is probably an 'elite controller', one of the 1% of people with HIV whose genetic make-up gives them an effective immune response to the virus. So he may have controlled his virus at the outset. However, his case raised the possibility that very early treatment could reduce or prevent the formation of long-lived reservoirs, as was demonstrated last year in 14 people with HIV in the VISCONTI (Viro-Immunological Sustained Control after Treatment Interruption) study in France. Christian's case also revealed the importance of the role of the T-cell immune response in controlling the virus — a major stimulus to HIV vaccine development.

With Brown, was the cure a reaction of the donor marrow against his immune system, a process called graft-versus-host disease? Was it down to the intensive conditioning treatment he received before the transplant? Or was it that the donor marrow was CCR5-negative? A promising treatment based on eliminating CCR5 using gene therapy was developed in a mouse model by a team including Holt, and is now being tested in clinical trials.

I enjoyed the book but I do have quibbles. Holt's discussions can be dense and detailed. Her interviews, which tend to focus on US-based leaders in HIV science, make it seem as if little discovery was being led from elsewhere, even though there have been significant contributions from many other countries, not least France, where the initial discovery of the virus was made. This is an important book, nevertheless.

Although the Berlin patients' case reports are anecdotes, they convinced a sceptical scientific world that a cure was possible, and inspired lines of enquiry and investment. On World AIDS Day 2013, US President Barack Obama announced that his administration would give an extra US\$100 million to research towards a cure. Most importantly, the cases belong to a significant handful that is giving hope to millions of people living with HIV. ■

**Sharon Lewin** is a clinician scientist working on approaches to finding a cure for HIV. She is professor and head of the department of infectious disease at Alfred Health and Monash University in Melbourne, Australia, and co-head of the Centre for Biomedical Research at the Burnet Institute in Melbourne.  
e-mail: sharon.lewin@monash.edu

## PHYSICS

# Inside utter strangeness

David Seery applauds a primer on the incongruous world of quantum mechanics.

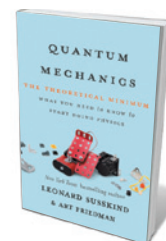
It is all too easy to compound the perplexities of quantum mechanics. Monographs are often weighed down by abstruse mathematics; other treatments struggle to separate physics from formalism. The problem is to communicate the subject's intrinsic strangeness without burdensome mathematical demands — but also without resorting to gee-whiz platitudes that assert, but do not explain, the incongruities between the quantum world and everyday experience.

Leonard Susskind and Art Friedman's *Quantum Mechanics* is the second entry in Susskind's *Theoretical Minimum* series, based on an Internet course of the same name and designed to satisfy a mathematically literate audience looking for more detail than can be found in a popular-science offering. The authors set their aims at the outset: "the goal", they say, "is not to hide the utter strangeness of quantum logic but to bring it out into the light of day".

To achieve this, Susskind, a physicist, and Friedman, a data engineer, eschew the analogies and qualitative descriptions typically used to explain quantum mechanics to a lay audience. Instead, readers are expected to invest time in getting to grips with mathematical concepts such as complex numbers, vector spaces, linear operators and tensor products, all of which are deftly explained in a series of interludes. In return, the authors offer self-contained chapters that vividly articulate aspects of the theory: the space of states, time evolution, uncertainty, entanglement, particle dynamics and so on, leading eventually to the harmonic oscillator, a quantized mechanical spring. This is the most important of all simple quantum systems because quantum field theory, the discipline's description of the forces in nature, interprets particles as harmonic oscillators.

The selection of concepts is close to what would be found in a typical undergraduate course. It steers clear of the philosophical morass surrounding interpretation and focuses on how quantum mechanics is used and understood today, rather than its development or the human stories behind it. This is a book about physics, not history.

The writing is fresh and immediate, with plenty of detail packaged into the smooth narrative. It will not teach anyone to carry out complex calculations, and it may leave the reader with questions that can be resolved



**Quantum Mechanics: The Theoretical Minimum: What You Need to Know to Start Doing Physics**

LEONARD SUSSKIND  
AND ART FRIEDMAN  
Basic Books/Allen  
Lane: 2014.

only by digging into more conventional textbooks. But on their own terms, I found Susskind and Friedman's explanations crisp and satisfying. The chapters on entanglement — in which particles interact in such a way that they cannot be described independently — are especially clear, taking pains to draw out the distinction between quantum entanglement and correlation. In either case, we can predict something

about the relationship between measurements in different parts of a composite system. The puzzling feature of entanglement is that, although we may know everything about the state, it might be impossible to predict anything about the outcome of these measurements individually.

Susskind and Friedman's choices will suit their intended readership, but might make the book less attractive to others. Those with the determination to navigate the complexities of Hermitian operators, normalizable wavefunctions or creation-annihilation operators will struggle to find a book that serves them better. Secondary-school pupils, however, may find the more detailed passages too demanding; university students might find that the early chapters proceed slowly, and that overall the book is too light on detail to serve as a principal text.

Still, I maintain a clear recollection of the bewilderment with which I struggled through my own university quantum-mechanics courses. For students in a similar position, trying to draw together the fragments of formalism into a clear conceptual whole, Susskind and Friedman's persuasive overview — and their insistence on explaining, with sharp mathematical detail, exactly what it is that is strange about quantum mechanics — may be just what is needed. ■

**David Seery** is reader in mathematics and physics at the University of Sussex in Brighton, UK.  
e-mail: d.seery@sussex.ac.uk

## ARTS

# Eclipse of power

Jay M. Pasachoff and Naomi Pasachoff appraise Alexander Borodin's solar-inspired opera.

**A**mong the astronomical phenomena that spur composers to creativity, total solar eclipses figure rarely. A great exception is the one that inspired the nineteenth-century opera *Prince Igor* by Alexander Borodin. Borodin, a composer, surgeon and research chemist, based the work on a twelfth-century epic poem about Russia's foundation, *The Lay of the Host of Igor*, which features a momentous eclipse. Now, for the first time in nearly a century, *Prince Igor* is being performed at New York's Metropolitan Opera, with star bass Ildar Abdrazakov in the title role.

The opera had a convoluted genesis. After working on it intermittently for 18 years, Borodin died in 1887, leaving it unfinished; Russian composers Nikolai Rimsky-Korsakov and Alexander Glazunov then provided most of the orchestrations. The Met's new production, a joint venture with Amsterdam's De Nederlandse Opera, reconceives the work, making use of decades of musicological research. Director Dmitri Tcherniakov and conductor Gianandrea Noseda have jettisoned much of the Rimsky-Korsakov and Glazunov material, incorporated newly found pieces by Borodin himself, and rearranged some scenes after referring to Borodin's notes.

This fresh version — sung in Russian for

the first time here — certainly makes for an effective spectacle. Projected video footage in black and white with vivid touches

of colour (such as red on a bloodied face) fleshes out aspects of the story. For instance, in the first act, conceived as a dream sequence of Igor's as he lies wounded in the field, the battle scenes are shown in this way. These are lent a certain poignancy by the fact that Borodin had worked as a military surgeon for a year. (He was, however, primarily a chemist. Best known for his research on aldehydes, he was also one of two independent discoverers of the aldol reaction, a means of forming carbon-carbon bonds in organic chemistry.)

The opera's plot hinges on the defeat, psychological journey and redemption of Prince Igor Svyatoslavich. A historical ruler of Putivl in modern-day Ukraine, he is at war against the Polovtsy nomads, who have laid waste to Russia. The eclipse appears just five minutes into the prologue, a portent of Igor's military failure. The light coming through the windows darkens for a few seconds. "The sky grows

## Prince Igor

*The Metropolitan Opera, New York City.*

*Until 8 March.*

*Live in HD worldwide transmission on 1 March, then available on DVD.*

dark? What does it mean? It is a sign from heaven," sings the chorus, begging the soldiers not to go to war. "The Sun is a crescent, like the Moon." The solar motif runs through the opera: in the third act, Igor, devastated by his defeat, evokes the Sun again: "I will save my people ... the Sun will shine again." Ultimately, Borodin throws off the pall of superstition to show that humans — not celestial events — are in charge. At the very end, the prince, with an abruptness that we found unconvincing, begins to salvage wood from the ruins to rebuild his city, once again leading his people.

Some six years before this magnificently staged and sung psychological drama reached the Met stage, we were on our way to Siberia to reconnoitre ahead of a total solar eclipse. Stopping off in St Petersburg, we encountered the eclipse-centred story of Prince Igor for the first time. A stunning 1942 painting by Russian artist Nicholas Roerich in the State Russian Museum shows Igor and his soldiers viewing the corona-rimmed lunar silhouette in the sky. Intrigued, we later consulted maps to find that there were indeed total solar eclipses visible from the Russian steppes in the twelfth century. Totality from the 1 May 1185 eclipse ended in what is now Ukraine — the very territory in which Prince Igor was jolted by daytime darkness. ■

**Jay M. Pasachoff** is *Field Memorial Professor of Astronomy at Williams College, Williamstown, Massachusetts, and Chair of the American Astronomical Society's Historical Astronomy Division*. **Naomi Pasachoff**, a research associate at Williams College, is a biographer of Marie Curie and other scientists.  
e-mail: [eclipse@williams.edu](mailto:eclipse@williams.edu)

## NATURE.COM

For more on science and opera:

[go.nature.com/dqsxzs](http://go.nature.com/dqsxzs)



Nicholas Roerich's 1942 painting *Igor's Campaign* depicts the eclipse at the heart of *Prince Igor*.

ALEXEY BUSHKIN/RIA NOVOSTI





John Sloboda at Milton Court, Guildhall School of Music & Drama in London.

## Q&A John Sloboda

# Melodic psychologist

*London-based music psychologist John Sloboda explores the subconscious connections and disjunctions between musicians and their audiences. He discusses his experiments on the 'emotional hotspots' experienced by listeners and the surprising power of improvisation.*

### What role does psychology have in classical music today?

There is something of a crisis in the classical music world. Audiences are less willing to treat composers like gods, with musicians as the faithful transmitters of their intentions. Concert attendance is declining. A culture of intense competition and elitism can set young musicians up to be either scared or dismissive of the public. Classical musicians may need to learn how to connect with their audiences better — to talk to them, look them in the eye and improvise. They need to remind audiences of the special unpredictability of live music. We are researching how audience motivation and engagement change when some of these aspects are introduced into concerts.

### How did you work with musicians early on?

From the start, my research was carried out in real rehearsal rooms, not in a darkened cubicle with buttons to press. I focused on what happened when instrumentalists

read musical notation, and found that good readers don't look at all of the notes, but seem to be able to pick out recurring patterns. This allows them to read with minimal effort and to make 'intelligent mistakes' that deviate from the score, but in musically appropriate ways. In an early study, I inserted deliberate mistakes into a piece of music. Poor readers painfully and slowly played the mistakes as written. Good readers played what they expected to be there, because they had extracted the essential structure of the piece. This raised a bigger question: how do we apprehend the aesthetic and emotional meaning of music?

### How did you begin to work with concert audiences?

From research on 'colder' cognitive areas such as memory and perception, I moved on to 'hotter' subjects — emotion, passion and motivation, the drivers that pull you out of bed in the morning. In an early study, I asked 100 people to tell me which specific moments

in recorded music triggered physical responses such as tears, shivers down their spine or hair standing on end. These 'emotional hotspots' tended to occur at moments that manipulated listeners' expectations, such as dissonant notes that were held but eventually resolved. When I shared my results with film composers and hotel bar pianists, they said: "Yeah yeah, we know this already." But it was one of the first scientific studies to show that listeners feel the strongest emotions in response to the unexpected.

### Does that have implications for musical improvisation?

In the eighteenth century, musicians would embellish and improvise, never playing a concerto the same way twice. A team of researchers at Imperial College London and the Guildhall School of Music & Drama, also in London, are investigating the impact of performances that reintroduce the lost art of classical improvisation to chamber music. In one experimental concert, we told audiences the two ways in which they would hear the same music, but we didn't tell them the order. One was a prepared composition; the other was improvised in real time by the performers. Using an electroencephalograph to measure brain activity, we found greater synchrony between the brains of musicians and listeners during the improvised performances, especially at moments involving a surprise, such as an unexpected shift in harmony or dynamics. In general, audiences rated improvised performances as more emotionally engaging.

### Tell me about your work in drawing audiences closer.

Before a November 2013 concert of Britten Sinfonia, a UK chamber ensemble, we held an open dress rehearsal and audience discussion on the nature and value of the collaboration between musicians in putting on a programme of contemporary work. After a concert earlier this month, the audience gave feedback to the musicians on what they heard and felt — an opportunity that was eagerly and thoughtfully grasped. Such initiatives show concert-goers that they are not 'ticket fodder', but more like consultants or collaborators. We deployed audience questionnaires at the November concert and will use focus groups to investigate the impact of these interventions. Also, at a workshop on 1 March, we will share first findings with the musicians and audiences involved. Although qualitative, our results may inform more intensive and controlled research, in which specific features are deliberately included or excluded from different events, to assess their impact. We don't know precisely how it will change the concert experience, but we are eager to find out. ■

INTERVIEW BY JASCHA HOFFMAN

# Correspondence

## Expand fundraising by Brazil's institutes

It is time for Brazil's cash-strapped universities to embrace the fundraising campaigns that are common at prestigious institutions worldwide.

For instance, the money raised by Harvard University in Cambridge, Massachusetts, in its latest campaign (<http://campaign.harvard.edu>) exceeds the individual annual budgets of two major Brazilian science-funding agencies. Furthermore, the £1.2 billion (US\$2 billion) raised by the University of Cambridge, UK, to mark its 800th anniversary in 2009 is comparable to the annual budget of the University of Sao Paulo.

Such initiatives are still unusual in Brazil, where government-funded universities are the main engine of higher education and science. The idea of private donations is widely regarded with suspicion, being perceived as a corrupt route for 'buying' illegal advantages or as potentially providing the state with an excuse to cut back investment.

A few of Brazil's leading academic institutions are starting to encourage private benefactors, so the challenge now is to increase that momentum and expand the fundraising enterprise.

**Tiago Campos Pereira**  
*University of Sao Paulo, Brazil.*  
[tiagocampospereira@ffclrp.usp.br](mailto:tiagocampospereira@ffclrp.usp.br)

## Stamina therapies: time to call a halt

Mauro Ferrari, the nominated chair of a committee set up to evaluate the controversial stem-cell therapy used by Italy's Stamina Foundation, participated last month in a popular television programme, *Le Iene* (see *Nature* <http://doi.org/rkj>; 2014).

Irrespective of the ambiguity of some of his comments, as explained in a Correction to your report, we believe that he should

have declined the TV interview, given that *Le Iene* is widely seen as an advocate of Stamina.

Stamina's therapy has, incredibly, flouted all the laws and rules that are in place to protect patients. The health ministry's national institute (ISS) and the Italian Medicines Agency (AIFA) have already forbidden the clinical use of cells created by the Stamina procedure because of their failure to comply with safety standards.

We have written to the health ministry calling for an end to Stamina's stem-cell treatments. The ministry needs to explain to Parliament that a scientific committee is no longer necessary, in the face of evidence that 36 patients treated with the Stamina protocol — whose clinical progress was followed by the Civil Hospital of Brescia — have shown no improvement.

**Silvio Garattini** *Mario Negri Institute for Pharmacological Research, Milan, Italy.*  
[silvio.garattini@marionegri.it](mailto:silvio.garattini@marionegri.it)  
**Giuseppe Remuzzi** *Mario Negri Institute, Bergamo, Italy.*  
**Gianluca Vago** *University of Milan, Italy.*  
**Alberto Zangrillo** *University Vita-Salute San Raffaele, Milan, Italy.*

## Stamina therapies: let the record stand

In our view, the Correction was not justified to your online News story reporting remarks made last month by Mauro Ferrari in a television interview about Italy's Stamina Foundation and its controversial stem-cell treatments (*Nature* <http://doi.org/rkj>; 2014). Ferrari is the proposed chair of the second scientific committee set to investigate the Stamina protocol.

First, we find it inappropriate that the Correction led to the removal of an ambiguous statement by Ferrari about the purported opportunities

Stamina's therapies might present for Italy.

Second, you corrected his alleged reference to Stamina as "the first important case for regenerative medicine [in Italy]", saying that he was in fact referring to the Stamina case as "the first important court case" in the country. However, there was no reference to a court case in Ferrari's statements in the TV interview as transmitted.

Ferrari also said in this interview that decisions following the committee's assessment would affect future generations of patients and "many other cases" to come. Regulation and approval of new therapies rests with the Italian Drug Agency operating within relevant laws, however, not with a scientific committee chair.

The Stamina case has made Italy a battlefield for local and international commercial interests and anti-regulatory lobbies. These misrepresent the regulation of new therapies as an obstacle to the rapid provision of cures to patients, rather than as a way of protecting people from abuse and fraud.

Last year, Italy came close to deregulating mesenchymal stem-cell therapies (as supposedly used in Stamina's protocol) by reclassifying them as transplants, which would bypass the Italian Drug Agency and open the way to peddlers of unproven therapies. This was fortunately blocked by Italian scientists. The 2014 Public Service Award later granted to three of us (P.B., E.C. and M.D.L.) by the International Society for Stem Cell Research is a token of the global impact of the issues, as raised by many similar cases around the world.

**Paolo Bianco** *Sapienza University of Rome, Italy.*  
[paolo.bianco@uniroma1.it](mailto:paolo.bianco@uniroma1.it)  
**Elena Cattaneo** *University of Milan, Italy.*  
**Michele De Luca** *University of Modena and Reggio Emilia, Modena, Italy.*  
**Luca Pani** *Italian Medicines Agency (AIFA), Rome, Italy.*

## Global fund needed for STEM education

To be competitive in today's global economy, developing countries need a workforce with a strong education in science, technology, engineering and mathematics (STEM). While the post-2015 United Nations development agenda is still under discussion, we propose that a global fund should be set up to back the most effective and innovative STEM programmes in the developing world and to improve the accessibility and quality of STEM education worldwide.

Existing STEM educational initiatives differ in their approach, scope, type, target populations and funding sources. A coordinated global STEM fund would bridge the gaps, provide more teachers, offer wider access to resources and programmes, stimulate innovation and recruit more women and students from minorities.

International organizations, such as the World Bank and the United Nations Educational, Scientific and Cultural Organization (UNESCO), could help to realize this STEM fund by providing crucial infrastructure, including access to the global educational network and to the management, financial and technical support it would need to begin operations.

**Fanuel Muindi** *Massachusetts Institute of Technology, Cambridge, USA.*  
[fmuindi@mit.edu](mailto:fmuindi@mit.edu)  
**Moytrayee Guha** *Brigham and Women's Hospital, Harvard Medical School, Boston, USA.*

### CONTRIBUTIONS

Correspondence may be sent to [correspondence@nature.com](mailto:correspondence@nature.com) after consulting the guidelines at [go.nature.com/cmchno](http://go.nature.com/cmchno). Alternatively, readers may comment online: [www.nature.com/nature](http://www.nature.com/nature).



## Is SIRT2 required for necroptosis?

ARISING FROM N. Narayan *et al.* *Nature* **492**, 199–204 (2012)

Sirtuins can promote deacetylation of a wide range of substrates in diverse cellular compartments to regulate many cellular processes<sup>1,2</sup>; recently, Narayan *et al.*<sup>3</sup> reported that SIRT2 was required for necroptosis on the basis of their findings that SIRT2 inhibition, knockdown or knockout prevented necroptosis. We sought to confirm and explore the role of SIRT2 in necroptosis and tested four different sources of the SIRT2 inhibitor AGK2, three independent short interfering RNAs (siRNAs) against *Sirt2*, and cells from two independently generated *Sirt2*<sup>-/-</sup> mouse strains; however, we were unable to show that inhibiting or depleting SIRT2 protected cells from necroptosis. Furthermore, *Sirt2*<sup>-/-</sup> mice succumbed to tumour-necrosis factor (TNF)-induced systemic inflammatory response syndrome (SIRS) more rapidly than wild-type mice, whereas *Ripk3*<sup>-/-</sup> mice were resistant. Our results therefore question the importance of SIRT2 in the necroptosis cell death pathway.

There are seven mammalian sirtuins, and work has focused on SIRT1, the closest homologue to the founding member of the sirtuin family, *Saccharomyces cerevisiae* Sir2. Mammalian SIRT2 has been reported to regulate cellular metabolism, division and differentiation<sup>1,2</sup>. A recent study suggested an additional role, namely that SIRT2 is required for programmed necrosis, otherwise known as necroptosis<sup>3</sup>. Using co-immunoprecipitation followed by mass-spectrometric analysis, Narayan *et al.*<sup>3</sup> found that SIRT2 interacted with RIPK3 (called RIP3 in ref. 3), a kinase that is essential for TNF-induced necroptosis<sup>4–6</sup>. Using a SIRT2 inhibitor, AGK2 (ref. 7), they observed that SIRT2 deacetylase activity was required for formation of the RIPK1–RIPK3 (RIPK1 is called RIP1 in ref. 3) complex in response to the necroptosis-inducing stimulus of TNF, plus the caspase inhibitor z-VAD-fmk, and the translation inhibitor cycloheximide. Narayan *et al.*<sup>3</sup> proposed that SIRT2-mediated deacetylation of a lysine

residue near the RIPK3-interacting RHIM motif of RIPK1 was required for RIPK1–RIPK3 association and necroptosis induction. Consistent with this hypothesis, they showed that knockdown, knockout or inhibition of *Sirt2*/SIRT2 prevented TNF-induced necroptosis *in vitro*<sup>3</sup>.

The necroptotic cell death pathway has attracted interest because inhibiting it, particularly in conjunction with blocking apoptosis, is thought to have the potential to ameliorate diverse inflammatory and possibly also degenerative diseases<sup>8–11</sup>. Notably, Narayan *et al.*<sup>3</sup> reported that genetic ablation or pharmacological blockade of *Sirt2*/SIRT2 afforded mice significant protection from injury caused by cardiac ischaemia reperfusion.

The therapeutic potential of these findings prompted us to confirm and explore the role of SIRT2 in necroptosis. We tested the ability of four different sources of the SIRT2 inhibitor, AGK2, at a broad range of concentrations, to inhibit necroptosis triggered by TNF, Smac mimetic and the caspase inhibitor Q-VD-OPh (TSQ), TNF plus z-VAD-fmk (TZ) or TNF plus z-VAD-fmk and cycloheximide (TCZ). In contrast to the findings of ref. 3, AGK2 failed to inhibit TNF-induced necroptosis in our experiments (Fig. 1a and Appendix Fig. 1). As previously described<sup>7</sup>, AGK2 (Sigma) increased levels of acetylated tubulin in NIH 3T3 cells, validating its ability to inhibit SIRT2 at the doses used (Appendix Fig. 1). Narayan *et al.*<sup>3</sup> found that two independent short hairpin RNAs (shRNAs) used to knock down *Sirt2* expression prevented TZ-induced necroptosis in L929 cells. In our experiments, three independent siRNAs, which reduced *Sirt2* expression by greater than 80%, failed to inhibit TZ-induced necroptosis in L929 cells (Fig. 1b and Appendix Fig. 1). We also tested mouse embryonic fibroblasts (MEFs) and bone-marrow-derived macrophages (BMDMs) from two independently

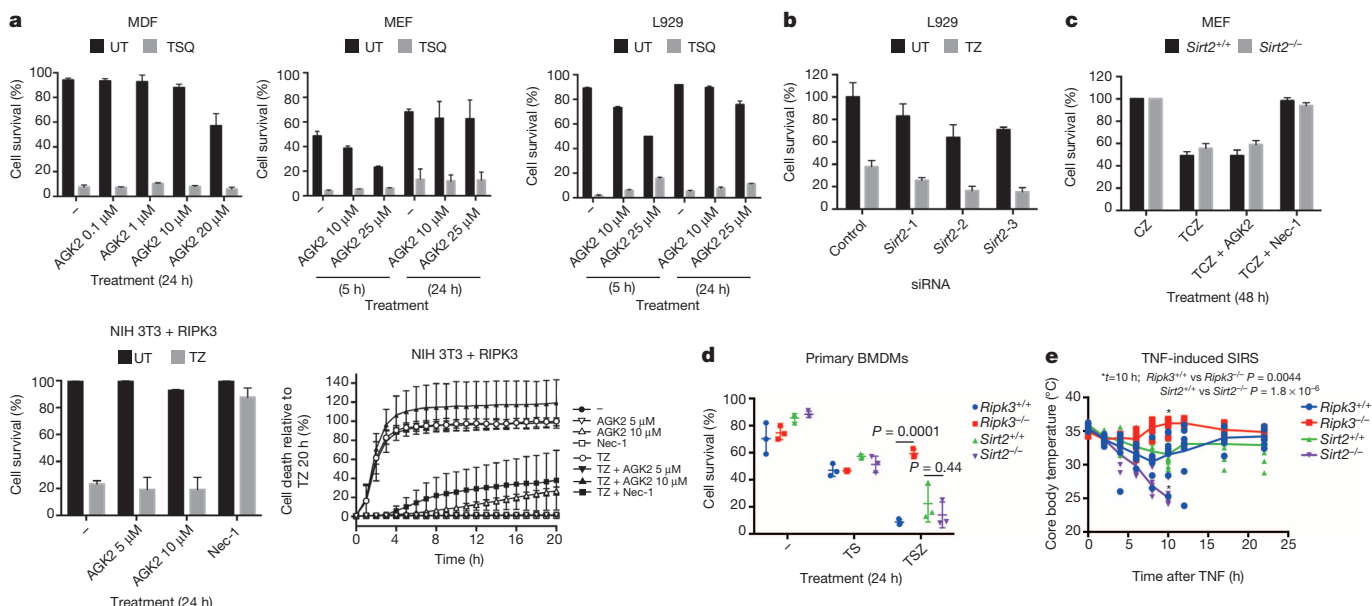


**Figure 1** | Neither chemical inhibition nor genetic depletion of SIRT2 inhibits TNF-induced necroptosis. **a**, Indicated cell lines were treated with the indicated necroptotic stimuli in the presence or absence of AGK2. **b**, L929 cells were transfected with siRNAs targeting *Sirt2* or a control siRNA before treatment with TZ. **c**, MEFs derived from *Sirt2*<sup>-/-</sup> and wild-type (*Sirt2*<sup>+/+</sup>) mice were treated with TCZ with or without the indicated inhibitors. Plots in panels **a–c** represent the mean  $\pm$  standard deviation (s.d.) of two biological

repeats (MEFs, mouse dermal fibroblasts (MDFs)) or the mean  $\pm$  s.d. of three independent repeats (L929, NIH 3T3). **d**, BMDMs isolated from *Sirt2*<sup>+/+</sup>, *Sirt2*<sup>-/-</sup>, *Ripk3*<sup>+/+</sup> or *Ripk3*<sup>-/-</sup> mice ( $n = 3$  per genotype) were treated with TSZ. **e**, Core body temperature of *Sirt2*<sup>+/+</sup>, *Sirt2*<sup>-/-</sup>, *Ripk3*<sup>+/+</sup> or *Ripk3*<sup>-/-</sup> mice ( $n = 10$  per genotype) injected with 300  $\mu\text{g kg}^{-1}$  TNF. An unpaired Student's *t*-test was used to determine *P* values in **d** and **e**. C, cycloheximide; Q, Q-VD-OPh; S, Smac mimetic; T, TNF; Z, z-VAD-fmk.

generated *Sirt2* knockout mouse strains (Appendix Fig. 1), but found neither cell type to be protected from TNF-induced necroptotic death (Fig. 1c, d).

Finally, Narayan *et al.*<sup>3</sup> observed that *Sirt2*-deficient mice were protected from cardiac ischaemia-reperfusion injury and concluded that transient inhibition of SIRT2 might provide protection from diseases involving necroptosis. Because RIPK3-deficient mice have not been tested for their ability to resist cardiac ischaemia-reperfusion injury, we tested the response of *Sirt2*<sup>-/-</sup> mice to a well-established RIPK3-dependent necroptotic insult: we injected wild-type, *Ripk3*<sup>-/-</sup> and *Sirt2*<sup>-/-</sup> mice with TNF and monitored their body temperature. As previously described<sup>8</sup>, the core body temperature of wild-type mice dropped rapidly after injection of 300 µg kg<sup>-1</sup> of TNF, and some of these animals died within the indicated time frame. In contrast, *Ripk3*<sup>-/-</sup> mice maintained normal body temperature and all survived. Far from being protected against this necroptosis-inducing insult, *Sirt2*<sup>-/-</sup> mice were more sensitive than their wild-type counterparts, and all died within the indicated time frame (Fig. 1e and Appendix Fig. 1).

These experiments, performed with SIRT2 inhibitors, *Sirt2* knock-down cells, *Sirt2*<sup>-/-</sup> mice and cells from two independently derived *Sirt2*<sup>-/-</sup> mice, raise doubts about the claimed role for SIRT2 in necroptotic cell death.

## METHODS

Data were generated by nine independent laboratories. We have endeavoured to provide key experimental information, and detailed experimental methods are available on request. AGK2 was sourced from TOCRIS Bioscience (3233), Sigma (A8231), Biovision and the Kazatsev laboratory<sup>7</sup>. Cell survival was measured using propidium iodide exclusion and flow cytometric analysis, Cell Titer Glo assay (Promega) and IncuCyte system counting of SYTOX-green-positive cells in real time. *Sirt2*<sup>-/-</sup> mice were provided by the Donmez and Auwerx laboratories<sup>12,13</sup>. TNF was sourced from Peprotech or made in house. Published protocols for siRNA, BMDM maturation and SIRS experiments were followed<sup>8,14,15</sup>.

**Kim Newton<sup>1</sup>, Joanne M. Hildebrand<sup>2,3</sup>, Zhirong Shen<sup>4</sup>, Diego Rodriguez<sup>5</sup>, Silvia Alvarez-Diaz<sup>2,3</sup>, Sean Petersen<sup>1</sup>, Saamil Shah<sup>6</sup>, Debra L. Dugger<sup>1</sup>, Chunzi Huang<sup>7</sup>, Johan Auwerx<sup>8</sup>, Peter Vandenabeele<sup>9,10,11</sup>, Douglas R. Green<sup>5</sup>, Avi Ashkenazi<sup>1</sup>, Vishva M. Dixit<sup>1</sup>, William J. Kaiser<sup>7</sup>, Andreas Strasser<sup>2,3</sup>, Alexei Degterev<sup>6</sup> & John Silke<sup>2,3</sup>**

<sup>1</sup>Genentech, Inc., South San Francisco, California 94080, USA.

<sup>2</sup>The Walter and Eliza Hall Institute of Medical Research, Parkville, Victoria 3052, Australia.

email: silke@wehi.edu.au

<sup>3</sup>Department of Medical Biology, University of Melbourne, Parkville, Victoria 3050, Australia.

<sup>4</sup>National Institute of Biological Sciences, Zhongguancun Life Science Park, Beijing 102206, China.

<sup>5</sup>Department of Immunology, St Jude Children's Research Hospital, Memphis, Tennessee 38105, USA.

<sup>6</sup>Department of Biochemistry, Tufts University, Boston, Massachusetts 02111, USA.

<sup>7</sup>Department of Microbiology and Immunology, Emory Vaccine Center, Emory University School of Medicine, Atlanta, Georgia 30322, USA.

<sup>8</sup>Laboratory of Integrative and Systems Physiology, EPFL, CH-1015 Lausanne, Switzerland.

<sup>9</sup>Molecular Signaling and Cell Death Unit, Inflammation Research Center, VIB, 9052 Gent, Belgium.

<sup>10</sup>Department of Biomedical Molecular Biology, Ghent University, 9052 Gent, Belgium.

<sup>11</sup>Methusalem BOF09/O1M00709, Ghent University, 9052 Gent, Belgium.

**Received 26 August 2013; accepted 8 January 2014.**

- Houtkooper, R. H., Pirinen, E. & Auwerx, J. Sirtuins as regulators of metabolism and healthspan. *Nature Rev. Mol. Cell Biol.* **13**, 225–238 (2012).
- Sebastian, C., Satterstrom, F. K., Haigis, M. C. & Mostoslavsky, R. From sirtuin biology to human diseases: an update. *J. Biol. Chem.* **287**, 42444–42452 (2012).
- Narayan, N. *et al.* The NAD-dependent deacetylase SIRT2 is required for programmed necrosis. *Nature* **492**, 199–204 (2012).
- Cho, Y. S. *et al.* Phosphorylation-driven assembly of the RIP1–RIP3 complex regulates programmed necrosis and virus-induced inflammation. *Cell* **137**, 1112–1123 (2009).
- He, S. *et al.* Receptor interacting protein kinase-3 determines cellular necrotic response to TNF-α. *Cell* **137**, 1100–1111 (2009).
- Zhang, D. W. *et al.* RIP3, an energy metabolism regulator that switches TNF-induced cell death from apoptosis to necrosis. *Science* **325**, 332–336 (2009).
- Outeiro, T. F. *et al.* Sirtuin 2 inhibitors rescue α-synuclein-mediated toxicity in models of Parkinson's disease. *Science* **317**, 516–519 (2007).
- Duprez, L. *et al.* RIP kinase-dependent necrosis drives lethal systemic inflammatory response syndrome. *Immunity* **35**, 908–918 (2011).
- Günther, C. *et al.* Caspase-8 regulates TNF-α-induced epithelial necroptosis and terminal ileitis. *Nature* **477**, 335–339 (2011).
- Piao, X. *et al.* c-FLIP maintains tissue homeostasis by preventing apoptosis and programmed necrosis. *Sci. Signal.* **5**, ra93 (2012).
- Welz, P. S. *et al.* FADD prevents RIP3-mediated epithelial cell necrosis and chronic intestinal inflammation. *Nature* **477**, 330–334 (2011).
- Beirowski, B. *et al.* Sir-two-homolog 2 (*Sirt2*) modulates peripheral myelination through polarity protein Par-3/atypical protein kinase C (aPKC) signaling. *Proc. Natl Acad. Sci. USA* **108**, E952–E961 (2011).
- Bobrowska, A., Donmez, G., Weiss, A., Guarente, L. & Bates, G. SIRT2 ablation has no effect on tubulin acetylation in brain, cholesterol biosynthesis or the progression of Huntington's disease phenotypes *in vivo*. *PLoS ONE* **7**, e34805 (2012).
- Murphy, J. M. *et al.* The pseudokinase MLKL mediates necroptosis via a molecular switch mechanism. *Immunity* **39**, 443–453 (2013).
- Wang, L., Du, F. & Wang, X. TNF-α induces two distinct caspase-8 activation pathways. *Cell* **133**, 693–703 (2008).

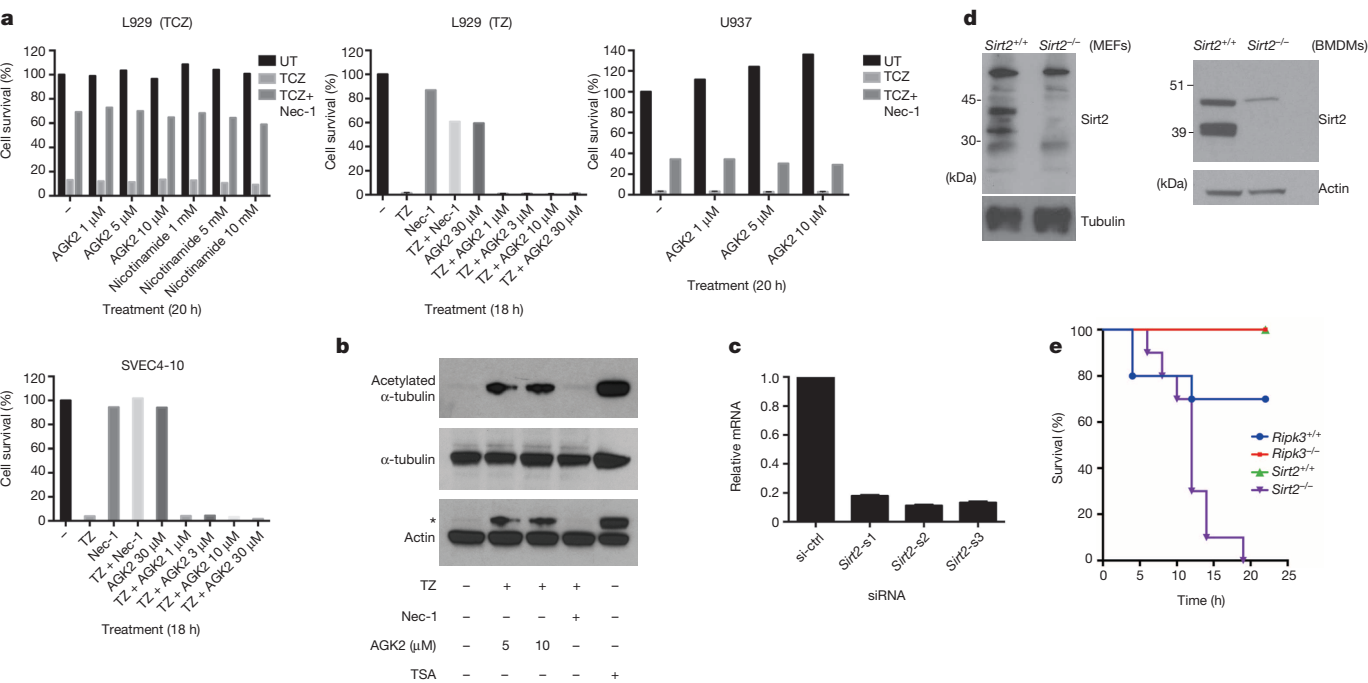
**Author Contributions** K.N., J.M.H., Z.S., D.R., S.A.-D., S.P., S.S., D.L.D. and C.H. designed and performed experiments and analysed data; J.A., P.V., D.R.G., A.A., V.M.D., W.J.K., A.S., A.D. and J.S. planned the project and performed data analysis; K.N., J.M.H., J.A., P.V., D.R.G., A.A., V.M.D., W.J.K., A.S., A.D. and J.S. wrote paper.

**Competing Financial Interests** Declared none.

doi:10.1038/nature13024



Appendix



**Appendix Figure 1 | Neither chemical inhibition nor genetic depletion of SIRT2 inhibits TNF-induced necroptosis. a**, L929 and U937 cells ( $5 \times 10^3$ ) were seeded into each well of a 96-well plate and allowed to grow overnight to confluency. Cells were pre-treated with the indicated concentration of AGK2 (Biovision) or nicotinamide (Sigma) for 1 h. z-VAD-fmk (20  $\mu$ M; Bachem) and cycloheximide (1  $\mu$ g ml<sup>-1</sup>; Sigma) were added for an additional hour and, finally, TNF (100 ng ml<sup>-1</sup>; produced in-house) was added for the last 20 h. Cell viability was then determined using CellTiter-Glo (Promega). L929 and SVEC4-10 cells ( $1 \times 10^5$ ) were seeded into each well of a 96-well plate. Cells were treated with the indicated concentrations of AGK2 (Biovision), TNF (25 ng ml<sup>-1</sup>; Peprotech), z-VAD-fmk (25  $\mu$ M; SM Biochemicals) and Nec-1 (30  $\mu$ M; EMD Millipore). At 18 h after treatment, cell viability was determined by CellTiter-Glo (Promega). Data are plotted as mean of three technical repeats. UT, untreated. NIH-3T3 cells overexpressing RIPK3 were incubated for 1 h with 0.5 ng ml<sup>-1</sup> of TNF and 50  $\mu$ M z-VAD-fmk in the absence or presence of 5–10  $\mu$ M AGK2 (Sigma), 30  $\mu$ M Nec-1 (Calbiochem) or trichostatin A (TSA, 1 mg ml<sup>-1</sup>, general deacetylase inhibitor). Cell lysates were separated by SDS-PAGE and acetylated tubulin and total tubulin detected by western blotting. Asterisk denotes residual acetylated tubulin

signal after re-blotting for actin. **c**, L929 cells were seeded into 6-well plates at the density of  $0.3 \times 10^6$  cells per well and then transfected with 10 pM of control siRNA and three independent siRNA oligonucleotides against murine Sirt2 for 3 days. Expression of murine Sirt2 was measured by qPCR. **d**, Left: cell lysates of primary wild-type and Sirt2<sup>-/-</sup> MEFs were separated by SDS-PAGE and western blotting performed using antibodies against SIRT2 (Sigma-Aldrich, S8447) and tubulin as a loading control (Cell Signaling). Right: 50  $\mu$ g of whole-cell lysates from primary wild-type and Sirt2<sup>-/-</sup> BMDMs were separated by SDS-PAGE and western blotting was performed using anti-SIRT2 (Cell Signaling; catalogue no. 12672) and light-chain-specific anti-rabbit-HRP (Jackson ImmunoResearch). SIRT2 is predicted to run at  $\sim 43$  kDa. **e**, Kaplan–Meier plot of survival of male C57BL/6 Ripk3<sup>+/+</sup> (wild-type controls), C57BL/6 Ripk3<sup>-/-</sup>, C57BL/6 Sirt2<sup>+/+</sup> (wild-type controls), and C57BL/6 Sirt2<sup>-/-</sup> mice aged 9–12 weeks ( $n = 10$  for each genotype) injected intravenously with murine TNF (300  $\mu$ g kg<sup>-1</sup>; R&D Systems). Body temperature was measured with a lubricated rectal thermometer. Mice with a temperature below 23.6 °C were euthanized for ethical reasons.

## TUBERCULOSIS

# Drug discovery goes *au naturel*

In a study that showcases the potential of semisynthetic drug design, structural modification of an existing antibiotic with little activity against *Mycobacterium tuberculosis* has generated a new class of effective antitubercular lead.

CLIFTON E. BARRY

Discovering useful drugs to treat tuberculosis is not an exercise for the faint of heart. Screening for agents that inhibit the growth of the causative mycobacterium produces very few hits, and optimizing those hits into drug-like 'lead' molecules is exceptionally difficult, owing to the bacterium's impermeable cell envelope. Even armed with a promising lead, animal models and early-stage clinical trials have little predictive value, and the long duration of therapy currently required to treat tuberculosis makes safety hurdles much higher than for most bacterial infections. So, an attractive strategy, and one that lies at the heart of a report by Lee *et al.*<sup>1</sup> in *Nature Medicine*, is to repurpose an existing antibiotic class that is already known to be safe and effective in other infections, but that has poor antitubercular activity.

The authors focused their efforts on spectinomycin, a natural product isolated from *Streptomyces* bacteria that has a long history of safe use for the treatment of gonorrhoea in patients who are allergic (or resistant) to penicillin. Despite targeting the bacterial ribosome — a complex of proteins and RNA molecules that is essential for cellular protein translation and that is highly evolutionarily conserved — spectinomycin shows little activity against *Mycobacterium tuberculosis*. Other translation inhibitors, such as streptomycin, kanamycin and amikacin, are widely used in antituberculosis chemotherapy, but their binding site on the ribosome is distinct from that of spectinomycin.

Armed with the crystal structure of spectinomycin bound to the bacterial ribosome<sup>2</sup> and a mutant strain of *M. tuberculosis* defective in a cellular efflux pump that showed increased susceptibility to spectinomycin, Lee and colleagues produced derivatives of the antibiotic, called spectinamides, that showed potent antituberculosis activity both *in vitro* and in mice. The co-crystal structure of the drug bound to the bacterial ribosome allowed the authors to deduce which sites in the drug were crucial for binding and which were not; they then focused on the latter, chemically modifying the natural product to improve cellular activity by reducing drug efflux. They assessed

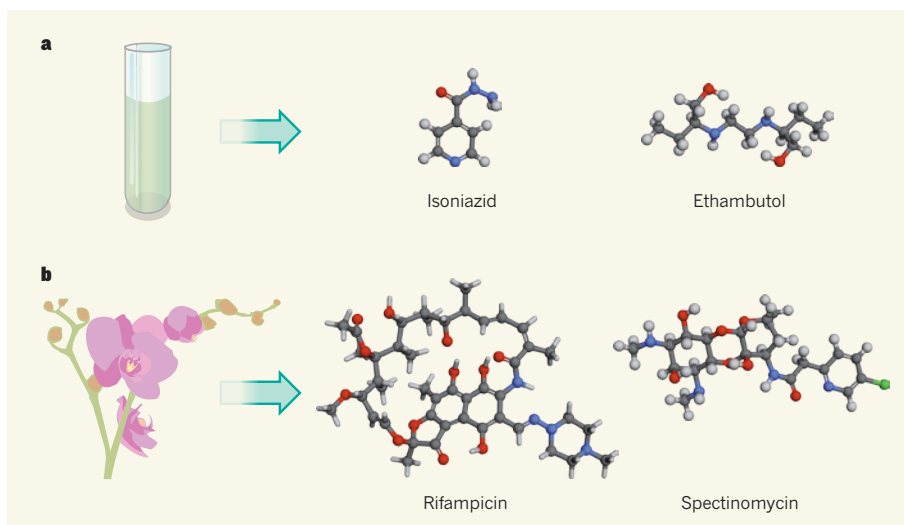


**Figure 1 | Natural complexity.** **a**, For several decades, pharmaceutical companies have focused their efforts in tuberculosis drug discovery on entirely synthetic drugs, such as isoniazid and ethambutol, which are cheap and easy to produce. **b**, The structural complexity of natural products (for example, rifampicin), however, provides advantages over simple synthetic structures, such as more-effective binding to therapeutic targets. Lee and colleagues' study<sup>1</sup> of spectinomycin demonstrates how our increasing knowledge of drug metabolism and protein structures makes semisynthetic alteration of natural compounds an efficient and effective alternative to complete chemical synthesis.

the effect of the modifications on efflux by comparing the activity of the compounds in wild-type and efflux-mutant bacteria, and used separate *in vitro* assays to monitor the modified products' ribosome-binding ability.

Drug developers have long had a love-hate relationship with natural products. On the one hand, the sheer complexity and three-dimensionality of natural products provides more opportunity for highly specific, tight binding to potential targets than do the small, flat synthetic molecules that are typical of the large libraries amassed by most pharmaceutical companies (Fig. 1). Many natural products have evolved as weapons deployed by bacteria to kill other bacteria, and taking advantage of that evolutionary war has obvious attractions. On the other hand, natural compounds rarely have the ideal pharmacological properties needed for direct use, and therefore require chemical transformation — a process called semisynthesis — to make them suitable as medicines. Such semisyntheses can be extraordinarily complex and require enormous investment to understand the chemical

properties of the parent molecule, thereby allowing a systematic exploration of where alterations can be made.

Current practice among scientists working in tuberculosis drug discovery is heavily weighted towards screening and optimizing small synthetic lead molecules. One such molecule, bedaquiline, was, in 2012, the first drug in 40 years to receive US Food and Drug Administration approval for use in the treatment of tuberculosis. However, over these past 40 years, about three-quarters of all approved antibacterial drugs have been the result of semisynthetic efforts from natural-product starting points<sup>3</sup>.

In fact, the biggest advance in tuberculosis chemotherapy so far was unquestionably the addition of rifampicin to multidrug cocktails in the 1970s. Before the introduction of rifampicin, 18–24 months of therapy with a combination of two or three different agents was required to achieve a sterile cure of tuberculosis. But, following landmark clinical trials in Africa by the British Medical Research Council, the standard therapy for tuberculosis



infections became combinations of four drugs, including rifampicin, for a mere six months<sup>4</sup>. The starting point for rifampicin development was a complex mixture of metabolites from the bacterium *Nocardia mediterranei*, isolated by the French pharmaceutical company Lepetit in 1957. It took 8 years for this company (partnering with Ciba-Geigy, based in Switzerland) to understand the various rifampicin-related metabolites and their chemistry sufficiently to allow the development of an orally available analogue, which became the basis of these new short-course chemotherapy regimens<sup>5</sup>.

The molecule described by Lee *et al.* is not the 'next rifampicin', but there are two exciting features of the authors' paper that should encourage more effort in the semisynthetic

modification of natural products for tuberculosis drug discovery. First, the authors took full advantage of recent advances in crystallography to guide their strategy for modifying the natural product. This allowed them to focus on a limited set of chemical modifications rather than the inefficient empirical approaches used in the past (for example, several hundred rifampicin analogues had to be explored before it even became clear which positions could be modified without completely losing biological activity). Second, they used our expanding understanding of the role of drug efflux in tuberculosis<sup>6</sup> to assess the efficacy of the modified compounds. The proof-of-concept achieved in this study will nudge the pendulum of interest back towards natural products

as viable starting points for tuberculosis drug developers. ■

**Clifton E. Barry** is in the Tuberculosis Research Section, National Institute of Allergy and Infectious Diseases, Bethesda, Maryland 20892-3206, USA.  
e-mail: cbarry@niaid.nih.gov

1. Lee, R. E. *et al.* *Nature Med.* <http://dx.doi.org/10.1038/nm.3458> (2014).
2. Borovinskaya, M. A., Shoji, S., Holton, J. M., Fredrick, K. & Cate, J. H. *ACS Chem. Biol.* **2**, 545–552 (2007).
3. Newman, D. J. & Cragg, G. M. *J. Nat. Prod.* **75**, 311–335 (2012).
4. Fox, W., Ellard, G. A. & Mitchison, D. A. *Int. J. Tuberc. Lung Dis.* **3**, S231–S279 (1999).
5. Sensi, P. *Rev. Infect. Dis.* **5**, S402–S406 (1983).
6. Balganes, M. *et al.* *Antimicrob. Agents Chemother.* **56**, 2643–2651 (2012).

## APPLIED PHYSICS

# Optical trapping for space mirrors

**Might it be possible to create mirrors for space telescopes, using nothing but microscopic particles held in place by light? A study that exploits a technique called optical binding provides a step towards this goal.**

DAVID MCGLOIN

The research field of optical manipulation, in which microscopic particles are confined and moved about by laser light, bears more than a passing resemblance to that staple of science-fiction movies, the tractor beam. Although it may be possible to push and pull a red blood cell, say, using a laser beam, it is rather a different matter to try the same trick with billions of particles and then to make a mirror out of them. With the aim of producing ultralow-weight space-based mirrors, that is exactly what Grzegorzczuk and colleagues propose, as they write in *Physical Review Letters*<sup>1</sup>.

The idea that a space mirror could be held in place using a laser beam dates back to the 1970s, when the astronomer Antoine Labeyrie proposed<sup>2</sup> a system in which a thin mirror called a pellicle, 10–100 metres in diameter, was trapped in the node of a standing wave formed by two counter-propagating laser beams; the node of a standing wave is the point at which the wave's amplitude is at its minimum. Furthermore, the curvature needed to enable the mirror to produce an image from incoming light could be generated naturally by the properties of the light holding the mirror in place. Two advantages of such a system are weight — large telescopes could be made that are micrometres thick and weigh much less than 1 kilogram — and, depending on how the pellicle is formed, the fact that they could be

tightly packed, reducing the volume required to deliver them into space. But how could such a mirror be created? A step towards the practical implementation of this optical device is at the heart of Grzegorzczuk and colleagues' work.

The research makes use of a technique called optical binding, in which microscopic particles illuminated by laser light scatter some of the light in a transverse direction to that of the illumination. The scattered light from all the particles helps to bind them together. In the

experimental part of their study, Grzegorzczuk *et al.* create an optically bound structure of around 150 spherical polystyrene particles, each with a diameter of 3 micrometres (Fig. 1). In contrast to Labeyrie's original proposal, this mirror is confined using only one laser beam, and is held in place by the laser pushing it against the wall of the experimental chamber. Also, unlike the situation in a practical implementation, the mirror is trapped in water, and the authors admit that there is a challenge in even this rudimentary experiment of trapping the mirror stably away from the chamber wall using a dual-beam system.

The major novelty in the latest work is the ability to use the structure as a mirror; an optically bound particle structure has already been created<sup>3</sup>. The imaging obtained by Grzegorzczuk *et al.* is fairly crude, showing the number 8 on a transparent ruler reflecting from the mirror surface. The work does not demonstrate the curved mirror surface that would probably be needed for a space telescope, and it is clear that the imaging quality is a long way short of that normally expected in a high-end optical instrument.

But Grzegorzczuk *et al.* examine the imaging ability of curved mirrors made from large numbers of particles using a numerical model, and find that focusing of incoming light should be possible. More importantly, the model also analyses how a more practical mirror design might operate. Such a mirror might be tens of metres in diameter, and require billions of particles. Although the total weight of such a structure is not an obstacle, its assembly would be. Optically bound matter becomes more unstable as the arrays of particles grow bigger, because they will contain larger numbers of structural defects known as dislocations.

Binding the particles together has the advantage that the mirror can 'self-heal' after being hit by a bit of space debris, but in the current design the binding does not scale well with particle number. This could be overcome by splitting the mirror into chunks, and the authors' modelling suggests that doing so

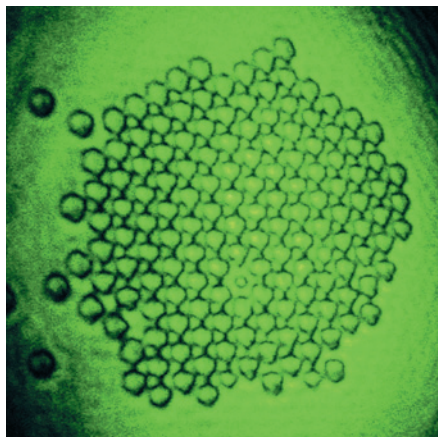


**Figure 1 | Laser-trapped beads.** Grzegorzczuk *et al.*<sup>1</sup> have used laser light to trap a collection of polystyrene beads, each 3 micrometres in diameter. The resulting optically bound structure forms a mirror.

would not adversely impair the imaging quality. This idea is also akin to one of Labeyrie and colleagues' more recent suggestions<sup>4</sup> that the pellicle-mirror telescope could be turned into one with a large imaging aperture by using many small, widely distributed mirrors, rather than a single big one. Their startling claim is that such a device could directly image extrasolar planets.

The realization of an optically trapped telescope remains a huge engineering task, and we are unlikely to see one anytime soon — Labeyrie's original proposal is 35 years old, after all. The underlying challenges include the assembly of the device; its stability over a long period of time, which requires stable,

long-lived lasers; and a factor not explicitly discussed in the paper: how to deal with laser heating of the mirror particles. In the current experiments, the heat produced in the samples is dissipated by their being submerged in water, but up in the vacuum of space, heating is likely to act to disrupt the optical binding. But by overcoming these challenges, we can bring science fiction a little closer to reality. To do so, new areas of optical manipulation must be explored, especially the emerging field of vacuum optical trapping of microscopic particles, an area rich with possibilities for better understanding quantum physics. It is to be hoped that such fundamental studies can also

lead to research at much larger length scales than those investigated here, so that the proposed space mirrors become a reality. We may just have to wait another few decades. ■

**David McGloin** is in the Division of Physics, University of Dundee, Dundee DD1 4HN, UK. e-mail: d.mcglain@dundee.ac.uk

1. Grzegorzczak, T. M., Rohner, J. & Fournier, J.-M. *Phys. Rev. Lett.* **112**, 023902 (2014).
2. Labeyrie, A. *Astron. Astrophys.* **77**, L1–L2 (1979).
3. Burns, M. M., Fournier, J.-M. & Golovchenko, J. A. *Science* **249**, 749–754 (1990).
4. Labeyrie, A. *et al.* *Pathways Towards Habitable Planets* 239–248; *Astron. Soc. Pacif. Conf. Ser. Vol.* 430 (2010).

randomly stitches the fragments together. RELA is a transcription factor in the NF- $\kappa$ B signalling pathway, which regulates many cellular processes. Whereas wild-type RELA is located in the cytoplasm unless it is activated, the C11orf95–RELA hybrid protein spontaneously translocates to the nucleus, where it activates the expression of target genes. The authors also show that transplantation of neural stem cells expressing this fusion gene into mouse brains induces ependymoma-like tumours, thus adding a new tumour-driving gene to the list of those associated with cancer.

But equally remarkable is what Parker *et al.* did not find: their sequencing of posterior fossa tumours did not reveal any recurrently mutated gene or translocation. Mack *et al.* also sequenced posterior fossa ependymomas, with the same puzzling result. Recent sequencing<sup>6</sup> of many adult tumour types has typically detected 25 to 200 amino-acid-changing mutations per tumour; most of these affect 'bystander' genes, but cancer-driving

## CANCER

# Tumours outside the mutation box

**Analyses of ependymoma brain tumours reveal a gene rearrangement in one subtype, but no DNA mutations in two others, suggesting that mechanisms for cancer initiation are broader than is typically thought. SEE ARTICLES P.445 & P.451**

ROGIER VERSTEEG

Ever since the identification<sup>1,2</sup> in 1982 of mutated human genes that drive cancer, a massive body of evidence has established the paradigm that cancer results from mutations in specific genes. The recent wave of genome sequencing of human tumours has confirmed this concept, but it has also identified some tumours with surprisingly few cancer-associated gene mutations. The results presented in this issue further urge us to revisit the role of gene mutations in cancer. In their genomic analyses of three subtypes of ependymoma brain tumour, Parker *et al.*<sup>3</sup> (page 451) and Mack *et al.*<sup>4</sup> (page 445) find that one subtype carries an intrachromosomal translocation that creates a new tumour-driving gene, another lacks tumour-driving mutations but has aberrant epigenetic modifications, and a third shows neither gene mutations nor epigenetic aberrations.

Ependymomas are tumours of the central nervous system that originate from the wall of the ventricular system along the entire cranio-spinal axis (Fig. 1). They can be treated by surgery and radiation, but chemotherapy is ineffective, and survival rates for patients with these cancers have not appreciably improved over the past decade. Locality and molecular data define the four subtypes of ependymoma — supratentorial, posterior fossa type A, posterior fossa type B and spinal-cord ependymoma — which also

differ in age of onset and prognosis<sup>5</sup>.

Parker *et al.* applied whole-genome sequencing to supratentorial and posterior fossa ependymoma cells. Among supratentorial tumours, they found frequent cases in which translocation of a region of chromosome 11 caused the fusion of two genes, *RELA* and *C11orf95*. These translocations resulted from chromothripsis — a mechanism that pulverizes a genomic region and

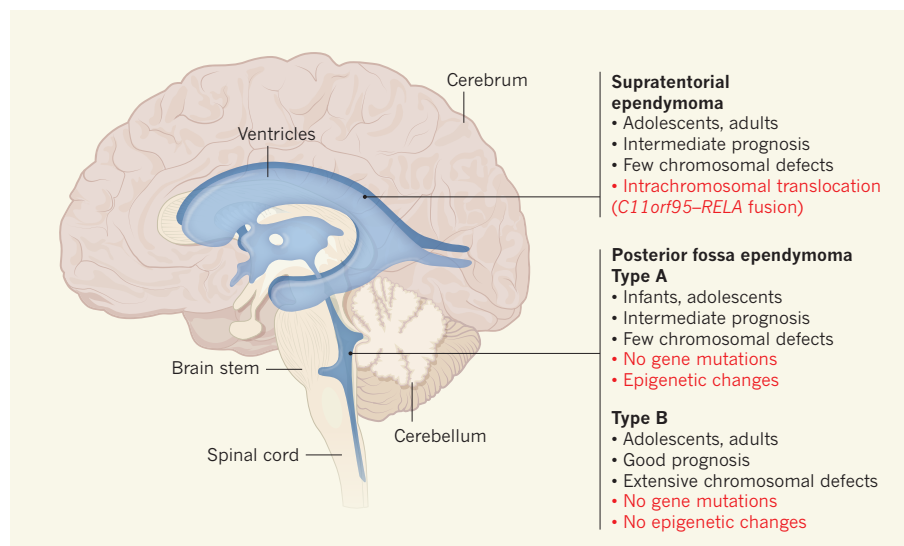


**Figure 1 | Genomic characterization of ependymomas.** Parker *et al.*<sup>3</sup> and Mack *et al.*<sup>4</sup> performed whole-genome analysis of three subtypes of ependymoma, which differ in their location in the central nervous system. The age of onset, patient prognosis and previously known molecular characteristics<sup>5</sup> of the tumour types are listed in black; new molecular findings from the sequence analyses are listed in red.



gene mutations expose themselves by their recurrence in multiple tumours. However, there are certain tumour types in which very few recurrently mutated genes — often only one or even none per tumour — have been detected, namely in childhood tumours such as medulloblastoma<sup>7</sup>, neuroblastoma<sup>8</sup> and rhabdoid tumours<sup>9</sup>. All current sequencing technologies sometimes miss mutations<sup>6</sup>, but the fact that this paucity of mutations was observed with diverse technologies, and only in childhood tumours, makes it unlikely that it results from technical artefacts. Now, these two papers report that posterior fossa ependymomas also seemingly lack recurrently mutated genes.

If not gene mutations, what else could cause cancer? It has long been suspected that defective epigenetic modifications — that is, non-sequence-changing alterations, such as the methylation or acetylation of DNA or DNA-associated chromatin proteins — might also be oncogenic. Several genes encoding enzymes that apply or remove these modifications have been shown to be mutated in tumours, confirming a role for epigenetics in cancer<sup>10</sup>, but such mutations were not detected in the ependymoma studies. However, Mack *et al.* did find increased DNA methylation of specific genes, as well as silencing of their expression, in type A, but not type B, posterior fossa ependymomas.

Expression of these same genes was previously found to be silenced in embryonic stem cells by the protein complex PRC2 (ref. 11), which mediates a common epigenetic modification: trimethylation of the amino acid lysine at position 27 in the histone protein H3 (H3K27me3). Indeed, Mack and colleagues found H3K27me3 marks on many of the genes with DNA methylation in posterior fossa type A tumours. They therefore hypothesize that the repression of these genes by PRC2 keeps these tumour cells in an embryonic and proliferative state.

A lack of model systems for experimental studies of posterior fossa ependymoma did not allow crucial testing of this hypothesis, and these data remain correlative, but preliminary testing of drugs targeting DNA methylation and H3K27me3 inhibited the proliferation of type A tumour cells *in vitro*. The key question emerging from these findings is whether and how a cell can escape the normal regulatory mechanisms governing epigenetic modifications such that oncogenic gene-expression patterns can persist, without having DNA-sequence mutations.

What remains are posterior fossa type B ependymomas, for which neither tumour-driving gene mutations nor epigenetic changes have yet been found. Both groups of authors refrain from any interpretation of this. Type B tumour cells differ from type A tumour cells by typically containing gains and losses of entire chromosomes or large chromosomal

fragments<sup>5</sup>. Chromosomal deletions occur frequently in almost all tumour types and are usually interpreted as part of a two-hit inactivation of a tumour-suppressor gene, in which one copy of the gene is destroyed by a mutation and the other copy by a deletion. However, genome-sequencing data have shattered the expectation that deletions will always involve a tumour-suppressor gene. Neuroblastoma tumours, for example, frequently show deletions of regions of chromosomes 1 and 11, but no recurrently mutated tumour-suppressor genes have been found on the corresponding section of the paired chromosome<sup>8,12,13</sup>.

Thus, it may be that some such deletions have an entirely different role in cancer. The deleted areas usually encompass hundreds of genes, and changes in the expression of large numbers of genes can be highly pathogenic. For example, one extra copy of chromosome 21 causes Down's syndrome, and third copies of any other chromosome are mostly lethal. Speculatively, cancer initiation could occur when a deleted region encompasses several inhibitory genes of a particular cell-signalling pathway, and a gained region contains several positive regulators of that pathway. The resulting modest changes in expression of each individual gene could together exponentially activate the pathway, and may drive cancer.

It will be challenging to test whether chromosomal gains and losses, or epigenetic modifications without gene mutations, can indeed drive cancer development. The clinical implications of such alternative oncogenic routes would, however, be far reaching. Much research focuses on drugs that target gene mutations. The C11orf95–RELA fusion protein identified by Parker and colleagues provides a new target for drugs against supratentorial ependymoma, but the treatment of posterior fossa tumours might require a fundamentally different approach. ■

**Rogier Versteeg** is in the Department of Oncogenomics, Academic Medical Center, University of Amsterdam, 1105 AZ Amsterdam, the Netherlands.  
e-mail: r.versteeg@amc.uva.nl

1. Tabin, C. J. *et al.* *Nature* **300**, 143–149 (1982).
2. Reddy, E. P., Reynolds, R. K., Santos, E. & Barbacid, M. *Nature* **300**, 149–152 (1982).
3. Parker, M. *et al.* *Nature* **506**, 451–455 (2014).
4. Mack, S. C. *et al.* *Nature* **506**, 445–450 (2014).
5. Witt, H. *et al.* *Cancer Cell* **20**, 143–157 (2011).
6. Vogelstein, B. *et al.* *Science* **339**, 1546–1558 (2013).
7. Rausch, T. *et al.* *Cell* **148**, 59–71 (2012).
8. Molenaar, J. J. *et al.* *Nature* **483**, 589–593 (2012).
9. Lee, R. S. *et al.* *J. Clin. Invest.* **122**, 2983–2988 (2012).
10. Plass, C. *et al.* *Nature Rev. Genet.* **14**, 765–780 (2013).
11. Ben-Porath, I. *et al.* *Nature Genet.* **40**, 499–507 (2008).
12. Sausen, M. *et al.* *Nature Genet.* **45**, 12–17 (2013).
13. Pugh, T. J. *et al.* *Nature Genet.* **45**, 279–284 (2013).

This article was published online on 19 February 2014.



## 50 Years Ago

In a statement made simultaneously in both Houses of Parliament on February 6, the Government announced that as a result of investigations undertaken jointly both the British and the French Governments considered that the construction of a rail Channel tunnel was technically possible, and that in economic terms it would represent a sound investment of their resources. The two Governments had therefore decided to go ahead with this project, and the next step would be to discuss further in particular the legal and financial problems involved.

From *Nature* 29 February 1964

## 100 Years Ago

The exceptionally mild character of the present winter is being maintained until its close, and for a persistent continuance of warm days in January and February it surpasses all previous records. At Greenwich the thermometer in the screen was above 50° for eighteen consecutive days from January 29 to February 15. Previous records since 1841 have no longer period than eleven days, in the months of January and February combined, with the thermometer continuously above 50°, and there are only four such periods ... The persistent continuance of the absence of frost is also very nearly a record ... The maximum temperatures in the two months have seldom been surpassed. In many respects there is a resemblance between the weather this winter and that in 1899, when in February blizzards and snowstorms were severe on the other side of the Atlantic, with tremendous windstorms in the open ocean, whilst on this side of the Atlantic the weather was exceptionally mild. It is to be hoped that this year we shall be spared the somewhat sharp frosts experienced in the spring of 1899.

From *Nature* 26 February 1914

## CONSERVATION

## Wind blown

One strategy for animal conservation is to create strips of habitat that allow individuals from isolated populations to travel long distances and so meet. Damschen *et al.* report in *Proceedings of the National Academy of Sciences* that habitat corridors can also affect seed dispersal by wind (E. I. Damschen *et al. Proc. Natl Acad. Sci. USA* <http://dx.doi.org/10.1073/pnas.1308968111>; 2014).

From models and studies of open areas in a forest, the authors find that prevailing winds veer towards the long axis of each corridor, accelerating within corridors and strengthening at the downwind ends, and that increased turbulence creates 'hotspots' of seed uplift.

These combined effects aid seed dispersal, especially in areas connected by corridors that align with prevailing winds. The researchers argue that their findings should be considered when planning conservation efforts for plants that depend on open habitats. [Andrew Mitchinson](#)



LARRY MILLER/SPL

## FUNDAMENTAL CONSTANTS

## The teamwork of precision

**A new value for the atomic mass of the electron is a link in a chain of measurements that will enable a test of the standard model of particle physics with better than part-per-trillion precision. [SEE LETTER P.467](#)**

EDMUND G. MYERS

One of the most amazing triumphs of modern physics is the agreement, at nearly the part-per-trillion level, between theory<sup>1</sup> and an experiment<sup>2</sup>, which uses a single electron confined by electric and magnetic fields in a device called a Penning trap, for the magnetic moment of the electron. Assuming the correctness of the theoretical calculations and experimental measurements, any difference between the two could indicate physics beyond the standard model of particle physics<sup>3</sup>. Because the theoretical prediction requires as input an independent value for the fundamental physical constant known as the fine-structure constant, and one method for obtaining the fine-structure constant requires a value for the atomic mass of the electron (the ratio of the mass of the electron to the mass of an atom of carbon-12), the atomic mass of the electron is an essential ingredient in the above comparison. For this reason, a new

measurement of the atomic mass of the electron, which has an uncertainty reduced by a factor of 13 compared with previous results<sup>4</sup>, as reported by Sturm *et al.*<sup>5</sup> on page 467 of this issue, could have an impact on fundamental physics.

For the magnetic moment of the electron, both the theory and experiment actually produce results in units of the Bohr magneton, the fundamental quantum unit of magnetic moment, and so the comparison is between two dimensionless numbers. The dominant contribution to the theoretical value for the electron's magnetic moment is obtained from quantum electrodynamics (QED), the archetypical quantum field theory. This contribution is expressed as a power series in the fine-structure constant ( $\alpha$ ), which can be thought of as the dimensionless parameter quantifying the strength of the electromagnetic interaction, and which has the approximate value  $1/137$ .

The latest QED results for the coefficients in this series, which is now complete up to  $(\alpha/\pi)^5$ ,

have required the monumental evaluation of thousands of complex tenth-order Feynman diagrams, with computers doing the underlying algebra and code generation, as well as the final numerical calculation. Including the small contributions due to the strong and weak interactions, the uncertainty in the theoretical calculation<sup>1</sup> is now estimated to be below 0.08 parts per trillion (p.p.t.). But, of course, because the theoretical result depends on  $\alpha$  (except for the first term of the power series, which is 1 and is the pre-QED result obtained by physicist Paul Dirac in the 1920s), to make a comparison with the experiment,  $\alpha$  must be determined experimentally. At present, the uncertainty in  $\alpha$  increases the uncertainty of the theoretical prediction by a factor of ten. This limits the precision of the comparison with the experiment<sup>2</sup>, which has an uncertainty of 0.28 p.p.t., to close to 1 p.p.t.

If all we wanted was the most precise value for  $\alpha$ , we could simply equate theory and the experiment for the electron's magnetic moment and solve for  $\alpha$ . But to test the theory we need a value for  $\alpha$  that is independent of the electron's magnetic moment. Currently, the most precise approach for obtaining such a value is the photon-recoil method. This technique is based on the equation  $\alpha^2 = (2R_\infty/c) (h/m_e)$ , where  $R_\infty$  is another fundamental constant, the Rydberg constant;  $h$  is Planck's constant;  $c$  is the speed of light; and  $m_e$  is the mass of the electron.

The Rydberg constant has been determined to an accuracy of 5 p.p.t., easily good enough here, by precision laser spectroscopy of atomic hydrogen<sup>4</sup>. Knowing  $R_\infty$ ,  $\alpha$  would follow if only



we knew  $h/m_e$ . However, it is not known how to measure  $h/m_e$  (or  $h$ ) to the required accuracy. But, using remarkable techniques of atom interferometry with ultracold atoms, in particular caesium<sup>6</sup> and rubidium<sup>7</sup>, it is practical to measure Planck's constant divided by an atom's mass,  $h/m_{\text{atom}}$ . This is obtained by measuring the recoil velocities of atoms that absorb and re-emit photons from a laser — hence the name photon-recoil method. In the case of rubidium, this has been done<sup>7</sup> to a precision of 1.3 parts per billion (p.p.b.). But then we need to convert between the masses  $m_{\text{atom}}$  and  $m_e$ . This is most accurately done using the relationship  $m_{\text{atom}}/m_e = A_r(\text{atom})/A_r(e)$ , where  $A_r(\text{atom})$  is the atomic mass of the atom used in the photon-recoil measurement, and  $A_r(e)$  is the atomic mass of the electron — which is where Sturm and colleagues' new result comes in.

However, the connections between Sturm and colleagues' work and the magnetic moment of the electron do not end there. The authors do not measure the atomic mass of the electron directly. Instead, they do so through the magnetic moment of the 'bound electron' — more precisely, the magnetic moment of a hydrogen-like ion, in their case,  $^{12}\text{C}^{5+}$ , which is an electron bound to a nucleus of carbon. Using a single  $^{12}\text{C}^{5+}$  ion in a Penning trap, the authors actually measure the ratio of the frequency of microwaves that flip the electron spin to the frequency of the ion's cyclotron motion in the trap's magnetic field. Their methods, which extend previous work by their group<sup>8</sup>, share many of the Penning-trap techniques developed for the magnetic moment of the free electron<sup>2,9,10</sup>, and also for measuring the atomic masses of rubidium and caesium<sup>11,12</sup>. And it is by combining their measured ratio with a theoretical calculation of the bound-electron magnetic moment — which is also based on QED<sup>13</sup> and, to a given order of QED, is much more challenging than for the free electron — that the authors derive the electron's atomic mass.

In fact, the existing value for  $A_r(e)$  provided by the CODATA compilation of fundamental constants<sup>4</sup> has an uncertainty of 0.4 p.p.b., to be compared with the 1.3 p.p.b. uncertainty of  $h/m_{\text{atom}}$  from the most precise photon-recoil measurements so far<sup>7</sup>. So,  $A_r(e)$  is not yet the precision-limiting link in the chain of measurements for determining  $\alpha$ . (The existing CODATA result for  $A_r(e)$  is mainly based on the group's previous work<sup>8</sup> with  $^{12}\text{C}^{5+}$ ; and the new result, with 0.03 p.p.b. uncertainty, is in agreement.) But improvements in  $h/m_{\text{atom}}$  are anticipated, so, without an improvement in  $A_r(e)$ , the uncertainty in  $A_r(e)$  would become the limitation for  $\alpha$  and the above test of the standard model. Thanks to Sturm and colleagues' remarkable 13-fold increase in precision, it is likely that this will not be the case for some years to come. ■

Edmund G. Myers is in the Department of Physics, Florida State University, Tallahassee,

Florida 32306-4350, USA.

e-mail: myers@nucmar.physics.fsu.edu

1. Aoyama, T. *et al.* *Prog. Theor. Exp. Phys.* **2012**, 01A107 (2012).
2. Hanneke, D. *et al.* *Phys. Rev. Lett.* **100**, 120801 (2008).
3. Gabrielse, G. *Phys. Today* **66**, 64 (2013).
4. Mohr, P. J. *et al.* *Rev. Mod. Phys.* **84**, 1527–1605 (2012).
5. Sturm, S. *et al.* *Nature* **506**, 467–470 (2014).
6. Wicht, A. *et al.* *Phys. Scripta* **T102**, 82 (2002).
7. Bouchendira, R. *et al.* *Phys. Rev. Lett.*

**106**, 080801 (2011).

8. Häffner, H. *et al.* *Phys. Rev. Lett.* **85**, 5308–5311 (2000).
9. Brown, L. S. & Gabrielse, G. *Rev. Mod. Phys.* **58**, 233–311 (1986).
10. Van Dyck, R. S. *et al.* *Phys. Rev. Lett.* **59**, 26–29 (1987).
11. Bradley, M. P. *et al.* *Phys. Rev. Lett.* **83**, 4510–4513 (1999).
12. Mount, B. J. *et al.* *Phys. Rev. A* **82**, 042513 (2010).
13. Pachucki, K. *et al.* *Phys. Rev. A* **72**, 022108 (2005).

This article was published online on 19 February 2014.

## CELL BIOLOGY

# Stressful genetics in Crohn's disease

**A common variant of the autophagy protein ATG16L1 is a risk factor for Crohn's disease. But the genetic alteration is revealed only when the protein is cleaved by the enzyme caspase 3 during cellular stress. SEE ARTICLE P.456**

ARTHUR KASER & RICHARD S. BLUMBERG

A single variation within the approximately six billion base pairs of human DNA is sufficient to magnify our risk of developing common complex diseases. For example, a single nucleotide change in the gene *ATG16L1* is one of the strongest genetic risk factors for Crohn's disease<sup>1</sup>, a chronic inflammatory disease of the digestive tract<sup>2</sup>. On page 456 of this issue, Murthy *et al.*<sup>3</sup> reveal a fascinating twist in the story of how this variant, which is present in more than 50% of the Caucasian population, may contribute to the disease. The authors report that the altered *ATG16L1* protein, which contains the substitution of an alanine amino-acid residue for a threonine at position 300 (T300A), is susceptible to cleavage by the enzyme caspase 3, which is activated when a cell senses stress.

Like all complex disorders, Crohn's disease emerges on a background of many genetic<sup>4</sup> and — mainly unknown — environmental factors. In Crohn's disease, these factors interact to disrupt the homeostasis between resident gut microorganisms, the epithelial layer lining the intestine and the immune system, resulting in chronic intestinal inflammation<sup>2</sup>. The identification<sup>1</sup> of the T300A-encoding variant of *ATG16L1* as a risk factor for the disease hinted at a role for autophagy in this inflammatory response.

Autophagy (or 'self-eating') is a process whereby intracellular content, such as organelles or macromolecules, are engulfed by double-membrane structures called autophagosomes — *ATG16L1* has a crucial role in the formation of autophagosomes<sup>5</sup>. These vesicles then fuse with other vesicles, lysosomes, which contain enzymes that degrade the contents<sup>6</sup>. Autophagy is a response

to starvation that allows the cell to catabolize its contents to regenerate basic cellular building blocks, including amino acids and macromolecules. But the process has also been co-opted for other biological functions, such as the degradation of intracellular pathogens,

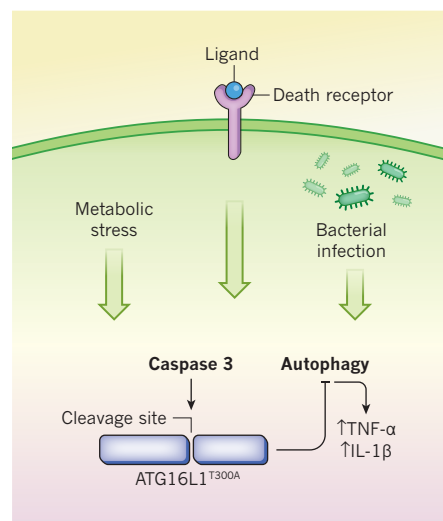


**Figure 1 | Fate determination by caspase 3.** A primary genetic risk factor for Crohn's disease is a variant of the autophagy protein *ATG16L1*. Murthy *et al.*<sup>3</sup> show that the single amino-acid change in the variant *ATG16L1*<sup>T300A</sup> renders it sensitive to cleavage by the enzyme caspase 3. In the absence of caspase-3 activity, *ATG16L1*<sup>T300A</sup> functions normally in the induction of autophagy. However, environmental stresses leading to the concomitant activation of autophagy and caspase 3, such as ligation of death receptors, bacterial infection or metabolic stress, result in destruction of *ATG16L1*<sup>T300A</sup> and hence impaired autophagy. The authors also find that this impaired autophagy causes increased release of inflammatory proteins such as TNF- $\alpha$  and IL-1 $\beta$ .

called xenophagy. Consequently, autophagy is involved in several diseases<sup>6</sup>, but the *ATG16L1*<sup>T300A</sup> variant is associated only with Crohn's disease.

Caspases are endoproteases that hydrolyse peptide bonds at specific sequences<sup>7</sup>. Depending on the target protein, this can lead to the protein's destruction or to the generation of an active protein. Active caspase 3 is required for the cellular signalling pathway that leads to apoptotic cell death; this pathway is initiated by the activity of other caspases that respond to signals from cell-surface death receptors or irreparable organelle dysfunction. Caspase-3 activity during apoptosis irreversibly sets in motion a sequence of events that leads to the demise of the cell. By contrast, low-level caspase-3 activity that is insufficient to trigger apoptosis has homeostatic and protective functions, including guarding stressed organs against cell death<sup>8</sup>.

Through clever alignment of the *ATG16L1* protein sequence from several species, Murthy *et al.* predicted and then directly demonstrated that the T300A variant protein (or the equivalent variant in mice, T316A) was highly sensitive to cleavage by caspase 3 (Fig. 1). The authors also show that, in human cells carrying the *ATG16L1*<sup>T300A</sup> risk variant, signalling initiated by binding of the protein tumour-necrosis factor- $\alpha$  (TNF- $\alpha$ ) to its cell-surface receptor (a death receptor), cellular stress caused by starvation, or infection with the pathogenic gut bacterium *Yersinia enterocolitica* all resulted in caspase-3-dependent degradation of *ATG16L1*<sup>T300A</sup>, and consequently in impaired autophagy and xenophagy responses to these stresses. In the case of *Y. enterocolitica* infection, there was also an increased production of inflammatory cytokine proteins, such as interleukin-1 $\beta$  and TNF- $\alpha$ , in mice engineered to express the *ATG16L1*<sup>T316A</sup> variant.

In stark contrast, the authors show that autophagosome formation was not impaired by the presence of *ATG16L1*<sup>T300A</sup> when autophagy was directly induced without caspase-3 activation. These findings suggest that the *ATG16L1*<sup>T300A</sup> risk variant, through its sensitivity to caspase-3-mediated cleavage, disables a host's ability to properly respond to environmental challenges that require a compensatory autophagy response. Such challenges may include infections, inflammatory stimuli and metabolic disturbances, all of which induce autophagy to remove pathogens or inflammatory organelles (such as inflammasomes<sup>9</sup>) and to provide nutrients to overcome and survive cellular stress. Caspase 3 is commonly activated during these stress conditions.

The cellular state known as endoplasmic reticulum (ER) stress can also activate both caspase 3 and autophagy, and is commonly observed in intestinal epithelial cells of individuals with Crohn's disease<sup>9</sup>. Previous studies in mice<sup>10</sup> showed that loss of

compensatory autophagy in ER-stressed intestinal epithelium, owing to deletion of the *Atg16l1* gene, results in Crohn's-disease-like inflammation of the small intestine. The identification of the sensitivity of this protein variant to caspase-3-mediated destruction may provide insight into how specific environmental exposures convert genetic disease risk into clinical symptoms.

Murthy and colleagues' study also helps to integrate other observations from work on Crohn's disease. For example, caspase-3 activation can be regulated by inhibitor-of-apoptosis proteins such as XIAP, variants of which are the cause of a single-gene form of Crohn's disease<sup>11</sup>. XIAP, in turn, directly interacts with other proteins involved in microbial sensing that are associated with genetic risk for Crohn's disease<sup>4,11</sup>, including RIPK2 and NOD2. The new data might also help to explain why agents targeting TNF- $\alpha$  are highly effective therapies for Crohn's disease<sup>2</sup> — in light of the authors' *Y. enterocolitica* infection studies, it seems plausible that TNF- $\alpha$  fuels an inflammatory feed-forward loop by inducing caspase-3-mediated degradation of *ATG16L1*<sup>T300A</sup>, which in turn results in increased TNF- $\alpha$  secretion. Although further studies are necessary to test the authors' biochemical and cellular observations in animal models and patients with

Crohn's disease, their observations provide an appealing and integrating hypothesis for how this common genetic element engenders disease risk. ■

**Arthur Kaser** is in the Division of Gastroenterology and Hepatology, Department of Medicine, Addenbrooke's Hospital, University of Cambridge, Cambridge CB2 0QQ, UK. **Richard S. Blumberg** is in the Division of Gastroenterology, Hepatology and Endoscopy, Department of Medicine, Brigham and Women's Hospital, Harvard Medical School, Boston, Massachusetts 02115, USA. e-mails: ak729@cam.ac.uk; rblumberg@partners.org

- Hampe, J. *et al.* *Nature Genet.* **39**, 207–211 (2007).
- Maloy, K. J. & Powrie, F. *Nature* **474**, 298–306 (2011).
- Murthy, A. *et al.* *Nature* **506**, 456–462 (2014).
- Jostins, L. *et al.* *Nature* **491**, 119–124 (2012).
- Saitoh, T. *et al.* *Nature* **456**, 264–268 (2008).
- Levine, B., Mizushima, N. & Virgin, H. W. *Nature* **469**, 323–335 (2011).
- McIlwain, D. R., Berger, T. & Mak, T. W. *Cold Spring Harb. Perspect. Biol.* **5**, a008656 (2013).
- Khalil, H. *et al.* *Mol. Cell. Biol.* **32**, 4523–4533 (2012).
- Deuring, J. J. *et al.* *Gut* <http://dx.doi.org/10.1136/gutjnl-2012-303527> (2013).
- Adolph, T. E. *et al.* *Nature* **503**, 272–276 (2013).
- Uhlig, H. H. *Gut* **62**, 1795–1805 (2013).

This article was published online on 19 February 2014.

#### ATMOSPHERIC SCIENCE

## Involatile particles from rapid oxidation

**How tiny aerosol particles form and grow from vapours produced by vegetation has been a mystery. The finding that highly oxygenated products form directly from volatile organic compounds may offer the solution. SEE LETTER P.476**

GORDON MCFIGGANS

On page 476 of this issue, Ehn *et al.*<sup>1</sup> report their identification of large yields of highly oxygenated compounds when volatile organic compounds emitted from biological sources are exposed to atmospherically relevant conditions. This observation may help to close the gap between the measured mass of organic aerosol particles in the atmosphere and that predicted by models. It might also forge a mechanistic link between biogenic volatile organic compounds and the formation of aerosol particles, and provide insight into one of the main climate feedback cycles.

Organic aerosol particles are widespread in the global atmosphere<sup>2</sup>. They consist of primary particles, which are emitted directly into the atmosphere, and secondary particles,

which form from the oxidation products of anthropogenic and biogenic volatile organic compounds. In the overall aerosol budget, the contribution of secondary particles that form from the oxidation of natural plant emissions is complex and highly uncertain. Secondary organic aerosol (SOA) probably dominates primary aerosol and, in some conditions, biogenic sources have been estimated<sup>3</sup> to contribute up to 90% of SOA.

Understanding the roles of naturally occurring atmospheric particles in the climate system has proved difficult. Because of mechanistic uncertainties, 'bottom-up' models that predict the concentrations of atmospheric aerosol particles by explicitly describing the emission and oxidation of their precursors have long been unable to predict the observed mass of SOA. Geographically widespread, long-term observations of high numbers of ultrafine





**Figure 1 | Forest haze.** Ehn and colleagues' discovery<sup>1</sup> of a mechanism by which highly oxygenated compounds form directly from biogenic emissions, such as those produced by boreal forests, may help to explain how naturally occurring ultrafine particles form and grow in the atmosphere.

particles in the atmosphere, particularly over forested regions (Fig. 1), has stimulated much research into how such aerosol particles form and grow<sup>4,5</sup>. So far, compounds of sufficiently low volatility to explain the growth of ultrafine particles have not been identified or quantified.

To address these problems, Ehn and colleagues made concurrent, direct measurements of the mass spectra of gaseous organic compounds in a chamber, and of the masses of 'seed' particles injected into the chamber, in experiments conducted under atmospherically reasonable conditions. They studied several biogenic volatile organic compounds (BVOCs), such as monoterpenes (members of the terpene family of naturally occurring hydrocarbons), and found that the oxidation products of these compounds had a high ratio of oxygen to carbon atoms. The products were irreversibly taken up by the seed particles, even at very low particle loadings. This irreversible condensation is expected for compounds that exhibit extremely low volatility, as highly oxygenated compounds generally do. Possibly the most surprising of the authors' findings is that such compounds are formed at high yields at an early stage of oxidation — in oxidation reactions of the primary compounds, rather than in subsequent oxidation reactions.

Observed atmospheric particle-growth rates are generally higher than previously proposed oxidation mechanisms can support, which has led to speculation that other mechanisms might play a part<sup>6</sup>. Ehn and co-workers' observation of a hitherto unmeasured class of gas-phase oxidation products obviates the need to invoke such mechanisms. The authors convincingly argue that this direct pathway to low-volatility compounds can contribute to observed particle formation and explain particle growth in boreal forest regions,

consistent with recent predictions<sup>7</sup>.

Ehn *et al.* propose that the products are formed efficiently in the reaction of endocyclic alkenes (chemical structures found in many abundant terpenes) with ozone. They suggest a mechanism consisting of a chain reaction in which a hydrogen atom is rapidly removed from a terpene molecule, forming a free radical to which an oxygen molecule attaches; this cycle repeats several times before terminating (see Extended Data Fig. 9a of the paper<sup>1</sup>). Their hypothesis may explain why models better approximate biogenic SOA if they allow the products of the first oxidation reactions of terpenes to be involatile<sup>8</sup>. In any case, inclusion of such products in atmospheric oxidation mechanisms can only improve our predictive capability and potentially close the gap between bottom-up models and atmospheric observations. The hypothesized mechanism also provides a means by which the particle-forming potential of BVOCs can be affected by anthropogenic emissions, because the extent of the chain reaction will be influenced by atmospheric levels of compounds produced by human activities.

The current study should provoke valuable developments in several areas. Attempts should be made to directly establish the oxidation mechanisms that so efficiently generate highly oxidized compounds, to identify the products and the kinetics of the participating reactions. This information will enable detailed analyses of the sensitivity of the SOA-formation process to different conditions, and of the sensitivities of components of previously proposed oxidation mechanisms to the newly described process.

Although Ehn and colleagues' logic is convincing, they did not directly determine the volatility of the observed products. It would

therefore be beneficial if their attribution of complete involatility (or extremely low volatility) to the products is substantiated by measurement. That said, measurement will be difficult: the compounds are likely to have several hydroperoxide groups (HOO) and/or peroxy acids (HOOC=O) on a monoterpene backbone, and so will probably be difficult to make. Estimating the compounds' volatilities will also be difficult, because hydroperoxides and peroxy acids are poorly represented in techniques used for such estimations.

The current work highlights the importance of accurately measuring atmospheric oxidant levels and BVOC emissions. Anthropogenic changes in the ratio of ozone to hydroxyl radicals (both of which are key oxidizers in the atmosphere), and in concentrations of nitrogen oxides (which affect atmospheric ozone levels) will influence climate through SOA and its effects on concentrations of cloud condensation nuclei, the particles that act as seeds for cloud-droplet formation.

Biogenic SOA particles probably have a substantial role in natural climate feedback cycles, whereby emissions of BVOCs are affected by the direct or indirect effects of the particles on the intensity of solar radiation that reaches the ground<sup>9,10</sup>. The influences of climate and of perturbations to terrestrial vegetation caused by human activities will also affect BVOC emissions. Mechanistic<sup>11</sup> and sensitivity<sup>12</sup> elements of the feedbacks mentioned above have received considerable recent attention. The mechanistic insights into the production of low-volatility compounds provided by Ehn *et al.* should lead to a better description of how aerosol particles and cloud condensation nuclei form, and of the associated climate feedbacks following BVOC emission changes, thereby improving the predictive capabilities of climate and Earth system models. ■

**Gordon McFiggans** is at the School of Earth, Atmospheric and Environmental Sciences, University of Manchester, Manchester M13 9PL, UK.  
e-mail: g.mcfiggans@manchester.ac.uk

1. Ehn, M. *et al.* *Nature* **506**, 476–479 (2014).
2. Jimenez, J. L. *et al.* *Science* **326**, 1525–1529 (2009).
3. Hallquist, M. *et al.* *Atmos. Chem. Phys.* **9**, 5155–5236 (2009).
4. Kulmala, M. *et al.* *J. Aerosol Sci.* **35**, 143–176 (2004).
5. Kulmala, M. *et al.* *Science* **339**, 943–946 (2013).
6. Donahue, N. M., Trump, E. R., Pierce, J. R. & Riipinen, I. *Geophys. Res. Lett.* **38**, L16801 (2011).
7. Donahue, N. M. *et al.* *Faraday Discuss.* **165**, 91–104 (2013).
8. Spracklen, D. V. *et al.* *Atmos. Chem. Phys.* **11**, 12109–12136 (2011).
9. Kulmala, M. *et al.* *Atmos. Chem. Phys.* **4**, 557–562 (2004).
10. Mentel, Th. F. *et al.* *Atmos. Chem. Phys.* **13**, 8755–8770 (2013).
11. Topping, D., Connolly, P. & McFiggans, G. *Nature Geosci.* **6**, 443–446 (2013).
12. Paasonen, P. *et al.* *Nature Geosci.* **6**, 438–442 (2013).

# Epigenomic alterations define lethal CIMP-positive ependymomas of infancy

S. C. Mack<sup>1,2,3\*</sup>, H. Witt<sup>4,5,6\*</sup>, R. M. Piro<sup>6,7</sup>, L. Gu<sup>6,8</sup>, S. Zuyderduyn<sup>9</sup>, A. M. Stütz<sup>6,10</sup>, X. Wang<sup>1,2</sup>, M. Gallo<sup>1</sup>, L. Garzia<sup>1</sup>, K. Zayne<sup>1</sup>, X. Zhang<sup>11</sup>, V. Ramaswamy<sup>1,2</sup>, N. Jäger<sup>6,8</sup>, D. T. W. Jones<sup>4,6</sup>, M. Sill<sup>6,12</sup>, T. J. Pugh<sup>13</sup>, M. Ryzhova<sup>4,6</sup>, K. M. Wani<sup>14</sup>, D. J. H. Shih<sup>1,2</sup>, R. Head<sup>1</sup>, M. Remke<sup>1,2</sup>, S. D. Bailey<sup>15,16</sup>, T. Zichner<sup>6,10</sup>, C. C. Faria<sup>1</sup>, M. Barszczyk<sup>1,2</sup>, S. Stark<sup>4,6</sup>, H. Seker-Cin<sup>4,6</sup>, S. Hutter<sup>4,6</sup>, P. Johann<sup>4,6</sup>, S. Bender<sup>4,6</sup>, V. Hovestadt<sup>6,7</sup>, T. Tzaridis<sup>4,6</sup>, A. M. Dubuc<sup>1,2</sup>, P. A. Northcott<sup>4,6</sup>, J. Peacock<sup>1,2</sup>, K. C. Bertrand<sup>1,2</sup>, S. Agnihotri<sup>1</sup>, F. M. G. Cavalli<sup>1</sup>, I. Clarke<sup>1</sup>, K. Nethery-Brook<sup>1</sup>, C. L. Creasy<sup>17</sup>, S. K. Verma<sup>17</sup>, J. Koster<sup>18</sup>, X. Wu<sup>1</sup>, Y. Yao<sup>1,2</sup>, T. Milde<sup>5,6,19</sup>, P. Sin-Chan<sup>1</sup>, J. Zuccaro<sup>1</sup>, L. Lau<sup>1</sup>, S. Pereira<sup>1</sup>, P. Castelo-Branco<sup>1</sup>, M. Hirst<sup>20,21</sup>, M. A. Marra<sup>21,22</sup>, S. S. Roberts<sup>23</sup>, D. Fuhs<sup>24</sup>, L. Massimi<sup>25</sup>, Y. J. Cho<sup>26</sup>, T. Van Meter<sup>27</sup>, W. Grajkowska<sup>28</sup>, B. Lach<sup>29</sup>, A. E. Kulozik<sup>5,6</sup>, A. von Deimling<sup>6,30</sup>, O. Witt<sup>5,6,19</sup>, S. W. Scherer<sup>1</sup>, X. Fan<sup>31,32</sup>, K. M. Muraszko<sup>32</sup>, M. Kool<sup>4,6</sup>, S. L. Pomeroy<sup>13</sup>, N. Gupta<sup>33</sup>, J. Phillips<sup>34</sup>, A. Huang<sup>1,35</sup>, U. Tabori<sup>1,35</sup>, C. Hawkins<sup>1,2</sup>, D. Malkin<sup>36</sup>, P. N. Kongkham<sup>1,2,3</sup>, W. A. Weiss<sup>34</sup>, N. Jabado<sup>37</sup>, J. T. Rutka<sup>1,2,3</sup>, E. Bouffet<sup>35</sup>, J. O. Korbel<sup>10</sup>, M. Lupien<sup>15,16,38</sup>, K. D. Aldape<sup>9</sup>, G. D. Bader<sup>9</sup>, R. Eils<sup>6,8</sup>, P. Lichter<sup>6,7</sup>, P. B. Dirks<sup>1,2,3,39</sup>, S. M. Pfister<sup>4,5,6</sup>, A. Korshunov<sup>6,31,40</sup> & M. D. Taylor<sup>1,2,3</sup>

**Ependymomas are common childhood brain tumours that occur throughout the nervous system, but are most common in the paediatric hindbrain. Current standard therapy comprises surgery and radiation, but not cytotoxic chemotherapy as it does not further increase survival. Whole-genome and whole-exome sequencing of 47 hindbrain ependymomas reveals an extremely low mutation rate, and zero significant recurrent somatic single nucleotide variants. Although devoid of recurrent single nucleotide variants and focal copy number aberrations, poor-prognosis hindbrain ependymomas exhibit a CpG island methylator phenotype. Transcriptional silencing driven by CpG methylation converges exclusively on targets of the Polycomb repressive complex 2 which represses expression of differentiation genes through trimethylation of H3K27. CpG island methylator phenotype-positive hindbrain ependymomas are responsive to clinical drugs that target either DNA or H3K27 methylation both *in vitro* and *in vivo*. We conclude that epigenetic modifiers are the first rational therapeutic candidates for this deadly malignancy, which is epigenetically deregulated but genetically bland.**

Ependymomas are malignancies that occur throughout the nervous system, but are more common in the hindbrain in children, as opposed to supratentorial and spinal cord tumours, which are more frequently diagnosed in adulthood. Despite being histologically identical, ependymomas from different regions of the nervous system are biologically and clinically distinct<sup>1</sup>. Current therapy for all ependymoma patients consists of maximal safe surgical resection, followed by radiation therapy<sup>2</sup>. Although adjuvant chemotherapy is routine for most children with

malignant brain tumours, it is not part of the current standard of care for ependymoma patients as multiple clinical trials have failed to show any survival benefit after cytotoxic chemotherapies<sup>3</sup>. Even at the time of disease recurrence, chemotherapy has not been shown to be effective for ependymomas; therefore, many children with recurrent ependymoma undergo a full but palliative second course of cranial irradiation<sup>4</sup>. Indeed, whereas treatment protocols for many other childhood malignancies have changed and improved in the past two decades, ependymoma

<sup>1</sup>Developmental & Stem Cell Biology Program, Arthur and Sonia Labatt Brain Tumour Research Centre, The Hospital for Sick Children, Toronto, Ontario M5G 1L7, Canada. <sup>2</sup>Laboratory Medicine and Pathobiology, University of Toronto, Toronto, Ontario M5S 1A8, Canada. <sup>3</sup>Division of Neurosurgery, University of Toronto, Toronto, Ontario M5S 1A8, Canada. <sup>4</sup>Division of Pediatric Neurooncology, German Cancer Research Center (DKFZ), 69120 Heidelberg, Germany. <sup>5</sup>Department of Pediatric Oncology, Hematology and Immunology, University of Heidelberg, Heidelberg 69120, Germany. <sup>6</sup>German Cancer Consortium (DKTK), Heidelberg 69120, Germany. <sup>7</sup>Division of Molecular Genetics, German Cancer Research Center (DKFZ), Heidelberg 69120, Germany. <sup>8</sup>Division of Theoretical Bioinformatics, German Cancer Research Center (DKFZ), Heidelberg 69120, Germany. <sup>9</sup>Department of Molecular Genetics, Banting and Best Department of Medical Research, The Donnelly Centre, University of Toronto, Toronto, Ontario M4N 1X8, Canada. <sup>10</sup>Genome Biology, European Molecular Biology, Laboratory Meyerhofstr. 1, Heidelberg 69117, Germany. <sup>11</sup>Department of Genetics, Norris Cotton Cancer Center, Dartmouth Medical School, Lebanon, New Hampshire 03756, USA. <sup>12</sup>Division of Bioinformatics, German Cancer Research Center (DKFZ), Heidelberg 69120, Germany. <sup>13</sup>Department of Neurology, Harvard Medical School, Children's Hospital Boston, MIT, Boston, Massachusetts 02115, USA. <sup>14</sup>Department of Pathology, The University of Texas MD Anderson Cancer Center, Houston, Texas 77030, USA. <sup>15</sup>Ontario Cancer Institute, Princess Margaret Cancer Centre—University Health Network, Toronto, Ontario M5G 1L7, Canada. <sup>16</sup>Ontario Institute for Cancer Research, Toronto, Ontario M5G 1L7, Canada. <sup>17</sup>Cancer Epigenetics Discovery Performance Unit, GlaxoSmithKline Pharmaceuticals, Collegeville, Pennsylvania 19426, USA. <sup>18</sup>Department of Oncogenomics, Academic Medical Center, Amsterdam 1105, The Netherlands. <sup>19</sup>CCU Pediatric Oncology, German Cancer Research Center (DKFZ), Heidelberg 69120, Germany. <sup>20</sup>Centre for High-Throughput Biology, Department of Microbiology & Immunology, University of British Columbia, Vancouver, V6T 1Z4 British Columbia, Canada. <sup>21</sup>Canada's Michael Smith Genome Sciences Centre, BC Cancer Agency, Vancouver, British Columbia V5Z 1L3, Canada. <sup>22</sup>Department of Medical Genetics, University of British Columbia, Vancouver, British Columbia V6H 3N1, Canada. <sup>23</sup>Department of Pediatrics and National Capital Consortium, Uniformed Services University, Bethesda, Maryland 20814, USA. <sup>24</sup>Department of Neurosurgery, University of Utah School of Medicine, Salt Lake City, Utah 84132, USA. <sup>25</sup>Pediatric Neurosurgery, Catholic University Medical School, Gemelli Hospital, Rome 00168, Italy. <sup>26</sup>Department of Neurology and Neurological Sciences, Stanford University School of Medicine, Stanford, California 94305, USA. <sup>27</sup>Department of Pediatrics, Virginia Commonwealth University, Richmond, Virginia 23298-0646, USA. <sup>28</sup>Department of Pathology, University of Warsaw, Children's Memorial Health Institute University of Warsaw, Warsaw 04-730, Poland. <sup>29</sup>Division of Anatomical Pathology, Department of Pathology and Molecular Medicine, McMaster University, Hamilton General Hospital, Hamilton, Ontario L8S 4K1, Canada. <sup>30</sup>Department of Neuropathology Ruprecht-Karls-University Heidelberg, Institute of Pathology, Heidelberg 69120, Germany. <sup>31</sup>University of Michigan Cell and Developmental Biology, Ann Arbor, Michigan 48109-2200, USA. <sup>32</sup>Department of Neurosurgery, University of Michigan Medical School, Ann Arbor, Michigan 48109, USA. <sup>33</sup>Department of Neurosurgery, University of California San Francisco, San Francisco, California 94143-0112, USA. <sup>34</sup>Departments of Neurology, Pediatrics, and Neurosurgery, University of California, San Francisco, The Helen Diller Family Cancer Research Building, San Francisco, California 94158, USA. <sup>35</sup>Department of Neuro-oncology, The Hospital for Sick Children, Toronto, Ontario M5G 1X8, Canada. <sup>36</sup>Department of Haematology and Oncology, The Hospital for Sick Children, Toronto, Ontario M5G 1X8, Canada. <sup>37</sup>Departments of Pediatrics and Human Genetics, McGill University and the McGill University Health Center Research Institute, Montreal, Quebec H3Z 2Z3, Canada. <sup>38</sup>Department of Medical Biophysics, University of Toronto, Toronto, Ontario M5G 1X8, Canada. <sup>39</sup>Department of Molecular Genetics, University of Toronto, Toronto, Ontario M5S 1A8, Canada. <sup>40</sup>CCU Neuropathology, German Cancer Research Center (DKFZ), Heidelberg 69120, Germany.

\*These authors contributed equally to this work.



therapy remains stagnant. The mechanisms underlying the chemoresistance of ependymoma are not known.

Within each anatomical compartment (supratentorial/hindbrain/spinal), there is additional inter-tumoral heterogeneity in the form of well-documented molecular subtypes of ependymoma<sup>5–7</sup>. Ependymoma subtypes are clinically and functionally relevant, as rational therapies may only be effective in a single subtype of the disease<sup>8</sup>. Ependymomas are thought to arise from the regionally distinct radial glial cells. Differences between these radial glial cell populations are likely carried forward in the neoplasm, and may account for a portion of the observed heterogeneity<sup>1,5</sup>. Hindbrain ependymomas occur within the posterior fossa of the skull, and are clinically referred to as ‘posterior fossa’ (PF) ependymomas. There are two clear and distinct subtypes of PF ependymoma; one that occurs in older children and adults with very good prognosis (posterior fossa group B, or PFB), and another found predominantly in infants, which is associated with poor prognosis in spite of maximally aggressive therapy (posterior fossa group A, or PFA)<sup>6,7</sup>.

## Ependymoma genome data

To uncover the biology of PF ependymomas, we undertook whole-genome sequencing of tumour and matching germline DNA from five ependymomas (3 PFA, 2 PFB), and whole-exome sequencing of an additional 42 PF ependymomas and their matching germline DNA (24 PFA and 18 PFB) (Fig. 1a, b, Supplementary Figs 1, 2 and Supplementary Tables 1, 2). Unlike some other childhood malignancies, the rate of somatic single nucleotide variants (SNVs) did not correlate significantly with the age at diagnosis (Supplementary Fig. 2)<sup>9</sup>. Further, the rate of somatic SNVs was extremely low in PF ependymomas, with an average of 5.0 somatic nonsynonymous SNVs per exome across the entire cohort (Fig. 1b), and low in both PFA (4.6 SNVs per tumour) and PFB ependymomas (5.6 SNVs per tumour, Supplementary Table 3). Perhaps the most surprising result was that there were zero significant recurrent mutations across the cohort of 47 PF ependymomas as detected by two different algorithms, MUTSIG<sup>10</sup> and MUSIC<sup>11</sup> (Fig. 1c and Supplementary Tables 3–6). Despite the absence of significant recurrent SNVs, PFB harboured frequent and recurrent large-scale copy number alterations (CNAs) indicative of chromosomal aneuploidy (Supplementary Fig. 3). Compared to other malignancies, PF ependymomas have a very low rate of SNVs per megabase, and the lowest number of recurrent significant SNVs, making PF ependymoma the first malignancy for which genome sequencing across a broad cohort ( $n = 47$ ) has failed

to identify any significantly and recurrently mutated genes (Fig. 1c and Supplementary Tables 3–7)<sup>9,12–25</sup>.

## Ependymoma epigenome data

A number of other childhood nervous system malignancies, including medulloblastoma, retinoblastoma, glioblastoma, atypical teratoid/rhabdoid tumour, and neuroblastoma, have recently been demonstrated to harbour a paucity of recurrent mutations, with a significant proportion of the recurrent events converging on epigenetic mechanisms<sup>9,22,24–33</sup>. Owing to the absence of recurrent and significant SNVs and CNAs, we proposed that PFA ependymomas could be driven by epigenetic mechanisms. We studied DNA methylation patterns in a discovery cohort of 79 ependymomas using methyl-CpG-binding domain protein 2 (MBD2) recovery followed by hybridization to NimbleGen 385K CpG Island Promoter Plus microarrays (MBD2-chip). Unsupervised consensus clustering of CpG methylation profiles yielded three distinct subgroups, composed of supratentorial, PF, and mixed spinal/PF tumours, in a pattern highly similar to that yielded by unsupervised clustering of gene expression profiles (Fig. 2a and Supplementary Fig. 4)<sup>6</sup>. The group of pure PF tumours corresponds to PFA ependymomas, whereas the PFB ependymomas cluster with the spinal ependymomas. We validated our discovery cohort findings through study of a non-overlapping cohort of 48 PF ependymomas using an orthogonal technology (Illumina Infinium 450K methylation arrays). In these validation experiments, the DNA methylome of PFA ependymomas was very distinct from PFB tumours (Fig. 2b and Supplementary Fig. 5). Unsupervised clustering of CpG methylation signatures was very robust, supporting two major molecular subtypes, even after applying a number of distinct bioinformatic and biostatistical techniques (Supplementary Fig. 5). We conclude that PFA and PFB ependymomas have very distinct methylomes, and that epigenetic biomarkers could be used to develop a clinically relevant molecular classification of PF ependymomas. To this end, we identified three genes that exhibited increased CpG methylation in most PFA tumours, but not in PFB tumours (Supplementary Fig. 6). We determined the presence of CpG hypermethylation representing PFA tumours using a mass spectrometry-based technology (Sequenom) on our training cohort (Supplementary Figs 6, 7 and Supplementary Table 8). We were able to validate our Sequenom-based biomarker panel on an independent cohort of ependymomas using formalin-fixed, paraffin-embedded tissues to predict both progression-free and overall survival (Supplementary Figs 6, 7 and Supplementary Table 8). We conclude that division

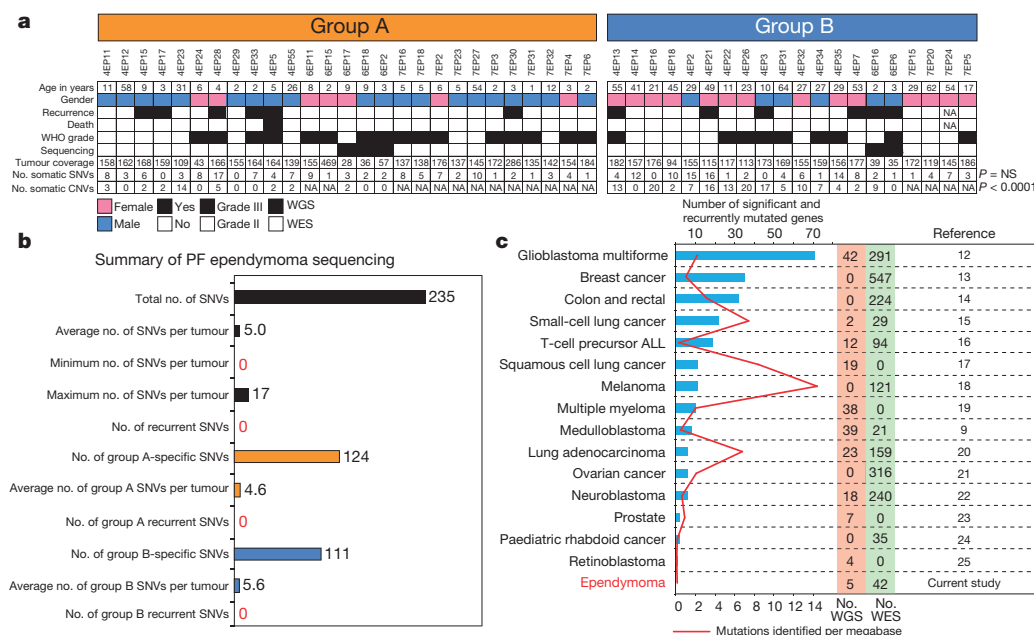


**Figure 1 | Somatic SNVs are rare in the posterior fossa ependymoma genome.** **a**, Summary of clinical and genomic details of PF ependymomas stratified according to group A and group B ependymoma (Wilcoxon rank-sum test). CNV, copy number variation; NA, not available; NS, not significant; WES, whole-exome sequencing; WGS, whole-genome sequencing. **b**, Bar graphs summarizing the numbers and frequencies of SNVs detected by whole-genome and whole-exome sequencing of PF ependymomas. **c**, Comparison of numbers of significant and recurrently mutated genes, and mutation rates, in several whole-genome and whole-exome sequencing studies of adult and paediatric cancers (false discovery rate (FDR) < 0.1).

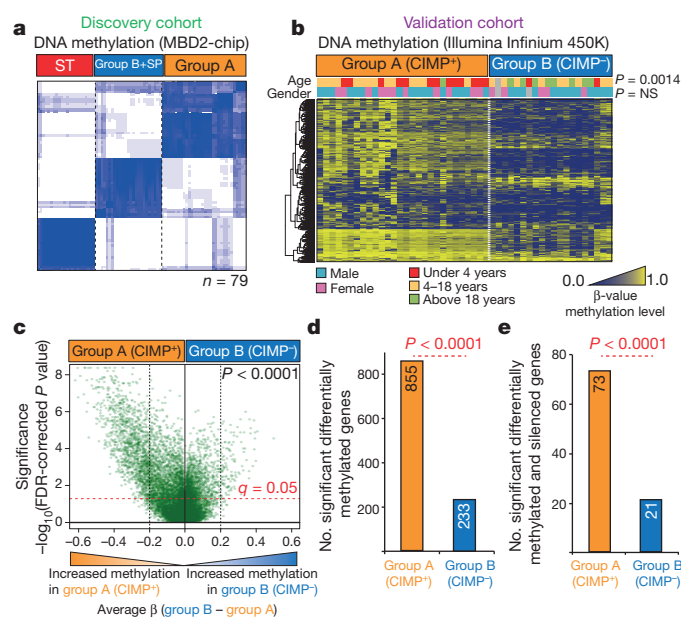


**Figure 2 | DNA-methylation profiles suggest that group A ependyomas demonstrate a CpG island methylator phenotype.** **a**, Unsupervised hierarchical clustering of 79 ependyoma DNA-methylation profiles. SP, spinal cord; ST, supratentorial. **b**, Heatmap of 48 PF ependyoma DNA-methylation profiles. Group A and group B clinical differences were assessed using a two-sided Fisher's exact test. **c**, Volcano plot comparing the number of significant methylated CpG sites between group A and group B ( $P < 0.05$ , Wilcoxon rank-sum test, FDR-corrected). **d**, **e**, Differences in the number of methylated genes (**d**) and methylated and silenced genes (**e**) in group A versus group B ( $P < 0.0001$ , binomial distribution test).

of PFA from PFB ependyomas using a mass spectrometry-based biomarker should be feasible in a clinical setting.

### CIMP phenotype in PFA ependyomas

We next compared the extent of promoter CpG methylation in PFA ependyomas to that of PFB ependyomas and found that PFA tumours have a much higher extent of CpG island methylation (Fig. 2c–e, Supplementary Figs 8, 9 and Supplementary Tables 9–14). In comparison to PFB ependyomas, PFA tumours have more methylated CpG sites (Fig. 2c), more genes with significant CpG methylation (Fig. 2d) and more genes that are transcriptionally silenced by CpG hypermethylation (Fig. 2e). We conclude that PFA ependyomas exhibit a 'CpG island methylator' or 'CIMP' phenotype, and suggest that PFA ependyomas be referred to as PFA CIMP-positive (PFA-CIMP<sup>+</sup>) ependyomas, and PFB as PFB CIMP-negative (PFB-CIMP<sup>-</sup>)<sup>34</sup> (Supplementary Table 15 and Supplementary Figs 8–12). To determine the mechanism by which CpG hypermethylation driving transcriptional silencing promotes the pathogenesis of PFA ependyoma, we performed a pathway analysis in our discovery cohort of PFA and PFB ependyomas studied by MBD2-chip (Fig. 3a and Supplementary Table 16). Although olfactory signalling was the only significant pathway enriched in PFB ependyomas, genes CpG methylated in PFA ependyoma showed a remarkable convergence on genes documented as silenced in embryonic stem (ES) cells by the Polycomb repressive complex 2 (PRC2). In our non-overlapping, independent validation data set studied by Illumina Infinium 450K arrays, we observed no significant pathways in the PFB ependyomas, whereas the PFA tumours exhibited the same convergence on gene targets that are silenced by PRC2 in ES cells (Fig. 3b and Supplementary Table 17). The PRC2 complex contains the histone methylase EZH2, which trimethylates H3K27, thereby driving gene silencing. Genes known to be required for differentiation and which are silenced by PRC2 have been documented to frequently undergo cancer-specific CpG methylation, and it is described that both DNA and histone methylation contribute to ongoing gene silencing in these cancers<sup>35</sup>.

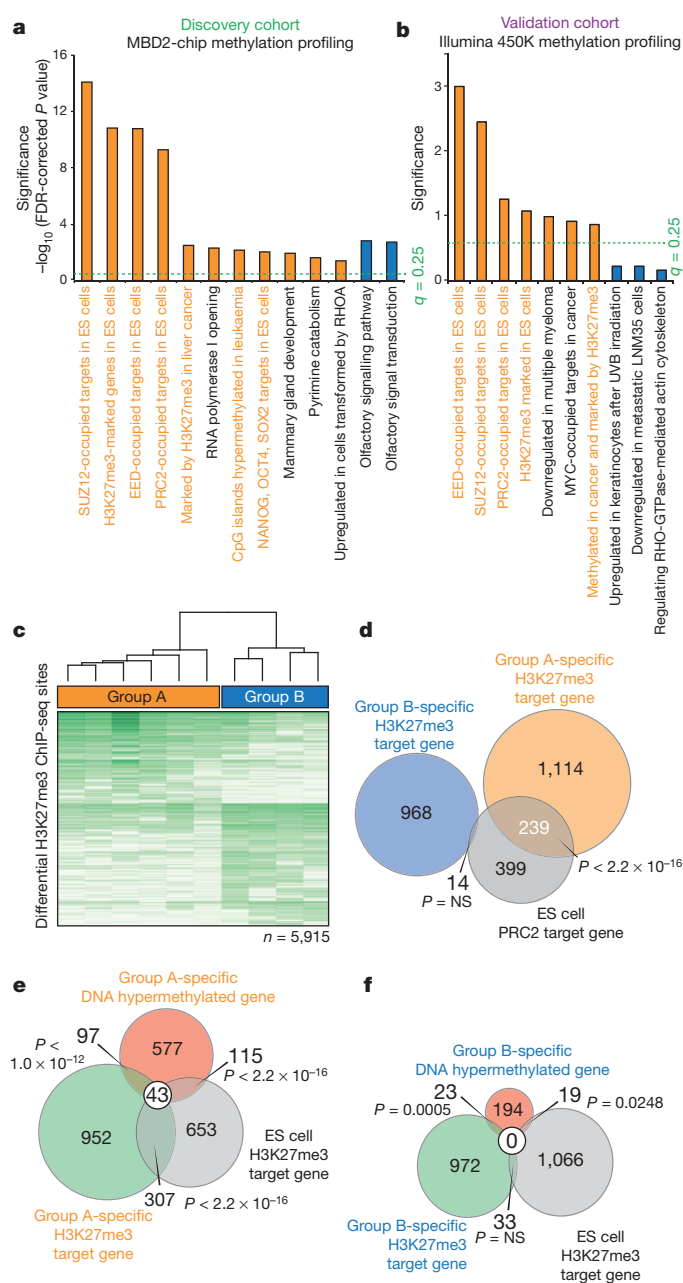


**Figure 3 | Group A (CIMP<sup>+</sup>) and group B (CIMP<sup>-</sup>) ependyomas are distinguished by CpG-hypermethylated and H3K27-trimethylated genes related to PRC2 occupancy in ES cells.** **a**, **b**, CpG-methylated pathways in group A (CIMP<sup>+</sup>) and group B (CIMP<sup>-</sup>) ependyomas in a discovery (**a**) and validation (**b**) cohort. **c**, Differential H3K27me3 binding sites distinguishing group A and group B ( $P < 0.01$  (MACSv2.0),  $P < 0.05$  (R:DiffBind)). **d**, **e**, Venn diagrams comparing group A and group B H3K27me3 genes with ES cell PRC2 genes (**d**) and group A H3K27me3 and DNA-hypermethylated genes with ES cell H3K27me3 genes (**e**). **f**, Group B H3K27me3 and DNA-hypermethylated genes with ES cell H3K27me3 genes (binomial distribution test)<sup>46</sup>.

### Convergence upon PRC2 targets

We next sought to validate these pathway findings by performing trimethylated H3K27 (H3K27me3) chromatin immunoprecipitation followed by massively parallel sequencing (ChIP-seq) in 11 primary PF ependyomas. Our findings demonstrate distinct H3K27me3 signatures in PFA-CIMP<sup>+</sup> versus PFB-CIMP<sup>-</sup> ependyomas (Fig. 3c, Supplementary Table 18 and Supplementary Figs 13, 14). Furthermore, the gene expression of H3K27me3 target genes can robustly stratify PFA-CIMP<sup>+</sup> from PFB-CIMP<sup>-</sup> tumours, thus highlighting the distinct epigenetic



differences between these subgroups (Supplementary Fig. 14). Examination of differential H3K27me3 targets demonstrated a convergence and significant overlap with PRC2 targets in ES cells observed exclusively in PFA-CIMP<sup>+</sup> tumours (Fig. 3d). Further, a significant proportion of shared PFA-CIMP<sup>+</sup> and ES cell H3K27me3 targets were CpG hypermethylated exclusively in PFA (CIMP<sup>+</sup>) tumours, a pattern that was not detected in PFB-CIMP<sup>-</sup> ependymoma (Fig. 3e, f and Supplementary Tables 18, 19). We propose, therefore, that hyperactivity of the PRC2 complex leading to tumour suppressor gene silencing with subsequent gene silencing by DNA CpG hypermethylation contributes to the pathogenesis of PFA-CIMP<sup>+</sup> ependymoma.

We next sought to expand our global analysis of CpG methylation by performing whole-genome bisulphite sequencing in 3 PFAs, 3 PFBs, 3 fetal normal brains and 3 adult normal brains (Supplementary Tables 20–22). Here we observed the same patterns of increased CpG methylation at CpG islands occurring specifically in PFA-CIMP<sup>+</sup> tumours consistent with a CpG island methylator phenotype (Fig. 4a, c and Supplementary Fig. 15). In line with other solid tumours we identified additional cancer-specific epigenome patterns including hypomethylation of repetitive elements (long interspersed nuclear elements, short interspersed nuclear elements and long terminal repeats) restricted to PFA-CIMP<sup>+</sup> ependymoma and subgroup-specific partially methylated domains (Fig. 4b, d and Supplementary Figs 15, 16). These findings illustrate genome-wide DNA-methylation alterations in PFA-CIMP<sup>+</sup> ependymoma, concurrent with a silent genome exhibiting few CNAs and no significant and recurrent somatic SNVs.

### CpG and histone methylation in tumour maintenance

Although our genomic and epigenomic data suggest that over-activity of the PRC2 complex, and/or subsequent promoter CpG hypermethylation, may be involved in driving the pathogenesis of PFA-CIMP<sup>+</sup> ependymomas, they do not address whether or not these mechanisms continue to be necessary for tumour maintenance, and would therefore constitute an effective target for therapy. Functional assessment of CpG and histone methylation in ependymoma is harshly limited by

the complete lack of established ependymoma cell lines, xenografts or transgenic mouse models<sup>1,5,6</sup>. To this end we established four short-term, patient-derived primary ependymoma cultures from two PFA-CIMP<sup>+</sup> tumours, and two childhood supratentorial ependymomas. We were unable to grow any PFB-CIMP<sup>-</sup> ependymomas *in vitro*. Treatment of PFA-CIMP<sup>+</sup> cultures with the DNA-demethylating agents 5-aza-2'-deoxycytidine (decitabine, here referred to as DAC) resulted in marked de-repression of gene sets enriched in EZH2 targets and known DNA-hypermethylated genes in other solid cancers (Fig. 4e, f). Furthermore, compared to supratentorial ependymoma primary cultures *in vitro*, DAC demonstrated significant anti-neoplastic effect on both PFA-CIMP<sup>+</sup> tumours at low-dose nanomolar levels (Fig. 4g). To model the effects of DAC on PFA-CIMP<sup>+</sup> cultures as early, and representative of the patient tumour as possible, we derived a passage zero *ex vivo* culture from a PFA-CIMP<sup>+</sup> metastasis. In this *ex vivo* culture we demonstrate significant impairment of neurosphere colony formation upon DNA-methylation blockade (Fig. 4h and Supplementary Fig. 17). Because DAC is FDA approved for the treatment of haematopoietic malignancies, we propose that it could be rapidly repurposed in a clinical trial for children with PFA-CIMP<sup>+</sup> ependymoma<sup>36</sup>. In addition, we observed additive effects on combining DAC and an FDA-approved histone deacetylase inhibitor (suberoylanilide hydroxamic acid, SAHA) against PFA-CIMP<sup>+</sup> ependymoma (Supplementary Fig. 18).

The tool compound 3-deazaneplanocin A (DZNep) is known to target the PRC2 complex and result in diminished trimethylation of H3K27 through degradation of PRC2 complex proteins<sup>37</sup>. Treatment of PFA-CIMP<sup>+</sup> ependymoma, but not supratentorial ependymoma, with DZNep is highly effective in the nanomolar range *in vitro* (IC<sub>50</sub> for E517, 95 nM; E520, 262 nM) (Fig. 5a). We also observed additive effects between DZNep and SAHA, and DZNep and DAC (Supplementary Fig. 18). Treatment of PFA-CIMP<sup>+</sup> ependymomas with DZNep, compared to controls, results in decreased expression of EZH2, decreased trimethylation of H3K27 and increased cleavage of PARP (Fig. 5b). *In vivo* treatment of established xenografts of human PFA-CIMP<sup>+</sup> ependymoma with DZNep using either a flank model (Fig. 5c), or an

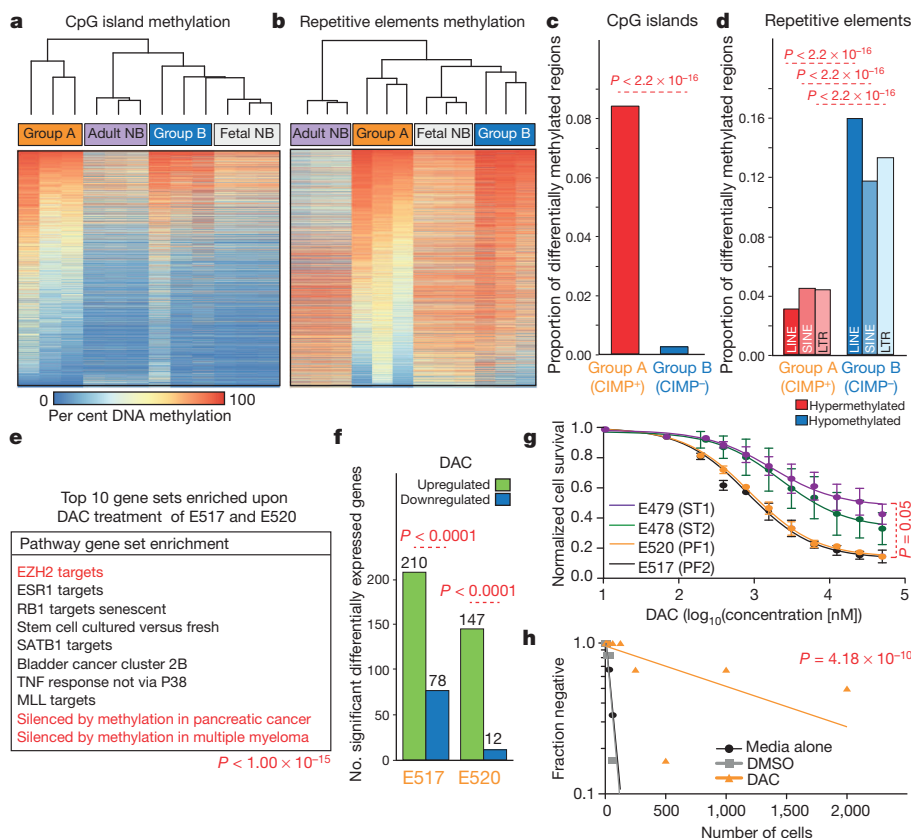


**Figure 4 | Whole-genome bisulphite sequencing validates a CpG island methylator phenotype in group A ependymoma.** **a, b**, Heatmap of DNA methylation at CpG islands (**a**) and repetitive regions (**b**) in group A (CIMP<sup>+</sup>) versus group B (CIMP<sup>-</sup>). NB, normal brain. **c, d**, Proportion of hypermethylated versus hypomethylated regions at CpG islands (**c**) and repetitive elements (**d**) in group A and group B ( $P < 2.2 \times 10^{-16}$ , binomial distribution test). LINE, long interspersed nuclear elements; LTR, long terminal repeats; SINE, short interspersed nuclear elements. **e, f**, Top 10 pathways upregulated (**e**) and differentially expressed (**f**) upon DAC treatment of E517-PF2 and E520-PF1 ( $P < 0.0001$ , binomial distribution test). **g**, Survival analysis of E478-ST2, E479-ST1, E517-PF2 and E520-PF1 cells treated for 7 days with DAC ( $P = 0.05$ , two-sided *t*-test, error bars, s.e.m.; technical ( $n = 6$ ) over biological ( $n = 2$ )). **h**, Limiting dilution assay of zero passage group A cells treated for 2 weeks with DAC ( $P = 4.18 \times 10^{-10}$ , chi-squared test). DMSO, dimethylsulphoxide.

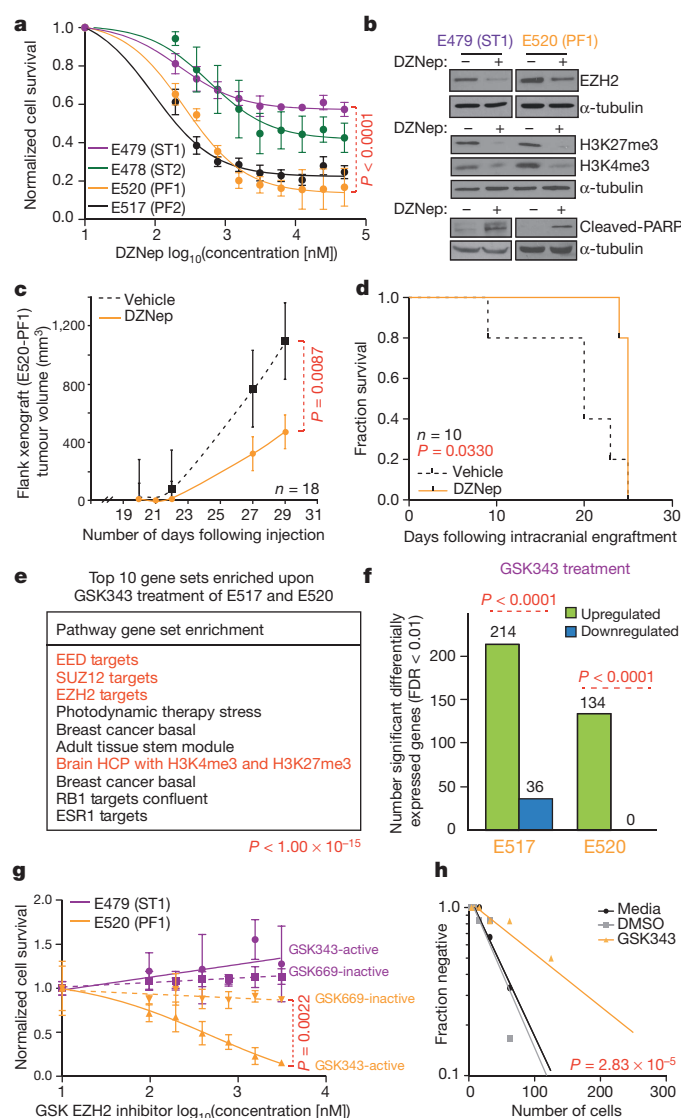


**Figure 5 | Modulation of H3K27 methylation has anti-neoplastic effects against group A ependymoma.** **a**, Survival of E479-ST1, E478-ST2, E520-PF1 and E517-PF2 cells treated for 7 days with DZNep ( $P < 0.0001$ , two-sided  $t$ -test, error bars = s.e.m., biological ( $n = 3$ )). **b**, EZH2, H3K27me3, H3K4me3 and cleaved-PARP protein expression in E520-PF1 and E479-ST1 cells treated for 7 days with DZNep (500 nM). **c**, E520-PF1 flank tumour volumes following treatment with DZNep ( $P = 0.0087$ , Wilcoxon-test, error bars = s.d.). **d**, Survival of E520-PF1 PF tumour-bearing mice treated with DZNep ( $P = 0.033$ , log-rank test). **e**, **f**, Top 10 pathways upregulated (**e**) and differentially expressed (**f**) upon treatment of E517 and E520 with GSK343. **g**, Cell proliferation of E520-PF1 and E479-ST1 cells treated for 11 days with GSK343 (active inhibitor) or GSK669 (inactive inhibitor) ( $P = 0.0022$ , two-sided  $t$ -test, error bars = s.e.m., technical ( $n = 9$ ) over biological ( $n = 3$ )). **h**, Limiting dilution assay of passage zero group A cells treated for 2 weeks with GSK343 ( $P = 2.83 \times 10^{-5}$ , chi-square-test). HCP, high-CpG-density promoter.

orthotopic intracerebellar xenograft model (Fig. 5d) results in decreased tumour volume and improved survival. Furthermore, PFA-CIMP<sup>+</sup> ependymoma cells isolated from tumour xenografts treated *in vivo* with DZNep have a markedly reduced colony-forming ability compared to controls, suggesting that the compound targeted ependymoma cells with clonogenic or tumour-initiating potential (Supplementary Fig. 17). In addition, treatment with a recently published, and extremely potent, highly selective *S*-adenosyl-L-methionine competitive small molecular inhibitor of EZH2 (GSK343) results in significant de-repression of gene expression in PFA-CIMP<sup>+</sup> ependymoma including genes which are known targets of PRC2 in ES cells (Fig. 5e, f)<sup>38</sup>. We found that treatment

with GSK343 but not an inactive compound with the same molecular backbone (GSK669) resulted in diminished levels of H3K27me3, and had a potent antineoplastic effect against PFA-CIMP<sup>+</sup> ependymoma (Fig. 5g and Supplementary Fig. 17). These findings are further supported in a passage zero PFA-CIMP<sup>+</sup> *ex vivo* culture treated immediately with GSK343, which significantly impaired neurosphere colony formation (Fig. 5h). We therefore propose that ongoing hypermethylation of promoter CpG islands and H3K27 contribute to the maintenance of PFA-CIMP<sup>+</sup> ependymoma, and that targeting these epigenetic mechanisms represents the first identified rational targets for this chemotherapy-resistant, epigenetically dysregulated and genetically bland childhood cancer.

## Discussion

A number of recent seminal publications have demonstrated that childhood nervous system tumours harbour very few recurrent genetic events, and that many of the recurrent events converge on genes important in epigenetic processes such as CpG hypermethylation, post-translational modification of histones, and even mutation of the actual histone genes<sup>9,24–31</sup>. Although mutation of *IDH1*, *IDH2*, *TET1*, *TET2* and/or *DNMT3A* has been documented in other types of cancer with a CIMP phenotype, we did not observe any such mutations in PF ependymomas<sup>39,40</sup> (Supplementary Table 23). Although a number of other paediatric malignancies have a very low incidence of recurrent somatic mutations, we are unaware of any other malignancies with zero significant recurrently mutated genes.

Subgroups of patients with a CIMP phenotype have a better prognosis for some cancer histologies<sup>34</sup>, but not others<sup>41–45</sup>, suggesting that CIMP-positive tumours represent distinct subgroups of disease, but that the CIMP phenotype itself is not intrinsically benign or responsive to therapy. PFA-CIMP<sup>+</sup> ependymomas have a nearly normal genetic code and a very poor prognosis in comparison to aneuploid PFB (CIMP<sup>−</sup>) ependymomas, for which five-year overall survival exceeds 95% of patients. Many of the cytotoxic chemotherapeutics currently used clinically function through promoting damage to the genomic DNA, which subsequently induces cancer cells with deranged and disorganized genomes to undergo apoptosis. In light of the nearly normal genetic code found in PFA-CIMP<sup>+</sup> ependymomas, perhaps it is not surprising that a therapy based on DNA damage has not shown efficacy in clinical trials.

Our data demonstrate hyperactivity of DNA CpG methylation and disparate PRC2 H3K27me3 signatures in poor-prognosis PF ependymomas that may be necessary for tumour maintenance. Drugs that target DNA CpG methylation, PRC2/EZH2, and/or histone deacetylase inhibitors represent the first rational strategies for therapy of this untreatable disease, and should be considered for testing in clinical trials for children with PFA-CIMP<sup>+</sup> ependymoma.

## METHODS SUMMARY

**Whole-genome and whole-exome sequencing of PF ependymoma.** Sequencing was performed using Illumina technologies (HiSeq2000). Median DNA sequence coverage was 35-fold for the five whole-genome cases (range 28–57×), whereas median on-target coverage in the whole-exome cohort ( $n = 42$ ) was 157-fold (range 43–469×). Exome capture was carried out initially with Agilent SureSelect V3 and for later samples Agilent SureSelect V4 (Human All Exon 50 Mb) in-solution reagents. Sequence data were aligned to the hg19 human reference genome assembly; uplicate and non-uniquely mapping reads were excluded from calling of somatic variants. A subset of sequence variants were validated using PCR and capillary sequencing.

**DNA methylation profiling of PF ependymoma.** MBD2 protein recovery was performed using MethylMiner (Invitrogen) followed by hybridization to NimbleGen 385K CpG Island Promoter Plus Arrays. Microarray data was quantile normalized using the R-LIMMA package. Log<sub>2</sub> ratios were then transformed into BATMAN methylation states<sup>47</sup>. Comparisons between subgroups were performed using a Wilcoxon rank-sum test, and  $P$  values were corrected for multiple testing using the Benjamini–Hochberg method.

Illumina Infinium 450K methylation analysis was performed on bisulphite-treated DNA (Zymo) at The Centre for Applied Genomics (Toronto). CpG probes  $P < 0.05$  were removed from the analysis, arrays were then normalized using the R-BMIQ algorithm<sup>42</sup>. Methylation values were then exported as  $\beta$ -values. Methylation probes were then filtered to CpG sites, which mapped to promoters containing CpG islands. A Wilcoxon rank-sum test was used to identify the differentially methylated



CpG sites between group A (CIMP<sup>+</sup>) and group B (CIMP<sup>-</sup>). *P* values for differentially methylated CpG sites identified were then corrected for multiple testing using the Benjamini–Hochberg method. Significant differences between numbers of CpG sites, genes, or methylated and silenced genes, was calculated using a binomial distribution test. Gene expression data for all of these samples can be found in our previous publication<sup>6</sup>.

**Online Content** Any additional Methods, Extended Data display items and Source Data are available in the online version of the paper; references unique to these sections appear only in the online paper

Received 10 March 2013; accepted 28 January 2014.

Published online 19 February 2014.

- Taylor, M. D. *et al.* Radial glia cells are candidate stem cells of ependymoma. *Cancer Cell* **8**, 323–335 (2005).
- Merchant, T. E. *et al.* Conformal radiotherapy after surgery for paediatric ependymoma: a prospective study. *Lancet Oncol.* **10**, 258–266 (2009).
- Bouffet, E. & Foreman, N. Chemotherapy for intracranial ependymomas. *Childs Nerv. Syst.* **15**, 563–570 (1999).
- Bouffet, E. *et al.* Survival benefit for pediatric patients with recurrent ependymoma treated with reirradiation. *Int. J. Radiat. Oncol. Biol. Phys.* **83**, 1541–1548 (2012).
- Johnson, R. A. *et al.* Cross-species genomics matches driver mutations and cell compartments to model ependymoma. *Nature* **466**, 632–636 (2010).
- Witt, H. *et al.* Delineation of two clinically and molecularly distinct subgroups of posterior fossa ependymoma. *Cancer Cell* **20**, 143–157 (2011).
- Wani, K. *et al.* A prognostic gene expression signature in intratentorial ependymoma. *Acta Neuropathol.* **123**, 727–738 (2012).
- Atkinson, J. M. *et al.* An integrated *in vitro* and *in vivo* high-throughput screen identifies treatment leads for ependymoma. *Cancer Cell* **20**, 384–399 (2011).
- Jones, D. T. *et al.* Dissecting the genomic complexity underlying medulloblastoma. *Nature* **488**, 100–105 (2012).
- Lawrence, M. S. *et al.* Mutational heterogeneity in cancer and the search for new cancer-associated genes. *Nature* **499**, 214–218 (2013).
- Dees, N. D. *et al.* MuSiC: identifying mutational significance in cancer genomes. *Genome Res.* **22**, 1589–1598 (2012).
- Brennan, C. W. *et al.* The somatic genomic landscape of glioblastoma. *Cell* **155**, 462–477 (2013).
- Koboldt, D. C. *et al.* Comprehensive molecular portraits of human breast tumours. *Nature* **490**, 61–70 (2012).
- Muzny, D. M. *et al.* Comprehensive molecular characterization of human colon and rectal cancer. *Nature* **487**, 330–337 (2012).
- Peifer, M. *et al.* Integrative genomic analyses identify key somatic driver mutations of small-cell lung cancer. *Nature Genetics* **44**, 1104–1110 (2012).
- Zhang, J. *et al.* The genetic basis of early T-cell precursor acute lymphoblastic leukaemia. *Nature* **481**, 157–163 (2012).
- Hammerman, P. S. *et al.* Comprehensive genomic characterization of squamous cell lung cancers. *Nature* **489**, 519–525 (2012).
- Hodis, E. *et al.* A landscape of driver mutations in melanoma. *Cell* **150**, 251–263 (2012).
- Chapman, M. A. *et al.* Initial genome sequencing and analysis of multiple myeloma. *Nature* **471**, 467–472 (2011).
- Imielinski, M. *et al.* Mapping the hallmarks of lung adenocarcinoma with massively parallel sequencing. *Cell* **150**, 1107–1120 (2012).
- Bell, D. *et al.* Integrated genomic analyses of ovarian carcinoma. *Nature* **474**, 609–615 (2011).
- Pugh, T. J. *et al.* The genetic landscape of high-risk neuroblastoma. *Nature Genetics* **45**, 279–284 (2013).
- Berger, M. F. *et al.* The genomic complexity of primary human prostate cancer. *Nature* **470**, 214–220 (2011).
- Lee, R. S. *et al.* A remarkably simple genome underlies highly malignant pediatric rhabdoid cancers. *J. Clin. Invest.* **122**, 2983–2988 (2012).
- Zhang, J. *et al.* A novel retinoblastoma therapy from genomic and epigenetic analyses. *Nature* **481**, 329–334 (2012).
- Northcott, P. A. *et al.* Subgroup-specific structural variation across 1,000 medulloblastoma genomes. *Nature* **488**, 49–56 (2012).
- Pugh, T. J. *et al.* Medulloblastoma exome sequencing uncovers subtype-specific somatic mutations. *Nature* **488**, 106–110 (2012).
- Robinson, G. *et al.* Novel mutations target distinct subgroups of medulloblastoma. *Nature* **488**, 43–48 (2012).
- Schwartzentruber, J. *et al.* Driver mutations in histone H3.3 and chromatin remodelling genes in paediatric glioblastoma. *Nature* **482**, 226–231 (2012).
- Sausen, M. *et al.* Integrated genomic analyses identify *ARID1A* and *ARID1B* alterations in the childhood cancer neuroblastoma. *Nature Genet.* **45**, 12–17 (2013).
- Wu, G. *et al.* Somatic histone H3 alterations in pediatric diffuse intrinsic pontine gliomas and non-brainstem glioblastomas. *Nature Genet.* **44**, 251–253 (2012).
- Versteeg, I. *et al.* Truncating mutations of hSNF5/INI1 in aggressive paediatric cancer. *Nature* **394**, 203–206 (1998).
- Northcott, P. A. *et al.* Multiple recurrent genetic events converge on control of histone lysine methylation in medulloblastoma. *Nature Genet.* **41**, 465–472 (2009).
- Noushmehr, H. *et al.* Identification of a CpG island methylator phenotype that defines a distinct subgroup of glioma. *Cancer Cell* **17**, 510–522 (2010).
- Ohm, J. E. *et al.* A stem cell-like chromatin pattern may predispose tumor suppressor genes to DNA hypermethylation and heritable silencing. *Nature Genet.* **39**, 237–242 (2007).
- Kantarjian, H. *et al.* Decitabine improves patient outcomes in myelodysplastic syndromes: results of a phase III randomized study. *Cancer* **106**, 1794–1803 (2006).
- Tan, J. *et al.* Pharmacologic disruption of Polycomb-repressive complex 2-mediated gene repression selectively induces apoptosis in cancer cells. *Genes Dev.* **21**, 1050–1063 (2007).
- McCabe, M. T. *et al.* EZH2 inhibition as a therapeutic strategy for lymphoma with EZH2-activating mutations. *Nature* **492**, 108–112 (2012).
- Turcan, S. *et al.* IDH1 mutation is sufficient to establish the glioma hypermethylator phenotype. *Nature* **483**, 479–483 (2012).
- Williams, K. *et al.* TET1 and hydroxymethylcytosine in transcription and DNA methylation fidelity. *Nature* **473**, 343–348 (2011).
- Fang, F. *et al.* Breast cancer methylomes establish an epigenomic foundation for metastasis. *Sci. Transl. Med.* **3**, 75ra25 (2011).
- Roman-Gomez, J. *et al.* Lack of CpG island methylator phenotype defines a clinical subtype of T-cell acute lymphoblastic leukemia associated with good prognosis. *J. Clin. Oncol.* **23**, 7043–7049 (2005).
- Zouridis, H. *et al.* Methylation subtypes and large-scale epigenetic alterations in gastric cancer. *Sci. Transl. Med.* **4**, 156ra140 (2012).
- Toyota, M. *et al.* CpG island methylator phenotype in colorectal cancer. *Proc. Natl Acad. Sci. USA* **96**, 8681–8686 (1999).
- Weisenberger, D. J. *et al.* CpG island methylator phenotype underlies sporadic microsatellite instability and is tightly associated with *BRAF* mutation in colorectal cancer. *Nature Genet.* **38**, 787–793 (2006).
- Ben-Porath, I. *et al.* An embryonic stem cell-like gene expression signature in poorly differentiated aggressive human tumors. *Nature Genet.* **40**, 499–507 (2008).
- Down, T. A. *et al.* A Bayesian deconvolution strategy for immunoprecipitation-based DNA methylome analysis. *Nature Biotechnol.* **26**, 779–785 (2008).

**Supplementary Information** is available in the online version of the paper.

**Acknowledgements** M.D.T. holds a Canadian Institutes of Health Research (CIHR) Clinician-Scientist Phase II Award, was a Sontag Foundation Distinguished Scholar, and is supported by The Garron Family Chair in Childhood Cancer Research. M.D.T. is supported by grants from the Cure Search Foundation, The Younger Foundation, the National Institutes of Health (R01CA148699 and R01CA159859), The Pediatric Brain Tumor Foundation, The Canadian Cancer Society, The Terry Fox Research Institute, and Brainchild. S.M., K.M.W. and A.D. are supported by Vanier Scholarships from CIHR. S.M. would like to thank K. Mack, R. Mack, S. Mack and K. Bertrand for their support of this project. This study was conducted with the support of the Ontario Institute for Cancer Research through funding provided by the Government of Ontario. This work was also supported by a Program Project Grant from the Terry Fox Research Institute, and a Grand Challenge Award from CureSearch for Children's Cancer. Additionally, this work was supported by the PedBrain Tumor Project contributing to the International Cancer Genome Consortium, funded by German Cancer Aid (109252) and by the German Federal Ministry of Education and Research (BMBF, grants 01KU1201A, MedSys 0315416C and NGFN<sup>plus</sup> 01GS0883). This study was supported by grants from the Sander Foundation and DKTK (Molecular Diagnostics of Pediatric Malignancies). For technical support and expertise of next-generation sequencing efforts we thank the DKFZ Genomics and Proteomics Core Facility, The EMBL Genomics Core Facility, and The Centre for Applied Genomics (Toronto). We thank S. Archer for technical writing and C. Smith for artwork. We thank A. Wittmann, L. Sieber and L. Linke for clinical assistance.

**Author Contributions** S.C.M., H.W., M.D.T., A.K. and S.M.P. conceived and led the study. S.C.M. performed sample preparation, data acquisition and bioinformatic analysis related to DNA methylation, ChIP-seq and transcriptional profiling experiments. S.C.M. also performed western blot analysis and contributed to *in vitro* and *in vivo* experiments. H.W. led whole-genome sequencing, whole-exome sequencing and whole-genome bisulphite sequencing efforts, with analytical support from R.M.P., L. Gu., N. Jäger, D.T.W.J., S.S., S.H., T.Z., A.M.S., T.J.P., M.S., H.S.-C., T.T., V.H. and J.O.K. S.Z. and G.D.B. developed and applied pathway analysis methods for all data sets in this study. K.N.-B., M.G., L. Garzia, K.Z., X. Wang, M.B., S.B., P.J., X. Wu, K.C.B., T.M., J.Z., P.S.-C., C.C.F., P.C.-B., Y.Y. and S.A. performed *in vitro*, *in vivo* and molecular/biochemical experiments central to the project. DNA methylation and ChIP-seq bioinformatic analysis and experimental design were supported by X.Z., V.R., P.N.K., A.M.D., P.A.N., D.J.H.S., J.P., M. Remke, F.M.G.C., L.L., S.P., S.W.S., S.D.B., M.G., J.K., I.C., R.H. and P.B.D., developed and characterized ependymoma primary cultures, and assisted with *in vitro* and *in vivo* experiments. C.L.C. and S.K.V. developed the EZH2 compounds and provided inhibitors for experimentation. S.S.R., L.M., Y.J.C., T.V.M., W.G., B.L., M. Ryzhova, A.K., N.G., J.P., K.W. and K.D.A. provided patient samples and clinical details that made this study possible. M.H., M.A.M., M.L., D.F., A.E.K., A.v.D., O.W., D.M., X.F., K.M.M., M.K., S.L.P., E.B., W.A.W., A.H., U.T., C.H., J.T.R., N. Jabado, J.O.K., R.E., P.L., G.D.B., K.D.A., P.B.D. and S.M.P. provided valuable input regarding study design, data analysis and interpretation of results. M.D.T., S.C.M., H.W., A.K. and S.M.P. wrote the manuscript. M.D.T. and S.M.P. provided financial and technical infrastructure and oversaw the study. M.D.T. and A.K. are joint senior authors and project co-leaders.

**Author Information** Illumina 450K CpG Methylation array data, NimbleGen 385K CpG Island Plus array data, and ChIP-seq data have been deposited at the Gene Expression Omnibus (GEO: <http://www.ncbi.nlm.nih.gov/geo/>) as a GEO super-series under the accession number GSE43353. Whole-genome and whole-exome sequencing data have been deposited in the European Genome-Phenome Archive (EGA: <https://www.ebi.ac.uk/ega/>) hosted by the EBI, under the accession number EGAS00001000443. Reprints and permissions information is available at [www.nature.com/reprints](http://www.nature.com/reprints). The authors declare no competing financial interests. Readers are welcome to comment on the online version of the paper. Correspondence and requests for materials should be addressed to A.K. (Andrey.Korshunov@med.uni-heidelberg.de) or M.D.T. (mdtaylor@sickkids.ca).

## METHODS

**Patients and tumour samples.** Tumour samples, clinical information and animal studies were processed in approval with local ethics board from both the institutions as described previously<sup>6</sup>. Informed consent was obtained from all patients, as described previously<sup>6</sup>. No patient underwent chemotherapy or radiotherapy before the surgical removal of the primary tumour. This study included only primary samples for analysis, and further excluded WHO grade I histological variants of ependymoma. Detailed clinical description of patient characteristics is shown for the sequencing cohort in Supplementary Table 2 and for the methylation cohort in Supplementary Table 8. Tumour subgrouping was based on gene expression profiling or immunohistochemical analysis as described previously<sup>6</sup>. At least 80% of tumour cell content was estimated in all tumour samples of the sequencing cohort by staining cryosections (~5 µm thick) of each sample with haematoxylin and eosin. Diagnoses were confirmed by histopathological assessment by at least two neuropathologists, including a central pathology review that used the 2007 WHO classification for central nervous system tumours.

**DNA library preparation and Illumina sequencing.** Tumour and control samples were individually processed, in every case thorough histological examination proved that each tumour consisted of >80% tumour cells, in most cases it was >95%. DNA from tumour and control samples (blood) was prepared and sequenced individually. The Agilent SureSelect Human All Exon 50 Mb target enrichment kit (v3 initially, switched to v4 subsequently) was used to capture all human exons for deep sequencing, using the vendor's protocol v2.0.1. The SureSelect Human All Exon Kit targets regions of 50 megabases (Mb) in total size, which is approximately 1.7% of the human genome. In brief, 3 µg of genomic DNA was sheared with a Covaris S2 to a mean size of 150 base pairs (bp). 500 ng of library was hybridized for 24 h at 65 °C with the SureSelect baits. The captured fragments of the tumour samples and controls were sequenced in 105-bp single-end mode on an Illumina HiSeq2000 deep sequencing instrument (based on Illumina, Inc., v3 sequencing chemistry). Median coverage of whole-exome-sequenced tumour samples was 157-fold (range 43–469×) and for control samples (blood DNA) 146-fold (range 80–222×). In addition, whole-genome libraries (before the exome hybridization step) were sequenced three lanes each in paired-end 105-bp mode on the HiSeq2000, as described by Jones *et al.*<sup>9</sup>.

To increase the coverage of the samples for whole-exome sequencing we used the following strategy: exome capture was initially carried out with Agilent SureSelect (Human All Exon 50 Mb) in-solution reagents using the default Illumina adapters (without barcode). To introduce Illumina Multiplex barcodes into the existing libraries at a later stage, 15 ng final exome-enriched library (without barcode) was used as a template in a 50 µl PCR reaction. The Herculase II Fusion enzyme (Agilent) was used together with the NEBNext Universal PCR primer for Illumina and NEBNext Index primer (NEB no. E7335S) with the following conditions: the initial denaturation step for 2 min at 98 °C was followed by 4 cycles of 30 s 98 °C, 30 s 57 °C, 1 min 72 °C, and a final 10 min at 72 °C step. 6–7 barcoded samples were then sequenced on the HiSeq2000 in 2 × 100-bp paired-end mode.

**DNA sequence data processing.** For each sequencing lane, read pairs were mapped to the human reference genome (hg19, NCBI build 37.1, downloaded from the UCSC genome browser at <http://genome.ucsc.edu/>) using BWA version 0.5.9-r16 with default parameters and maximum insert size set to 1 kilobase (kb). We used SAMtools to generate a chromosomal coordinate-sorted BAM file. Post-processing of the aligned reads included merging of lane-level data and removal of duplicate read pairs per sequencing library using Picard tools (version picard-1.48, <http://picard.sourceforge.net>). Lane, library and sample information was captured in the read group tag in the header of the merged final BAM file. Only uniquely aligned reads (minimum mapping quality of 1) were considered for downstream mutation analysis. Coverage calculations following duplicate removal considered all informative bases of the reference genome (excluding Ns, where N indicates that neither A, C, G or T DNA base could be accurately called). A mean Phred-scaled base quality of at least 25 across the length of the read was required. For target capture sequencing, only bases of reads overlapping the targets ± 100 bases were considered for coverage calculations. Sequencing statistics are given in Supplementary Tables 1 and 2.

**SNV detection.** Our analysis pipeline for SNV detection integrates publicly available tools with custom in-house software and applies several filtering and annotation steps. SNV calling is based on SAMtools mpileup and bcftools (version 0.1.17), using parameter adjustments to allow calling of somatic variants. Default settings of bcftools are designed for diploid samples, but owing to tumour heterogeneity, polyploidy and normal cell contamination, tumour genomes often have a significantly lower mutant allele frequency than that seen in normal diploid genomes. Therefore, somatic SNVs are often not called by standard tools designed for detection of single nucleotide polymorphisms, for example, in population studies such as the 1000 Genomes Project (<http://www.1000genomes.org/>). Initial SNV candidates were identified by using SAMtools mpileup for each tumour

sample, considering only reads with a minimum mapping quality of 30 and bases with a minimum base quality of 13, after application of the extended base alignment quality (BAQ) model. BAQ is the Phred-scaled probability of a read base being misaligned, and it is designed to reduce false SNV calls caused by misalignments. After the pileup of high-quality bases at each position of the input BAM file, bcftools applies the prior and performs the actual SNV calling. We changed the default probability of calling a variant if  $P(\text{ref}[D]) < 0.5$  to 1.0, which results in all positions containing at least one high-quality non-reference base to be reported as a variant. Therefore, this initial set of SNV candidates contains a high fraction of false positive calls, but ensures that true somatic mutations with low allele frequency (well below the expected 50% allele frequency) are reported. This initial SNV call set is then subjected to various filters. SNVs covered by fewer than three reads in the tumour and control samples, with somatic allele frequency <10%, or with only one read supporting the variant, were excluded. In addition, a minimum of 10 high-quality reads available at the corresponding position in the control sample were required, in order to be able to distinguish somatic from germline variants. Local sequence context can lead to incorrect base calls, but typically involves reads sequenced from a single strand only. Thus, if the variant call was supported by reads from only one strand, the ± 10 bases around the SNV were automatically screened for Illumina-specific error profiles and excluded if a profile was matched. For all tumour SNV calls the pipeline generates a pileup of the bases in the normal sample considering only uniquely mapping reads. SNV calls were categorized as germline or somatic according to whether there was evidence for the same event at the same locus in the BAM file of the tumour-matched control sample. Filtered calls were annotated with RefSeq gene annotations, dbSNP build 135 and variants from the 1000 Genomes project. Calls matching the position of known dbSNP (up to version 131) or known 1000 Genome variants were excluded from the high-confidence somatic call set (calls matching the position of dbSNP version >131 but not the position of 1000 Genome variants were retained because cancer-relevant somatic mutations, such as several *TP53* mutations, have been included in more recent dbSNP versions). In addition, we filtered out SNVs that were found in at least 1% of the control samples or at least 1% of a set of 162 unrelated controls from other studies, because they constitute likely unannotated, naturally occurring SNPs and/or false positives, for example, artefacts related to sequencing and mapping. The pipeline integrates Annovar (<http://www.openbioinformatics.org/annovar/>) to determine whether the observed amino acid change has synonymous, nonsynonymous, nonsense or splice-site-changing properties on the encoded protein. Variants were further annotated with genes listed in the Cancer Gene Census (<http://www.sanger.ac.uk/genetics/CGP/Census/>) and entries from the Catalogue of Somatic Mutations version 57 (COSMIC, <http://www.sanger.ac.uk/genetics/CGP/cosmic/>), in addition to the full RefSeq gene summary, full gene name and genomic size. A subset of sequence variants and indels were validated by capillary sequencing by Sanger using purified PCR products. Primer sequences are available upon request.

**Small insertion and deletion (indel) detection.** Small insertions and deletions were identified with SAMtools and bcftools. The indel discovery pipeline is similar to the SNV pipeline (as described above), but using default bcftools parameters, to reduce the known high false positive rate associated with current indel detection methods for deep sequencing data. To call an indel a germline event, we only required one indel-supporting read in the matching normal sample, again to reduce the high fraction of false-positive somatic indel calls. Calls overlapping simple repeat or microsatellite regions were excluded as such regions are commonly observed to yield false-positive calls. Annotation of indels was identical to SNV annotation.

**Computation of recurrently mutated genes.** To search for genes mutated at significant frequency, we applied the MutSig algorithm, a method that corrects for background mutation rate and gene length. Details can be found at Broad CGA tools website (<http://www.broadinstitute.org/cancer/cga/mutsig>) including previously published studies<sup>10</sup>.

**Identification of rearrangements and generating of Circos plots.** Structural rearrangements, namely deletions, tandem duplications, inversions and translocations, were detected using DELLY, which is based on paired-end mapping. The structural rearrangement calls were filtered using the corresponding ependymoma germline samples, germline data of additional medulloblastoma samples<sup>9</sup>, and phase I 1000 Genomes Project (<http://1000genomes.org>) genome data to exclude germline structural variants as well as rearrangement calls caused by mapping artefacts. We only considered those rearrangements for further analysis, which were present in at most 0.5% of the 1000 Genomes Project samples assessed and not in the additional germline samples. Two rearrangement calls were considered to be identical, hence constituting a likely germline variant if they displayed an overlap in terms of genomic coordinates with their end coordinates differing by less than 5 kb. Furthermore, rearrangement calls with less than 10 supporting pairs



as well as supporting pairs with average mapping quality less than 20 were excluded for further analysis. The circular whole-genome plots were generated using Circos. **Identification of pathways affected by SNVs.** A pathway association test was used to identify groups of functionally related genes that contained a greater than expected number of SNVs in one or the other ependymoma subtype. For each gene set, SNVs were stratified by subtype (PFA versus PFB). The number of SNVs in all genes and the number of SNVs observed in a given gene set were tallied for each subtype. A Fisher's exact test was performed with the null hypothesis that the frequency of SNVs in a given gene set was equal in the two subtypes. To correct for multiple testing, gene names were randomly shuffled and the analysis repeated to obtain a null *P* value for a given gene set. Randomization was done 10,000 times and, for each gene set, the percentage of null *P* values that were the same or lower than that obtained from the actual data was used as an estimate of the FDR.

**Generation of copy number profiles from Illumina 450K methylation data.** Low-resolution (450K probes) copy number variations were detected from the 450K Infinium methylation array in a custom approach using the sum of both methylated and unmethylated signals. Probes found to be highly variant in the six normal cerebellum samples were excluded from the analysis according to the following criteria: removal of probes not within the 0.05 and 0.85 quantile of median summed values or over the 0.8 quantile of the median absolute deviation. Log-ratios of samples to the median value of control samples were calculated, and sample noisiness was determined as the median absolute deviation of adjacent probes. Probes were then combined by joining 20 adjacent probes, and resulting genomic windows less than 100 kb in size were iteratively merged with adjacent windows of smaller size. Windows of more than 5 Mb were excluded from analysis, resulting in a total of 8,654 windows throughout the genome. For each window, the median probe value was calculated and shifted to minimize the median absolute deviation from all windows to zero for every sample. Segmentation was performed by applying the circular binary algorithm.

**MBD2-assisted recovery and sample preparation.** Genomic DNA was isolated according to previous methods<sup>6</sup>. DNA (6 µg) was immunoprecipitated using the MBD2 protein and quantified using the Qubit fluorometer (Invitrogen). Enrichment was assessed by quantitative PCR for positive controls: *RASSF1A*, *DLK1*, *H19* and negative controls: *ACTB* and *GAPDH*. Bound and unbound fractions from the MBD2 pulldown were whole-genome-amplified (SIGMA-WGA2) in triplicate, pooled, quantified using Qubit, and subjected to another round of quantitative PCR for the above control targets. DNA was sent to NimbleGen to be hybridized to Nimblegen 385K CpG Island Promoter Plus arrays, in which 'Immunoprecipitated-IP' fraction was labelled with Cy5 and 'unbound' fraction with Cy3.

**Methylation analysis of MBD2-chip data.** Microarray data was quantile normalized using the LIMMA Bioconductor package. Log<sub>2</sub> ratios were then imported into Agilent Genomics Workbench (Agilent Technologies), following which the BATMAN algorithm was used to infer the methylation statuses associated with each probe<sup>47</sup>. Mean methylation states were calculated for probes within a 1,000-bp window and termed a region of interest (ROI). ROIs were then filtered to those with greater than 4 probes and mapped to autosomal chromosomes. ROIs exhibiting a standard deviation greater than 0.65 were used for subgroup assignment as described below. Comparisons between subgroups were performed using a Wilcoxon rank-sum test, and *P* values were corrected for multiple testing using the Benjamini–Hochberg method. For comparisons of DNA methylation and other factors in this manuscript a Wilcoxon test was used and corrected for multiple testing, such that no assumptions were made regarding the normality of the data distributions.

**Illumina Infinium 450K methylation sample preparation and data analysis.** Genomic DNA was isolated according to previous methods<sup>6</sup>. DNA (1 µg) was used for bisulphite treatment (Qiagen, EpiTect plus) with the use of DNA protect buffer, particularly in the case of DNA from formalin-fixed paraffin-embedded tissue. Bisulphite-treated DNA was then quantified using spectrophotometry (Nanodrop). >500 ng was sent to The Centre for Applied Genomics (TCAG, Toronto) for hybridization to Illumina 450K Methylation Arrays. Array pre-processing was performed using GenomeStudio (Illumina) with background subtraction adjustment applied. Arrays were also normalized using the BMIQ method, which produced the same finding of a group A-specific CIMP. Methylation values were then exported as  $\beta$ -values (estimates of actual CpG methylation levels). Probes that overlapped with known single nucleotide polymorphisms, which mapped to chromosomes X and Y, and were Illumina control probes, were removed from the analysis. Methylation probes were then filtered to CpG sites, which mapped to promoters containing CpG islands. A Wilcoxon rank-sum test (Mann–Whitney) was used to identify the differentially methylated CpG sites between group A (CIMP<sup>+</sup>) and group B (CIMP<sup>−</sup>). *P* values for differentially methylated CpG sites identified were then corrected for multiple testing using the Benjamini–Hochberg method. Significant differences between numbers of CpG sites, genes or methylated and silenced genes, was calculated using a binomial distribution test. Methylated

and silenced genes were identified in two ways: (1) by identifying genes which were methylated and downregulated following comparison between group A and B using a Wilcoxon rank-sum test; or (2) by performing a Pearson correlation between the methylation status of a CpG site with the corresponding downstream gene. Methylated and silenced genes (within the same tumour) were identified by genes demonstrating significant and preferential methylation in a particular subgroup and evidence of downregulation as compared to a collection of normal brain samples. Gene expression data for these samples can be found in our previous publication<sup>6</sup>.

**Subgroup analysis of gene expression and methylation data.** To detect robust sample clusters from the gene expression data (Affymetrix Exon 1.0ST) we performed hierarchical clustering using the top 1,000 varying probes as described previously in Witt *et al.*<sup>6</sup>. For clustering of MBD2-chip data we performed consensus hierarchical clustering with agglomerative average linkage as our method for consensus clustering. (R package: ConsensusClusterPlus). The change in area under the cumulative distribution function curve was used to identify the principal number of subgroups for a given clustering method. Silhouette analysis was performed to evaluate cluster representation of samples (R package: cluster). To evaluate the concordance between gene expression and DNA-methylation subgroup stratification we calculated the Rand index, with the significance assessed by permutation of sample labels and computing the Rand index over 10,000 iterations in order to generate a null distribution. Illumina 450K methylation data was clustered using the probes exhibiting a standard deviation of >0.2 as described previously. A variety of consensus clustering methods was performed: K-means, non-negative matrix factorization, hierarchical clustering and self-organizing maps were used. The distance metric used in the case of K-means was Euclidean, whereas a Pearson correlation was used for all other methods. Principal component analysis was performed within Partek Genomics Suite (Partek Inc.) to compare group A (CIMP<sup>+</sup>) and group B (CIMP<sup>−</sup>) posterior fossa subtypes with the same genes or CpG sites used for consensus hierarchical clustering and consensus K-means clustering, respectively.

**H3K27me3 and EZH2 ChIP-seq profiling and analysis in PF ependymoma samples.** 10–20 mg of fresh–frozen primary tumour samples was homogenized in 1% formaldehyde and allowed to incubate at room temperature for 6–10 min. Crosslinking was stopped with the addition of 125 mM of glycine, and samples were washed twice with ice-cold PBS containing 1% BSA and 10% FBS. Samples were then sonicated to ~200-bp fragments using a Biorupter (Diagenode). The chromatin immunoprecipitation was then performed using 5 mg of EZH2 antibody (no. 39875-Active Motif) or H3K27me3 antibody (C15410069-Diagenode) overnight at 4 °C as described previously<sup>48</sup>. DNA was quantified using PicoGreen (Invitrogen) and libraries were prepared using NEBNext ChIP-seq Illumina Sequencing library preparation kit (NEB). Samples were barcoded (NEB Next Barcodes) and pooled in equimolar amounts such that up to 6 samples could be sequenced by paired-end Illumina HiSeq 2000 sequencing (Illumina).

ChIP-seq reads were aligned using the BWA algorithm with removal of redundant reads (Picard Algorithm) likely to represent ChIP-seq PCR library artefacts, yielding uniquely mapped ChIP-seq reads. Peaks were identified using MACS (version 2) with a *P* value cutoff of 0.01. Differential peaks were identified using the R: Bioconductor DiffBind package (*P* < 0.05) and annotated to the nearest gene  $\pm$  5 kb using Cistrome (<http://cistrome.org/ap/root>). Overlap analysis between H3K27me3 genes or EZH2 target genes was assessed statistically using a binomial distribution test. Unsupervised consensus clustering of H3K27me3-predicted target genes was performed using the top 1,000 genes exhibiting the greatest standard deviation. Supervised analysis of predicted H3K27me3 target genes was also performed using significant analysis of microarrays (SAM) with an FDR cutoff of 0.01.

**Sequenom analysis of ependymoma samples.** Validation of gene methylation was performed using Sequenom Mass Spectrometry. Primers were designed using Sequenom: EpiDesigner and tested on bisulphite-treated universally methylated DNA (Invitrogen) by standard PCR (Qiagen) followed by Sanger Sequencing. For bisulphite-treated tumour samples, following PCR amplification, amplicons were sent to Genome Quebec for quantification using Sequenom Mass Spectrometry.

**Subgroup stratification of ependymoma samples in a validation cohort.** Sequenom primers were designed to three highly methylated genes in group A (CIMP<sup>+</sup>), *PKP1*, *CRIP1*, *CYP26C1*, as selected by CpG coverage and PCR efficiency. PCR amplification was performed in a training data set consisting of the samples, which were analysed by Illumina 450K methylation arrays. These three methylated genes were used to train a classification model using the Prediction Analysis for Microarrays algorithm. Class prediction was performed on a non-overlapping cohort of 82 samples collected from The Hospital for Sick Children, Children's Hospital Boston, University of Michigan, and the MD Anderson Cancer Center. Posterior probabilities corresponding to Group A (CIMP<sup>+</sup>) or Group B (CIMP<sup>−</sup>) were calculated for each sample, and an odds ratio >2-fold (probability group A/probability group B) for either subgroup was used to classify tumours. Survival was graphed throughout the manuscript using Kaplan–Meier curves and assessed statistically using a log-rank test.

**Pathway analysis of DNA-methylation data.** A pathway association test was used to identify groups of functionally related genes that contained a greater than expected number of methylation events in one or the other ependymoma subtype. A gene was considered to be methylated if all profiled sites within 1,000 bp upstream of the transcription start site showed a variance of no more than 0.1 and a mean score of  $>0.5$ . For each gene set, methylation events were classified by subtype. The number of methylation events in all genes and the number of methylation events observed in a given gene set were totalled for each subtype. A Fisher's exact test was performed with the null hypothesis that the frequency of methylation events in a given gene set was equal in the two subtypes. To correct for multiple testing, gene names were randomly shuffled and the analysis repeated to obtain a null  $P$  value for a given gene set. Randomization was done 10,000 times and, for each gene set, the percentage of null  $P$  values that were the same or lower than that obtained from the actual data was used as an estimate of the false discovery rate.

**Whole-genome bisulphite sequencing, DNA preparation and differentially methylated region (DMR) analysis.** To prepare strand-specific MethylC-seq libraries, adaptor-ligated DNA fragments with insert lengths of 200–250 bp were bisulphite-converted using the EZ DNA Methylation kit (Zymo Research). After PCR amplification in six parallel reactions using the FastStart High Fidelity PCR kit (Roche), library aliquots were pooled per sample and sequenced using the Illumina HiSeq 2000 platform. This yielded an average of 513 million ( $\pm$  102 million (s.d.)) 101-bp paired-end reads per sample.

For analysis of DMR enrichment in specific genomic sites, we first extracted genomic features from UCSC genome browser. Then the percentage of total genomic CpGs for each genomic feature was calculated as a background value. Thereafter, the percentage of total hypermethylated/hypomethylated CpGs in each genomic feature was calculated on the basis of the DMR list. The enrichment fold change was then set as the ratio between the two percentages above. To test the significance of the enrichment/depletion, we randomly permuted the CpGs from all DMRs in the whole genome for 10,000 times and used Fisher's exact test to determine the significance of the difference between the observed and simulated results.

**Whole-genome bisulphite sequencing DMR and partially methylated domain (PMD) calling.** Whole-genome bisulphite sequencing data was mapped to hg19 using BSMAP (version 2.74). The potential duplications were removed afterwards using Picard tools. BisSNP (version 0.82.2) was then used to detect and remove SNPs and CpGs with potential technical biases before DMR calling. BSmooth was used to smooth bisulphite sequencing data and call candidate DMRs as described previously<sup>49</sup>. PMDs were detected using MethylSeekR.

**Ependymoma short-term primary cell culture and *in vitro* drug treatment.** Primary ependymoma cells were isolated from patients and cultured on Laminin (Sigma)-coated plates in Neurobasal media (Invitrogen) consisting of N2 (Invitrogen), B27 (Invitrogen), glutamine (Invitrogen), BSA (Sigma), heparin (Sigma), human EGF (Invitrogen) and human basic FGF (Invitrogen). Media was replenished every other day while leaving ~50% conditioned media to encourage continued cell proliferation. Cell viability assays were performed in 96 wells using an Alamar Blue stain (Invitrogen) or MTS Aqueous One (Promega) according to manufacturer's instructions. DAC (Sigma) was dissolved to a stock concentration of 2 mM in PBS and stored in aliquots at  $-20^{\circ}\text{C}$ . DAC was prepared fresh and added to treatment media on a daily basis at the appropriate final concentration, for a total of 7 days. DZNep (Cayman Chemical) was dissolved to a stock concentration of 25 mM in DMSO and stored in aliquots at  $-20^{\circ}\text{C}$ . DZNep treatments were performed every other day along with replenishment of cell culture medium for a total of 7 days. GSK343 (active compound) and GSK669 (inactive compound) were dissolved in DMSO and used to treat cells at varying concentrations with media replenishment every other day for a total of 11 days.

**Gene expression profiling of DAC- and GSK343-treated cultures.** Primary cell cultures were treated for 5 days in DAC (500 nM) or GSK343 (500 nM), following

which RNA was isolated using the Trizol (Invitrogen) method. RNA libraries were prepared according to the manufacturer's recommendations and hybridized to Affymetrix Gene 1.0ST arrays. The RMA method with quantile normalization was used for gene expression array normalization. Differentially expressed genes were detected using significance of microarray analysis (FDR  $<0.01$ ).

**Western blot analysis.** Ependymoma cell cultures were lysed in PLC lysis buffer containing deoxycholate, with sonication to facilitate the release of nuclear histones. SDS-PAGE analysis was performed in a 12% gel, loading 20  $\mu\text{g}$  of protein, as quantified by BCA (Pierce). Membranes were blocked with 5% BSA (Roche) diluted in TBST. Western blot antibodies were used at the following concentrations in overnight incubations (2% BSA): EZH2 (Abcam: ab110646, 1:5,000), H3K27me3 (Cell Signaling: no. 9733, 1:5,000), H3K4me3 (Cell Signaling: no. 9751, 1:5,000), cleaved PARP (Cell Signaling: no. 5625, 1:1,000) and  $\alpha$ -tubulin (Cell Signaling: no. 2148, 1:20,000). Secondary antibodies were used at a concentration of 1:5,000 for all primary antibodies, and 1:20,000 for  $\alpha$ -tubulin.

**Flank injections and *in vivo* treatments of immunodeficient mice.** For all animal studies, following engraftment of tumour cells, mice were then randomly assigned a treatment of vehicle versus treatment to control for assignment biases and other confounding factors. 50,000 E520-PF1 ependymoma cells were injected subcutaneously into flanks of 5–8-week-old female immunodeficient NOD-SCID gamma mice. Tumours were allowed to develop for 7 days until either visible or palpable. DZNep or vehicle (Sigma: Cremophor) was administered 3 consecutive days a week at a dosage of 3 mg per kg per day via intraperitoneal injections. Tumours were monitored and measured continuously using a caliper. Experimental end point was determined when tumours reached 15 mm in size. Final tumour volumes were determined using caliper measurements. Investigators were blinded during measurement of tumour volumes. A comparison between tumour volumes of DZNep- versus vehicle-treated mice was calculated using a Wilcoxon rank-sum test. For all animal studies, adequate sample sizes were chosen such that any result could be appropriately evaluated statistically using a two-sided nonparametric test. For flank xenograft experiments this entailed a Wilcoxon rank-sum test, and for intracranial experiments this involved a log-rank test.

**Cerebellar xenografts and *in vivo* treatments of immunodeficient mice.** 10,000 cells were xenografted by stereotactic injection into PFs of female immunodeficient NOD-SCID gamma mice of 5–8 weeks old. Tumours were allowed to develop for 7 days, following which DZNep (3 mg per kg day) or vehicle (Sigma: Cremophor) was administered by intraperitoneal injection. Mice were treated according to the same protocol for flank-tumour-bearing mice (above). Survival of mice was visualized using a Kaplan–Meier curve and quantified using a log-rank test.

**Limiting dilution assays (LDAs) of primary ependymoma patient samples or ependymoma xenografts.** Cells from a lung metastasis resection or tumour xenograft were dissociated according to previously published protocols<sup>50</sup>. LDAs were performed in a 96-well plate format. LDAs from xenografts were not treated with inhibitors but monitored for neurosphere colony formation. For primary patient samples serial dilutions of cells were performed to reach cell doses of 2,000 cells per well at the highest dose and 4 cells per well at the lowest dose. A total of 10 cell doses were tested with 6 technical replicates per dose. Cells were treated with selected compounds about 5 h post-surgery. GSK343 was used at a concentration of 3  $\mu\text{M}$ , and DAC was used at 0.5  $\mu\text{M}$ . Fresh media and drugs were added to the cells after 7 days. Wells were scored for sphere formation on day 14. Statistical analysis was performed with the Extreme Limiting Dilution Analysis web-based software.

48. Lupien, M. *et al.* FoxA1 translates epigenetic signatures into enhancer-driven lineage-specific transcription. *Cell* **132**, 958–970 (2008).
49. Hansen, K. D. *et al.* Increased methylation variation in epigenetic domains across cancer types. *Nature Genet.* **43**, 768–775 (2011).
50. Gallo, M. *et al.* A tumorigenic MLL-homeobox network in human glioblastoma stem cells. *Cancer Res.* **73**, 417–427 (2013).



# *C11orf95*–*RELA* fusions drive oncogenic NF- $\kappa$ B signalling in ependymoma

Matthew Parker<sup>1,2\*</sup>, Kumarasampet M. Mohankumar<sup>3\*</sup>, Chandanamali Punchihewa<sup>4\*</sup>, Ricardo Weinlich<sup>5\*</sup>, James D. Dalton<sup>1,4</sup>, Yongjin Li<sup>1,2</sup>, Ryan Lee<sup>4</sup>, Ruth G. Tatevossian<sup>1,4</sup>, Timothy N. Phoenix<sup>3</sup>, Radhika Thiruvengatam<sup>3</sup>, Elsie White<sup>3</sup>, Bo Tang<sup>1,4</sup>, Wilda Orisme<sup>1,4</sup>, Kirti Gupta<sup>4</sup>, Michael Rusch<sup>2</sup>, Xiang Chen<sup>2</sup>, Yuxin Li<sup>2,6</sup>, Panduka Nagahawhatte<sup>2</sup>, Erin Hedlund<sup>2</sup>, David Finkelstein<sup>2</sup>, Gang Wu<sup>2</sup>, Sheila Shurtleff<sup>4</sup>, John Easton<sup>1,4</sup>, Kristy Boggs<sup>1</sup>, Donald Yergeau<sup>1</sup>, Bhavin Vadodaria<sup>1</sup>, Heather L. Mulder<sup>1</sup>, Jared Becksford<sup>4</sup>, Pankaj Gupta<sup>2</sup>, Robert Huether<sup>6</sup>, Jing Ma<sup>1</sup>, Guangchun Song<sup>1</sup>, Amar Gajjar<sup>1,7</sup>, Thomas Merchant<sup>8</sup>, Frederick Boop<sup>9</sup>, Amy A. Smith<sup>10</sup>, Li Ding<sup>1,11,12</sup>, Charles Lu<sup>1,11</sup>, Kerri Ochoa<sup>1,11,12</sup>, David Zhao<sup>1,2</sup>, Robert S. Fulton<sup>1,11</sup>, Lucinda L. Fulton<sup>1,11,12</sup>, Elaine R. Mardis<sup>1,11,12,13</sup>, Richard K. Wilson<sup>1,11,12,13</sup>, James R. Downing<sup>1,4</sup>, Douglas R. Green<sup>5</sup>, Jinghui Zhang<sup>1,2</sup>, David W. Ellison<sup>1,4</sup> & Richard J. Gilbertson<sup>1,3</sup>

**Members of the nuclear factor- $\kappa$ B (NF- $\kappa$ B) family of transcriptional regulators are central mediators of the cellular inflammatory response. Although constitutive NF- $\kappa$ B signalling is present in most human tumours, mutations in pathway members are rare, complicating efforts to understand and block aberrant NF- $\kappa$ B activity in cancer. Here we show that more than two-thirds of supratentorial ependymomas contain oncogenic fusions between *RELA*, the principal effector of canonical NF- $\kappa$ B signalling, and an uncharacterized gene, *C11orf95*. In each case, *C11orf95*–*RELA* fusions resulted from chromothripsis involving chromosome 11q13.1. *C11orf95*–*RELA* fusion proteins translocated spontaneously to the nucleus to activate NF- $\kappa$ B target genes, and rapidly transformed neural stem cells—the cell of origin of ependymoma—to form these tumours in mice. Our data identify a highly recurrent genetic alteration of *RELA* in human cancer, and the *C11orf95*–*RELA* fusion protein as a potential therapeutic target in supratentorial ependymoma.**

Ependymomas are tumours of the brain and spinal cord<sup>1</sup>. Surgery and irradiation remains the mainstay of treatment of this disease as chemotherapy is ineffective in most patients. Consequently, ependymoma is incurable in up to 40% of cases<sup>2</sup>.

Although ependymomas from the different regions of the central nervous system (CNS) are histologically similar, they possess site-specific prognoses, transcriptional profiles and DNA copy number alterations<sup>3–7</sup>, suggesting that they are different diseases that are likely to require different treatments. We recently generated the first mouse model of supratentorial ependymoma by amplifying *EPHB2*—a common DNA copy number alteration of these tumours—in mouse forebrain neural stem cells (NSCs)<sup>6</sup>. Preclinical studies using this model have identified new treatments that are now in clinical trial<sup>8</sup>. Drugs that target genetic alterations in the other types of ependymoma could provide new therapies, but the identity of these alterations remains largely unknown.

## The *C11orf95*–*RELA* translocation

To identify additional genetic alterations that drive ependymoma, we carried out whole-genome sequencing (WGS) of 41 tumours and matched normal blood, and RNA sequencing (RNA-seq) of the transcriptomes of 77 tumours (Fig. 1, Extended Data Fig. 1 and Supplementary Tables 1–3).

Single nucleotide variations, insertion/deletions, and focal copy number variations (less than five genes) were rare in ependymomas, but structural

variations were detected relatively frequently<sup>9</sup>, especially in supratentorial tumours (median structural variations, supratentorial tumours = 23 versus posterior fossa tumours = 7.5,  $P = 0.0006$ , Wilcoxon ranked sum test; Extended Data Fig. 2a, b, Supplementary Information, Supplementary Figs 1–7 and Supplementary Tables 4–11). All nine supratentorial ependymomas analysed by WGS contained structural variations that clustered within chromosome 11q12.1–11q13.3, producing catastrophic disruption of the locus and an oscillating copy number state compatible with chromothripsis (chromosome 11: 50–60 Mb,  $FWER = 9.6 \times 10^{-5}$  and chromosome 11: 60–70 Mb,  $FWER = 7.8 \times 10^{-7}$ , Mann–Whitney test; Fig. 1, Extended Data Fig. 2c, Supplementary Information and Supplementary Table 12)<sup>10</sup>. Although the chromothripsis region differed in each tumour, eight of the nine cases shared a common region (~63 to ~67 Mb) in which the reordered chromosome fragments fused a poorly characterized gene, *C11orf95*, to *RELA*, the principal effector of canonical NF- $\kappa$ B signalling<sup>11,12</sup> (Extended data Figs 3 and 4a, b). These genes are normally separated by 1.9 Mb containing 73 genes (Extended Data Fig. 4a, Supplementary Figs 8–10 and Supplementary Tables 1 and 13). The *C11orf95*–*RELA* translocation was validated in all eight cases by independent orthogonal sequencing and interphase fluorescence *in situ* hybridization (FISH) using ‘break-apart’ probes to *C11orf95* and *RELA* (Fig. 1, Extended Data Fig. 4c, Methods, Supplementary Figs 8 and 9, and Supplementary Tables 14 and 15). In marked contrast, neither chromothripsis nor *C11orf95*–*RELA* translocations

<sup>1</sup>St. Jude Children’s Research Hospital – Washington University Pediatric Cancer Genome Project, Memphis, Tennessee 38105, USA. <sup>2</sup>Department of Computational Biology and Bioinformatics, St. Jude Children’s Research Hospital, Memphis, Tennessee 38105, USA. <sup>3</sup>Department of Developmental Neurobiology, St. Jude Children’s Research Hospital, Memphis, Tennessee 38105, USA. <sup>4</sup>Department of Pathology, St. Jude Children’s Research Hospital, Memphis, Tennessee 38105, USA. <sup>5</sup>Department of Immunology, St. Jude Children’s Research Hospital, Memphis, Tennessee 38105, USA. <sup>6</sup>Structural Biology, St. Jude Children’s Research Hospital, Memphis, Tennessee 38105, USA. <sup>7</sup>Department of Oncology, St. Jude Children’s Research Hospital, Memphis, Tennessee 38105, USA. <sup>8</sup>Department of Radiological Sciences, St. Jude Children’s Research Hospital, Memphis, Tennessee 38105, USA. <sup>9</sup>Department of Surgery, St. Jude Children’s Research Hospital, Memphis, Tennessee 38105, USA. <sup>10</sup>MD Anderson Cancer Center Orlando, Pediatric Hematology/Oncology, 92 West Miller MP 318, Orlando, Florida 32806, USA. <sup>11</sup>The Genome Institute, Washington University School of Medicine in St. Louis, St. Louis, Missouri 63108, USA. <sup>12</sup>Department of Genetics, Washington University School of Medicine in St. Louis, St. Louis, Missouri 63108, USA. <sup>13</sup>Siteman Cancer Center, Washington University School of Medicine in St. Louis, St. Louis, Missouri 63108, USA.

\*These authors contributed equally to this work.

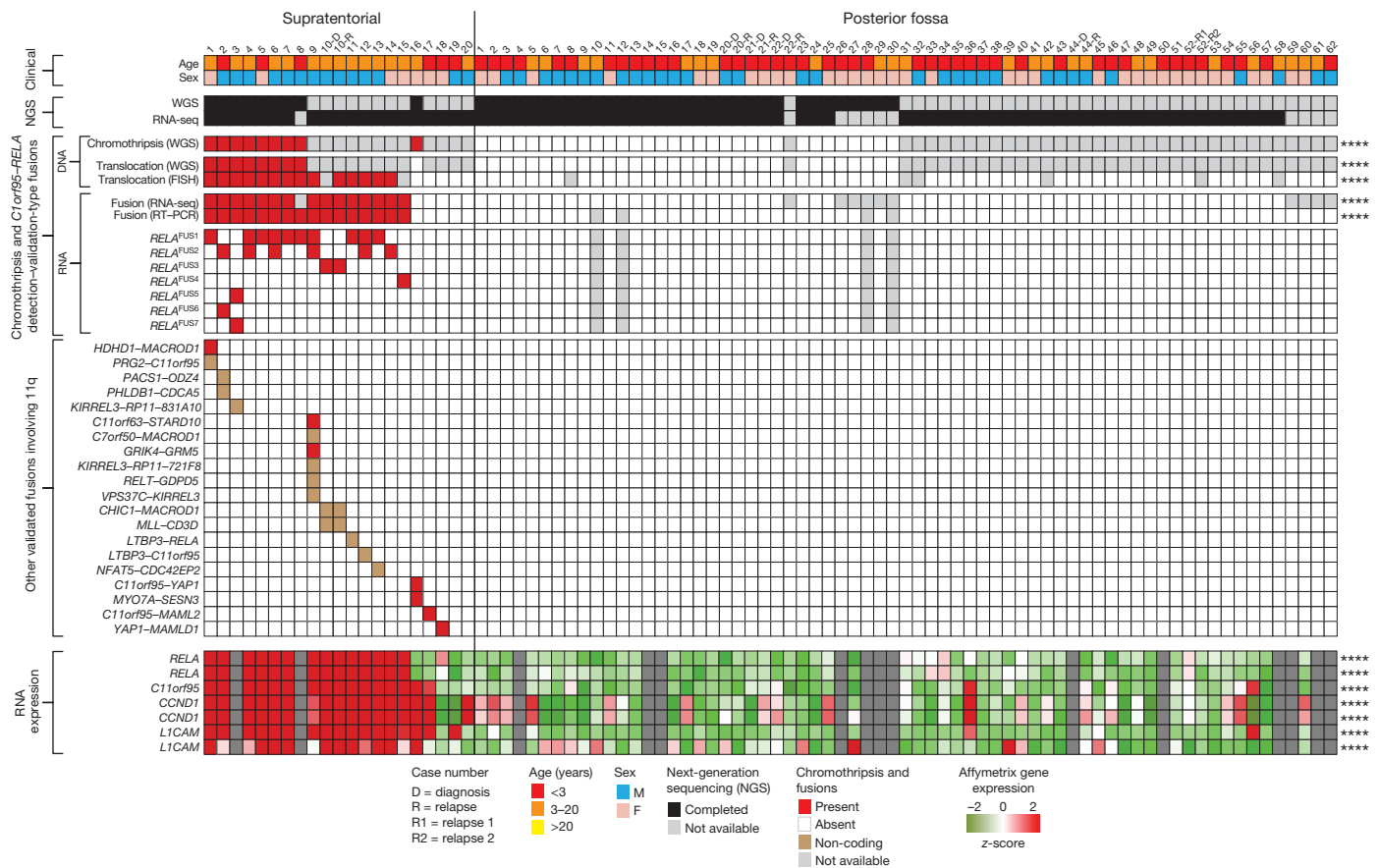


**Figure 1 | Recurrent *C11orf95-RELA* translocations in human supratentorial ependymoma.** Summary of results of molecular assays of translocations in tumours from 82 patients with ependymoma

(\*\*\*\* $P < 0.0001$  Fisher's exact test for supratentorial versus posterior fossa tumour). 'RNA expression' at bottom reports Affymetrix array data (\*\*\*\* $Q < 0.0001$  for supratentorial versus posterior fossa tumour).

were detected in any of the 32 posterior fossa tumours analysed by WGS ( $P < 0.0001$ , Fisher's exact test).

Next, using a novel algorithm, we looked for *C11orf95-RELA* fusion transcripts in the 77 ependymomas analysed by RNA-seq (Fig. 1 and Supplementary Methods). Fusion transcripts were validated by polymerase chain reaction with reverse transcription (RT-PCR) and Sanger sequencing (Fig. 2a and Extended Data Fig. 5a). *C11orf95-RELA* transcripts were detected in all eight supratentorial tumours in which the translocation was detected by WGS (Fig. 1 and Supplementary Table 16a). Fusion transcripts were also detected in an additional seven supratentorial tumours: FISH detected the *C11orf95-RELA* translocation in six of these with available material (Fig. 1). *C11orf95-RELA* transcripts were not detected in supratentorial tumours that lacked the translocation or in any posterior fossa ependymomas (Fig. 1;  $P < 0.0001$ , Fisher's exact test).

Translocation-positive tumours contained mature, spliced, in-frame fusion transcripts together with premature fusion transcripts containing intronic or intergenic DNA breakpoints (Fig. 2a and Extended Data Figs 4c and 6; see also Supplementary Information and Supplementary Fig. 10 for details of all fusion breakpoints). Thus, splicing is required to generate mature *C11orf95-RELA* transcripts. Seven distinct, mature *C11orf95-RELA* fusion transcripts were observed (Fig. 2a and Extended Data Fig. 5b). The most frequent (which we refer to here as *RELA*<sup>FUS1</sup>)

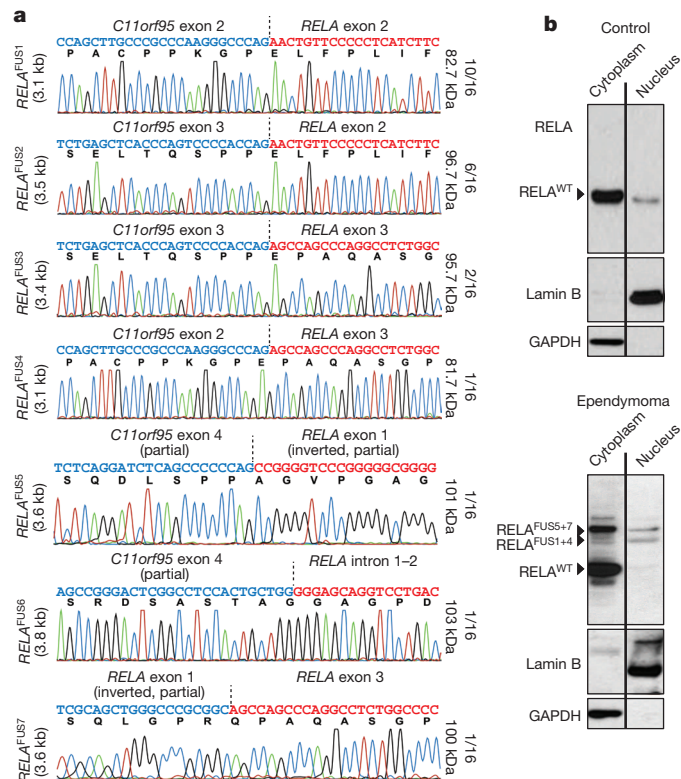
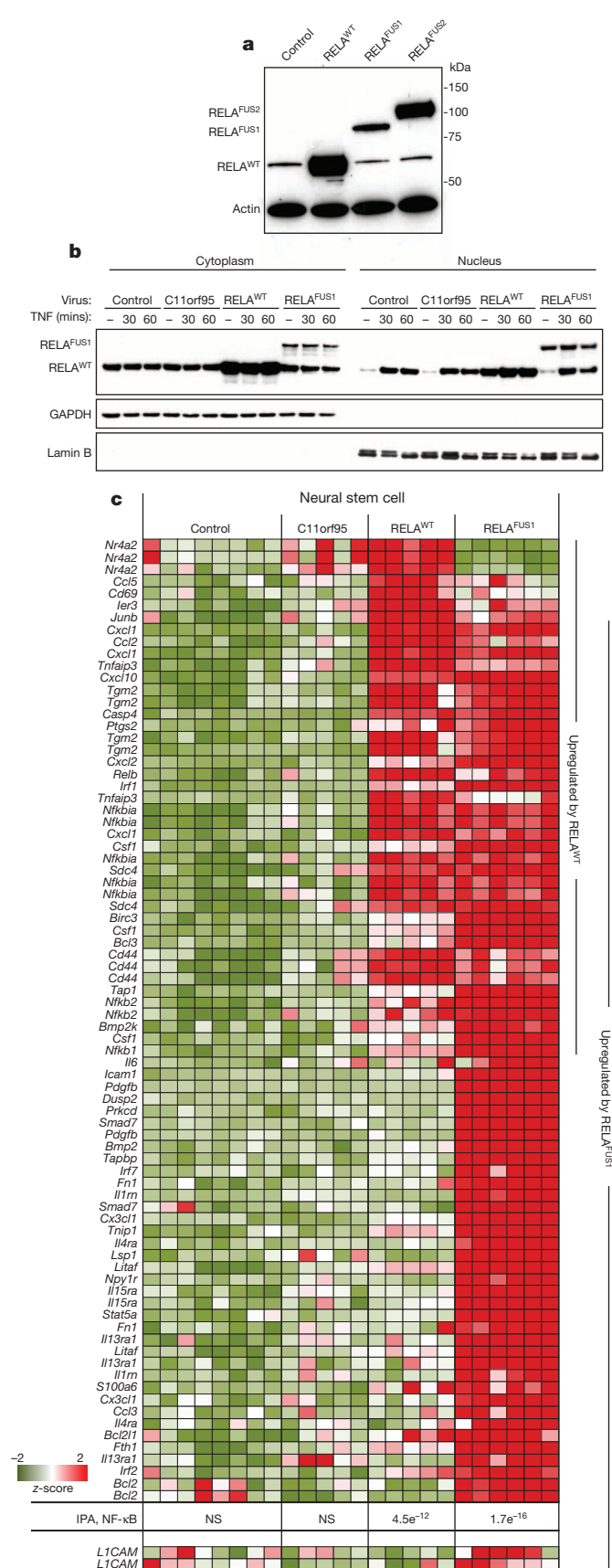


**Figure 2 | *C11orf95-RELA* fusion transcripts and proteins.**

**a**, Electropherograms of seven distinct *RELA* fusion transcripts detected in ependymoma. The proportion of tumours containing the corresponding fusion transcript, and the predicted protein product size are shown on the right. **b**, Western blot analysis of *RELA* proteins in cytoplasmic and nuclear extracts of 'control' human 293T cells (top) and supratentorial ependymoma ST3 (bottom).





included exons 1 and 2 of *C11orf95* and, except for the first two codons, the entire open reading frame of *RELA* (Figs 1 and 2a). Six other fusion transcripts (*RELA*<sup>FUS2</sup>–*RELA*<sup>FUS7</sup>) were detected less frequently, but

**Figure 3 | Cell trafficking and transcriptional activity of wild-type and fusion *RELA* proteins.** **a**, *RELA* western blot analysis of 293T cells transduced with the indicated retroviruses. **b**, Western blot analysis of *RELA* proteins in cytoplasmic and nuclear extracts of 293T cells transduced with the indicated virus, treated with TNF (50 ng ml<sup>-1</sup>). **c**, Expression of NF-κB target genes upregulated in mouse NSCs transduced by the indicated retrovirus. *P* value of NF-κB pathway activation detected by IPA and expression of L1CAM are shown at the bottom (see Methods for sources of target genes). NS, not significant.

each was observed in tumours lacking *RELA*<sup>FUS1</sup>, suggesting that they may be oncogenic.

Western blot analysis detected wild-type *RELA* (*RELA*<sup>WT</sup>) protein in supratentorial ependymoma ST3 (supratentorial 3) and human control (293T) cells (Fig. 2b). ST3, but not control cells, also expressed at least four *RELA* proteins that corresponded to the appropriately sized products of fusion transcripts detected in this tumour by RNA-seq and RT-PCR (Figs 1 and 2b, and Extended Data Fig. 6). *RELA* fusion and *RELA*<sup>WT</sup> proteins segregated differently in ST3 cells, with fusion products accumulating preferentially in the nucleus relative to the wild-type protein.

To validate further the *C11orf95*–*RELA* translocation we analysed a separate cohort of 89 formalin-fixed paraffin-embedded (FFPE) ependymomas using FISH and RT-PCR (Extended Data Fig. 7 and Supplementary Table 1). FISH detected the *C11orf95*–*RELA* translocation in 67% (*n* = 14 of 21) of primary FFPE supratentorial ependymomas, but in none of 64 posterior fossa tumours, and RT-PCR confirmed the presence of fusion transcripts exclusively in translocation-positive tumours (*P* < 0.0001 Fisher's exact test; Extended Data Fig. 7a).

These data identify *C11orf95*–*RELA* translocations as the most recurrent genetic alteration in ependymoma, affecting approximately 70% of supratentorial tumours (*n* = 29 of 41) and occurring preferentially in older patients (mean age translocation-positive, translocation-negative supratentorial tumours = 8.3 ± 0.9 years, 3.5 ± 1.7 years, respectively; *P* < 0.05, Mann-Whitney test, Fig. 1). We are currently interrogating a larger cohort of supratentorial ependymomas to assess the prognostic significance of the *C11orf95*–*RELA* translocation.

RNA-seq identified 20 other fusion transcripts involving chromosome 11q (Fig. 1, Supplementary Fig. 11 and Supplementary Table 16b, c). Thirteen of these occurred in tumours containing *C11orf95*–*RELA* and are predicted to be non-coding, suggesting they are 'passenger' events. However, four of seven 'coding' fusion transcripts occurred in ependymomas that lacked a *C11orf95*–*RELA* translocation. Two of these fused *C11orf95* to alternative transcriptional regulators: *C11orf95*–*YAP1* and *C11orf95*–*MAML2* (Fig. 1 and Extended Data Fig. 5b). Thus, the zinc finger domains of *C11orf95* are likely to be essential oncogenic elements of these fusions, possibly altering the trafficking, degradation or target specificity of partner transcription factors.

### *C11orf95*–*RELA* drives NF-κB signalling

Members of the NF-κB family of transcriptional regulators are central mediators of the cellular inflammatory response<sup>13</sup>. Although constitutive NF-κB signalling is present in most human tumours, mutations in pathway members are rare, complicating efforts to understand and block aberrant NF-κB activity in cancer<sup>14–16</sup>. We therefore examined whether *C11orf95*–*RELA* fusions drive aberrant NF-κB signalling in ependymoma.

RNA-seq and Affymetrix gene expression profiling detected increased expression of *C11orf95* and *RELA* in translocation-positive ependymomas, as well as high levels of *CCND1*—a direct transcriptional target of NF-κB signalling<sup>17,18</sup>—and *L1CAM* that is associated with aberrant cell–cell adhesion, invasion and NF-κB activation in tumours<sup>19,20</sup> (*Q* < 0.0001; Fig. 1). *CCND1* and *L1CAM* protein expression were also strongly associated with the *C11orf95*–*RELA* translocation in FFPE supratentorial ependymomas (*P* < 0.0001, Fisher's exact test; Extended Data Fig. 7a, b). Upstream stimuli, for example, tumour necrosis factor (TNF), activate the NF-κB pathway by causing *RELA*-containing heterodimers to translocate to the nucleus and drive gene transcription<sup>13</sup>.

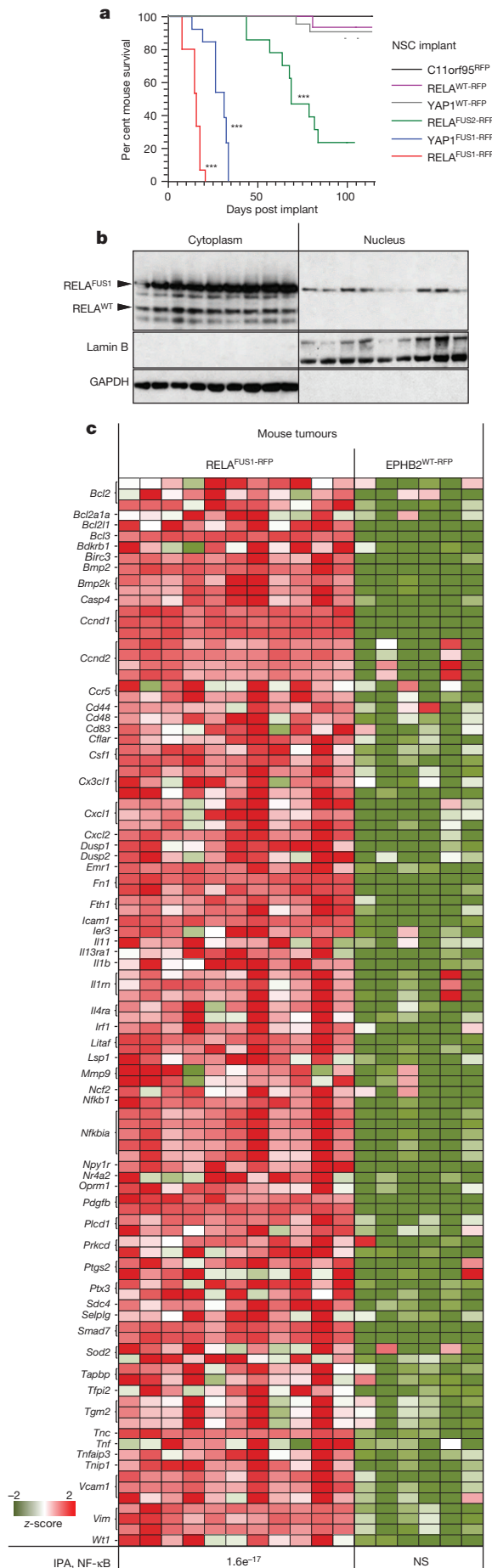


**Figure 4** | *C11orf95-RELA* and *C11orf95-YAP1* fusions drive brain tumorigenesis. **a**, Survival curves of mice implanted with the indicated NSCs. (\*\*\*)  $P < 0.0001$ , log-rank test relative to control NSCs. **b**, Western blot analysis of RELA proteins in cytoplasmic and nuclear extracts of nine independent mouse RELA<sup>FUS1-RFP</sup> brain tumours. **c**, Expression of NF-κB target genes significantly upregulated in RELA<sup>FUS1-RFP</sup> relative to EPHB2<sup>WT-RFP</sup> brain tumours. Bottom,  $P$  value of NF-κB activation detected by IPA.

However, RELA fusion proteins seem to accumulate preferentially in the nucleus of ependymoma cells relative to RELA<sup>WT</sup> protein (Fig. 2b). Therefore, we examined RELA protein trafficking in cells engineered to express exogenous C11orf95, RELA<sup>WT</sup> or RELA<sup>FUS1</sup> (Fig. 3a). As expected, endogenous RELA<sup>WT</sup> was sequestered in the cytoplasm of unstimulated control and C11orf95-transduced cells, but translocated to the nucleus to activate an NF-κB transcriptional reporter after exposure to TNF (Fig. 3b and Extended data Fig. 8). Conversely, overexpression of RELA<sup>WT</sup> resulted in spontaneous nuclear translocation and NF-κB transcription, supporting the idea that high levels of wild-type RELA can overwhelm the IκB inhibitory system<sup>21</sup>. Therefore, we titrated down the expression of the RELA<sup>FUS1</sup> fusion to approximate that of endogenous RELA<sup>WT</sup>. Even at this reduced level, RELA<sup>FUS1</sup> translocated spontaneously to the nucleus and activated NF-κB transcription (Fig. 3b and Extended data Fig. 8).

We next investigated whether C11orf95-RELA drives an aberrant NF-κB transcriptional program in mouse NSCs that we have shown previously serve as cells-of-origin of ependymoma<sup>6</sup> (Fig. 3c). Neither control nor C11orf95 transduction altered gene expression in NSCs; but exogenous RELA<sup>WT</sup> upregulated 20% ( $n = 25$  of 129) of a series of validated NF-κB target genes in NSCs, and ingenuity pathway analysis (IPA) confirmed highly significant activation of NF-κB signalling in these cells (IPA  $P = 4.5 \times 10^{-12}$ ; Supplementary Information and Supplementary Table 17). Expression of RELA<sup>FUS1</sup> produced even greater activation of NF-κB target genes in NSCs, and also upregulated L1cam (IPA,  $P = 1.7 \times 10^{-16}$ ; Fig. 3c, Supplementary Fig. 12 and Supplementary Table 17). Although L1CAM has been reported to activate NF-κB signalling in tumours<sup>16,17</sup>, our NSC and tumour data suggest that it may itself be a target of aberrant C11orf95-RELA signalling (Figs 1 and 3c, and Extended Data Fig. 7b). RELA<sup>FUS1</sup> had a profound impact on the expression of several other genes that regulate focal adhesion, compatible with the notion that aberrant NF-κB signalling disrupts cell-cell adhesion in cancer<sup>13,19</sup> ( $Q = 1.5 \times 10^{-10}$ ; Supplementary Table 18b).

### *C11orf95-RELA* drives ependymoma

To test the transforming capacity of RELA fusion proteins, we isolated NSCs from *Ink4a/Arf*-null *Blbp-eGFP* (enhanced green fluorescent protein) transgenic mice as described previously<sup>6</sup>, and transduced these with either C11orf95-red fluorescence protein (C11orf95<sup>RFP</sup>), RELA<sup>WT-RFP</sup>, RELA<sup>FUS1-RFP</sup> or RELA<sup>FUS2-RFP</sup> retroviruses. To begin to understand the relevance of the other fusions detected in ependymoma we also transduced NSCs with C11orf95-YAP1 (YAP1<sup>FUS1-RFP</sup>), or wild-type YAP1 (YAP1<sup>WT-RFP</sup>). NSCs ( $1.5 \times 10^6$  RFP<sup>+</sup> NSCs) transduced with each virus were implanted separately into the cerebrum of 15 female 6-week-old CD1-nude mice. C11orf95<sup>RFP</sup>, RELA<sup>WT-RFP</sup>, or YAP1<sup>WT-RFP</sup> NSCs formed very few or no brain tumours in mice (median follow up 155 days; Fig. 4a). In marked contrast, all mice implanted with RELA<sup>FUS1-RFP</sup> NSCs succumbed within 20 days to brain tumours that recapitulated the 'clear cell' and finely branched vasculature characteristic of 'vascular-variant' human supratentorial ependymoma<sup>22</sup> ( $P < 0.0001$  log-rank test; Fig. 4a and Extended Data Fig. 7b). Similar to their human counterpart, mouse RELA<sup>FUS1</sup> ependymomas expressed nuclear phospho-Ser276-RELA that is indicative of, and required for, RELA transcriptional activity<sup>23-25</sup>, as well as CCND1 and L1CAM (Extended Data Fig. 7a, b). Consistent with the human disease, nuclei of mouse RELA<sup>FUS1</sup> ependymomas also accumulated



RELA<sup>FUS1</sup> protein relative to the wild-type protein (Figs 2b and 4b, and Extended Data Fig. 7b). RELA<sup>FUS2-RFP</sup> NSCs also generated tumours, albeit with a lower penetrance ( $n = 10$  of 15 mice) and longer latency (median survival 68 days) than RELA<sup>FUS1-RFP</sup> NSCs, potentially explaining the biased selection of RELA<sup>FUS1</sup> versus RELA<sup>FUS2</sup> in human ependymomas. YAP1<sup>FUS-RFP</sup> NSCs formed brain tumours with high efficiency, indicating that other ependymoma translocations are oncogenic (Fig. 4a).

Finally, to determine whether C11orf95–RELA drives a specific, oncogenic NF- $\kappa$ B transcription program, we compared the transcriptomes of mouse RELA<sup>FUS1-RFP</sup> brain tumours with those of our supratentorial ependymoma mouse model driven by *EPHB2* (ref. 6). RELA<sup>FUS1-RFP</sup> mouse brain tumours displayed marked upregulation of NF- $\kappa$ B target genes (IPA,  $P = 1.6 \times 10^{-17}$ ; Fig. 4c and Supplementary Fig. 13). Conversely, *EPHB2*<sup>WT-RFP</sup> mouse ependymomas expressed much lower levels of phospho-Ser276-RELA, L1CAM and CCND1 proteins and lacked NF- $\kappa$ B signal activation. Thus, C11orf95–RELA translocations are potent oncogenes that most probably transform NSCs by driving an aberrant NF- $\kappa$ B transcription program.

Aberrant NF- $\kappa$ B signalling is an established driver of solid tumours, but genetic evidence of pathway involvement has been lacking. We identify a highly recurrent genetic alteration that activates *RELA*, the principal effector of canonical NF- $\kappa$ B signalling, in human cancer. Furthermore, we show that C11orf95 is likely to be an essential partner in these translocations, possibly disrupting the cell trafficking of *RELA* and other partner transcription factors. We are currently investigating the mechanism by which *RELA* fusion proteins transform NSCs, and their potential to serve as a therapeutic target.

## METHODS SUMMARY

Human tumour and matched blood samples were obtained with informed consent using an protocol approved by the institutional review board at St. Jude Children's Research Hospital. WGS, RNA-seq and analysis of all sequence data were performed as described previously<sup>26</sup>. Details of sequence coverage, custom capture and other validation procedures are provided in Supplementary Information (Supplementary Tables 2–6). Interphase FISH, immunohistochemistry of human and mouse tissues, western blot analysis, and RT–PCR were performed using standard techniques as described (Methods). Human and mouse messenger RNA profiles were generated using Affymetrix U133 2.0 and 430v2 arrays, respectively (Methods). NSCs were isolated and transduced with indicated retro- and lentiviruses in stem cell cultures as described previously<sup>4,6,27</sup> (see also Supplementary Information). All mouse studies were conducted according to protocols approved by the St. Jude Children's Research Hospital Animal Care and Usage Committee. NSCs were implanted under stereotactic control into the forebrain of immunocompromised mice and tumour growth monitored clinically and by bioluminescence<sup>8</sup>. All mouse brains were inspected by macroscopic dissection post-mortem. Fresh tumour cells were recovered from mouse brains as described previously<sup>6</sup>.

**Online Content** Any additional Methods, Extended Data display items and Source Data are available in the online version of the paper; references unique to these sections appear only in the online paper.

Received 25 June 2013; accepted 28 January 2014.

Published online 19 February 2014.

- Kleihues, P. *et al.* The WHO classification of tumors of the nervous system. *J. Neuropathol. Exp. Neurol.* **61**, 215–225; discussion 226–219 (2002).
- Merchant, T. E. *et al.* Conformal radiotherapy after surgery for paediatric ependymoma: a prospective study. *Lancet Oncol.* **10**, 258–266 (2009).
- Modena, P. *et al.* Identification of tumor-specific molecular signatures in intracranial ependymoma and association with clinical characteristics. *J. Clin. Oncol.* **24**, 5223–5233 (2006).
- Taylor, M. D. *et al.* Radial glia cells are candidate stem cells of ependymoma. *Cancer Cell* **8**, 323–335 (2005).
- Puget, S. *et al.* Candidate genes on chromosome 9q33–34 involved in the progression of childhood ependymomas. *J. Clin. Oncol.* **27**, 1884–1892 (2009).

- Johnson, R. A. *et al.* Cross-species genomics matches driver mutations and cell compartments to model ependymoma. *Nature* **466**, 632–636 (2010).
- Witt, H. *et al.* Delineation of two clinically and molecularly distinct subgroups of posterior fossa ependymoma. *Cancer Cell* **20**, 143–157 (2011).
- Atkinson, J. M. *et al.* An integrated *in vitro* and *in vivo* high-throughput screen identifies treatment leads for ependymoma. *Cancer Cell* **20**, 384–399 (2011).
- Wang, J. *et al.* CREST maps somatic structural variation in cancer genomes with base-pair resolution. *Nature Methods* **8**, 652–654 (2011).
- Stephens, P. J. *et al.* Massive genomic rearrangement acquired in a single catastrophic event during cancer development. *Cell* **144**, 27–40 (2011).
- Nolan, G. P., Ghosh, S., Liou, H. C., Tempst, P. & Baltimore, D. DNA binding and I $\kappa$ B inhibition of the cloned p65 subunit of NF- $\kappa$ B, a *rel*-related polypeptide. *Cell* **64**, 961–969 (1991).
- Hansen, S. K., Baeuerle, P. A. & Blasi, F. Purification, reconstitution, and I kappa B association of the c-Rel-p65 (RelA) complex, a strong activator of transcription. *Mol. Cell. Biol.* **14**, 2593–2603 (1994).
- DiDonato, J. A., Mercurio, F. & Karin, M. NF- $\kappa$ B and the link between inflammation and cancer. *Immunol. Rev.* **246**, 379–400 (2012).
- Perkins, N. D. The diverse and complex roles of NF- $\kappa$ B subunits in cancer. *Nature Rev. Cancer* **12**, 121–132 (2012).
- Baud, V. & Karin, M. Is NF- $\kappa$ B a good target for cancer therapy? Hopes and pitfalls. *Nature Rev. Drug Discov.* **8**, 33–40 (2009).
- Chaturvedi, M. M., Sung, B., Yadav, V. R., Kannappan, R. & Aggarwal, B. B. NF- $\kappa$ B addiction and its role in cancer: 'one size does not fit all'. *Oncogene* **30**, 1615–1630 (2011).
- Guttridge, D. C., Albanese, C., Reuther, J. Y., Pestell, R. G. & Baldwin, A. S. NF- $\kappa$ B controls cell growth and differentiation through transcriptional regulation of cyclin d1. *Mol. Cell. Biol.* **19**, 5785–5799 (1999).
- Hinz, M. *et al.* NF- $\kappa$ B function in growth control: regulation of cyclin d1 expression and G0/G1-to-S-phase transition. *Mol. Cell. Biol.* **19**, 2690–2698 (1999).
- Kiefel, H., Pfeifer, M., Bondong, S., Hazin, J. & Altevogt, P. Linking L1CAM-mediated signaling to NF- $\kappa$ B activation. *Trends Mol. Med.* **17**, 178–187 (2011).
- Kiefel, H. *et al.* EMT-associated up-regulation of L1CAM provides insights into L1CAM-mediated integrin signalling and NF- $\kappa$ B activation. *Carcinogenesis* **33**, 1919–1929 (2012).
- Courtois, G. & Gilmore, T. D. Mutations in the NF- $\kappa$ B signaling pathway: implications for human disease. *Oncogene* **25**, 6831–6843 (2006).
- Godfraind, C. *et al.* Distinct disease-risk groups in pediatric supratentorial and posterior fossa ependymomas. *Acta Neuropathol.* **124**, 247–257 (2012).
- Chen, L.-F. & Greene, W. C. Shaping the nuclear action of NF- $\kappa$ B. *Nature Rev. Mol. Cell Biol.* **5**, 392–401 (2004).
- Zhong, H., Voll, R. E. & Ghosh, S. Phosphorylation of NF- $\kappa$ B p65 by PKA stimulates transcriptional activity by promoting a novel bivalent interaction with the coactivator CBP/p300. *Molecular Cell* **1**, 661–671 (1998).
- Okazaki, T. *et al.* Phosphorylation of serine 276 is essential for p65 NF- $\kappa$ B subunit-dependent cellular responses. *Biochem. Biophys. Res. Commun.* **300**, 807–812 (2003).
- Zhang, J. *et al.* The genetic basis of early T-cell precursor acute lymphoblastic leukaemia. *Nature* **481**, 157–163 (2012).
- Robinson, G. *et al.* Novel mutations target distinct subgroups of medulloblastoma. *Nature* **488**, 43–48 (2012).
- Korbel, J. O. & Campbell, P. J. Criteria for inference of chromothripsis in cancer genomes. *Cell* **152**, 1226–1236 (2013).

**Supplementary Information** is available in the online version of the paper.

**Acknowledgements** This research was supported as part of the St. Jude Children's Research Hospital, Washington University Pediatric Cancer Genome Project. This work was supported by grants from the National Institutes of Health (R01CA129541, P01CA96832 and P30CA021765 to R.J.G.), the Collaborative Ependymoma Research Network (CERN), and by the American Lebanese Syrian Associated Charities (ALSAC). We are grateful to S. Temple for the gift of reagents and the staff of the Hartwell Center for Bioinformatics and Biotechnology, Animal Imaging Center, and Flow Cytometry and Cell Sorting Shared Resource at St. Jude Children's Research Hospital for technical assistance.

**Author Contributions** M.P., K.M.M., C.P., R.W., J.D.D., R.L., R.G.T., T.N.P., R.T., E.W., B.T., W.O., K.G., M.R., X.C., P.N., E.H., D.F., G.W., S.S., J.E., K.B., D.Y., B.V., H.L.M., J.B., P.G., R.H., J.M., G.S., L.D., C.L., K.O., D.Z., R.S.F., L.L.F., Y.O., L., Y.L., A.G., A.A.S., F.B. and T.M. contributed to the design and conduct of experiments and to the writing. E.R.M., R.K.W., J.R.D. and D.R.G. contributed to experimental design and to the writing. J.Z., D.W.E. and R.J.G. conceived the research and designed, directed and wrote the study.

**Author Information** Sequence and array data were deposited in the European Bioinformatics Institute (EBI) under accession number EGAS00001000254. Reprints and permissions information is available at [www.nature.com/reprints](http://www.nature.com/reprints). The authors declare no competing financial interests. Readers are welcome to comment on the online version of the paper. Correspondence and requests for materials should be addressed to R.J.G. (Richard.Gilbertson@stjude.org), D.W.E. (David.Ellison@stjude.org) or J.Z. (Jinghui.Zhang@stjude.org).

# A Crohn's disease variant in *Atg16l1* enhances its degradation by caspase 3

Aditya Murthy<sup>1</sup>, Yun Li<sup>1</sup>, Ivan Peng<sup>1</sup>, Mike Reichelt<sup>2</sup>, Anand Kumar Katakam<sup>2</sup>, Rajkumar Noubade<sup>1</sup>, Merone Roose-Girma<sup>3</sup>, Jason DeVoss<sup>1</sup>, Lauri Diehl<sup>2</sup>, Robert R. Graham<sup>4</sup> & Menno van Lookeren Campagne<sup>1</sup>

Crohn's disease is a debilitating inflammatory bowel disease (IBD) that can involve the entire digestive tract. A single-nucleotide polymorphism (SNP) encoding a missense variant in the autophagy gene *ATG16L1* (rs2241880, Thr300Ala) is strongly associated with the incidence of Crohn's disease. Numerous studies have demonstrated the effect of *ATG16L1* deletion or deficiency; however, the molecular consequences of the Thr300Ala (T300A) variant remains unknown. Here we show that amino acids 296–299 constitute a caspase cleavage motif in *ATG16L1* and that the T300A variant (T316A in mice) significantly increases *ATG16L1* sensitization to caspase-3-mediated processing. We observed that death-receptor activation or starvation-induced metabolic stress in human and murine macrophages increased degradation of the T300A or T316A variants of *ATG16L1*, respectively, resulting in diminished autophagy. Knock-in mice harbouring the T316A variant showed defective clearance of the ileal pathogen *Yersinia enterocolitica* and an elevated inflammatory cytokine response. In turn, deletion of the caspase-3-encoding gene, *Casp3*, or elimination of the caspase cleavage site by site-directed mutagenesis rescued starvation-induced autophagy and pathogen clearance, respectively. These findings demonstrate that caspase 3 activation in the presence of a common risk allele leads to accelerated degradation of *ATG16L1*, placing cellular stress, apoptotic stimuli and impaired autophagy in a unified pathway that predisposes to Crohn's disease.

Genome-wide association studies have contributed substantial insight into genetically complex diseases such as cancer and chronic inflammatory diseases<sup>1</sup>. Although disease-contributing polymorphisms provide correlative evidence for the involvement of specific genes in pathology, mechanistic consequences of the majority of polymorphisms have yet to be unravelled. To date, over 150 susceptibility loci have been identified for Crohn's disease<sup>2</sup>. Crohn's disease can affect the entire gastrointestinal tract, with disease most commonly found in the distal small intestine (terminal ileum) and ascending colon. Significant changes in local cytokine production, intestinal microflora, mucosal barrier function and epithelial cell renewal are simultaneously observed<sup>3</sup>. Genome-wide association studies performed in geographically distant populations have consistently identified SNPs in the genes *Irgm*, *Card15/Nod2*, *Il23r*, *Lrrk2* and *Atg16l1* as strongly associated variants in Crohn's disease<sup>2,4</sup>. More recently, cooperation between autophagy and the clinically relevant endoplasmic reticulum stress response gene *Xbp1* was shown to synergistically prevent ileal inflammation<sup>2,5</sup>. Ontologically, these findings implicate autophagy, cellular stress regulation and microbial pathogen sensing as key pathways in intestinal inflammation.

Macroautophagy (herein referred to as autophagy) is a cellular recycling process where cytosolic cargo is engulfed in a double-membrane vesicle and targeted for degradation by lysosomal fusion (reviewed in ref. 6). Xenophagy is a targeted form of autophagy where intracellular pathogens are sequestered in autophagosomes for lysosomal degradation, and bridges pathogen sensors and the canonical autophagy machinery<sup>7</sup>. The autophagy gene *Atg16l1* is a central adaptor required for the formation of a mature autophagosome, and the A > G SNP (rs2241880, where A = non-risk, G = risk for Crohn's disease) encodes a Thr 300-to-Ala variant (Thr = non-risk and Ala = risk for Crohn's disease) in exon 9. Since its identification, this SNP has remained one of the most clinically

significant variants in Crohn's disease<sup>8</sup>. Numerous *in vivo* and *in vitro* model systems have emerged to delineate the contribution(s) of *ATG16L1* loss-of-function to canonical autophagy, xenophagy and inflammatory signalling<sup>9–16</sup>. Despite intense investigation, definitive proof that T300A is the causal allele on the risk haplotype is elusive, and the key mechanism(s) underpinning the consequences of T300A variant remain unresolved. This study demonstrates that the T300A variant sensitizes *ATG16L1* to caspase-3-mediated degradation, thereby revealing a functional connection between Crohn's disease, caspase activation and autophagy.

## T300A variant enhances *ATG16L1* cleavage

We initiated our studies by performing multiple sequence alignment of *ATG16L1* protein, focusing on the region proximal to Thr 300. *ATG16L1* is an adaptor consisting of an amino-terminal coiled-coil domain followed by seven WD-repeat domains. Five isoforms have been described for human *ATG16L1* (NP\_110430.5, NP\_060444.3, NP\_942593.2, NP\_001177195.1 and NP\_001177196.1). *ATG16L1*α and β are the major isoforms expressed in intestinal epithelium<sup>8</sup> and macrophages (current study), and all isoforms encode exon 9, which contains Thr 300. Murine cells express detectable levels of additional variants (termed *ATG16L1*α' and β', described elsewhere<sup>13</sup>). Multiple sequence alignment analysis revealed conserved putative caspase target sequences (DxxD) at amino acids 296–299 and 319–322 of human *ATG16L1* (NP\_110430.5, Fig. 1a). *In-vitro*-translated *ATG16L1*β was incubated with recombinant active caspase 3, and the T300A variant showed significantly enhanced cleavage. Abolishing the 296–299 consensus caspase cleavage site by site-directed mutagenesis of D299E completely prevented *ATG16L1*β processing (Fig. 1b). Recombinant active caspase 1 and 6 also processed the T300A variant of *ATG16L1*β, but with lower efficiency compared to caspase 3

<sup>1</sup>Department of Immunology, Genentech, Inc., 1 DNA Way, South San Francisco, California 94080, USA. <sup>2</sup>Department of Pathology, Genentech, Inc., 1 DNA Way, South San Francisco, California 94080, USA.

<sup>3</sup>Department of Molecular Biology, Genentech, Inc., 1 DNA Way, South San Francisco, California 94080, USA. <sup>4</sup>ITGR Human Genetics, Genentech, Inc., 1 DNA Way, South San Francisco, California 94080, USA.

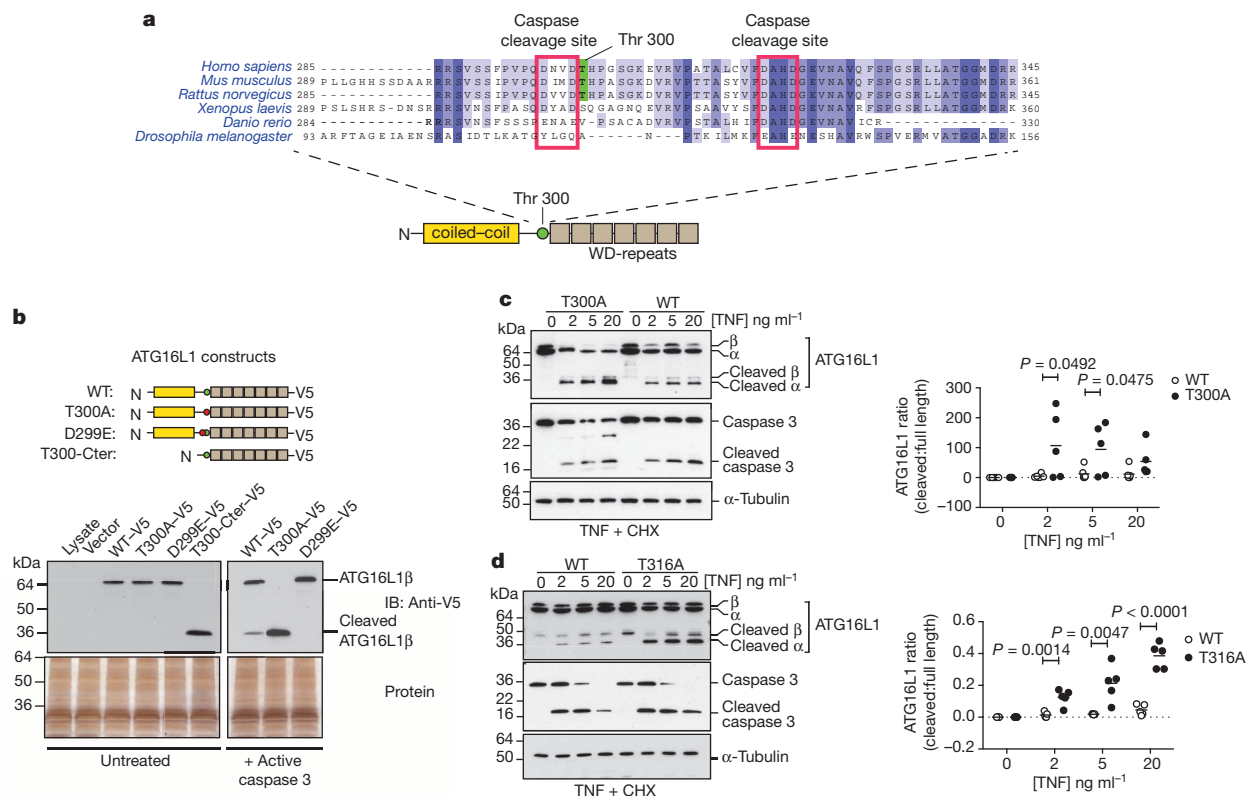


**Figure 1 | T300A variant sensitizes ATG16L1 to caspase-mediated cleavage at the D299–T300 scissile site.** **a**, Multiple sequence alignment of ATG16L1 (NP\_110430.5). Protein accession numbers shown in Supplementary Table 3. **b**, Carboxy-terminal V5 immunoblot of full-length (68 kDa) and cleaved (36 kDa) ATG16L1 $\beta$ . Silver stain (bottom gels) depicts total protein. Data represent 3 independent experiments. IB, immunoblot. **c**, TNF- $\alpha$ -mediated

processing of human ATG16L1 in monocyte-derived macrophages. Scatter plot of immunoblot densitometry depicts a ratio of cleaved:full-length ATG16L1 (Extended Data Fig. 2).  $n = 7$  donors. **d**, TNF- $\alpha$ -mediated processing of murine ATG16L1 in macrophages. Immunoblot represents 5 independent experiments. Scatterplot represents data pooled from 5 independent experiments. WT, wild type.

(Extended Data Fig. 1a). Transfection of HeLa cells with the same constructs demonstrated that death-receptor-mediated apoptosis by tumour necrosis factor (TNF)- $\alpha$  cleaves ATG16L1 $\beta$ ; this is enhanced by the T300A variant and abrogated in the D299E mutant (Extended Data Fig. 1b). Overexpression of ATG16L1 in cell lines results in degradation of excess protein, indicating that an upper limit of ATG16L1 protein level is maintained by cells<sup>13</sup> through constitutive ATG16L1 $\beta$  cleavage in addition to that induced by TNF- $\alpha$  stimulation (see 0 h time points, Extended Data Fig. 1b). The consensus caspase cleavage sites flanking the ATG16L1 T300A SNP are highly conserved in human and mouse (Fig. 1a). We reconstituted ATG16L1-deficient murine bone marrow progenitors with wild-type, T316A (corresponding to human T300A) or D315E (human D299E) variants of ATG16L1 $\beta$  (Extended Data Fig. 1c). TNFR1 (also known as TNFRSF1A) stimulation of these cells demonstrated that, consistent with human ATG16L1, cleavage of murine ATG16L1 $\beta$  is enhanced by the T316A variant but abolished by the D315E variant (Extended Data Fig. 1d). Importantly, these data also indicate that amino acids 319–322 do not constitute a caspase cleavage site. We next assessed ATG16L1 processing in primary cells. First, peripheral blood monocyte-derived macrophages from human donors homozygous for non-risk (wild-type) or T300A variant of ATG16L1 were treated with increasing doses of TNF- $\alpha$  in the presence of cycloheximide to induce caspase 3 activation. Immunoblotting for ATG16L1 indicated that the T300A variant significantly enhanced its processing, as indicated by the emergence of 36-kDa and 34-kDa caspase cleavage products. Densitometry analysis of immunoblots analysing the 36-kDa and 34-kDa fragments vs full-length ATG16L1 from a number of donors revealed that the T300A variant measurably increased the caspase cleavage product in a TNF- $\alpha$  dose-dependent manner (Fig. 1c). Caspase 3

cleavage or the generation of cleaved PARP, an independent caspase 3 substrate, was not increased in donor cells with the T300A variant (Extended Data Fig. 2), confirming that accelerated processing of the T300A variant is not due to increased caspase 3 activity. We generated C57BL/6N mice with a T316A knock-in mutation to recapitulate the Crohn's disease-associated SNP *in vivo* (Extended Data Fig. 3a, b). Mice were grossly normal, and no overt developmental (data not shown) or inflammatory phenotypes were observed by flow cytometry analysis of immune organs (Extended Data Fig. 4). Histological analysis showed no abnormal morphology of small intestine (Extended Data Fig. 5a) or colon (data not shown). Quantification of small intestine Paneth cell granules showed comparable morphology at baseline conditions between wild-type and T316A mice (Extended data Fig. 5b–d). Bone-marrow-derived macrophages from these mice were treated with TNF- $\alpha$  in the presence of cycloheximide to assess ATG16L1 cleavage as in human macrophages. Murine ATG16L1 cleavage was greatly increased by the T316A mutation in a TNF- $\alpha$  dose-dependent manner (Fig. 1d). Specific comparison of the  $\alpha$  and  $\beta$  isoforms showed that whereas ATG16L1 $\alpha$  is expressed at higher levels, ATG16L1 $\alpha$  and  $\beta$  are processed equally after TNF- $\alpha$  treatment (Extended Data Fig. 6a). Together, these data reveal that substitution of threonine with alanine at the P1' residue of a caspase cleavage site enhances processing of ATG16L1, whereas disruption of the caspase cleavage site (D299E in human, D315E in mouse) abolishes its processing. Compatible with these findings, bioinformatics and biochemical studies have indicated that alanine is preferred over threonine as a P1' amino acid for caspase-mediated cleavage<sup>17,18</sup>. Finally, we tested whether the T300A or T316A variants inherently decreased protein stability of ATG16L1. *In-vitro*-translated ATG16L1 showed comparable stability between all variants in the absence of caspases,



indicating that basal stability of the T300A protein is not compromised (Fig. 1b, untreated samples). We next tested stability of endogenous ATG16L1 in primary murine macrophages using  $^{35}\text{S}$ -labelling pulse-chase. Immunoprecipitation of ATG16L1 using an antibody that preferentially detects the N-terminus of ATG16L1 (data not shown) showed comparable turnover between wild-type and T316A variants of ATG16L1 when chased over 2 hours (Extended Data Fig. 6b). Thus, the T300A/T316A variants do not compromise ATG16L1 protein stability under basal conditions. Together these data demonstrate that cellular stress resulting in caspase activation is a requirement for accelerated degradation of the T300A/T316A variants of ATG16L1.

### Caspase 3 cleaves ATG16L1

We noted that human or murine ATG16L1 is cleaved in a caspase-dependent manner following induction of apoptosis by death-receptor engagement or staurosporine (Extended Data Fig. 7a, b). Given that numerous caspases recognize similar cleavage motifs in their substrates<sup>19</sup>, we aimed to identify the physiologically relevant caspase responsible for ATG16L1 processing. TNFR1 engagement by TNF- $\alpha$  induces type I apoptosis whereby death receptor stimulation activates caspase 8, which directly activates effector caspases 3 and/or 7<sup>20</sup>. In type II apoptosis, caspase-8-mediated activation of pro-apoptotic Bcl-family proteins (for example, Bid, Bax) leads to the activation of executor caspases 3 and/or 7. Short interfering RNA (siRNA)-mediated knockdown of initiator caspases 8 or 9 demonstrated that caspase 8 is required for death-receptor-, but not staurosporine-mediated cleavage of ATG16L1, whereas caspase 9 is dispensable for ATG16L1 processing (Fig. 2a, b). We further assessed ATG16L1 processing after induction of type II apoptosis in colon carcinoma epithelial cells lacking the pro-apoptotic Bcl-family member *Bax*. Activation of caspase 3 in *Bax*<sup>+/+</sup> HCT116 cells by TNF- $\alpha$  robustly induced ATG16L1 cleavage as measured by immunoblotting; however, HCT116 cells lacking *Bax* failed to cleave ATG16L1 under these conditions (Extended Data Fig. 7c). To delineate the effector caspases responsible for ATG16L1 cleavage, we first used siRNA-mediated knockdown of caspase 3 or 7 followed by TNF- $\alpha$  or staurosporine treatment. Knockdown of caspase 3 alone was sufficient to eliminate ATG16L1 cleavage following either TNF- $\alpha$  or staurosporine treatment (Fig. 2c and Extended Data Fig. 7d). Induction of apoptosis in caspase-3-deficient MCF-7 cells also showed that caspase 7 activation was not sufficient to cleave ATG16L1 (Extended Data Fig. 7e). Finally, we generated primary bone-marrow-derived macrophages from *Casp3*-knockout mice and treated them with TNF- $\alpha$  or Staurosporine. Loss of *Casp3* clearly abolished ATG16L1 cleavage under

both conditions, despite activation of effector caspase 7 (Fig. 2d). Thus, independent of cell type, caspase 3 is the effector caspase that directly cleaves ATG16L1, whereas caspase 8 and Bax are important upstream factors that promote ATG16L1 processing. Activation of the NLRP3 inflammasome in bone-marrow-derived macrophages failed to cleave ATG16L1 (Extended Data Fig. 7f). These results demonstrate that apoptotic and not inflammatory caspase activation is required for ATG16L1 processing.

### Defective autophagy via metabolic stress

During the early stages of autophagosome maturation, ATG16L1 acts as an adaptor, stabilizing the interaction between ubiquitin-like protein ATG12 and the E3 ubiquitin ligase-like protein ATG5. This 'ATG16L1 complex' acts in an E3-ligase-like manner to lipidate ATG8 (also known as LC3 or Map1lc3a), a requirement for the elongation of the nascent autophagosomal membrane<sup>6</sup>. Nutrient deprivation (glucose or amino-acid starvation) is an established method to investigate canonical autophagy<sup>21–23</sup>, and has been reported to activate apoptotic caspases in cells<sup>24–26</sup>. As the T300A variant facilitated ATG16L1 processing by caspase 3, we asked whether this would result in decreased levels of total ATG16L1 during periods of nutrient starvation. Glucose-starved macrophages from T316A knock-in mice displayed a lower mean fluorescence intensity of ATG16L1, indicative of a ~50% decrease in total ATG16L1 protein (Fig. 3a, b). We next determined if the SNP has a functional consequence on starvation-induced autophagy<sup>13,14,27</sup>. Glucose or amino acid starvation followed by immunoblotting showed that cells from T316A knock-in mice sensed metabolic stress (AMPK $\alpha$  phosphorylation) and initiated autophagy (emergence of LC3-II) (Fig. 3c and Extended Data Fig. 8a). By assessing the fluorescence intensity and total cellular area occupied by LC3-II punctae<sup>23</sup> during glucose or amino acid starvation, we were able to enumerate the LC3-II punctae (termed spot count) per cell. Glucose starvation resulted in a significant decrease of cellular area occupied by lipidated LC3 in T316A knock-in macrophages (Fig. 3d) and a small but measurable decrease in LC3-II spot count (Extended Data Fig. 8b). Amino acid starvation similarly resulted in decreased LC3-II area in T316A macrophages (Extended Data Fig. 8c). Given the association between nutrient deprivation and induction of apoptosis, we asked whether the observed decrease in ATG16L1 protein and LC3-II area following glucose starvation correlated with an induction of caspase activity. Either glucose or amino acid starvation induced caspase 3 activity which was comparable between wild-type and T316A macrophages (Fig. 3e and Extended Data Fig. 8d), whereas treatment with the mTOR inhibitor rapamycin showed a similar increase in LC3-II

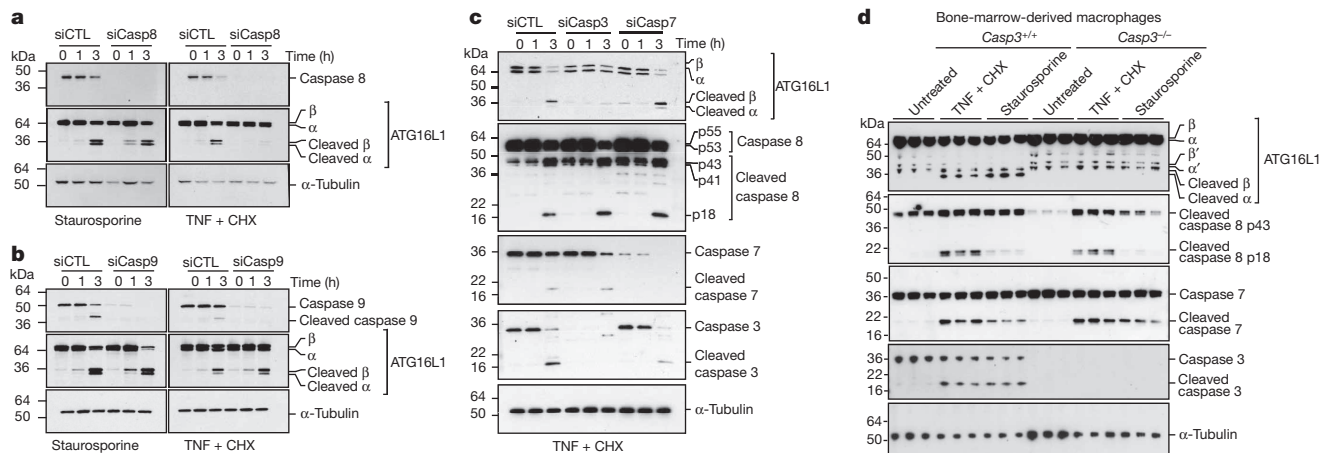


**Figure 2 | Caspase 3 activation is required for ATG16L1 processing.** **a**, HeLa cells transfected with control siRNA (siCTL) or siCaspase 8 were stimulated with 2.0  $\mu\text{M}$  staurosporine or 20 ng ml<sup>-1</sup> TNF + 10  $\mu\text{g}$  ml<sup>-1</sup> CHX. **b**, HeLa cells transfected with control siRNA or siCaspase 9 were stimulated as in **a**. **c**, HeLa cells transfected with control, caspase-3- or caspase-7-specific

siRNAs were stimulated with 20 ng ml<sup>-1</sup> TNF + 10  $\mu\text{g}$  ml<sup>-1</sup> CHX. **d**, Wild-type or caspase-3-knockout macrophages were stimulated with 2.0  $\mu\text{M}$  staurosporine or 20 ng ml<sup>-1</sup> TNF + 10  $\mu\text{g}$  ml<sup>-1</sup> CHX. Data in **a–c** represent 2 independent experiments; data in **d** represent 4 independent experiments.

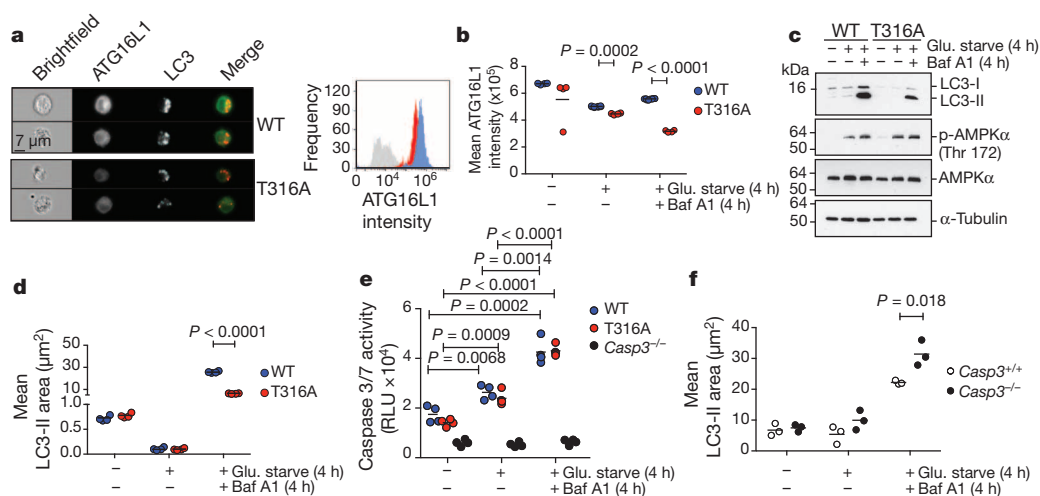


**Figure 3 | T316A variant reduces ATG16L1 levels and decreases autophagic flux upon nutrient starvation of murine macrophages.** **a**, Intracellular staining for LC3 and ATG16L1 following glucose starvation in the presence of bafilomycin A1. White mask in LC3 channel illustrates punctate LC3 staining, representing LC3-II. Histogram depicts mean fluorescence intensity of 10,000 cells per sample. **b**, Quantification of mean ATG16L1 fluorescence intensity in **a**,  $n = 4$  mice. Glu., glucose. **c**, Immunoblot of phosphorylated (p-) AMPK $\alpha$

(Thr 172) and lipidated LC3 (LC3-II). **d**, Quantification of mean LC3-II area in murine macrophages,  $n = 4$  mice. **e**, Caspase 3 activity in murine macrophages following glucose starvation,  $n = 3$  mice. RLU, relative light units. **f**, Quantification of mean LC3-II area in wild-type (*Casp3*<sup>+/+</sup>) or *Casp3*-knockout (*Casp3*<sup>-/-</sup>) macrophages,  $n = 3$  mice. Data in **a–f** represent 2 independent experiments.

area between wild-type and T316A macrophages (Extended Data Fig. 8e), and did not result in caspase 3 activation (Extended Data Fig. 8f). Finally, macrophages from *Casp3*-knockout mice showed significantly increased LC3-II area following glucose starvation in the presence of bafilomycin A1 (Fig. 3f). These findings indicate that, in addition to the inhibition of mTOR signalling, nutrient starvation affects autophagy through apoptotic caspase activation. Defective autophagy emerges in cells with the T316A variant when caspase 3 activation is induced by metabolic stress such as nutrient deprivation. Consistent with a loss-of-function caused by the T316A variant, macrophages lacking ATG16L1 (*LysMCre*<sup>+</sup> *Atg16l1*<sup>loxP/loxP</sup> cells) showed a significant reduction of LC3-II area and spot count under glucose-starvation conditions (Extended Data Fig. 8g, h).

We expanded our study of autophagy to human cells harbouring endogenous T300A mutations in a genetically heterogeneous background by analysing Epstein–Barr virus (EBV)-transformed B-cell lines obtained from donors with Northern and Western European ancestry as part of the CEPH collection (CEU) of the International HapMap project<sup>28</sup> (Supplementary Table 1). We noted that GG homozygosity was observed at a frequency of 0.286 in the CEU cohort. Thus carriers for the T300A SNP comprise a majority of the European Caucasian population. Analysis of additional polymorphisms revealed SNPs in *Card9* (rs10870077) and *Il18rap* (rs917997) were present in the majority of the population, whereas disease-associated polymorphisms in *Irgm* (also known as *Irgm1*; rs10065172), *Il23r* (rs11209026) or *Lrrk2* (rs11564258) were not found in the CEU cohort (Supplementary Table 2). Finally, cytogenetic analysis of selected individuals with non-risk or T300A variants of *ATG16L1* showed normal karyotypes with no aneuploidies in any of the cell lines (data not shown).

Measuring ATG16L1 mean fluorescence intensity showed that T300A EBV-transformed B cells, in contrast to murine macrophages, had decreased ATG16L1 levels when compared to non-risk (wild-type) controls at baseline (Fig. 4a). This is consistent with a significantly higher baseline caspase 3 activation in EBV-transformed B cells versus primary murine bone-marrow-derived macrophages (~fivefold increase, compare Fig. 3e vs Fig. 4b, y axis). Similar to murine macrophages and compatible with increased caspase 3 activation following metabolic stress, we observed a smaller LC3-II area in T300A compared to non-risk control (wild-type) cells following nutrient deprivation (Fig. 4c). Presence of early autophagosomes in these cells was independently

assessed at the ultrastructural level using transmission electron microscopy following bafilomycin A1 treatment. As with flow cytometry analysis, we observed a decrease in early mature autophagosome-like structures in T300A cells (red arrows) and increased accumulation of multivesicular structures (blue arrows) resembling autolysosomes compared to non-risk (wild-type) controls (Fig. 4d; graph quantifies cytosolic area occupied by autophagosomes per cell). Cumulatively, we uncovered a defect in starvation-induced autophagy conferred by the T300A variant, which is dependent on caspase 3 activation. The defect in starvation-induced autophagy induced by the SNP is conserved in murine and human cells, and prevails in a genetically heterogeneous population, underscoring a strong penetrance of this variant.

### T300A/T316A variants compromise xenophagy

Defective autophagy is emerging as a contributor to numerous human diseases<sup>29,30</sup>. However, the specific association of the T300A SNP to Crohn's disease is indicative of a unique role for autophagy in the intestinal environment. Both small and large intestines are colonized by diverse microflora that have a critical role in mucosal health<sup>31,32</sup>. To date, three studies have implicated the T300A variant in the invasion and survival of *Salmonella typhimurium* in fibroblast or epithelial cell lines<sup>13,14,27</sup>. *S. typhimurium* predominantly colonizes the murine colon and caecum<sup>33</sup>, whereas *Yersinia enterocolitica* infects the ileum through M cells into local Peyer's patches where they invade macrophages and subsequently enter mesenteric lymph nodes<sup>34</sup>. The T300A SNP is uniquely associated with ileal Crohn's disease<sup>8,35</sup>, thus making *Y. enterocolitica* a physiologically relevant pathogen to investigate the effect of the murine T316A variant on inflammation of the small intestine. Infection of peripheral blood monocyte-derived macrophages from healthy donors expressing non-risk (wild-type) or T300A variants of *Atg16l1* demonstrated that the T300A variant resulted in defective clearance of *Y. enterocolitica* (Fig. 5a). We next assessed pathogen clearance in murine macrophages. Macrophage and dendritic cell apoptosis is known to be induced by *Y. enterocolitica* infection<sup>36–38</sup>; consistently, we observed caspase 3 activation in both wild-type and T316A macrophages 6 hours after *Y. enterocolitica* infection (Extended Data Fig. 9a). As with human macrophages, murine T316A mutant macrophages were unable to clear *Y. enterocolitica* as efficiently as wild-type cells (Fig. 5b). ATG16L1-deficient macrophages from *LysMCre*<sup>+</sup> *Atg16l1*<sup>loxP/loxP</sup> mice also showed a defect in bacterial clearance, indicating that the T316A

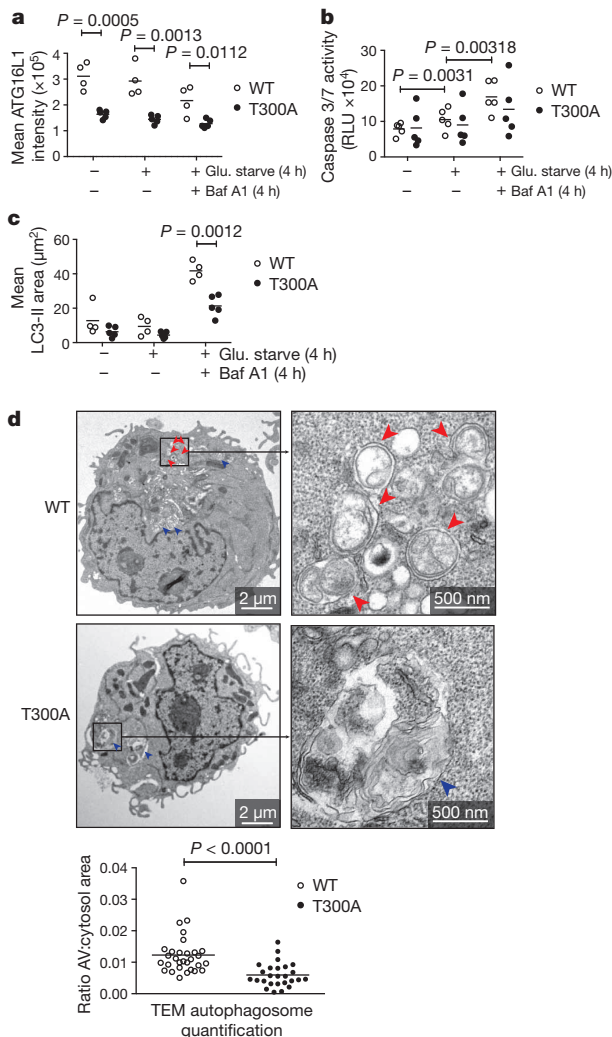


**Figure 4 | Human T300A variant reduces autophagic flux upon nutrient starvation of genetically heterogeneous B cells.** **a**, Quantification of ATG16L1 mean fluorescence intensity by image-based flow cytometry of 10,000 cells,  $n = 4$  (wild-type, WT), 5 (T300A). Data represent 3 independent experiments. **b**, Quantification of caspase 3 activity upon glucose starvation of  $2 \times 10^4$  cells,  $n = 5$ . Data represent 2 independent experiments. **c**, Quantification of mean LC3-II area of samples in **a**. Data represent 3 independent experiments. **d**, Visualization of early autophagosomes by transmission electron micrographs (TEM). Red arrows, early autophagosomes, characterized by vesicular structures with a double-membrane. Blue arrows, multivesicular lysosomal structures, identified by degraded intravesicular cargo. Micrographs representative of 10–12 images per donor,  $n = 4$  (WT),  $n = 3$  (T300A). A total of 29 (WT) and 26 (T300A) images containing autophagosomes was analysed. Histogram quantifies autophagic vesicles as a ratio of autophagosome:cytosolic area.

mutation conferred a loss-of-function phenotype (Extended Data Fig. 9b). We further tested if the differences in bacterial load were due to an altered capacity of primary T316A mutant macrophages to clear invading bacteria and observed that, whereas the T316A SNP significantly impaired bacterial clearance 6 hours after infection at several multiplicities of infection (m.o.i.), *Y. enterocolitica* invasion was comparable between wild-type and T316A mutant macrophages (Extended Data Fig. 9c, d), indicating that the SNP does not affect invasion of *Y. enterocolitica* in primary murine macrophages as opposed to a colon epithelial cell line<sup>14</sup>. Given our initial finding that Thr 300 (Thr 316 in mouse) resides at the P1' residue of a caspase-cleavage site, we asked whether cleavage of mutant ATG16L1 at this site indeed drives the increased bacterial burden. Bone marrow progenitor cells (immortalized by expression of oestrogen receptor–Hoxb8 fusion protein, ER–HoxB8) lacking

*Atg16l1* were complemented with wild-type, T316A or D315E variants of murine ATG16L1, differentiated into macrophages and infected with *Y. enterocolitica*. Cells lacking *Atg16l1* (vector transduced controls) showed a significantly higher bacterial burden 6 hours after infection when compared to cells expressing wild-type *Atg16l1* (Fig. 5c). As with primary murine macrophages, ER–HoxB8-immortalized macrophages expressing T316A mutant *Atg16l1* maintained a high bacterial burden, similar to ATG16L1-deficient cells. Abolishing the caspase-3 cleavage site by site-directed mutagenesis (D315E variant) restored bacterial clearance (Fig. 5c). These findings demonstrate that caspase-mediated degradation of the T300A/T316A variants of ATG16L1 results in defective xenophagy by macrophages.

### T316A variant enhances cytokine response

To determine if defective bacterial clearance triggers a pro-inflammatory response by macrophages, we analysed cytokine response in *Y. enterocolitica*-infected cells. Levels of inflammatory cytokines TNF- $\alpha$ , IL-1 $\beta$  and IL-6 were increased in cell culture media of T316A knock-in macrophages at various time points following infection (Fig. 5d). Deletion of the coiled-coil domain of ATG16L1 in murine macrophages has been shown to result in elevated IL-1 $\beta$  release following lipopolysaccharide (LPS)-endotoxin challenge<sup>9</sup>. To delineate whether elevated cytokine production was reflective of pathogen burden or enhanced sensitization of T316A macrophages to bacterial components, we stimulated the cells with heat-killed *Y. enterocolitica* (HKYe) or Toll-like receptor (TLR) and NOD2 ligands. TNF- $\alpha$  transcription and release were comparable between wild-type and T316A macrophages following stimulation with HKYe (Extended Data Fig. 10a). In contrast, transcription of *Il1 $\beta$*  (also known as *Il1b*) was comparable, but levels of secreted IL-1 $\beta$  and its target IL-6 were elevated in T316A macrophages after treatment with HKYe (Extended Data Fig. 10b, c). Stimulation of specific TLRs showed comparable TNF- $\alpha$  and IL-6 release following LPS (TLR4) or CpG-ODN (TLR9) treatment, and a modest increase of TNF- $\alpha$  and IL-6 levels in T316A macrophages following Pam3CSK4 (TLR1/2) treatment (Extended Data Fig. 10d, e). NOD2 stimulation by muramyl dipeptide (MDP) in the presence of LPS resulted in elevated IL-1 $\beta$  release by T316A macrophages (Extended Data Fig. 10f). These data indicate that enhanced TNF- $\alpha$  production in *Y. enterocolitica*-infected T316A macrophages reflects increased pathogen burden, whereas elevated IL-1 $\beta$  release is compatible with a role for autophagy as a negative regulator of inflammasome activation, consistent with previous independent observations<sup>9,39,40</sup>.

Given the relevance of *Y. enterocolitica* in ileitis, we next tested the physiological effect of the T316A SNP in bacterial clearance and inflammation. On the basis of our *in vitro* findings, we asked whether the T316A mutation would result in defective pathogen clearance and enhance cytokine production *in vivo*. Oral ingestion of *Y. enterocolitica* resulted in specific inflammation of the ileum but not of the colon (Fig. 5e). The low level of intestinal inflammation induced by this pathogen prevented the identification of histological differences in ileal inflammation between wild-type and T316A mice (Extended Data Fig. 10g). Serum cytokine analysis identified elevated IL-1 $\beta$  levels in T316A mice 48 h after *Y. enterocolitica* oral gavage (Extended Data Fig. 10h). Measurement of cytokine transcription in the mesenteric lymph nodes of infected mice showed increased mRNA levels of *Tnf $\alpha$* , *Il6*, *Il1a* and *Il1b* in T316A compared to wild-type mice (Fig. 5f), consistent with an increased bacterial burden and pro-inflammatory signalling in the mesenteric lymph nodes of T316A mutant mice (Fig. 5g). Thus, the T300A/T316A variants confer an increased response to specific bacterial components by macrophages and a defect in *Y. enterocolitica* clearance, resulting in an elevated inflammatory cytokine response.

### Discussion

In a healthy intestine, the turnover of ATG16L1 is dependent on basal caspase 3 activity. However, in the presence of the T300A SNP, the persistence of apoptotic stimuli in the form of metabolic or endoplasmic



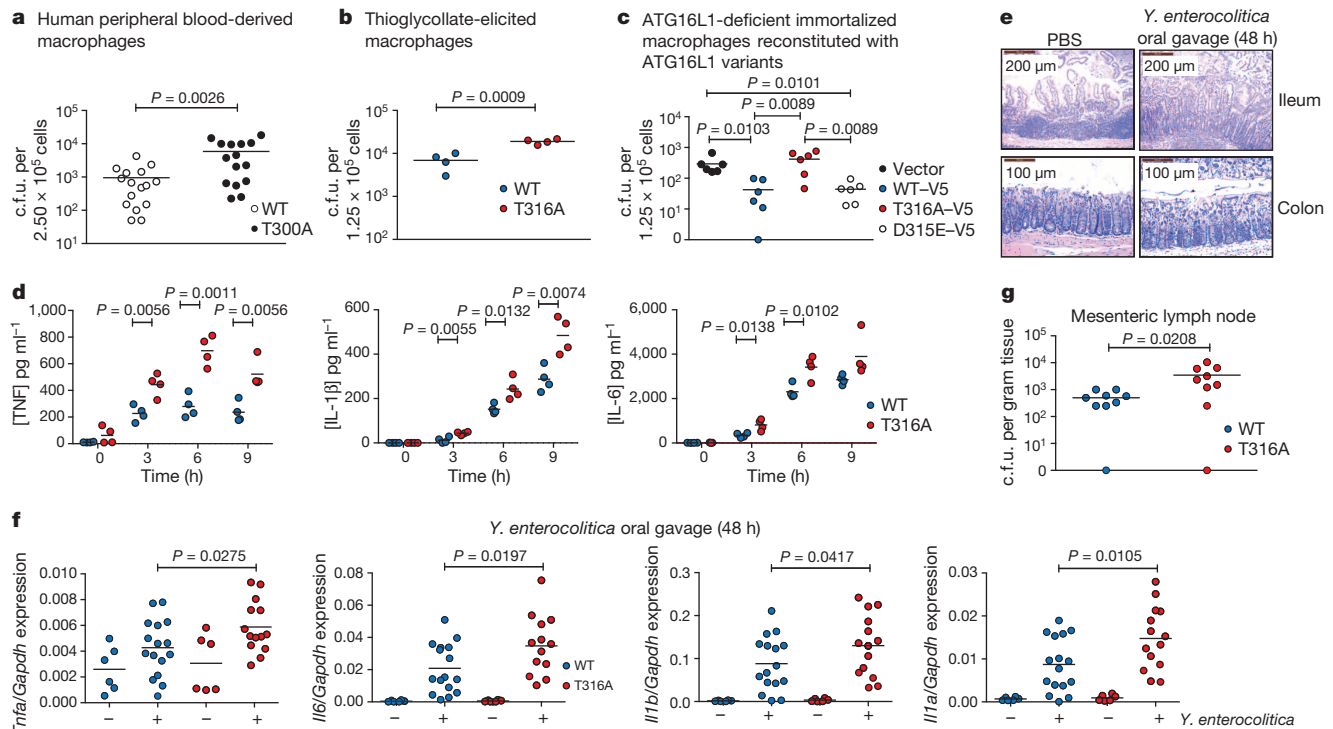


**Figure 5 | T300A/T316A variants of ATG16L1 confer defective clearance of *Y. enterocolitica* and elevated cytokine production.** **a–c**, *Y. enterocolitica* colony forming units (c.f.u.) in human and murine macrophages infected for 6 h (20 m.o.i.). Data in **a** are pooled from 4 independent cohorts of 3 or 4 donors per genotype, total  $n = 16$  (non-risk, WT), 15 (T300A, risk). Data in **b** represent 3 independent experiments,  $n = 4$  mice. Data in **c** represent 3 independent experiments,  $n = 4$  mice. **d**, TNF- $\alpha$ , IL-1 $\beta$  and IL-6 levels in culture media of WT and T316A macrophages infected with 20 m.o.i. *Y. enterocolitica*. Data represent 2 independent experiments,  $n = 4$  mice. **e**, Ileum and colon

histology (haematoxylin and eosin staining) of WT mice. Images are representative of 3 (PBS) and 8 (*Y. enterocolitica*) treated male mice. **f**, Measurement of cytokine mRNA transcripts in mesenteric lymph nodes. Data are pooled from 2 independent experiments of 3 mice (PBS) and 7 mice (*Y. enterocolitica*) per experiment. Transcripts are normalized to *Gapdh* ( $2^{-\Delta\Delta Ct}$ ). **g**, *Y. enterocolitica* c.f.u. in mesenteric lymph nodes of WT and T316A knock-in mice 48 h following oral gavage. Data represent 3 independent experiments,  $n = 9$  male mice.

reticulum stress, death receptor activation or pathogen infection significantly enhances ATG16L1 cleavage, thereby diminishing basal autophagy. This in turn triggers inflammatory cytokine production, thereby generating a chronic inflammatory state in the intestine (illustrated in Fig. 6). Recent work<sup>2</sup> implicates autophagy as a mechanism to prevent apoptosis upon endoplasmic reticulum stress. Our study now in turn strongly supports a role for apoptotic caspases in the regulation of autophagy through degradation of ATG16L1.

Our findings uncover a functional consequence of the T300A variant, namely its sensitization to caspase-3-mediated cleavage. This is a critical initial step leading to defects observed in pathogen handling and stress response by cells of the intestine. T300A is a common variant of ATG16L1, and its high prevalence in independent populations supports the observations that the T300A genotype does not confer complete loss-of-function of autophagy. Our *in vitro* and *in vivo* findings are consistent with the phenotypes associated with ATG16L1 loss-of-function<sup>2,9–12,16,41</sup>, and consistent with our understanding that a genetically complex disease such as Crohn's disease is influenced by multiple risk loci, each contributing only partly to the disease phenotype<sup>31</sup>. Importantly, the observation that the T300A variant increases susceptibility to proteolytic degradation opens up the possibility that therapeutic inhibition of pathways that lead to caspase 3 activation may restore autophagy and gut homeostasis in part by stabilizing ATG16L1.

## METHODS SUMMARY

**Donors.** Healthy human donors were genotyped for the T300A variant (rs2241880). Written informed consent was obtained from study participants and the study protocols were reviewed and approved by the Western Institutional Review Board. **Mice.** *Atg16l1* T316A knock-in mice were generated using C57BL/6 embryonic stem cells (Supplementary Fig. 5a). Deletion of *Atg16l1* was generated by crossing *LysMCre*<sup>+</sup> (macrophage-specific, described in ref. 42) with *Atg16l1*<sup>loxP/loxP</sup> mice (Extended Data Fig. 3c, d). Caspase 3-knockout mice<sup>43</sup> were obtained from Jackson Laboratories. All *in vivo* experiments were performed using age-matched mice and littermate controls. All mice were bred into the C57BL/6 background, and all protocols were approved by the Genentech Institutional Animal Care and Use Committee.

**Macrophage ATG16L1 cleavage assay.** Macrophages were stimulated with indicated doses of recombinant TNF- $\alpha$  (Peprotech) + 10  $\mu$ g ml $^{-1}$  cycloheximide (CHX,

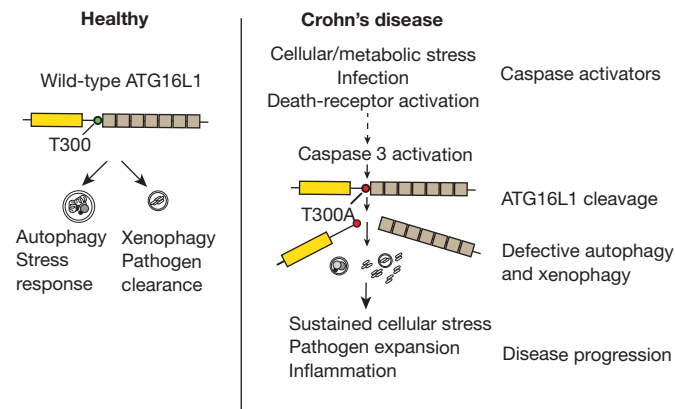


**Figure 6 | Mechanism of T300A variant contribution to Crohn's disease pathogenesis.** An inflamed intestinal environment induces cellular stress and caspase activation, thereby enhancing caspase-3-mediated cleavage of the T300A variant of ATG16L1. This results in defective stress-induced autophagy and bacterial clearance by xenophagy, establishing a chronic inflammatory state.

Sigma) or 2.0  $\mu$ M staurosporine to induce ATG16L1 processing. Full-length and cleavage products were visualized by immunoblotting.

**Nutrient starvation assays.** All cells were cultured for 4 hours in glucose-deficient DMEM + GlutaMAX without serum (glucose starvation), or in amino-acid deficient RPMI without GlutaMAX or serum (amino acid starvation). Bafilomycin A1 was added at 400 nM where indicated (Sigma).

**Bacterial protection assay.** *Yersinia* spp. *enterocolitica* (ATCC 27729) grown at 25 °C was added at an m.o.i. of 20 and cells were spin-infected at ~300g for 10 min. After further incubation for 30 min, cells were washed in macrophage culture media containing 100  $\mu$ g ml<sup>-1</sup> gentamycin (Gibco). Cells were lysed in 0.1% TX-100 + PBS and plated for colony formation.

**In vivo Y. enterocolitica studies.** Mice were fasted overnight before infection.  $2 \times 10^7$  colony forming units (c.f.u.) *Y. enterocolitica* was administered directly from frozen stock by oral gavage. c.f.u. in mesenteric lymph nodes were analysed 48 h after infection. For cytokine analysis, bacteria was grown overnight at 25 °C on tryptic soy agar with sheep blood, and  $2 \times 10^9$  c.f.u. bacteria was administered.

**Online Content** Any additional Methods, Extended Data display items and Source Data are available in the online version of the paper; references unique to these sections appear only in the online paper.

Received 30 August 2013; accepted 17 January 2014.

Published online 19 February 2014.

- Manolio, T. A. Bringing genome-wide association findings into clinical use. *Nature Rev. Genet.* **14**, 549–558 (2013).
- Adolph, T. E. et al. Paneth cells as a site of origin for intestinal inflammation. *Nature* **503**, 272–276 (2013).
- Abraham, C. & Cho, J. H. Inflammatory bowel disease. *N. Engl. J. Med.* **361**, 2066–2078 (2009).
- Gardet, A. & Xavier, R. J. Common alleles that influence autophagy and the risk for inflammatory bowel disease. *Curr. Opin. Immunol.* **24**, 522–529 (2012).
- Kaser, A. et al. XBP1 links ER stress to intestinal inflammation and confers genetic risk for human inflammatory bowel disease. *Cell* **134**, 743–756 (2008).
- He, C. & Klionsky, D. J. Regulation mechanisms and signaling pathways of autophagy. *Annu. Rev. Genet.* **43**, 67–93 (2009).
- Baxt, L. A., Garza-Mayers, A. C. & Goldberg, M. B. Bacterial subversion of host innate immune pathways. *Science* **340**, 697–701 (2013).
- Hampe, J. et al. A genome-wide association scan of nonsynonymous SNPs identifies a susceptibility variant for Crohn disease in ATG16L1. *Nature Genet.* **39**, 207–211 (2007).
- Saitoh, T. et al. Loss of the autophagy protein Atg16L1 enhances endotoxin-induced IL-1 $\beta$  production. *Nature* **456**, 264–268 (2008).
- Cadwell, K. et al. A key role for autophagy and the autophagy gene *Atg16l1* in mouse and human intestinal Paneth cells. *Nature* **456**, 259–263 (2008).
- Cadwell, K. et al. Virus-plus-susceptibility gene interaction determines Crohn's disease gene *Atg16L1* phenotypes in intestine. *Cell* **141**, 1135–1145 (2010).
- Cooney, R. et al. NOD2 stimulation induces autophagy in dendritic cells influencing bacterial handling and antigen presentation. *Nature Med.* **16**, 90–97 (2010).
- Fujita, N. et al. Differential involvement of Atg16L1 in Crohn disease and canonical autophagy: analysis of the organization of the Atg16L1 complex in fibroblasts. *J. Biol. Chem.* **284**, 32602–32609 (2009).
- Messer, J. S. et al. The Crohn's disease associated ATG16L1 variant and *Salmonella* invasion. *BMJ Open* **3**, e002790 (2013).
- Sorbara, M. T. et al. The protein ATG16L1 suppresses inflammatory cytokines induced by the intracellular sensors Nod1 and Nod2 in an autophagy-independent manner. *Immunity* **39**, 858–873 (2013).
- Conway, K. L. et al. Atg16l1 is required for autophagy in intestinal epithelial cells and protection of mice from *Salmonella* infection. *Gastroenterology* **145**, 1347–1357 (2013).
- Stennicke, H. R., Renatus, M., Meldal, M. & Salvesen, G. S. Internally quenched fluorescent peptide substrates disclose the substrate preferences of human caspases 1, 3, 6, 7 and 8. *Biochem. J.* **350**, 563–568 (2000).
- Rawlings, N. D., Barrett, A. J. & Bateman, A. MEROPS: the database of proteolytic enzymes, their substrates and inhibitors. *Nucleic Acids Res.* **40**, D343–D350 (2012).
- McStay, G. P., Salvesen, G. S. & Green, D. R. Overlapping cleavage motif selectivity of caspases: implications for analysis of apoptotic pathways. *Cell Death Differ.* **15**, 322–331 (2008).
- Jost, P. J. et al. XIAP discriminates between type I and type II FAS-induced apoptosis. *Nature* **460**, 1035–1039 (2009).
- McAlpine, F., Williamson, L. E., Toze, S. A. & Chan, E. Y. Regulation of nutrient-sensitive autophagy by uncoordinated 51-like kinases 1 and 2. *Autophagy* **9**, 361–373 (2013).
- Mizushima, N., Yoshimori, T. & Levine, B. Methods in mammalian autophagy research. *Cell* **140**, 313–326 (2010).
- Klionsky, D. J. et al. Guidelines for the use and interpretation of assays for monitoring autophagy. *Autophagy* **8**, 445–544 (2012).
- Bialik, S. et al. The mitochondrial apoptotic pathway is activated by serum and glucose deprivation in cardiac myocytes. *Circ. Res.* **85**, 403–414 (1999).
- Caro-Maldonado, A. et al. Glucose deprivation induces an atypical form of apoptosis mediated by caspase-8 in Bax-, Bak-deficient cells. *Cell Death Differ.* **17**, 1335–1344 (2010).
- Altman, B. J. & Rathmell, J. C. Metabolic stress in autophagy and cell death pathways. *Cold Spring Harb. Perspect. Biol.* **4**, a008763 (2012).
- Kuballa, P., Huett, A., Rioux, J. D., Daly, M. J. & Xavier, R. J. Impaired autophagy of an intracellular pathogen induced by a Crohn's disease associated ATG16L1 variant. *PLoS ONE* **3**, e3391 (2008).
- Altshuler, D. M. et al. Integrating common and rare genetic variation in diverse human populations. *Nature* **467**, 52–58 (2010).
- Mizushima, N., Levine, B., Cuervo, A. M. & Klionsky, D. J. Autophagy fights disease through cellular self-digestion. *Nature* **451**, 1069–1075 (2008).
- Choi, A. M., Ryter, S. W. & Levine, B. Autophagy in human health and disease. *N. Engl. J. Med.* **368**, 651–662 (2013).
- Jostins, L. et al. Host-microbe interactions have shaped the genetic architecture of inflammatory bowel disease. *Nature* **491**, 119–124 (2012).
- Brown, E. M., Sadarangani, M. & Finlay, B. B. The role of the immune system in governing host-microbe interactions in the intestine. *Nature Immunol.* **14**, 660–667 (2013).
- Grassl, G. A., Valdez, Y., Bergstrom, K. S., Vallance, B. A. & Finlay, B. B. Chronic enteric *Salmonella* infection in mice leads to severe and persistent intestinal fibrosis. *Gastroenterology* **134**, 768–780 (2008).
- Dube, P. H., Revell, P. A., Chaplin, D. D., Lorenz, R. G. & Miller, V. L. A role for IL-1 $\alpha$  in inducing pathologic inflammation during bacterial infection. *Proc. Natl Acad. Sci. USA* **98**, 10880–10885 (2001).
- Prescott, N. J. et al. A nonsynonymous SNP in ATG16L1 predisposes to ileal Crohn's disease and is independent of CARD15 and IBD5. *Gastroenterology* **132**, 1665–1671 (2007).
- Mills, S. D. et al. *Yersinia enterocolitica* induces apoptosis in macrophages by a process requiring functional type III secretion and translocation mechanisms and involving YopP, presumably acting as an effector protein. *Proc. Natl Acad. Sci. USA* **94**, 12638–12643 (1997).
- Erfurth, S. E. et al. *Yersinia enterocolitica* induces apoptosis and inhibits surface molecule expression and cytokine production in murine dendritic cells. *Infect. Immun.* **72**, 7045–7054 (2004).
- Denecker, G. et al. *Yersinia enterocolitica* YopP-induced apoptosis of macrophages involves the apoptotic signaling cascade upstream of bid. *J. Biol. Chem.* **276**, 19706–19714 (2001).
- Nakahira, K. et al. Autophagy proteins regulate innate immune responses by inhibiting the release of mitochondrial DNA mediated by the NALP3 inflammasome. *Nature Immunol.* **12**, 222–230 (2011).
- Shi, C. S. et al. Activation of autophagy by inflammatory signals limits IL-1 $\beta$  production by targeting ubiquitinated inflammasomes for destruction. *Nature Immunol.* **13**, 255–263 (2012).
- Marchiando, A. M. et al. A deficiency in the autophagy gene *Atg16L1* enhances resistance to enteric bacterial infection. *Cell Host Microbe* **14**, 216–224 (2013).
- Clausen, B. E., Burkhardt, C., Reith, W., Renkawitz, R. & Forster, I. Conditional gene targeting in macrophages and granulocytes using LysMcre mice. *Transgenic Res.* **8**, 265–277 (1999).
- Kuida, K. et al. Decreased apoptosis in the brain and premature lethality in CPP32-deficient mice. *Nature* **384**, 368–372 (1996).

**Supplementary Information** is available in the online version of the paper.

**Acknowledgements** The authors would like to thank M. Zepeda for coordinating human donors, R. A. Flavell for providing Casp3-knockout mice, J. E. Cupp, W. Ortmann, J. Borneo, J. Ruan, J. Ting and L. Rangell for technical assistance, D. Holmes, N. Kayagaki, C. J. Spooner, M. E. Keir, A. Ashkenazi and T. W. Behrens for critical evaluation of the manuscript.

**Author Contributions** A.M. and M.v.L.C. conceptualized the study and designed experiments; A.M. and Y.L. conducted experiments; I.P. and J.D. performed *in vivo* administration of *Y. enterocolitica*; M.R. and A.K.K. performed electron microscopy; R.N. performed <sup>35</sup>S pulse-chase assays on ATG16L1; M.R.-G. designed the T316A knock-in construct and coordinated generation of the mutant mouse; L.D. performed histological analysis; R.R.G. provided EBV-transformed cells, guided HapMap analysis and discussed the study; A.M. and M.v.L.C. wrote the manuscript.

**Author Information** Reprints and permissions information is available at [www.nature.com/reprints](http://www.nature.com/reprints). The authors declare competing financial interests: details are available in the online version of the paper. Readers are welcome to comment on the online version of the paper. Correspondence and requests for materials should be addressed to M.v.L.C. ([menno@gene.com](mailto:menno@gene.com)).

# A single low-energy, iron-poor supernova as the source of metals in the star SMSS J031300.36–670839.3

S. C. Keller<sup>1</sup>, M. S. Bessell<sup>1</sup>, A. Frebel<sup>2</sup>, A. R. Casey<sup>1</sup>, M. Asplund<sup>1</sup>, H. R. Jacobson<sup>2</sup>, K. Lind<sup>3</sup>, J. E. Norris<sup>1</sup>, D. Yong<sup>1</sup>, A. Heger<sup>4</sup>, Z. Magic<sup>1,5</sup>, G. S. Da Costa<sup>1</sup>, B. P. Schmidt<sup>1</sup> & P. Tisserand<sup>1</sup>

The element abundance ratios of four low-mass stars with extremely low metallicities (abundances of elements heavier than helium) indicate that the gas out of which the stars formed was enriched in each case by at most a few—and potentially only one—low-energy supernova<sup>1–4</sup>. Such supernovae yield large quantities of light elements such as carbon but very little iron. The dominance of low-energy supernovae seems surprising, because it had been expected that the first stars were extremely massive, and that they disintegrated in pair-instability explosions that would rapidly enrich galaxies in iron<sup>5</sup>. What has remained unclear is the yield of iron from the first supernovae, because hitherto no star has been unambiguously interpreted as encapsulating the yield of a single supernova. Here we report the optical spectrum of SMSS J031300.36–670839.3, which shows no evidence of iron (with an upper limit of  $10^{-7.1}$  times solar abundance). Based on a comparison of its abundance pattern with those of models, we conclude that the star was seeded with material from a single supernova with an original mass about 60 times that of the Sun (and that the supernova left behind a black hole). Taken together with the four previously mentioned low-metallicity stars, we conclude that low-energy supernovae were common in the early Universe, and that such supernovae yielded light-element enrichment with insignificant iron. Reduced stellar feedback both chemically and mechanically from low-energy supernovae would have enabled first-generation stars to form over an extended period. We speculate that such stars may perhaps have had an important role in the epoch of cosmic reionization and the chemical evolution of early galaxies.

Whereas the solar spectrum contains many thousands of spectral lines due to iron and other elements, the high-resolution ( $R = 28,000$ ) optical spectrum of SMSS J031300.36–670839.3 (hereafter SMSS 0313–6708) is remarkable for the complete absence of detectable iron lines. Figure 1 shows a portion of the spectrum that possesses a signal-to-noise ratio ( $S/N$ ) of 100 per resolution element in the vicinity of one of the strongest iron lines (Fe I at 385.9 nm wavelength). The non-detection of iron lines places an upper limit on the iron abundance of the star,  $[Fe/H] < -7.1$ , at a  $3\sigma$  confidence level. (Here  $[A/B] = \log_{10}(N_A/N_B)_{\text{star}} - \log_{10}(N_A/N_B)_{\odot}$ , where  $N_A/N_B$  is the number ratio of atoms of elements A and B, and the subscript  $\odot$  refers to the solar value.) This upper limit is 30 times lower than the iron abundance in HE 1327–2326, which has  $[Fe/H] = -5.6$  (ref. 2), and is the most iron-deficient star previously known.

The paucity of absorption lines in the spectrum of SMSS 0313–6708 allows us to derive the abundance of only four chemical elements. The calcium abundance is determined to be  $[Ca/H] = -7.0$ . Given that existing studies have shown that  $[Ca/Fe] = +0.4$  for the majority of extremely metal-poor stars<sup>6</sup>, the  $[Ca/H]$  value that we determine would be consistent with an extraordinary low iron abundance limit. We suggest below, however, that the Ca abundance in SMSS 0313–6708

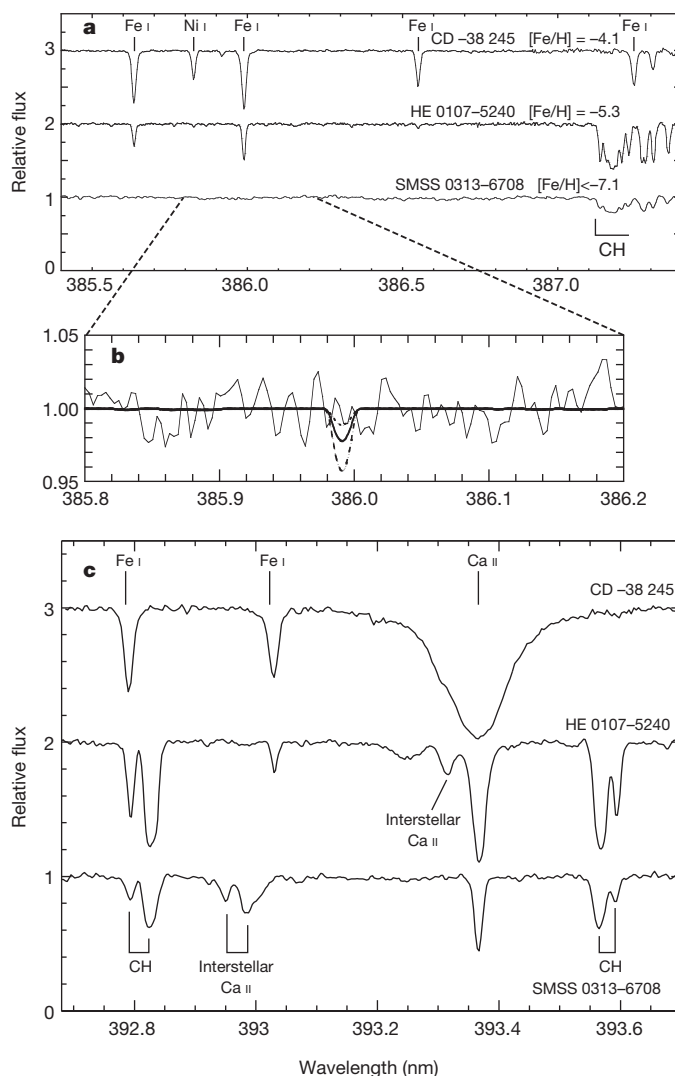


**Figure 1 | A comparison of the spectrum of SMSS 0313–6708 to that of other extremely metal-poor stars.** **a–c**, Metal-poor stars of similar temperature and surface gravity are chosen from the literature. The spectrum of SMSS 0313–6708 shows an absence of detectable Fe I lines (**a**) and is dominated by molecular features of CH (**c**). Panel **b** shows the vicinity of what should be one of the strongest iron lines in the ultraviolet/optical wavelength region. Overlaid are synthesized line profiles (1D LTE) for  $[Fe/H] = -7.5$  (dotted line),  $-7.2$  (solid line) and  $-6.9$  (long dashed line).

<sup>1</sup>Research School of Astronomy and Astrophysics, Mount Stromlo Observatory, Cotter Road, Weston, Australian Capital Territory 2611, Australia. <sup>2</sup>Department of Physics, Massachusetts Institute of Technology and Kavli Institute for Astrophysics and Space Research, Cambridge, Massachusetts 02139, USA. <sup>3</sup>Institute of Astronomy, University of Cambridge, Madingley Road, Cambridge CB3 0HA, UK. <sup>4</sup>School of Mathematical Sciences, Monash University, Victoria 3800, Australia. <sup>5</sup>Max-Planck-Institut für Astrophysik, Karl-Schwarzschild-Strasse 1, Garching 85741, Germany.



has its origin in a specific process and no coupling to the Fe abundance is expected. Magnesium ( $[\text{Mg}/\text{H}] = -3.8$ ) and carbon ( $[\text{C}/\text{H}] = -2.6$ ), however, are both highly enhanced relative to iron and calcium (see Fig. 2). Table 1 presents the details of our chemical abundance analysis procedure and derived abundances and abundance limits. Figure 3 presents the abundance pattern of SMSS 0313–6708.

For the most iron-poor stars, the degree of chemical diversity increases with decreasing metallicity<sup>6</sup>, indicative of the diversity of the few supernovae that enriched the gas before formation of these stars. Yields from supernovae with explosion energies typical of those seen in the nearby Universe are required to explain the observed abundances in stars with  $[\text{Fe}/\text{H}] > -3.5$ , except for a few elements<sup>6</sup>. For the most iron-poor stars, however, the supernovae required to explain the chemical abundances suggest unusual low-explosion-energy black-hole-forming events<sup>7</sup>.

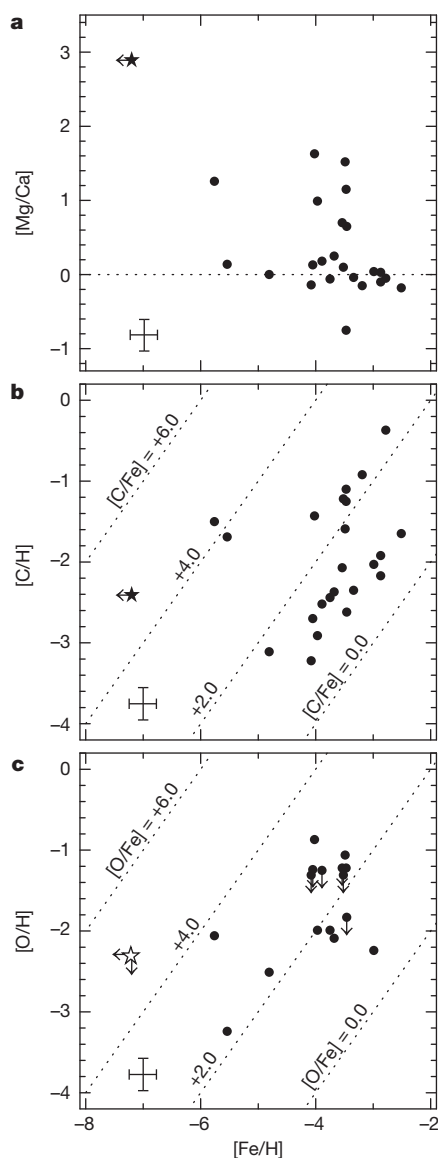


**Figure 2** | A comparison of the element abundance ratios observed in SMSS 0313–6708 with those of other extremely metal-poor stars. **a**,  $[\text{Mg}/\text{Ca}]$  as a function of  $[\text{Fe}/\text{H}]$ . The dashed line is the solar abundance ratio. **b**,  $[\text{C}/\text{H}]$  as a function of  $[\text{Fe}/\text{H}]$ , where dashed lines show lines of  $[\text{C}/\text{Fe}]$ . **c**,  $[\text{O}/\text{H}]$  against  $[\text{Fe}/\text{H}]$ . In each panel, our target is marked as a star symbol, and data from extremely metal-poor carbon-enhanced stars from ref. 23 are plotted as filled circles. Indicative 1 s.d. error bars are shown at bottom left in each panel. For consistency with the data from table 4 of ref. 23, the 1D LTE abundances for SMSS 0313–6708 are plotted.

Stochastic models of galactic chemical evolution that invoke low-explosion-energy supernovae<sup>8</sup> with a burst of formation of population III stars over the redshift range 25–17 reveal that stars such as SMSS 0313–6708 are the result of star formation in gas enriched by only one population III supernova. Whereas more iron-rich stars ( $[\text{Fe}/\text{H}] > -4.5$ ) may be interpreted as composites of supernovae yields, galactic chemical evolution models show that stars with the iron abundance of SMSS 0313–6708 follow from a single supernova event.

We have compared the abundance pattern of SMSS 0313–6708 to the nucleosynthetic yields of model population III supernovae over a range of progenitor mass, explosion energy and internal mixing<sup>9</sup>. We find that a  $1.8 \times 10^{51}$  erg explosion of a  $60 M_{\odot}$  star of primordial initial composition with a small amount of ejecta mixing due to Rayleigh–Taylor instabilities<sup>10</sup> is the optimal match to the observed abundance pattern (see Fig. 3). In this model, a central black hole is formed into which the core of the massive star is subsumed. The extensive fallback of material into the black hole traps the centrally located iron and other heavy elements synthesized during the star’s lifetime. Lighter elements, for example carbon and magnesium, residing at larger radii within the supernova progenitor are dispersed in the explosion.

The observed abundance pattern of SMSS 0313–6708 does not support supernova progenitors outside the mass range  $10\text{--}70 M_{\odot}$ . Supernovae of mass less than  $10 M_{\odot}$  release large amounts of iron, and those of greater than  $70 M_{\odot}$  do not produce the observed carbon enhancement and lead to excessive nitrogen<sup>9</sup>. In particular, pair-instability supernovae are expected to yield  $[\text{C}/\text{Fe}] \approx 0$ , rather than the  $[\text{C}/\text{Fe}] > 4.5$  observed<sup>10</sup>.

Our observations argue against a significantly non-axisymmetric supernova, such as one in which much of the explosion energy is channelled into a jet, because this would entrain and eject material from the core region. Any appreciable jet would lower  $[\text{Mg}/\text{Fe}]$  below that observed<sup>11</sup>. Furthermore, the relatively low nitrogen abundance (implied by the upper limit on that quantity), compared to carbon, suggests a slowly rotating progenitor star<sup>12</sup>.

Interestingly, the calcium released in our model of a  $60 M_{\odot}$  progenitor is not synthesized in the supernova explosion itself; rather, it is produced during the stable hydrogen-burning phase. In the metal-free progenitor, thermal equilibrium is obtained only once the core of the star attains significantly higher temperature and density compared with metal-rich stars. Under such conditions, the triple-alpha process enables the synthesis of small amounts of carbon, nitrogen and oxygen

**Table 1** | Chemical abundances of SMSS 0313–6708

Element <i>X</i>	$[\text{X}/\text{H}]_{1\text{D, LTE}}$	$[\text{X}/\text{H}]_{<3\text{D}>}$
Li I	0.7*	0.7*
C (CH)	−2.4	−2.6†
N (NH)	<−3.5	<−3.9†
O I	<−2.3	<−2.4†
Na I	<−5.5	<−5.5‡
Mg I	−4.3	−3.8‡
Al I	<−6.2	
Si I	<−4.3	
Ca II	−7.2	−7.0‡
Sc II	<−5.0	
Ti II	<−6.3	
V II	<−3.3	
Cr I	<−6.3	
Mn I	<−5.8	
Fe I	<−7.3	<−7.1‡
Co I	<−4.9	
Ni I	<−6.4	
Cu I	<−3.5	
Zn I	<−3.4	
Sr II	<−6.7	
Ba II	<−6.1	
Eu II	<−2.9	

Abundance ratios for SMSS 0313–6708 as derived from our Magellan/MIKE spectra. Typical ( $1\sigma$ ) observational uncertainties in the quoted abundances are 0.1 decades in metallicity, except in the case of C and N where 0.2 is appropriate.

\* Lithium abundance is expressed as  $A(\text{Li}) = \log_{10}(N(\text{Li})/N(\text{H}) + 12$ .

† Abundances based on  $<3\text{D}>$ , LTE calculations.

‡ Abundances based on  $<3\text{D}>$ , NLTE calculations.

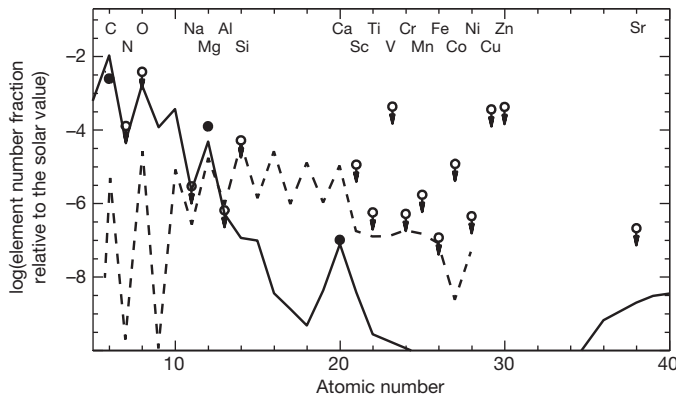


**Figure 3 | The element abundance pattern for SMSS 0313–6708 compared to model values.** Determined abundances are shown as filled symbols (observational uncertainties are smaller than the symbol size). Owing to the paucity of observable absorption lines, the majority of abundances are  $3\sigma$  upper limits (open circles). The solid line shows the abundances predicted for a  $60M_{\odot}$  population III star of relatively low explosion energy ( $1.8 \times 10^{51}$  erg) and low levels of internal mixing (see ref. 10 for details). The dashed line shows the expected yield from a  $200M_{\odot}$  supernova (with a pair-instability explosion mechanism). Such a massive progenitor leads to a [Mg/Ca] ratio that is much lower than that observed.

that subsequently catalyse the CNO energy production cycle<sup>13</sup>. Calcium production is the result of breakout from the CNO cycle<sup>14</sup>. As a consequence, we expect the calcium abundance to be decoupled from those of heavier elements in the most metal-poor stars. Such synthesis is only appreciable in initially metal-free stars where internal temperatures are sufficiently elevated.

Including SMSS 0313–6708, there are now five stars known with  $[\text{Fe}/\text{H}] < -4.5$ . The metallicity distribution function of stars reflects the integrated iron production from previous generations of supernovae. A simple model of instantaneous gas mixing<sup>15</sup> shows that the number of stars at a given low metallicity drops by a factor of ten for each factor of ten reduction in  $[\text{Fe}/\text{H}]$ . This simple model proves appropriate<sup>6</sup> for  $[\text{Fe}/\text{H}] > \sim -4$ . With the addition of SMSS 0313–6708, the five most iron-poor stars span a range in iron abundance of at least 2.5 decades in metallicity. The probability of such an observed metallicity density function arising from the simple model by chance is low ( $< 1.6\%$ ; assuming they are drawn from a completeness-corrected sample normalized to the known 30 stars with  $-4.0 < [\text{Fe}/\text{H}] < -3.5$ ). This suggests that for  $[\text{Fe}/\text{H}] < -4.5$  the assumption of instantaneous mixing of star-forming gas no longer holds.

The rate of mixing and enrichment from population III supernovae has an important effect on the epoch of reionization. Studies have highlighted that galaxies at  $z = 6-8$  do not produce sufficient ionizing photons to lead to the reionization of the intergalactic medium<sup>16</sup>. With a mass function dominated by massive stars, population III stars produce about ten times the ionizing radiation over their lifetimes compared with population II stars that constitute the observable galaxies at  $z = 6-8$ . Prodigious radiation output by population III stars at  $z \approx 20$  offers a potential resolution to the ionizing radiation shortfall.

However, simulations of the early Universe that include energetic pair-instability supernovae result in very rapid mixing of supernova ejecta, leading to the pollution of large volumes of gas with metals. This would rapidly terminate formation of population III stars, and hence population III would be extinguished before it contributed significant ionizing radiation<sup>17</sup>. On the other hand, supernovae with low explosion energy and low metal yield, which our observations reveal, would result in slow mixing and enrichment of the interstellar medium. This would enable the formation of population III stars over a protracted time, thus allowing the population to release substantial ionizing radiation that could potentially account for the apparent radiation shortfall, although we are unable to quantify this at present.

## METHODS SUMMARY

SMSS 0313–6708 is located at right ascension 03 h 13 min 00.4 s, declination  $-67^{\circ} 08' 39''$  (equinox 2000) and has an apparent visual magnitude  $V = 14.7$ . It was discovered in the continuing SkyMapper Southern Sky Survey<sup>18</sup>. Stellar parameters were determined from low-resolution spectrophotometry to be effective temperature  $T_{\text{eff}} = 5,125$ , and surface gravity  $\log g = 2.3$  (with  $g$  in cgs units; Extended Data Fig. 1). We adopt a microturbulent velocity of  $2.0 \text{ km s}^{-1}$  (the derived abundances are not sensitive to this choice). The temperature and gravity are consistent with the stellar hydrogen line profiles and the derived lithium abundance (Extended Data Fig. 2). The uncertainty in temperature is of the order of 100 K, and for surface gravity it is 0.2. Two model atmospheres are considered as the basis for abundance analysis; a Castelli–Kurucz one-dimensional hydrostatic model<sup>19</sup>, and a spatially and temporally averaged three-dimensional hydrodynamical model from the Stagger grid<sup>20</sup> which we denote  $<3D>$ . Corrections for departures from local thermodynamic equilibrium (NLTE) are computed for the  $<3D>$  model following ref. 21. The abundances of Li, C and upper limits for N and O have been derived from spectrum synthesis of the lithium 670.7 nm doublet, the carbon G-band, an NH band (336.0 nm), and [O I] at 630 nm, respectively. Apart from the molecular features due to CH, only one Ca II (393 nm), one Li I (671 nm), and five Mg I (382.9, 383.2, 383.8, 517.2 and 518.4 nm) lines are detectable in our high S/N spectrum. Solar abundances for elements are from ref. 22. The upper limit to the iron abundance in the star (Fig. 1 and Extended Data Fig. 3) was determined through Markov Chain Monte Carlo analysis of addition of the strongest iron lines.

**Online Content** Any additional Methods, Extended Data display items and Source Data are available in the online version of the paper; references unique to these sections appear only in the online paper.

Received 9 July; accepted 5 December 2013.

Published online 9 February 2014.

- Christlieb, N. *et al.* A stellar relic from the early Milky Way. *Nature* **419**, 904–906 (2002).
- Frebel, A. *et al.* Nucleosynthetic signatures of the first stars. *Nature* **434**, 871–873 (2005).
- Norris, J. E. *et al.* HE 0557–4840: ultra-metal-poor and carbon-rich. *Astrophys. J.* **670**, 774–788 (2007).
- Caffau, E. *et al.* An extremely primitive halo star. *Nature* **477**, 67–69 (2011).
- Hirano, S. *et al.* One hundred first stars: protostellar evolution and the final masses. *Astrophys. J.* (in the press); preprint at <http://arXiv.org/abs/1308.4456> (2013).
- Yong, D. *et al.* The most metal-poor stars. II. Chemical abundances of 190 metal-poor stars including 10 new stars with  $[\text{Fe}/\text{H}] < -3.5$ . *Astrophys. J.* **762**, 27 (2013).
- Umeda, H. & Nomoto, K. First-generation black-hole-forming supernovae and the metal abundance pattern of a very iron-poor star. *Nature* **422**, 871–873 (2003).
- Karlsson, T., Bromm, V. & Bland-Hawthorn, J. Pregalactic metal enrichment: the chemical signatures of the first stars. *Rev. Mod. Phys.* **85**, 809–848 (2013).
- Heger, A. & Woosley, S. E. The nucleosynthetic signature of Population III. *Astrophys. J.* **567**, 532–543 (2002).
- Joggerst, C. C., Woosley, S. E. & Heger, A. Mixing in zero- and solar-metallicity supernovae. *Astrophys. J.* **693**, 1780–1802 (2009).
- Tominaga, N. *et al.* The connection between gamma-ray bursts and extremely metal-poor stars: black hole-forming supernovae with relativistic jets. *Astrophys. J.* **657**, L77–L80 (2007).
- Ekström, S., Maeder, G., Chiappini, C., Hirschi, R. & Maeder, A. Effects of rotation on the evolution of primordial stars. *Astron. Astrophys.* **489**, 685–698 (2008).
- Ezer, D. & Cameron, A. G. W. The evolution of hydrogen-helium stars. *Astrophys. Space Sci.* **14**, 399–421 (1971).
- Wiescher, M., Gorres, J. & Schatz, H. Break-out reactions from the CNO cycles. *J. Phys. G* **25**, 133–161 (1999).
- Hartwick, F. D. A. The chemical evolution of the Galactic halo. *Astrophys. J.* **209**, 418–423 (1976).
- Robertson, B. E. *et al.* New constraints on cosmic reionization from the 2012 Hubble ultra deep field campaign. *Astrophys. J.* **768**, 71 (2013).
- Kulkarni, G., Hennawi, J. F., Rollinde, E. & Vangioni, E. Chemical constraints on the contribution of Population III stars to cosmic reionization. Preprint at <http://arXiv.org/abs/1310.0684> (2013).
- Keller, S. C. *et al.* The SkyMapper telescope and the southern sky survey. *Publ. Astron. Soc. Aust.* **24**, 1–12 (2007).
- Castelli, F. & Kurucz, R. L. New grids of ATLAS9 model atmospheres. Preprint at <http://arXiv.org/abs/astro-ph/0405087> (2004).
- Magic, Z. *et al.* The Stagger grid: a grid of 3D stellar atmosphere models. *Astron. Astrophys.* **557**, A26 (2013).
- Lind, K., Asplund, M. & Barklem, P. Departures from LTE for neutral Li in late-type stars. *Astron. Astrophys.* **503**, 541–544 (2009).
- Asplund, M., Grevesse, N., Sauval, A. J. & Scott, P. The chemical composition of the Sun. *Annu. Rev. Astron. Astrophys.* **47**, 481–522 (2009).
- Norris, J. E. *et al.* The most metal-poor stars. IV. The two populations with  $[\text{Fe}/\text{H}] < -3.0$ . *Astrophys. J.* **762**, 28 (2013).

**Acknowledgements** Australian access to the Magellan Telescopes was supported through the National Collaborative Research Infrastructure Strategy of the Australian Federal Government. M.A., M.S.B., A.R.C., G.D.C., S.K., J.E.N. and D.Y. acknowledge the

support of Australian Research Council (grants DP120101237, DP0984924, DP0878137 and LF0992131). A.F. acknowledges support from NSF grant AST-1255160. A.R.C. acknowledges support from the Australian Prime Minister's Endeavour Award Research Fellowship. K.L. acknowledges support from the European Union FP7 programme through ERC grant number 320360.

**Author Contributions** The SkyMapper telescope was developed by B.P.S., G.S.D., M.S.B., P.T. and S.C.K. The SkyMapper data reduction procedure required to provide calibrated photometry from which the star was drawn was developed by S.C.K. M.S.B. obtained the intermediate-resolution spectrum and drew the target to the team's attention. H.R.J., A.R.C., A.F. and S.C.K. obtained the high-resolution spectrum of the

target, reduced the data and performed the chemical abundance analysis using the spectral analysis package developed by A.R.C. The MCMC calculations to provide the upper limit to  $[\text{Fe}/\text{H}]$  were performed by A.R.C. K.L. performed NLTE calculations, Z.M. and M.A. constructed the  $\langle 3\text{D} \rangle$  atmosphere models, and A.H. the supernova models. B.P.S., A.H. and D.Y. contributed to supernova yields and MDF analysis. All authors discussed the results and commented on the manuscript.

**Author Information** Reprints and permissions information is available at [www.nature.com/reprints](http://www.nature.com/reprints). The authors declare no competing financial interests. Readers are welcome to comment on the online version of the paper. Correspondence and requests for materials should be addressed to S.C.K. ([stefan.keller@anu.edu.au](mailto:stefan.keller@anu.edu.au)).



## METHODS

**Discovery.** SMSS 0313–6708 is located at RA = 03 h 13 min 00.4 s, dec. =  $-67^{\circ} 08' 39''$  (equinox 2000) and has an apparent visual magnitude  $V = 14.7$ . On the basis of photometry obtained with the SkyMapper telescope<sup>18</sup> on 2 October 2012, the star was predicted to be of particularly low metallicity. The SkyMapper telescope utilizes a novel filter set that places tight constraints on the fundamental properties of the stars surveyed, namely effective temperature, surface gravity and stellar metallicity.

**Abundance analysis.** Two model atmospheres are considered as the basis for abundance analysis; a Castelli–Kurucz 1D hydrostatic model<sup>19</sup>, and a spatially and temporally averaged 3D hydrodynamical model from the Stagger grid<sup>20</sup> which we denote <3D>. Corrections for departures from local thermodynamic equilibrium (NLTE) are computed for the <3D> model following ref. 21. The abundances of Li and C and upper limits for N and O have been derived from spectrum synthesis of the lithium 670.7 nm doublet, carbon G-band, NH band (336.0 nm), and [O I] at 630 nm, respectively. Apart from the molecular features due to CH, only one Ca II (393 nm), one Li I (671 nm) and 5 Mg I (382.9, 383.2, 383.8, 517.2 and 518.4 nm) lines are detectable in our high S/N spectrum. Solar abundances for elements are from ref. 22. Observational uncertainties in the derived abundances (Table 1) are 0.1 decades in metallicity. The local S/N ratio in the observed spectrum governs the uncertainty. In the case of upper limits to abundance, these were determined by matching synthesized spectra to the local average minima in the vicinity of the line in question. Observational uncertainties are larger in the case of C and N ( $\sigma = 0.2$  decades in metallicity) where synthetic spectra are compared to the multiple features of molecular bands.

**Medium-resolution spectroscopy.** The star's extremely metal-poor status was confirmed through medium-resolution spectroscopy with the WiFeS spectrograph<sup>24</sup> on the ANU 2.3 m telescope on 2 January 2013.

**High-resolution spectroscopy.** We observed SMSS 0313–6708 on five different nights (namely 23–25 January and 6–7 February 2013) with the Magellan Inamori Kyocera Echelle (MIKE) spectrograph<sup>25</sup> at the 6.5 m Magellan Clay telescope, Chile. All observations were taken using a 1.0'' slit, providing a spectral resolution of  $R = 28,000$  in the blue arm and  $R = 22,000$  in the red arm. Calibration frames were taken at the start of each night, including 20 flat-field frames and 10 Th-Ar arc lamp exposures for wavelength calibration. Data reduction used the Carpy data reduction pipeline<sup>26</sup>. Each reduced echelle order was carefully normalized using a third order spline with defined knot spacing. Normalized orders were stitched together to provide a single one-dimensional spectrum from 336 to 940 nm.

**Adopted stellar parameters.** The WiFeS/ANU 2.3 m spectrum was flux calibrated by comparison with spectrophotometric standard stars as described in ref. 27. Model atmosphere fluxes in ref. 28 were then compared to those observed from SMSS 0313–6708 as described in ref. 29 to determine the best match to the spectrum. Extended Data Fig. 1 shows the result of the fit to SMSS 0313–6708. We have adopted the  $T_{\text{eff}}$  and  $\log g$  resulting from this analysis in the subsequent abundance analysis:  $T_{\text{eff}} = 5,125$  K, and surface gravity  $\log g = 2.3$  [cgs]. We adopt a microturbulent velocity of  $2.0 \text{ km s}^{-1}$  (the derived abundances are not sensitive to this choice). To confirm that the values used are appropriate, we have made a comparison between the Balmer line profiles observed and those of stars with bracketing  $T_{\text{eff}}$  and  $\log g$  observed with the same instrument and settings (seen in Extended Data Fig. 2 a, b). The uncertainty in temperature is of the order of 100 K, and for surface gravity it is 0.2.

Lines of interstellar absorption of Ca-K and Na-D are apparent in the spectrum. We determine the equivalent width of the Na-D1 line to be 10.9 pm. The relation between equivalent width and interstellar reddening from ref. 30 provides  $E(B - V) = 0.04 \pm 0.01$  which we adopt. Using the infrared flux method for the BVJHK system<sup>31</sup> (BV photometry from APASS<sup>32</sup>; JHK from 2MASS<sup>33</sup>) we derive a photometric temperature of  $T_{\text{eff}} = 5,210 \pm 64$  K. From utilization of griJHK<sup>31</sup> (gri from APASS) we determine  $T_{\text{eff}} = 5,265 \pm 76$  K. These values and those determined through spectrophotometric analysis are in concordance.

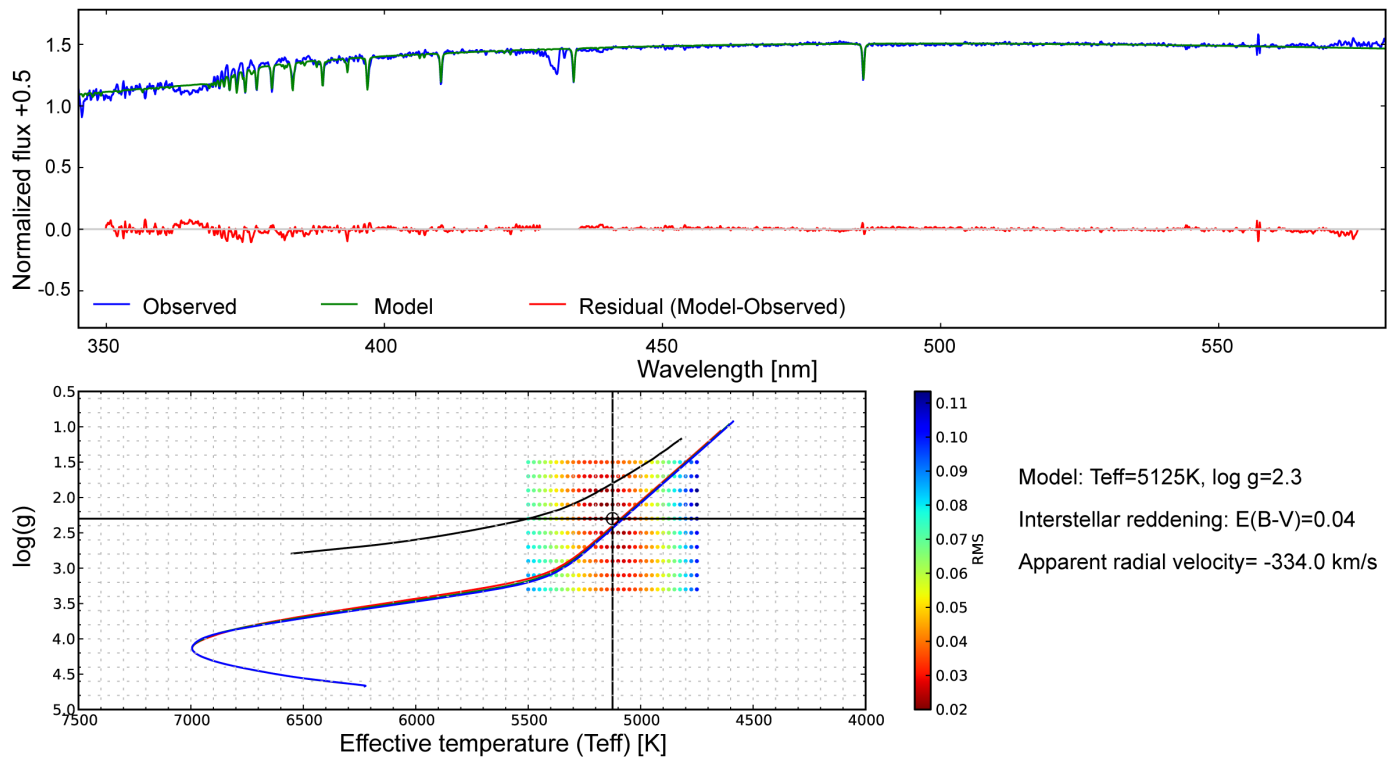
**Lithium.** Lithium is detected in the star at a level  $A(\text{Li}) = \log_{10}(N(\text{Li}))/N(\text{H}) + 12 = 0.7$  that displays significant depletion from the primordial Big Bang level ( $A(\text{Li}) = 2.72$ )<sup>34</sup>. Such lithium depletion is expected within a metal-poor first ascent red giant branch star<sup>21</sup> due to cycling of material in regions of high temperature where lithium is destroyed and subsequent dilution in an extensive convective

envelope. This evolutionary status is in line with the adopted  $\log g$  for SMSS 0313–6708.

**Derivation of upper limit on iron abundance.** An upper limit to the iron content has been calculated from a Markov Chain Monte Carlo analysis. The emcee package<sup>35</sup> was used, which is a Python (<http://www.python.org>) implementation of an affine-invariant ensemble sampler<sup>36</sup>. Walkers (200) were used to explore the parameter space and maximize the log-likelihood. The likelihood function computes synthetic spectra using the MOOG code<sup>37</sup> and a 1D model atmosphere<sup>19</sup> for SMSS 0313–6708 ( $T_{\text{eff}} = 5,125$  K,  $\log g = 2.3$ ,  $[\text{Fe}/\text{H}] = -5$ , microturbulent velocity  $v_t = 2 \text{ km s}^{-1}$ ) and compares it to portions of the normalized observed spectrum. The spectral regions surrounding the Fe lines at 385.9 nm and 371.9 nm were synthesized for different Fe abundances, smoothed with a Gaussian kernel (FWHM =  $9.6 \text{ km s}^{-1}$ ) to match the observations, and shifted to zero wavelength before being stacked. With logarithmic oscillator strengths of  $-0.431$  and  $-0.710$  respectively, these excitation potential  $\chi_{\text{exc}} = 0.0$  eV transitions are the strongest Fe absorption lines available from our near-ultraviolet to infrared spectrum. The observed spectrum surrounding these Fe lines is similarly stacked with uncertainties added in quadrature based on the S/N of individual spectra, allowing for the  $\chi^2$  difference between the model and observed spectra to be calculated. This model includes five free parameters: noise jitter, a constant scaling value for the stacked normalized spectrum, a residual velocity offset for each absorption line, and Fe/H. Using linear metallicity as a parameter (instead of logarithmic metallicity  $[\text{Fe}/\text{H}]$ ) allows for both positive and approximate negative (that is, emission spectra) column depths.

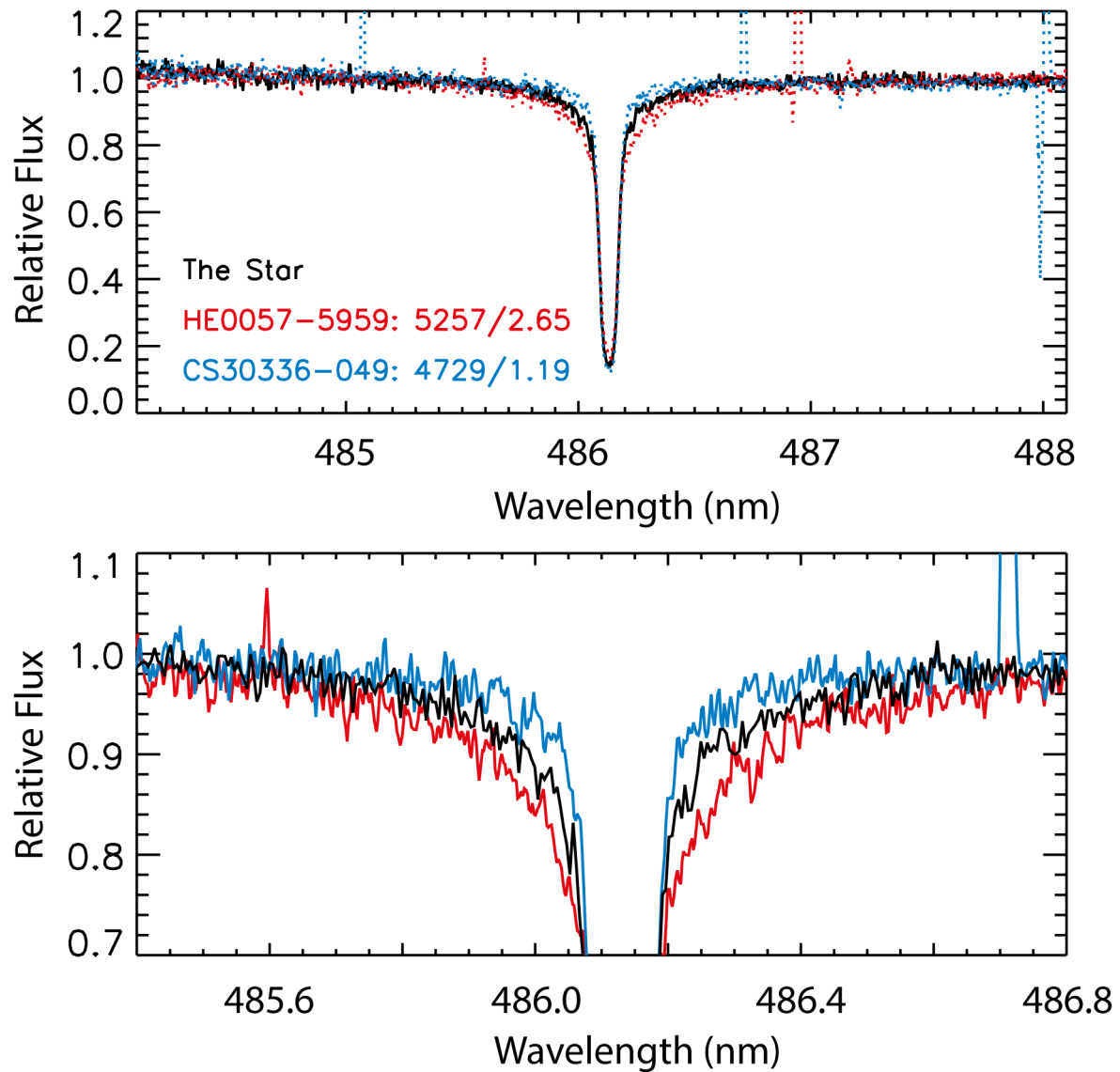
A uniform prior between  $[0, 1]$  was used for the noise jitter, and a uniformly distributed linear prior between  $[\text{Fe}/\text{H}] = -5.5$  to  $-4.5$  was adopted for metallicity. As the observed spectra is already at rest-frame and the laboratory wavelengths of these transitions are very well known, the velocity offset for each transition was treated as a Gaussian prior with mean = 0 and s.d. =  $0.5 \text{ km s}^{-1}$ . The continuum scaling factor prior was also treated as a Gaussian distribution, with mean = 1, s.d. = 0.02. After 600 walker steps, an asymptotically-approaching mean acceptance fraction of 0.369 and a minimum reduced  $\chi^2$  of 1.49 was observed. The resultant 67.8%, 95% and 99.7% upper limits for  $[\text{Fe}/\text{H}]_{\text{ID,LTE}}$  are  $<-7.7$ ,  $<-7.5$  and  $<-7.3$ . This is demonstrated in Extended Data Fig. 3, where stacked synthetic spectra for each metallicity is overlaid upon the stacked observed spectrum for the Fe lines used. After corrections for 3D and non-LTE effects, the 99.7% upper limit becomes  $[\text{Fe}/\text{H}]_{\text{3D,NLTE}} = <-7.1$ .

24. Dopita, M. A. *et al.* The wide field spectrograph (WiFeS): performance and data reduction. *Astrophys. Space Sci.* **327**, 245–257 (2010).
25. Bernstein, R., Shectman, S. A., Gunnels, S. M., Mochnacki, S. & Athey, A. E. MIKE: A Double Echelle Spectrograph for the Magellan Telescopes at Las Campanas Observatory. *SPIE Conf. Ser.* **4841**, 1694–1704 (2003).
26. Carnegie Observatories Software Repository. MIKE pipeline <http://code.obs.carnegiescience.edu/mike> (2012).
27. Bessell, M. S. Measuring the Balmer Jump and the effective gravity in FGK stars. *Publ. Astron. Soc. Pacif.* **119**, 605–615 (2007).
28. Gustafsson, B. *et al.* A grid of MARCS model atmospheres for late-type stars. I. methods and general properties. *Astron. Astrophys.* **486**, 951–970 (2008).
29. Norris, J. E. *et al.* The most metal-poor stars. IV. The two populations with  $[\text{Fe}/\text{H}] < -3.0$ . *Astrophys. J.* **762**, 28 (2013).
30. Munari, U. & Zwitter, T. Equivalent width of Na I and K I lines and reddening. *Astron. Astrophys.* **318**, 269–274 (1997).
31. Casagrande, L., Ramirez, I., Melendez, J., Bessell, M. & Asplund, M. An absolutely calibrated  $T_{\text{eff}}$  scale from the infrared flux method. Dwarfs and subgiants. *Astron. Astrophys.* **512**, A54–A64 (2010).
32. Henden, A. A. *et al.* The AAVSO Photometric All-Sky Survey DR7 <http://www.aavso.org/apass> (2013).
33. Skrutskie, M. F. *et al.* The Two Micron All Sky Survey (2MASS). *Astron. J.* **131**, 1163–1183 (2006).
34. Coc, A., Gorioli, S., Xu, Y., Saimpert, M. & Vangioni, E. Standard Big Bang nucleosynthesis up to CNO with an improved extended nuclear network. *Astrophys. J.* **744**, 158 (2012).
35. Foreman-Mackey, D., Hogg, D. W., Lang, D. & Goodman, J. emcee: The MCMC hammer. *Publ. Astron. Soc. Pacif.* **125**, 306–312 (2013).
36. Goodman, J. & Weare, J. Ensemble samplers with affine invariance. *Commun. Appl. Math. Comput. Sci.* **5**, 65–80 (2010).
37. Sneden, C. <http://www.as.utexas.edu/~chris/moog.html> (2013).



**Extended Data Figure 1 | The summary of spectrophotometric analysis of SMSS 0313–6708.** In the top frame, the blue line shows the observed spectrum and the green line is the best-fitting model spectrum. The red line beneath shows the residual spectrum. In the lower frame, the cross-hair marks

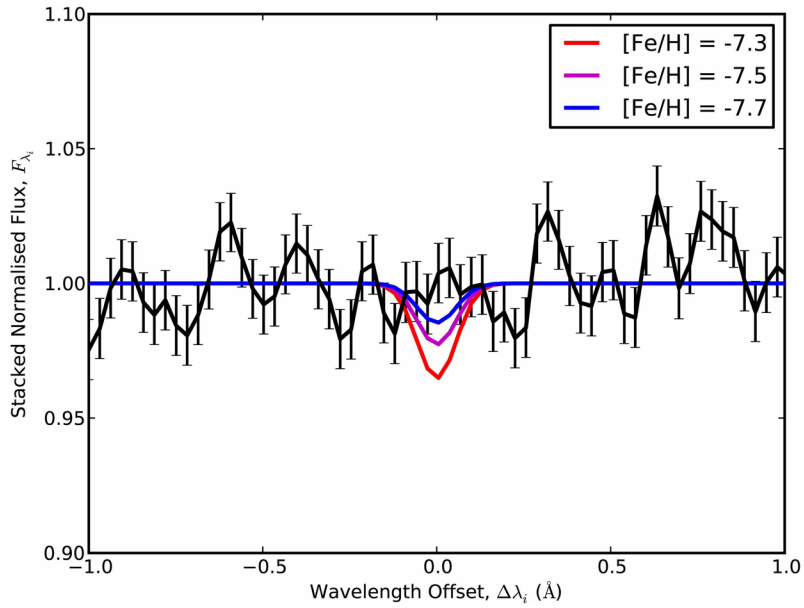
the location of the best-fitting  $T_{\text{eff}}$  and  $\log g$  and the r.m.s. values of the fit are represented in colour for a subgrid. Halo isochrones are shown to assist in the selection of the most likely parameters. The interstellar reddening is found to be  $E(B - V) = 0.04$ .



**Extended Data Figure 2 | The comparison of the H $\beta$  Balmer line profile of SMSS 0313–6708 to stars of bracketing stellar parameters reported in the literature.** We use this comparison as a qualitative verification of the stellar parameters for SMSS 0313–6708 determined from spectrophotometric analysis. Literature values for  $T_{\text{eff}}$  and  $\log g$  respectively are stated in the top

panel adjacent to the star identifier. The top panel shows a comparison of the intensity in the vicinity of the H $\beta$  Balmer line for SMSS 0313–6708 (black line), HE 0057–5959 (red line) and CS 30336–049 (blue line). The bottom panel is an enhanced zoom to show the line profile wings.





**Extended Data Figure 3 | Determination of upper limits to the iron abundance.** The black line with associated uncertainties (error bars, s.d.) is the observed spectrum stacked in the vicinity of the strongest iron lines. The coloured lines show 67.8% (blue), 95% (magenta) and 99.7% (red) confidence

upper limits for  $[\text{Fe}/\text{H}]_{\text{ID,NLTE}}$ . The vertical axis is the normalized spectral intensity formed from the addition of regions of spectrum centred on strong iron lines ( $2 \text{ \AA}$  wide). The horizontal axis is the wavelength shifted such that each iron line lies at the origin.

# High-precision measurement of the atomic mass of the electron

S. Sturm<sup>1</sup>, F. Köhler<sup>1,2</sup>, J. Zatorski<sup>1</sup>, A. Wagner<sup>1</sup>, Z. Harman<sup>1,3</sup>, G. Werth<sup>4</sup>, W. Quint<sup>2</sup>, C. H. Keitel<sup>1</sup> & K. Blaum<sup>1</sup>

The quest for the value of the electron's atomic mass has been the subject of continuing efforts over the past few decades<sup>1–4</sup>. Among the seemingly fundamental constants that parameterize the Standard Model of physics<sup>5</sup> and which are thus responsible for its predictive power, the electron mass  $m_e$  is prominent, being responsible for the structure and properties of atoms and molecules. It is closely linked to other fundamental constants, such as the Rydberg constant  $R_\infty$  and the fine-structure constant  $\alpha$  (ref. 6). However, the low mass of the electron considerably complicates its precise determination. Here we combine a very precise measurement of the magnetic moment of a single electron bound to a carbon nucleus with a state-of-the-art calculation in the framework of bound-state quantum electrodynamics. The precision of the resulting value for the atomic mass of the electron surpasses the current literature value of the Committee on Data for Science and Technology (CODATA<sup>6</sup>) by a factor of 13. This result lays the foundation for future fundamental physics experiments<sup>7,8</sup> and precision tests of the Standard Model<sup>9–11</sup>.

Over the past few decades, the atomic mass of the electron has been determined using several Penning-trap experiments, because exploration of the scope of validity of the Standard Model requires an exceedingly precise knowledge of  $m_e$ . The uniform magnetic field of these traps makes it possible to compare the cyclotron frequency of the electron with that of another ion of known atomic mass, typically carbon ions or protons. The first such direct determination dates back to 1980, when Gräff *et al.* made use of a Penning trap to compare the cyclotron frequencies of a cloud of electrons with that of protons, which were alternately confined in the same magnetic field, yielding a relative precision of about 0.2 parts per million (ref. 2). Since then, a number of experiments have improved the precision by about three orders of magnitude<sup>1,4,12,13</sup>. The latest version of the CODATA compilation of fundamental constants of 2010 lists a relative uncertainty of  $4 \times 10^{-10}$ , resulting from the weighted average of the most precise measurements. Given that the cyclotron frequency of the extremely light electron is subject to troublesome relativistic mass shifts if not held at the lowest possible energy, direct ultrahigh precision mass measurements are particularly delicate. To circumvent this problem, the currently most precise measurements, including this work, pursue an indirect method that allows a previously unprecedented accuracy to be achieved.

A single electron is bound directly to the reference ion, in this case a bare carbon nucleus (Fig. 1). In this way, it becomes possible to calibrate the magnetic field  $B$  at the very place of the electron through a measurement of the cyclotron frequency

$$\nu_{\text{cyc}} = \frac{1}{2\pi} \frac{q}{m_{\text{ion}}} B \quad (1)$$

of the heavy-ion system with mass  $m_{\text{ion}}$  and charge  $q$ . The cyclotron frequency of the strongly bound electron is of no further relevance, but the precession frequency of the electron spin, which depends on the electron's magnetic moment  $\mu_e$  as follows

$$\nu_L = \frac{2\mu_e B}{h} = \frac{g}{4\pi} \frac{e}{m_e} B \quad (2)$$

is well defined and reveals information about the mass of the electron  $m_e$ . A measurement of the ratio of these two frequencies yields  $m_e$  in units of the ion's mass

$$m_e = \frac{g}{2} \frac{e}{q} \frac{\nu_{\text{cyc}}}{\nu_L} m_{\text{ion}} \equiv \frac{g}{2} \frac{e}{q} \frac{1}{\Gamma} m_{\text{ion}} \quad (3)$$

where  $\Gamma$  denotes the experimentally determined ratio  $\nu_L/\nu_{\text{cyc}}$ . When determining  $\Gamma$  of a hydrogen-like carbon ion, which is the defining particle for the atomic mass (apart from the mass and binding energies of the missing electrons, which are sufficiently well known), the remaining unknown in equation (3) is the  $g$ -factor. Advances in quantum electrodynamics (QED) theory in recent years allow us to calculate this value with the highest precision<sup>14</sup>.

Here we present an ultra-precise measurement of the frequency ratio and a state-of-the-art QED calculation for the case of hydrogen-like  $^{12}\text{C}^{5+}$ , which allows us to determine  $m_e$  with unprecedented accuracy. Exposing the electron to the binding Coulomb field of an atomic nucleus has a profound influence on the  $g$ -factor. The largest difference from the free-electron case can be deduced from a solution of the Dirac equation in the presence of the Coulomb potential of a nucleus of charge  $Z$  and an external, constant and homogeneous magnetic field:  $g_{\text{Dirac}} = \frac{2}{3} + \frac{4}{3} \sqrt{1 - (Z\alpha)^2}$  (ref. 15). This result must be complemented by various other effects, originating mainly from QED (see Fig. 2). Many of those effects, like the one-loop self-energy and vacuum polarization terms, and the nuclear recoil contribution, are known with sufficient numerical accuracy<sup>14,16,17</sup>. The main challenge in further improving the theoretical predictions is related to the two-loop QED effect. This contribution is known only to the first few terms of its expansion in terms of  $(Z\alpha)^n [\ln(Z\alpha)^{-2}]^k$ . The calculation of the expansion coefficients with  $n \geq 5$  is beyond the current state of the art, defining the overall theoretical uncertainty. However, we have been able to estimate the uncalculated higher-order contribution  $g_{2L}^{\text{higher-order}}$  and thus improve on the theoretical value with the help of our recent experimental value  $g_{\text{exp}}^{\text{Si}}$  of the  $g$ -factor of hydrogen-like silicon ( $Z = 14$ )<sup>18,19</sup>. This contribution, which dominates the theoretical uncertainty, can be determined from the difference of the experimentally determined  $g$ -factor and the theoretical prediction, which is the sum of all known terms excluding  $g_{2L}^{\text{higher-order}}$

$$g_{2L}^{\text{higher-order}}(Z = 14) = g_{\text{exp}}^{\text{Si}} - g_{\text{theory}}^{\text{Si}} = 2 \frac{\nu_L}{\nu_{\text{cyc}}} \frac{m_e}{m_{\text{ion}}} 13 - g_{\text{theory}}^{\text{Si}} \quad (4)$$

We assume an analytical form of the  $Z$ -dependence  $g_{2L}^{\text{higher-order}}(Z)$ , and thus obtain an estimate of  $g_{2L}^{\text{higher-order}}(Z = 6)$  for carbon, presented in Supplementary Table II. Equation (4), together with a second formula for the  $Z$  dependence on those higher-order terms (see Supplementary equation (15)), can be solved to yield more accurate values for two variables, namely, the theoretical  $g$ -factor value for

<sup>1</sup>Max-Planck-Institut für Kernphysik, Saupfercheckweg 1, 69117 Heidelberg, Germany. <sup>2</sup>GSI Helmholtzzentrum für Schwerionenforschung, Planckstraße 1, 64291 Darmstadt, Germany. <sup>3</sup>ExtreMe Matter Institute EMMI, Planckstraße 1, 64291 Darmstadt, Germany. <sup>4</sup>Institut für Physik, Johannes Gutenberg-Universität, Staudingerweg 7, 55128 Mainz, Germany.

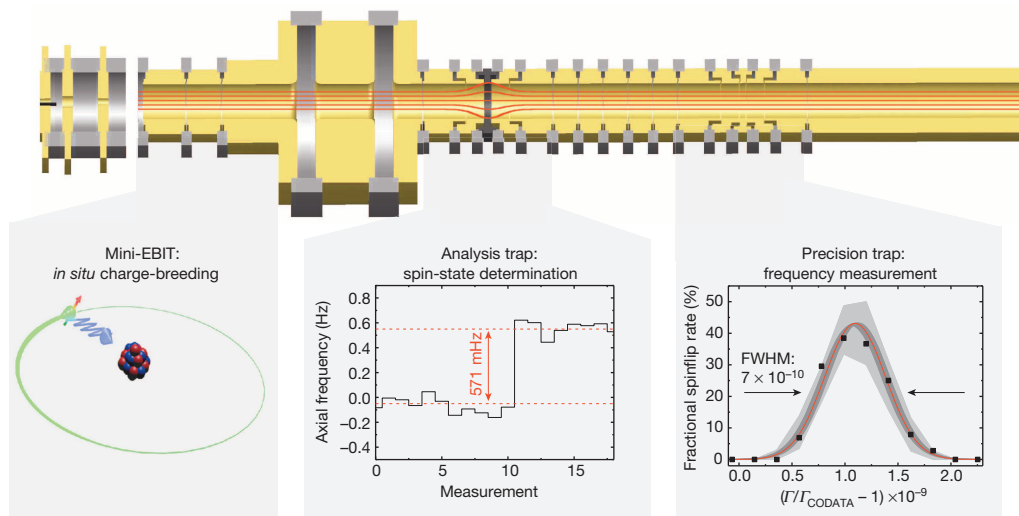


**Figure 1 | The triple Penning-trap setup used in this Letter.** Electrodes are yellow, insulation rings are grey and magnetic field lines are red (sketch). Highly charged ions can be created *in situ* inside the hermetically closed cryogenic vacuum with the miniature electron-beam ion trap (EBIT), allowing for almost infinite measurement time (lower panels). The magnetic bottle in the analysis trap, used for the spin-state detection, is spatially separated from the very homogeneous field in the precision trap, which allows precise measurements of the ion's eigenfrequencies. The lower middle panel shows one

carbon, and the electron mass. The technical details of this calculation and related uncertainty are described in the Supplementary Information.

The key tool for our measurements is the Penning trap (Fig. 1). The homogeneous magnetic field (in our case 3.7 T), which causes the precession of the spin, also forces the ion into a circular cyclotron motion and in this way confines it in the plane perpendicular to the field (the 'radial' plane). To retain the ion sufficiently long for a precision measurement, we add an electrostatic quadrupole potential, which yields a harmonic motion of the ion along the magnetic field lines ('axial') with frequency  $\nu_z$ . Simultaneously, the quadrupole generates two uncoupled harmonic eigenmotions in the radial plane: the modified cyclotron and the magnetron motion, with frequencies  $\nu_+$  and  $\nu_-$ , respectively. The trap eigenfrequencies are connected to the free-space cyclotron frequency via the invariance relation  $\nu_{\text{cyc}} = \sqrt{\nu_+^2 + \nu_z^2 + \nu_-^2}$  (ref. 20). To determine these frequencies, a superconducting tank circuit in resonance with the axial motion of the ion

serves to transform tiny currents that the ion induces by its oscillation between the trap electrodes into small yet measurable voltage signals. The interaction with the tank circuit also results in a weak damping, which brings the ion into thermal equilibrium with the resonator. Electronic noise feedback techniques allow further cooling, until the effective temperature is well below that of the environment (4.2 K), greatly reducing systematic errors. At thermal equilibrium, the ion exactly cancels the thermal noise of the tank circuit, leaving a characteristic 'dip' in the detected spectrum (Fig. 3). A fit with a well-known lineshape directly reveals the axial frequency of the ion to sufficient precision. The remaining eigenfrequencies, which do not couple to the resonator directly, must be detected via mode-coupling to the axial motion. The recent development of the 'pulse and amplify' technique<sup>21</sup> has enabled us to perform phase-sensitive measurements

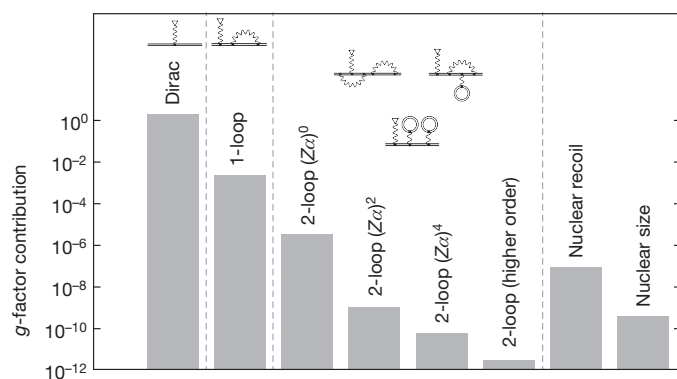


**Figure 2 | The magnitude of the relevant theoretical contributions to the bound electron  $g$ -factor in  $^{12}\text{C}^{5+}$ .** The leading Dirac contribution, one- and two-loop bound-state-QED corrections, and nuclear effects (see also the Supplementary Information). Some representative Feynman diagrams<sup>16</sup> corresponding to the QED terms are shown. 'Higher order' means corrections higher than order 4 in powers of  $(Z\alpha)$ .

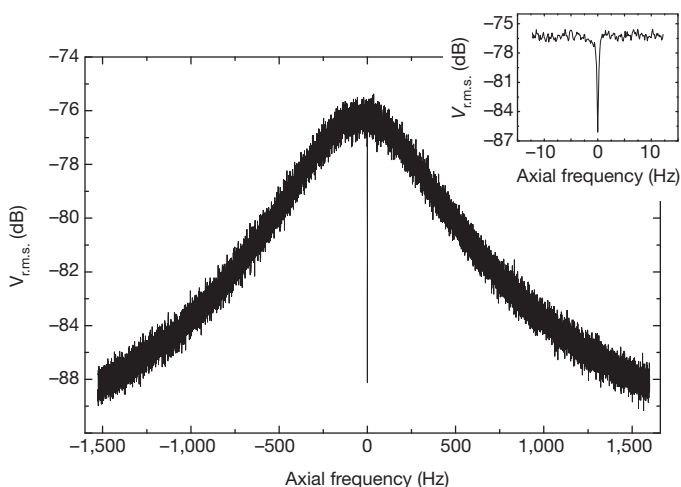


**Figure 3 | Axial dip signal of a single  $^{12}\text{C}^{5+}$  ion, used to determine the axial frequency.** The voltage-noise density of the tank circuit, detected by the cryogenic amplifier, shows the short-cut at the axial frequency of the ion. The linewidth is only about 0.4 Hz. The inset shows a close-up of the dip feature.  $V_{\text{r.m.s.}}$  root mean square voltage. The axial frequency has been offset by 670,963.26 Hz.



of the modified cyclotron frequency at very low energies below the detection threshold of the image-current amplifier, a significant improvement on the established ‘pulse and probe’ technique<sup>22</sup>. Combined with the axial and magnetron frequency information from dip fits, the invariance relation allows us to calculate the free-space cyclotron frequency, which is a measure of the magnetic field at the ion’s location.

The Larmor precession frequency, nominally 105 GHz in our case, cannot be detected directly with the image current detector. Instead, the Zeeman splitting of the bound electron’s spin is probed with a microwave excitation. The key requirement for this is the ability to detect the spin state with the continuous Stern–Gerlach effect<sup>23</sup>. To this end, a strong magnetic field inhomogeneity, is generated by an electrode made from ferromagnetic material. In our setup the quadratic portion of this bottle-shaped field amounts to  $B_2 = 10^4 \text{ T m}^{-2}$  (ref. 24). In this inhomogeneous field, the magnetic moment couples to the axial motion and causes a small, spin-dependent frequency difference. Provided all other influences on the axial frequency, notably the ion’s energy and the voltages applied to the trap, can be sufficiently well controlled, the determination of the axial frequency of the ion becomes a quantum non-demolition measurement of the electron’s spin. We use a double-trap setup to spatially separate the spin analysis in the inhomogeneous field of the ‘analysis trap’ (AT) and the high-precision eigenfrequency measurement in the ‘precision trap’ (PT) (Fig. 1). During the experiment, the ion is adiabatically shuttled between these two traps. After determining the initial spin-state in the AT, the ion is transported to the PT, where a microwave excitation at a random frequency offset with respect to the expected Larmor frequency probes the Zeeman splitting at the same time as the ‘pulse and amplify’ measurement of the cyclotron frequency is performed, which suppresses fluctuations of the magnetic field. The axial frequency, which is basically independent of the magnetic field, is measured before and after the ‘pulse and amplify’ cycle and interpolated. After transporting the ion back to the AT, an analysis of the spin state allows us to detect a possible successful spin-flip in the PT. By repeating this process (see Supplementary Fig. 1) several hundred times it becomes possible to map the probability of spin-flips in the homogeneous magnetic field of the PT as a function of the frequency ratio  $F$  (right panel of Fig. 1).

The dominant systematic uncertainty arises from the self-interaction mediated by image charges and currents in the trap electrodes (see Table 1). In contrast to the free electron case<sup>9</sup>, the retardation of the field and the resultant damping through a coupling to modes of the trap acting as a cavity is negligible owing to the very much higher cyclotron wavelength. However, instead, the influence of the immediate Coulomb interaction—that is, image charges—is enhanced. Even though the resultant shift can be readily calculated, finite machining accuracies and the imperfect knowledge of the ion’s geometric position impose a relative uncertainty of  $\delta v_{\text{cyc}}/v_{\text{cyc}} = 1.5 \times 10^{-11}$ .

The extrapolated frequency ratio  $F'_0 \cong F(E_+ = 0)$ , corrected for all systematic shifts (Table 1), yields the final value  $F_0 = 4376.21050089(11)(7)$ , with the statistical and systematic uncertainties, respectively, given in parentheses.

The theoretical prediction of the  $g$ -factor presented here (see Supplementary Table II) permits the calculation of the mass of the electron in units of the ion’s mass. By correcting for the mass of the missing electrons and their respective atomic binding energies<sup>25</sup>, we can finally calculate  $m_e$  in atomic mass units:

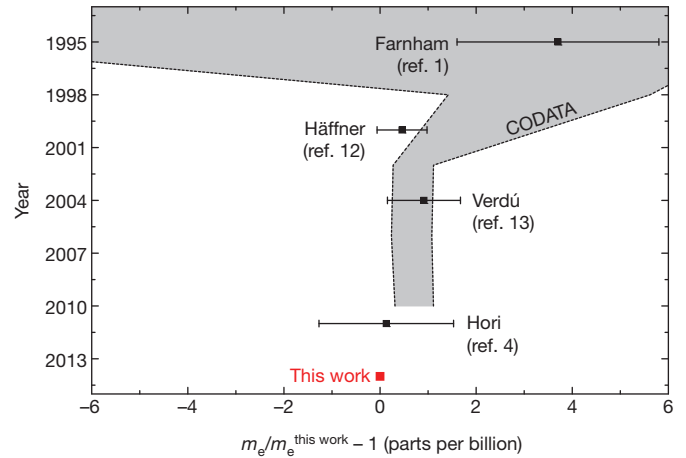


**Figure 4 | History of electron mass measurements.** The last direct cyclotron frequency determination dates back to 1995; the more recent values are all indirect determinations based on QED predictions of  $g$ -factors or transition energies<sup>1,4,12,13</sup>. The grey band is the  $1\sigma$  confidence interval of the CODATA evaluations of the respective years. Recently, a flaw in the handling of systematic shifts in one of the input values was found, suggesting a world average value about  $0.5\sigma$  smaller than the current CODATA value<sup>6</sup>. For details see the Supplementary Information. The error bar of the new value (red square) is hidden by the symbol.

$$m_e = 0.000548579909067(14)(9)(2) \quad (5)$$

The first two errors are the statistical and systematic uncertainties of the measurement, and the third error represents the uncertainties of the theoretical prediction of the  $g$ -factor and the electron binding energies. The theoretical result for the  $g$ -factor, with corrections obtained from the experimentally determined value for hydrogen-like  $^{28}\text{Si}^{13+}$  (ref. 18), implicitly assumes the correctness of QED. However, the thus-far-untested higher-order contribution determined in this work scales with  $(Z\alpha)^5$  and thus contributes less than  $10^{-11}$  in relative terms for the  $^{12}\text{C}^{5+}$  system.

The relative precision of  $3 \times 10^{-11}$  for  $m_e$  obtained in this work surpasses that of the current CODATA<sup>6</sup> averaged literature value by a factor of 13 and the previous best measurement<sup>3</sup> by a factor of 17 (see Fig. 4). Furthermore, our result gives the electron–proton mass ratio with a relative precision of 94 parts per trillion, solely limited by the uncertainty (in parentheses) of the proton mass value

$$m_p/m_e = 1836.15267377(17) \quad (6)$$

The main limitations seen in our work are the uncertainty resulting from the ion’s self-interaction with its own image-charge in the trap electrodes and the temperature of the ion in connection with the temporal stability of the magnetic field.

Our result sets the stage for future ultrahigh precision tests of the Standard Model at low energies. One example is the determination of the fine-structure constant  $\alpha$  via a measurement of the recoil momentum exerted on an atom upon absorption of a photon<sup>26</sup>. The electron atomic

**Table 1 | Relative systematic corrections and their uncertainties applied to the measured frequency ratio**

Effect	Correction (parts per trillion)	Uncertainty (parts per trillion)
Image charge	−282.4	14.1
Image current	2.2	0.5
Residual electrostatic anharmonicity	0	0.25
Axial and magnetron temperature	0.04	0.04
Ionic mass $^{12}\text{C}^{5+}$	0	0.1

The small shift due to the residual cyclotron energy is eliminated by an extrapolation of the frequency ratios measured at different energies. For details see the Supplementary Information.

mass presented in this Letter, combined with the Rydberg constant<sup>6</sup>, the atomic mass of rubidium<sup>27</sup> and an atom interferometric measurement of  $h/m_{\text{Rb}}$  (ref. 26), yields a value for  $\alpha$ . By inserting this value into the Kinoshita theory<sup>10</sup> for the  $g$ -factor of the free electron, it is possible to test the Standard Model through the Gabrielse experiment<sup>9</sup> and, among other things, to observe the unification of the electro-weak interaction at low energies and probe the existence of light dark-matter particles<sup>11</sup>. Furthermore, the new value for  $m_e$  paves the way to probing the validity of QED at much higher field strengths through  $g$ -factor determinations in heavy, highly charged ions<sup>7,8,18</sup>.

Received 5 October 2013; accepted 6 January 2014.

Published online 19 February 2014.

- Farnham, D. L., Van Dyck, R. S., Jr & Schwinberg, P. B. Determination of the electron's atomic mass and the proton/electron mass ratio. *Phys. Rev. Lett.* **75**, 3598–3601 (1995).
- Gräff, G., Kalinowsky, H. & Traut, J. A direct determination of the proton electron mass ratio. *Z. Phys. A* **297**, 35–39 (1980).
- Beier, T. *et al.* New determination of the electron's mass. *Phys. Rev. Lett.* **88**, 011603 (2001).
- Hori, M. *et al.* Two-photon laser spectroscopy of antiprotonic helium and the antiproton-to-electron mass ratio. *Nature* **475**, 484–488 (2011).
- Cottingham, W. N. & Greenwood, D. A. *An Introduction to the Standard Model of Particle Physics* (Cambridge Univ. Press, 2007).
- Mohr, P. J., Taylor, B. N. & Newell, D. B. CODATA recommended values of the fundamental physical constants: 2010. *Rev. Mod. Phys.* **84**, 1527–1605 (2012).
- Shabaev, V. M. *et al.*  $g$ -Factor of heavy ions: a new access to the fine structure constant. *Phys. Rev. Lett.* **96**, 253002 (2006).
- Shabaev, V. M. *et al.*  $g$ -Factor of high- $Z$  lithiumlike ions. *Phys. Rev. A* **65**, 062104 (2002).
- Hanneke, D., Fogwell, S. & Gabrielse, G. New measurement of the electron magnetic moment and the fine structure constant. *Phys. Rev. Lett.* **100**, 120801 (2008).
- Aoyama, T., Hayakawa, M., Kinoshita, T. & Nio, M. Tenth-order QED contribution to the electron  $g - 2$  and an improved value of the fine structure constant. *Phys. Rev. Lett.* **109**, 111807 (2012).
- Böhm, C. & Silk, J. A new test for dark matter particles of low mass. *Phys. Lett. B* **661**, 287–289 (2008).
- Häffner, H. *et al.* High-accuracy measurement of the magnetic moment anomaly of the electron. *Phys. Rev. Lett.* **85**, 5308–5311 (2000).
- Verdú, J. *et al.* Electronic  $g$  factor of hydrogenlike oxygen  $^{16}\text{O}^{7+}$ . *Phys. Rev. Lett.* **92**, 093002 (2004).
- Pachucki, K., Czarnecki, A., Jentschura, U. D. & Yerokhin, V. A. Complete two-loop correction to the bound-electron  $g$  factor. *Phys. Rev. A* **72**, 022108 (2005).
- Breit, G. The magnetic moment of the electron. *Nature* **122**, 649 (1928).
- Beier, T. The  $g$  factor of a bound electron and the hyperfine structure. *Phys. Rep.* **339**, 79–213 (2000).
- Yerokhin, V. A., Indelicato, P. & Shabaev, V. M. Evaluation of the self-energy correction to the  $g$  factor of S states in H-like ions. *Phys. Rev. A* **69**, 052503 (2004).
- Sturm, S. *et al.*  $g$ -factor measurement of hydrogenlike  $^{28}\text{Si}^{13+}$  as a challenge to QED calculations. *Phys. Rev. A* **87** (3), 030501 (2013).
- Sturm, S. *et al.*  $g$  Factor of hydrogenlike  $^{28}\text{Si}^{13+}$ . *Phys. Rev. Lett.* **107**, 023002 (2011).
- Gabrielse, G. Why is sideband mass spectrometry possible with ions in a Penning trap? *Phys. Rev. Lett.* **102**, 172501 (2009).
- Sturm, S., Wagner, A., Schabinger, B. & Blaum, K. Phase-sensitive cyclotron frequency measurements at ultralow energies. *Phys. Rev. Lett.* **107**, 143003 (2011).
- Cornell, E. A. *et al.* Single-ion cyclotron resonance measurement of  $M(\text{CO}^+)/M(\text{N}_2^+)$ . *Phys. Rev. Lett.* **63**, 1674–1677 (1989).
- Dehmelt, H. Continuous Stern-Gerlach effect: principle and idealized apparatus. *Proc. Natl Acad. Sci. USA* **83**, 2291–2294 (1986).
- Brown, L. S. & Gabrielse, G. Geonium theory: physics of a single electron or ion in a Penning trap. *Rev. Mod. Phys.* **58**, 233–311 (1986).
- Kramida, A. *Atomic Energy Levels and Spectra Bibliographic Database* (version 2.0). <http://physics.nist.gov/PhysRefData/ASD/ionEnergy.html> (Physical Measurement Laboratory, Quantum Measurement Division, NIST).
- Bouchendira, R., Cladé, P., Gouellati-Khélifa, S., Nez, F. & Biraben, F. New determination of the fine structure constant and test of the quantum electrodynamics. *Phys. Rev. Lett.* **106**, 080801 (2011).
- Mount, B. J., Redshaw, M. & Myers, E. G. Atomic masses of  $^6\text{Li}$ ,  $^{23}\text{Na}$ ,  $^{39,41}\text{K}$ ,  $^{85,87}\text{Rb}$  and  $^{133}\text{Cs}$ . *Phys. Rev. A* **82**, 042513 (2010).

**Supplementary Information** is available in the online version of the paper.

**Acknowledgements** This work was supported by the Max Planck Society, the EU (ERC grant number 290870; MEFUCO), the IMPRS-QD, GSI and the Helmholtz Alliance HA216/EMMI.

**Author Contributions** S.S., F.K. and A.W. performed the experiment. S.S. and F.K. performed the data analysis. J.Z. performed the QED calculations. S.S., F.K., K.B., J.Z. and Z.H. prepared the manuscript. S.S. and F.K. prepared the experimental part of the Supplementary Information. J.Z. and Z.H. prepared the theoretical part of the Supplementary Information. All authors discussed the results and contributed to the manuscript at all stages.

**Author Information** Reprints and permissions information is available at [www.nature.com/reprints](http://www.nature.com/reprints). The authors declare no competing financial interests. Readers are welcome to comment on the online version of the paper. Correspondence and requests for materials should be addressed to S.S. (sven.sturm@mpi-hd.mpg.de).

# Quantum droplets of electrons and holes

A. E. Almand-Hunter<sup>1,2</sup>, H. Li<sup>1</sup>, S. T. Cundiff<sup>1,2</sup>, M. Mootz<sup>3</sup>, M. Kira<sup>3</sup> & S. W. Koch<sup>3</sup>

Interacting many-body systems are characterized by stable configurations of objects—ranging from elementary particles to cosmological formations<sup>1–3</sup>—that also act as building blocks for more complicated structures. It is often possible to incorporate interactions in theoretical treatments of crystalline solids by introducing suitable quasiparticles that have an effective mass, spin or charge<sup>4,5</sup> which in turn affects the material's conductivity, optical response or phase transitions<sup>2,6,7</sup>. Additional quasiparticle interactions may also create strongly correlated configurations yielding new macroscopic phenomena, such as the emergence of a Mott insulator<sup>8</sup>, superconductivity or the pseudogap phase of high-temperature superconductors<sup>9–11</sup>. In semiconductors, a conduction-band electron attracts a valence-band hole (electronic vacancy) to create a bound pair, known as an exciton<sup>12,13</sup>, which is yet another quasiparticle. Two excitons may also bind together to give molecules, often referred to as biexcitons<sup>14</sup>, and even polyexcitons may exist<sup>15,16</sup>. In indirect-gap semiconductors such as germanium or silicon, a thermodynamic phase transition may produce electron–hole droplets whose diameter can approach the micrometre range<sup>17,18</sup>. In direct-gap semiconductors such as gallium arsenide, the exciton lifetime is too short for such a thermodynamic process. Instead, different quasiparticle configurations are stabilized dominantly by many-body interactions, not by thermalization. The resulting non-equilibrium quantum kinetics is so complicated that stable aggregates containing three or more Coulomb-correlated electron–hole pairs remain mostly unexplored. Here we study such complex aggregates and identify a new stable configuration of charged particles that we call a quantum droplet. This configuration exists in a plasma and exhibits quantization owing to its small size. It is charge neutral and contains a small number of particles with a pair-correlation function that is characteristic of a liquid. We present experimental and theoretical evidence for the existence of quantum droplets in an electron–hole plasma created in a gallium arsenide quantum well by ultrashort optical pulses.

The new quasiparticle that we call a quantum droplet has a pair-correlation function that is characteristic of a liquid; thus it is a droplet and not a polyexciton. However, it contains a small number of electron–hole pairs and the pair-correlation function exhibits the effects of quantization; thus it is distinct from a macroscopic droplet. It can form via Coulomb interaction in direct-gap semiconductors such as gallium arsenide (GaAs) on an ultrafast timescale, long before a thermodynamic equilibrium is reached. To be stable, a quantum droplet's binding energy must be higher than that of other quasiparticles, including excitons and biexcitons. Figure 1a sketches the hierarchy of the most relevant quasiparticle states in semiconductors. As for any liquid-like state, we expect quantum droplets to emerge only above a certain density threshold. Because quantum droplets should have discrete eigenenergies, it should be possible to detect quantum beats in suitable time-resolved experiments. Such quantum-dynamic evolution is absent for thermodynamic transitions.

We present experimental evidence for quantum electron–hole droplets in the absorption spectrum of a GaAs quantum well that has been excited by an ultrafast laser pulse. Absorption of light from the excitation pulse creates electron–hole pairs with a density that increases monotonically

with the pulse intensity and puts the system in a non-equilibrium state. Thus, the number of injected quasiparticles can be controlled by the excitation-pulse intensity and additionally by the photon energy. If the excitation is tuned well above the exciton resonance, it initially generates an electron–hole plasma that may evolve into excitons only via relatively slow equilibration<sup>19</sup>. If the excitation is resonant with the exciton, it is rapidly converted into a mixture of excitons and electron–hole plasma<sup>20</sup> and only further equilibration may then bind excitons into biexcitons<sup>14</sup>. However, biexcitons can be generated more efficiently by tuning the photon energy below that of the exciton in order to match the biexciton binding.

In our experiments, absorption spectra are recorded using a weak time-delayed probe pulse that is spectrally resolved after passing through the sample (see Supplementary Information). The pump–probe delay  $\Delta t$  is defined as the temporal separation of pump and probe pulse centres. For  $\Delta t > 0$ , the pump pulse arrives at the sample before the probe pulse. The absorption spectra at a fixed pump–probe delay of  $\Delta t = 2$  ps are shown in Fig. 1b as a function of probe-photon energy and number of photons in the pump pulse,  $N_{\text{pump}}$ . We quote the photon number because the number of generated quasiparticles is not necessarily linearly proportional to  $N_{\text{pump}}$  owing to saturation effects, and because the mixture of quasiparticles varies<sup>20</sup> with  $N_{\text{pump}}$ . At very low excitation density, the absorption spectrum shows a clear heavy-hole exciton resonance 9 meV below the bandgap (not shown) that also defines an exciton's binding

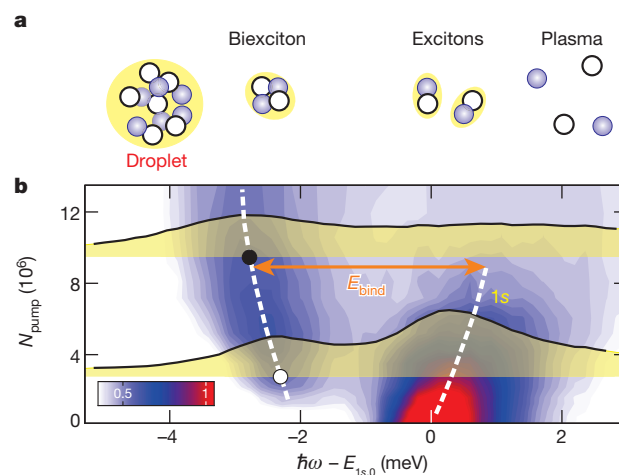


**Figure 1 | Quasiparticles in classical spectroscopy.** **a**, Schematic quasiparticles in direct-gap semiconductors. Open circles, holes; grey filled circles, electrons. See text for details. **b**, Measured absorption spectra as a function of the number of photons in the pump pulse,  $N_{\text{pump}}$ , for pump–probe delay  $\Delta t = 2$  ps; the pump and probe have opposite circular polarization. The dark (white) colours denote the regions with strong (weak) absorption (see colour scale; peak absorption is normalized to one); the transparent yellow shaded areas with black lines on top show actual spectra corresponding to  $N_{\text{pump}} = 2.8 \times 10^6$  (lower) and  $N_{\text{pump}} = 9.5 \times 10^6$  (upper). The dashed lines indicate the shifts of the resonances,  $\hbar\omega$  defines the photon energy,  $E_{1s,0}$  is the low-density exciton energy, and  $E_{\text{bind}}$  denotes the binding energy.

<sup>1</sup>JILA, University of Colorado and National Institute of Standards and Technology, Boulder, Colorado 80309-0440, USA. <sup>2</sup>Department of Physics, University of Colorado, Boulder, Colorado 80309-0390, USA. <sup>3</sup>Department of Physics, Philipps-University Marburg, Renthof 5, 35032 Marburg, Germany.



energy with respect to the electron–hole plasma. For increasing pump intensity, the Coulomb renormalizations move the bandgap to a lower energy<sup>2</sup>. At the same time, the exciton binding energy is reduced due to the weakening of the Coulomb interaction by screening<sup>21</sup> and Pauli blocking of low-energy states. Interplay of these three effects yields an overall blue shift of the exciton energy, as expected<sup>20,22,23</sup>.

Additionally, a second resonance appears below the exciton resonance for pump strengths exceeding  $1.5 \times 10^6$  photons. The binding energy of this state,  $E_{\text{bind}}$ , is defined with respect to the exciton resonance (arrow in Fig. 1b). It has a value of just over 2 meV at low excitation levels and grows to about 3 meV as  $N_{\text{pump}}$  increases. Because excitons may lower their energy by forming a molecule, one expects  $E_{\text{bind}}$  to indicate the existence of a bound biexciton state. However, this assignment conflicts with the increase of  $E_{\text{bind}}$  with elevated  $N_{\text{pump}}$  because the biexciton's binding energy should track the exciton's binding energy. In other words, the biexcitonic  $E_{\text{bind}}$  should decrease as the Coulomb interaction weakens at elevated  $N_{\text{pump}}$ . Furthermore, we see that the second resonance remains much more pronounced than the high- $N_{\text{pump}}$  exciton resonance. We have confirmed the increase of  $E_{\text{bind}}$  as a function of  $N_{\text{pump}}$  not only by using another sample but also by using a different experimental technique, two-dimensional Fourier transform spectroscopy, which produces more detailed information about the quasiparticles<sup>24</sup>, as presented in Supplementary Information.

Because the behaviour of  $E_{\text{bind}}$  is inconsistent with the low-energy resonance remaining biexcitonic, it is reasonable to surmise that although this resonance initially corresponds to the biexciton, it cannot be due to the biexciton at higher excitation levels, but rather must be due to the excitation of a different quasiparticle, which we hypothesize to be a quantum droplet. To test this assignment, we analyse the properties of the experimentally detected resonance and check if they are consistent with a many-body state where electrons and holes form a liquid confined within a small droplet with radius  $R$ . As the principal hallmark of liquids, the particle-position correlations form a ring pattern where the ring separation corresponds roughly to the average particle separation<sup>25–27</sup>. This fundamental property can be formulated using the pair-correlation function  $g(r) = \rho_e \rho_h + \Delta g(r)$  that determines the conditional distribution of electrons when a hole is at the origin and vice versa. The product of electron and hole densities,  $\rho_e \rho_h$ , describes the evenly spread plasma contribution in a homogeneous system. The quasiparticle clusters are determined by the correlated part,  $\Delta g(r)$ , that contains the  $r$  dependence.

A quantum droplet has a well-defined radius  $R$  such that the  $\Delta g(r)$  correlation vanishes for distances greater than  $R$ . Physically, a quantum droplet can be viewed as a correlation bubble that is held together by the Fermi pressure created by the surrounding high-density plasma. Because electron–hole pairs are quantum confined inside a bubble, the pair wavefunction exhibits a standing wave within a circular shell because the quantum well is two-dimensional. Therefore, for simplicity, we start by assuming that the droplet has a hard shell at  $r = R$  and implement a standing-wave ansatz  $\Delta g(r) = |g_0 \phi(r)|^2$  defined by

$$\phi(r) = J_0 \left( x_n \frac{r}{R} \right) e^{-\kappa r} \theta(R-r) \quad (1)$$

where  $x_n$  is the  $n$ th zero of the Bessel function  $J_0(x)$ ,  $\kappa$  is an additional decay constant, the Heaviside  $\theta(x)$  function confines  $\Delta g(r)$  inside the shell, and  $g_0$  determines the strength of the correlations. As discussed in the Supplementary Information, the specific ( $g_0$ ,  $\kappa$ ,  $R$ ) values also fix  $\rho_{\text{eh}} \equiv \rho_e = \rho_h$  within the quantum droplet. We adjust the density to match the external  $\rho_{\text{eh}}$  of the plasma, and fix  $\kappa$  and  $g_0$  coefficients for a given carrier density when the droplet has radius  $R$  and  $n$  rings.

Figure 2a illustrates the pair-correlation function  $g(r)$  of a quantum droplet with  $R = 91$  nm,  $n = 4$ , and electron–hole density  $\rho_{\text{eh}} = 2.5 \times 10^{10} \text{ cm}^{-2}$ . The shell of the droplet is indicated by the cylinder. Outside the shell,  $g(r)$  has a constant value  $\rho_e \rho_h$  (grey area) and  $\Delta g(r)$  (yellow area) is non-zero only within the shell. Here,  $\Delta g(r)$  has four rings, including the central part that appears because the electrons and holes attract each other. This behaviour is different from typical liquids that

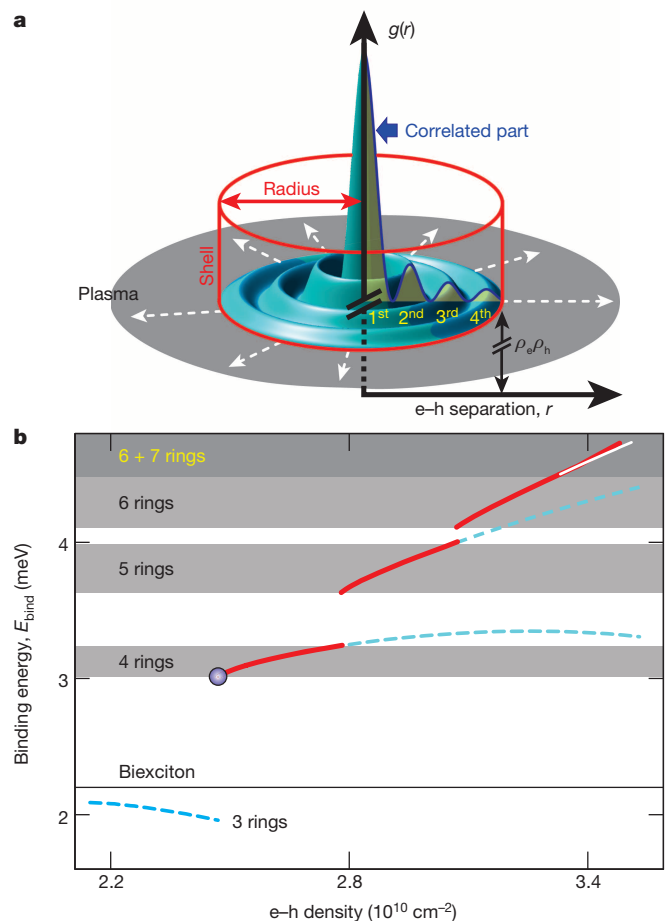


**Figure 2 | Quantum droplet properties.** **a**, Computed  $g(r)$  of a quantum droplet having radius  $R = 91$  nm,  $n = 4$  and  $\rho_{\text{eh}} \equiv \rho_e = \rho_h = 2.5 \times 10^{10} \text{ cm}^{-2}$ . The cylinder represents the droplet shell, the correlated part ( $\Delta g(r)$ ) is indicated by a yellow area, and the grey area corresponds to the plasma ( $\rho_e \rho_h$ ). **b**, Computed binding energy as a function of  $\rho_{\text{eh}}$ . Energy dispersion for each droplet is continued as a dashed line after the next higher quantum droplet becomes the lowest-energy state; the white line continues the 6-ring  $E_{\text{bind}}$ . The horizontal line indicates the biexciton binding energy. The shaded areas denote the ground-state bands. The filled circle defines the binding energy for the configuration presented in **a**.

show a correlation hole at the centre of  $g(r)$  (refs 25–27) because particles in a typical liquid repel each other at short distances.

To determine the energetics of quantum droplets, we generalize the Wannier equation<sup>13,28</sup> to compute the energy per electron–hole pair probed by an infinitesimally weak pair excitation when the system initially contains an  $n$ -ring quantum droplet (see Supplementary Information). The red solid lines in Fig. 2b define the highest  $E_{\text{bind}}$  as a function of  $\rho_{\text{eh}}$  found among quantum droplets with a different number of rings. The dashed curves continue the energy dispersion of the  $n$ -ring droplet for higher densities where it is no longer the lowest-energy state. In general, we always find a discrete droplet–energy relation where new energy levels appear as sharp transitions when  $\rho_{\text{eh}}$  is increased; allowed energy ranges are indicated by the shaded bands. Because each jump in the ground state  $E_{\text{bind}}$  increases  $n$  by one, the number of rings also defines the quantum number for the discrete energy levels. We show in Supplementary Information that quantum droplets confined inside a finite wall produce essentially the same energetics as the hard-wall ansatz, equation (1); we also find that the skin depth of the quantum droplet's edge is then 7 nm, which is comparable with the exciton Bohr radius of  $a_B = 12$  nm, whereas the quantum-droplet radius itself is roughly 8 times larger than  $a_B$ .

The relative excitation level can be estimated from the Pauli-blocking (or the phase-space filling) factor of the zero-momentum electrons and holes in the excitonic system. It is unity at vanishing density and 0.41 (0.32) when the  $n = 4$  (6)-ring quantum droplet emerges. Therefore, the exciton resonance is already strongly broadened in Fig. 1b, indicating that the quantum rings appear at elevated electron–hole densities  $\rho_{\text{eh}}$ . This conclusion is consistent with the need for a sufficiently large Fermi pressure to create conditions favourable for the correlation bubbles surrounded by the plasma. As shown in Supplementary Information, we also find that the  $n$ -ring quantum droplet has essentially  $n$  electron–hole pairs just after the sharp transition in the  $E_{\text{bind}} - \rho_{\text{eh}}$  diagram.

Both the magnitude and excitation-induced increase of the calculated quantum-droplet binding energy agree with the experimental results presented in Fig. 1b. However, the calculated  $E_{\text{bind}}$  shows a series of abrupt jumps whenever a ring is added. As such jumps are not directly evident in the experimental results, we reanalyse the data through differential absorption  $\Delta\alpha$  that excels at revealing the effect of many-body correlations. However, a simple differential absorption  $\Delta\alpha_{\text{class}}$  (with respect to classical changes in the pump) monitors all effects down to the single-particle level<sup>2</sup>, which masks the effect of the individual many-body states. To overcome this obstacle, we use the projection protocol described in ref. 23 to directly access the effect of the distinct many-body states via the projected differential absorption  $\Delta\alpha_{\text{MB}}$ . Technically, one only needs to measure the quantum-well absorption for a large ensemble of  $N_{\text{pump}}$  values, as is done in Fig. 1b, and apply the projection protocol to generate  $\Delta\alpha_{\text{MB}}$  that becomes a differential to the quantum-optical fluctuations in the pump source<sup>23</sup>. As elaborated in the Supplementary Information, we follow this protocol and project  $\Delta\alpha_{\text{MB}}$  to ‘slanted’ Schrödinger cat states that are superpositions of two different coherent states with unequal amplitudes. The resulting  $\Delta\alpha_{\text{MB}}$  is designed (see Supplementary Information) to access the response from many-body correlations involving three or more electron–hole pairs. Therefore, one gains a significant enhancement of sensitivity to highly correlated quasiparticles when analysing  $\Delta\alpha_{\text{MB}}$  instead of  $\Delta\alpha_{\text{class}}$ .

A contour plot of the  $\Delta\alpha_{\text{MB}}$  spectra generated from the experimental results is presented in Fig. 3a as a function of  $N_{\text{pump}}$  and  $E_{\text{bind}}$  for  $\Delta t = 16$  ps. The binding energy is defined with respect to the  $N_{\text{pump}}$ -dependent 1s energy. Spectra at three different values of  $N_{\text{pump}}$ , indicated by the circles, are shaded. For low  $N_{\text{pump}}$ , there is a clear resonance at the biexciton energy (horizontal line). The position of the biexciton resonance is stationary, in contrast to the experimental results presented in Fig. 1b. However, the resonance jumps abruptly at  $N_{\text{pump}} = 1.3 \times 10^6$  while maintaining its width. As  $N_{\text{pump}}$  is increased further, we find two more sharp transitions at  $N_{\text{pump}} = 3.5 \times 10^6$  and  $5.0 \times 10^6$  such that three quantized energy levels are resolved. More specifically, these energy levels have  $E_{\text{bind}}$  that exceeds the biexciton binding by 0.9 meV, 1.60 meV or 2.4 meV.

The shaded bands in Fig. 3a indicate each quantized energy level, deduced from the computation in Fig. 2b. The positions of the measured quantized energy levels agree well with the calculated energies for the 4-ring, 5-ring and 6 (7)-ring quantum droplets, which is consistent with the assignment of the low-energy resonance to quantum droplets at excitation levels above  $N_{\text{pump}} = 1.3 \times 10^6$ . Also, the predicted merging of 6- and 7-ring features seems to appear in  $\Delta\alpha_{\text{MB}}$  (see Supplementary Information), even though our signal-to-noise ratio starts to deteriorate in this weak absorption range. Quantum droplets with two and three rings (not shown) have a binding energy smaller than the biexciton, which make them undetectable in the cross-circular pump–probe measurement. Because the quantum droplets are highly correlated, these quantized levels become clearly visible only in the  $\Delta\alpha_{\text{MB}}$  spectra that are sensitive to three-pair effects and beyond. Classical spectroscopy cannot resolve the individual quantum droplet levels as seen in Fig. 1b. Instead, quantum droplets appear in classical spectra as a gradual increase in  $E_{\text{bind}}$ , because classical light yields a mixture of biexcitons and quantum droplets via Coulomb and phonon scattering<sup>2</sup>, preventing sharp resonances.

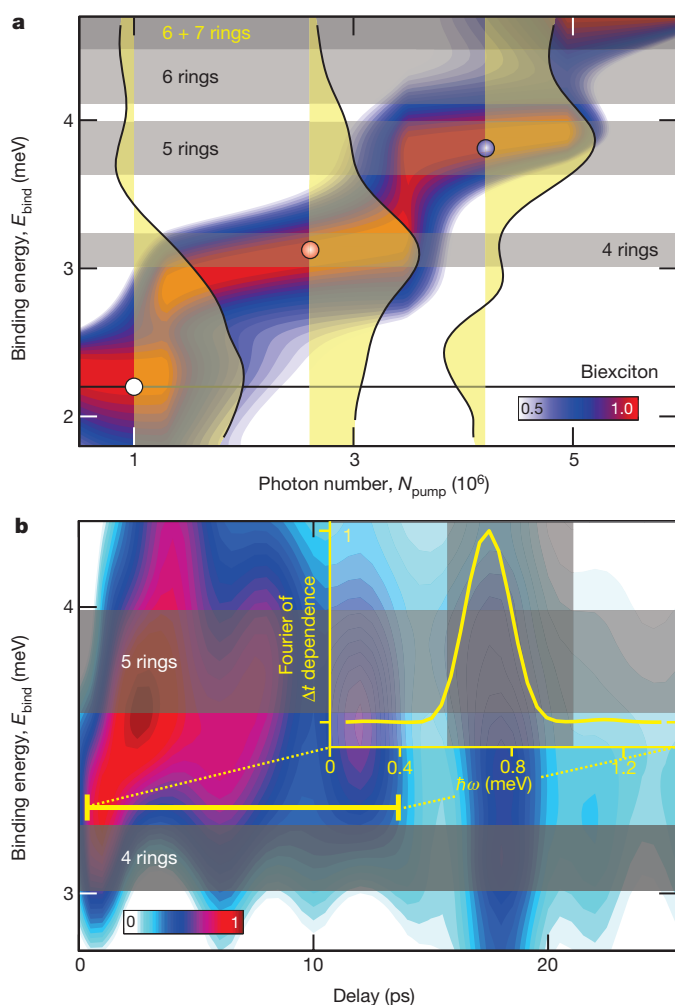


**Figure 3 | Detection of quantum droplets via quantum spectroscopy.**

**a**, Contour plot of  $\Delta\alpha_{\text{MB}}$  (on colour scale) as a function of  $N_{\text{pump}}$  and  $E_{\text{bind}}$ . The dark (white) contours indicate the regions with large (small) increase in  $\Delta\alpha_{\text{MB}}$ . The biexciton  $E_{\text{bind}}$  (horizontal line) matches the low-density binding in Fig. 1b. Grey shaded horizontal bands denote the computed energy ranges of 4-, 5-, 6- and 7-ring droplets. The yellow areas with black traces show  $\Delta\alpha_{\text{MB}}$  at  $N_{\text{pump}} = 1.0 \times 10^6$  (left, open circle),  $2.6 \times 10^6$  (middle, red sphere) and  $4.2 \times 10^6$  (right, blue sphere). **b**, Temporal evolution of  $\Delta\alpha_{\text{MB}}$  for  $N_{\text{pump}} = 3.8 \times 10^6$ . Grey shaded horizontal bands denote the 4- and 5-ring bands. Inset, Fourier-transformed  $\Delta\alpha_{\text{MB}}$  at  $E_{\text{bind}} = 3.3$  meV (horizontal yellow line in **b**). The vertical grey shaded rectangle determines the expected range for 4–5 ring splitting.

We also show in Supplementary Information that the quantum-droplet levels cannot be explained by polyexcitons. More specifically, we have performed a control measurement in which the generation of polyexcitons is excluded owing to antibonding of the excited states, and yet the control measurement produces identical quantum-droplet bands. Hence, the constituents of quantum droplets are not excitons, but collectively bound electron–hole complexes. We note that a polyexciton is also forbidden in direct-gap systems at low densities<sup>29</sup>.

To track the quantum dynamics of quantum droplets, we measure and generate  $\Delta\alpha_{\text{MB}}$  as a function of the pump–probe delay  $\Delta t$ . Because each value of  $\Delta t$  labels an independent  $N_{\text{pump}}$ -measurement ensemble that is projected into  $\Delta\alpha_{\text{MB}}$ , the  $\Delta t$  dependence of  $\Delta\alpha_{\text{MB}}$  reveals the quantum dynamics of the quantum droplets independently from the pure energetics deduced from the  $N_{\text{pump}}$  dependence alone (Fig. 3a). The accuracy of the  $\Delta\alpha_{\text{MB}}$  projection is 6% from the spectral peak height. Figure 3b shows the  $\Delta t$  dependence of  $\Delta\alpha_{\text{MB}}$  spectra for a fixed  $N_{\text{pump}} = 3.8 \times 10^6$ . The spectral peak is first created at the 4-ring quantum

droplet energy and it then moves vertically towards the 5-ring energy. This is followed by oscillations that are also visible in a horizontal cut at fixed  $E_{\text{bind}} = 3.3$  meV (horizontal thick yellow line), as a function of time. The Fourier transform of this horizontal cut is presented in the inset, where the vertical shaded area indicates the expected transition energy range between the 4- and 5-ring states, based on Fig. 2b. The  $\Delta\alpha_{\text{MB}}$  resonance not only oscillates between the 4- and 5-ring droplets, but the oscillation frequency matches the energy splitting between these levels. The observed quantum beats provide independent evidence for the existence of quantum droplets with discrete energy states.

The  $\Delta\alpha_{\text{MB}}$  dynamics provide further insight into the properties of the quantum droplets. Three-photon correlations create the quantum droplet essentially instantly, as seen in Fig. 3b from the immediate emergence of the resonance at the first quantized level just after  $\Delta t = 0$ . The results also show that the quantum droplet has a lifetime of roughly 25 ps. These transient features, as well as the quantum beats, cannot appear for thermodynamic transitions.

Although we cannot directly measure  $\Delta\alpha_{\text{MB}}$  because suitable quantum-light sources do not yet exist, the projected measurements analysed in Fig. 3b suggest that one might still detect the quantum-droplet beats as a function of pump-probe delay directly in absorption measurements at an appropriate excitation level. Furthermore, we can enhance the effect of higher-order correlations by measuring the differential  $\Delta\alpha_{\text{class}}$  due to modulation of the pump intensity, rather than just the absorption itself. The details of the experiment are given in the Supplementary Information. The measured values of  $\Delta\alpha_{\text{class}}$  at the first quantum-droplet energy are shown in Fig. 4. We note pronounced beats that match the splitting between the 4- and 5-ring droplets, and also note beats that match the splitting between the 4- and 6-ring droplets, providing further independent evidence for the existence of quantum droplets. The simultaneous presence of multiple droplet resonances is also consistent with the incapability of the classical spectroscopy to resolve the individual quantum-droplet states. In the Supplementary Information, we report an additional control measurement that we have performed, where we study quantum droplets at 70 K, which is expected to be a high enough temperature that the quantum droplets are ionized by phonon scattering. We find that the 70 K measurement indeed does not produce quantum droplets.

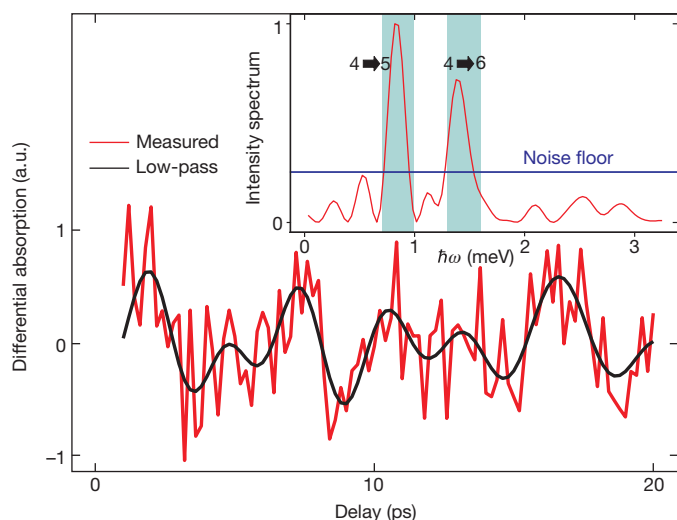


**Figure 4 | Direct measurement of quantum-droplet signatures.** Main figure, differential absorption trace recorded at 3 meV binding energy as a function of pump-probe delay. The measured (red line) and low-pass filtered (black line) traces are shown. Inset, corresponding intensity spectra (red line) together with the experimental noise floor (blue horizontal line) and energy ranges (vertical cyan shaded rectangles) expected for transitions between the 4- and 5-ring droplet and the 4- and 6-ring droplet, identified in Fig. 2b. a.u., arbitrary units.

Because a quantum droplet of electrons and holes has a microscopic size, quantized energy and quantized transitions, we suggest this new quasiparticle be called simply a droplet. Conceptually, a droplet is in between a quantum version of the Thomson atom<sup>30</sup> and the real multi-electron atom, because the positive charge is not uniform, as in the Thomson atom, but is localized around the electrons, although it is not as extremely localized as in an atomic nucleus due to the strong force. Our analysis shows that the individual droplet levels can be accessed using ultrafast light pulses whose quantum fluctuations are tailored to match the particle correlations within the droplet. Owing to the droplet's relatively long life time, it appears to be stable enough for systematic studies on interactions between quantum light and highly correlated matter states.

## METHODS SUMMARY

We excite various quasiparticles in the GaAs quantum well by varying the intensity of an ultrafast high-quality pump pulse. The resulting quasiparticles are characterized by measuring linear absorption with a weak probe pulse that is delayed with respect to the pump. This part of the process records a systematic set of high-precision absorption spectra as a function of pump intensity, for each fixed pump-probe delay. The high precision of our measurements allows each of these sets to be independently projected into a differential absorption spectrum with respect to changes only in the pump field's three-photon fluctuations. We use an experimentally robust protocol demonstrated in ref. 23. As the central feature of quantum-optical spectroscopy<sup>2</sup>, such a differential absorption is exclusively sensitive to correlations of three electron-hole pairs excited in the system. Consequently, we can then directly follow how correlations among three electron-hole pairs evolve, which allows us to detect quasiparticles that remain virtually hidden to classical spectroscopies. The Supplementary Information elaborates both the experimental set-up and the exact projection algorithm used.

Received 29 July; accepted 12 December 2013.

- Lissauer, J. Chaotic motion in the solar system. *Rev. Mod. Phys.* **71**, 835–845 (1999).
- Kira, M. & Koch, S. W. *Semiconductor Quantum Optics* 1st edn (Cambridge Univ. Press, 2011).
- Oganessian, Y. *et al.* Synthesis of nuclei of the superheavy element 114 in reactions induced by  $^{48}\text{Ca}$ . *Nature* **400**, 242–245 (1999).
- Kittel, C. *Introduction to Solid State Physics* 7th edn (Wiley, 2004).
- Laughlin, R. Anomalous quantum Hall effect: an incompressible quantum fluid with fractionally charged excitations. *Phys. Rev. Lett.* **50**, 1395–1398 (1983).
- Datta, S. *Electronic Transport in Mesoscopic Systems* 1st edn (Cambridge Univ. Press, 1997).
- Papon, P., Leblond, J. & Meijer, P. *The Physics of Phase Transitions: Concepts and Applications* 2nd edn (Springer, 2006).
- Endres, M. *et al.* Observation of correlated particle-hole pairs and string order in low-dimensional Mott insulators. *Science* **334**, 200–203 (2011).
- Vershinin, M. *et al.* Local ordering in the pseudogap state of the high- $T_c$  superconductor  $\text{Bi}_2\text{Sr}_2\text{CaCu}_2\text{O}_{8+\delta}$ . *Science* **303**, 1995–1998 (2004).
- Kanigel, A. *et al.* Evolution of the pseudogap from Fermi arcs to the nodal liquid. *Nature Phys.* **2**, 447–451 (2006).
- Daou, R. *et al.* Broken rotational symmetry in the pseudogap phase of a high- $T_c$  superconductor. *Nature* **463**, 519–522 (2010).
- Frenkel, J. On the transformation of light into heat in solids. *Phys. Rev.* **37**, 17–44 (1931).
- Wannier, G. The structure of electronic excitation levels in insulating crystals. *Phys. Rev.* **52**, 191–197 (1937).
- Kim, J. C., Wake, D. R. & Wolfe, J. P. Thermodynamics of biexcitons in a GaAs quantum well. *Phys. Rev. B* **50**, 15099–15107 (1994).
- Steele, A., McMullan, W. & Thewalt, M. Discovery of polyelectrons. *Phys. Rev. Lett.* **59**, 2899–2902 (1987).
- Turner, D. & Nelson, K. Coherent measurements of high-order electronic correlations in quantum wells. *Nature* **466**, 1089–1092 (2010).
- Jeffries, C. Electron-hole condensation in semiconductors. *Science* **189**, 955–964 (1975).
- Suzuki, T. & Shimano, R. Time-resolved formation of excitons and electron-hole droplets in Si studied using terahertz spectroscopy. *Phys. Rev. Lett.* **103**, 057401 (2009).
- Kaindl, R. A., Carnahan, M. A., Hagele, D., Lovenich, R. & Chemla, D. S. Ultrafast terahertz probes of transient conducting and insulating phases in an electron-hole gas. *Nature* **423**, 734–738 (2003).
- Smith, R. P. *et al.* Extraction of many-body configurations from nonlinear absorption in semiconductor quantum wells. *Phys. Rev. Lett.* **104**, 247401 (2010).
- Huber, R. *et al.* How many-particle interactions develop after ultrafast excitation of an electron-hole plasma. *Nature* **414**, 286–289 (2001).



22. Khitrova, G., Gibbs, H. M., Jahnke, F., Kira, M. & Koch, S. W. Nonlinear optics of normal-mode-coupling semiconductor microcavities. *Rev. Mod. Phys.* **71**, 1591–1639 (1999).
23. Kira, M., Koch, S. W., Smith, R. P., Hunter, A. E. & Cundiff, S. T. Quantum spectroscopy with Schrödinger-cat states. *Nature Phys.* **7**, 799–804 (2011).
24. Cundiff, S. T. Optical two-dimensional Fourier transform spectroscopy of semiconductor nanostructures. *J. Opt. Soc. Am. B* **29**, A69–A81 (2012).
25. Barker, J. A. & Henderson, D. What is “liquid”? Understanding the states of matter. *Rev. Mod. Phys.* **48**, 587–671 (1976).
26. Jorgensen, W. L., Chandrasekhar, J., Madura, J. D., Impey, R. W. & Klein, M. L. Comparison of simple potential functions for simulating liquid water. *J. Chem. Phys.* **79**, 926–935 (1983).
27. Sastry, S. & Angell, C. Liquid–liquid phase transition in supercooled silicon. *Nature Mater.* **2**, 739–743 (2003).
28. Mootz, M., Kira, M. & Koch, S. W. Pair-excitation energetics of highly correlated many-body states. *New J. Phys.* **15**, 093040 (2013).
29. Hirschfelder, J. O. The energy of the triatomic hydrogen molecule and ion, V. *J. Chem. Phys.* **6**, 795–806 (1938).
30. Thomson, J. On the structure of the atom. *Phil. Mag.* **7**, 237–265 (1904).

**Supplementary Information** is available in the online version of the paper.

**Acknowledgements** We thank R. Mirin at NIST-Boulder for growing the quantum well samples. The work at Philipps-University Marburg was supported by the Deutsche Forschungsgemeinschaft under grant KI 917/2-1, and the work at JILA was supported by the NSF under grant 1125844 and by NIST. S.T.C. acknowledges support from the Alexander von Humboldt Foundation.

**Author Contributions** All authors contributed substantially to this work. The experiments were performed by the JILA group whereas the Philipps-University Marburg group was predominantly responsible for the theory.

**Author Information** Reprints and permissions information is available at [www.nature.com/reprints](http://www.nature.com/reprints). The authors declare no competing financial interests. Readers are welcome to comment on the online version of the paper. Correspondence and requests for materials should be addressed to M.K. ([mackillo.kira@physik.uni-marburg.de](mailto:mackillo.kira@physik.uni-marburg.de)).

# A large source of low-volatility secondary organic aerosol

Mikael Ehn<sup>1,2</sup>, Joel A. Thornton<sup>2,3</sup>, Einhard Kleist<sup>4</sup>, Mikko Sipilä<sup>2</sup>, Heikki Junninen<sup>2</sup>, Iida Pullinen<sup>1</sup>, Monika Springer<sup>1</sup>, Florian Rubach<sup>1</sup>, Ralf Tillmann<sup>1</sup>, Ben Lee<sup>3</sup>, Felipe Lopez-Hilfiker<sup>3</sup>, Stefanie Andres<sup>1</sup>, Ismail-Hakki Acir<sup>1</sup>, Matti Rissanen<sup>2</sup>, Tuija Jokinen<sup>2,5</sup>, Siegfried Schobesberger<sup>2</sup>, Juha Kangasluoma<sup>2</sup>, Jenni Kontkanen<sup>2</sup>, Tuomo Nieminen<sup>2,6</sup>, Theo Kurtén<sup>7</sup>, Lasse B. Nielsen<sup>8</sup>, Solveig Jørgensen<sup>8</sup>, Henrik G. Kjaergaard<sup>8</sup>, Manjula Canagaratna<sup>9</sup>, Miikka Dal Maso<sup>10</sup>, Torsten Berndt<sup>5</sup>, Tuukka Petäjä<sup>2</sup>, Andreas Wahner<sup>1</sup>, Veli-Matti Kerminen<sup>2</sup>, Markku Kulmala<sup>2</sup>, Douglas R. Worsnop<sup>2,9</sup>, Jürgen Wildt<sup>4</sup> & Thomas F. Mentel<sup>1</sup>

Forests emit large quantities of volatile organic compounds (VOCs) to the atmosphere. Their condensable oxidation products can form secondary organic aerosol, a significant and ubiquitous component of atmospheric aerosol<sup>1,2</sup>, which is known to affect the Earth's radiation balance by scattering solar radiation and by acting as cloud condensation nuclei<sup>3</sup>. The quantitative assessment of such climate effects remains hampered by a number of factors, including an incomplete understanding of how biogenic VOCs contribute to the formation of atmospheric secondary organic aerosol. The growth of newly formed particles from sizes of less than three nanometres up to the sizes of cloud condensation nuclei (about one hundred nanometres) in many continental ecosystems requires abundant, essentially non-volatile organic vapours<sup>4–6</sup>, but the sources and compositions of such vapours remain unknown. Here we investigate the oxidation of VOCs, in particular the terpene  $\alpha$ -pinene, under atmospherically relevant conditions in chamber experiments. We find that a direct pathway leads from several biogenic VOCs, such as monoterpenes, to the formation of large amounts of extremely low-volatility vapours. These vapours form at significant mass yield in the gas phase and condense irreversibly onto aerosol surfaces to produce secondary organic aerosol, helping to explain the discrepancy between the observed atmospheric burden of secondary organic aerosol and that reported by many model studies<sup>2</sup>. We further demonstrate how these low-volatility vapours can enhance, or even dominate, the formation and growth of aerosol particles over forested regions, providing a missing link between biogenic VOCs and their conversion to aerosol particles. Our findings could help to improve assessments of biosphere–aerosol–climate feedback mechanisms<sup>6–8</sup>, and the air quality and climate effects of biogenic emissions generally.

We studied the oxidation of several monoterpenes and other VOCs under atmospherically relevant conditions in the highly instrumented Jülich Plant Atmosphere Chamber, JPAC<sup>9</sup>, a continuously stirred tank reactor (see Methods for experimental details). We focus here on  $\alpha$ -pinene, as it alone constitutes nearly 50% of global monoterpene emissions<sup>10</sup>. Using a high-resolution chemical ionization mass spectrometer, CI-API-TOF<sup>11</sup> (see Methods) we detected highly oxygenated, high-molecular-mass gas-phase oxidation products from several precursors following both ozonolysis and reaction with the hydroxyl radical (OH). Figure 1 depicts an  $\alpha$ -pinene ozonolysis spectrum displaying monomer ( $C_{10}H_{14-16}O_{7-11}$ ) and dimer ( $C_{19-20}H_{28-32}O_{10-18}$ ) patterns. We collectively refer to such products, both monomers and dimers, as extremely low-volatility organic compounds (ELVOCs<sup>12</sup>). We estimate an uncertainty of  $\pm 50\%$  for absolute concentrations of ELVOCs (see Methods) whereas relative changes are precise to  $<10\%$ . Importantly, with the experimental conditions

probed in JPAC, we could closely replicate both daytime and nighttime ELVOC mass spectra recorded at a boreal forest site in Hyytiälä, Finland (Extended Data Fig. 1a, b).

During steady-state  $\alpha$ -pinene ozonolysis experiments, the total ELVOC concentration had a near-linear dependence on the amount of  $\alpha$ -pinene reacting with  $O_3$  (Fig. 2a), indicative of first-generation products. The majority of the data are explained by ELVOC molar yields of 6–8%. Owing to the large molecular masses of the ELVOCs, a 6% molar yield translates to a mass yield of 14% (see Methods). On the basis of structure–activity relationships<sup>13</sup>, ELVOCs have vapour pressures orders of magnitude lower than most previously identified gas-phase oxidation products of VOCs, and should thus condense irreversibly to form a substantial component of  $\alpha$ -pinene secondary organic aerosol (SOA)<sup>10,14</sup>. Consistent with this idea, the addition of 100-nm solid ammonium sulphate particles to the chamber under constant  $\alpha$ -pinene ozonolysis conditions caused both a clear decrease in ELVOC concentration (quantitatively explained by diffusion-limited condensation to the ammonium sulphate particles) and a corresponding increase in SOA (Fig. 2b). Gas-phase concentrations of abundant semi-volatile organic compounds (SVOCs) such as pinic and pinonic acid were not observed to decrease appreciably when seed aerosol was added (Extended Data Fig. 2b).

At low total aerosol loadings, the measured SOA mass in our experiments was almost entirely explained by ELVOCs lost via condensation to the ammonium sulphate particles (Fig. 2c). Even at higher SOA loadings ( $\sim 10 \mu g m^{-3}$ ), at which SVOCs probably begin contributing more via absorptive partitioning<sup>15</sup>, roughly two-thirds of the SOA mass was still explained by ELVOC condensation. Additionally, the formed SOA and the condensed ELVOCs had essentially the same O/C and H/C elemental ratios of  $0.7 \pm 0.1$  and  $1.5 \pm 0.1$ , respectively (Extended Data Fig. 3). This further supports ELVOCs being the main SOA source at low loadings, and to our knowledge, we provide the first demonstration of mass closure between condensation of gas-phase oxidation products and SOA mass formed during monoterpene oxidation.

Although it is perhaps surprising that a previously unmeasured class of gas-phase oxidation products can dominate  $\alpha$ -pinene ozonolysis SOA at low loadings, irreversible ELVOC condensation helps explain seemingly disparate characteristics of  $\alpha$ -pinene SOA. Relatively high SOA mass yields have been found<sup>16</sup> at low loadings, which suggests the presence of a very low-volatility product. Additionally, several independent methods suggest that  $\alpha$ -pinene SOA formed at low loadings is semi-solid with slow evaporation, consistent with the presence of a very low-volatility, highly oxygenated, high-molecular-mass component<sup>14,17,18</sup>. These characteristics have called into question the use of equilibrium absorptive partitioning theory to describe  $\alpha$ -pinene SOA<sup>18</sup>. Our results

<sup>1</sup>Institute for Energy and Climate Research (IEK-8), Forschungszentrum Jülich, 52425 Jülich, Germany. <sup>2</sup>Department of Physics, PO Box 64, 00014 University of Helsinki, Finland. <sup>3</sup>Department of Atmospheric Sciences, University of Washington, Seattle, Washington 98195, USA. <sup>4</sup>Institute of Bio- and Geosciences (IBG-2), Forschungszentrum Jülich, 52425 Jülich, Germany. <sup>5</sup>Institute for Tropospheric Research (TROPOS), 04318 Leipzig, Germany. <sup>6</sup>Helsinki Institute of Physics, PO Box 64, 00014 University of Helsinki, Finland. <sup>7</sup>Department of Chemistry, PO Box 55, 00014 University of Helsinki, Finland. <sup>8</sup>Department of Chemistry, University of Copenhagen, Universitetsparken 5, 2100 Copenhagen Ø, Denmark. <sup>9</sup>Aerodyne Research, Inc., 45 Manning Road, Billerica, Massachusetts 01821, USA. <sup>10</sup>Department of Physics, Tampere University of Technology, PO Box 692, 33101 Tampere, Finland.

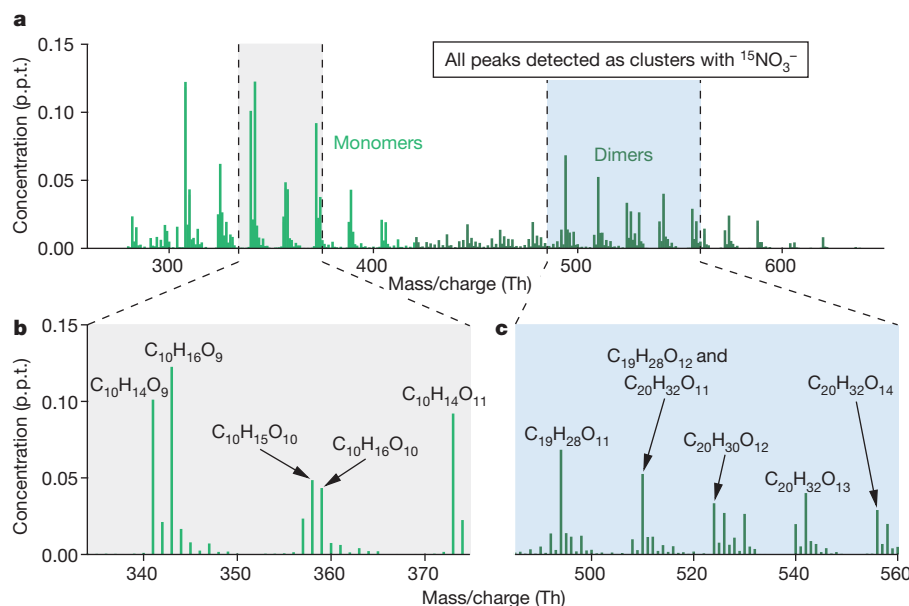


**Figure 1 | Mass spectrum of ELVOCs produced by  $\alpha$ -pinene ozonolysis.** The spectral fingerprint (a) displays clear 'monomer' ( $C_{10}H_{14-16}O_{7-11}$ , example peaks in b) and 'dimer' ( $C_{19-20}H_{28-32}O_{10-18}$ , example peaks in c) distributions. Such compounds have been previously identified, but never quantified, in naturally charged ions<sup>30</sup>. The detection of ELVOCs in the CI-API-TOF, used in the measurements reported here, relies on their efficient clustering with isotopically labelled nitrate reagent ions. Only a few other  $\alpha$ -pinene ozonolysis products are detected outside the plotted range, owing to the selectivity of nitrate clustering in the CI-API-TOF. Mass/charge ratio is plotted in units of thomsons (Th), which equal daltons (Da) per elementary charge ( $e$ ). p.p.t., parts per trillion.

do not contradict absorptive partitioning theory. Rather, our findings will significantly improve its predictive capability by quantifying the formation of extremely low vapour pressure compounds into which SVOCs can presumably partition or react as loadings increase.

In light of the importance of ELVOCs illustrated above, we performed additional experiments and kinetic model calculations aimed at understanding their chemical properties and formation mechanisms. Our detailed findings (Methods) are consistent with a pathway mainly driven by organic peroxy radical ( $RO_2$ ) chemistry, supported in part by our ability to directly detect certain highly oxygenated  $RO_2$ , and the response of these radicals and ELVOCs to nitric oxide (NO)

additions. We hypothesize, backed by experiments using isotopically labelled reactants, that a fraction of  $RO_2$  formed from ozonolysis achieve a high oxygen content by rapid molecular oxygen ( $O_2$ ) additions following intramolecular hydrogen abstractions. This process has only recently been proposed to occur under atmospheric conditions<sup>19,20</sup>, and the successive H-abstractions/ $O_2$ -additions have typically been assumed to terminate before molecules could reach the high O/C ratios we observe. Ozonolysis of endocyclic alkenes (such as  $\alpha$ -pinene) appears to be especially efficient at producing ELVOCs, probably because this reaction forms products where subsequent H-abstractions are favoured, though significant amounts were also produced from OH-oxidation of

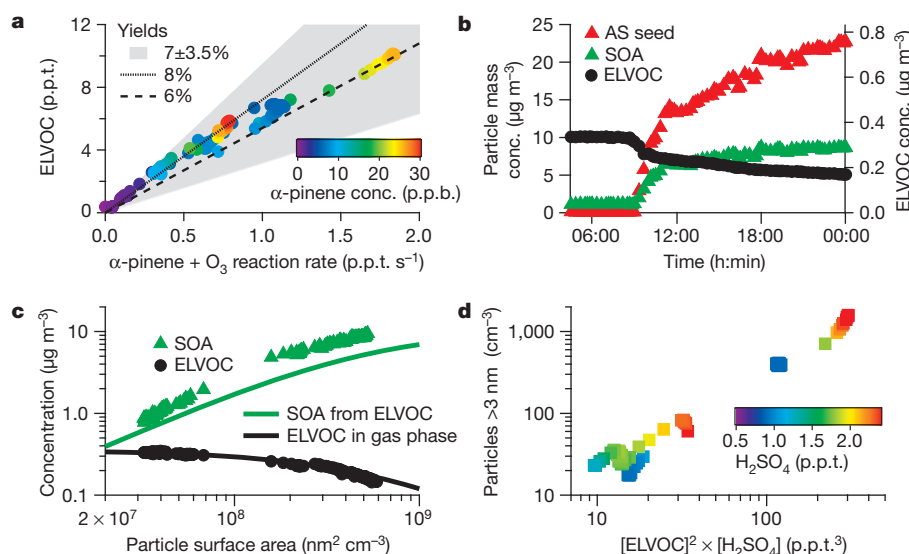


**Figure 2 | ELVOC chamber experiments.** a, Measured total ELVOCs plotted against  $\alpha$ -pinene ozonolysis rate. Points are coloured by  $\alpha$ -pinene concentration, showing that ELVOC concentrations only depend on the product of  $[O_3]$  and  $[\alpha$ -pinene]. The lines correspond to ELVOC molar yields (see key) from  $\alpha$ -pinene ozonolysis, the shaded area denotes a 50% uncertainty. The hydroxyl radical makes a minor contribution to ELVOCs under these conditions (Extended Data Fig. 2a). b, Ammonium sulphate (AS) seed addition (red triangles, left axis) causes a decrease in ELVOCs (black dots, right axis) due to an increased particulate condensation sink, and a corresponding increase in SOA mass (green triangles, left axis) is detected. c, The dependence of ELVOC

and SOA concentrations on particle surface area (condensation sink). Measured data points (symbols) correspond to those in b. The lines depict the theoretically expected behaviour (see Methods) of ELVOCs (black line) and the corresponding accumulated SOA mass from ELVOC condensation (green line). The different chamber lifetimes ( $t_{SOA} \approx 45$  min,  $t_{ELVOC} < 1.5$  min) cause the enhancement of SOA mass compared to condensed ELVOC mass (see Methods). d, The concentration of particles larger than 3 nm is strongly dependent on both  $H_2SO_4$  and ELVOC concentrations, with  $[ELVOC]^2 \cdot [H_2SO_4]$  producing a near-linear slope.



most VOCs. Based on insights from the above experiments, ELVOCs are likely to contain multiple hydroperoxide moieties, in accordance with their high O/C and H/C ratios. The competition between sequential H-abstractions and termination reactions with other RO<sub>2</sub> and NO in high-loading or high-NO<sub>x</sub> experiments, respectively, will potentially change the chemical nature of the SOA by reducing ELVOC formation in favour of less oxidized compounds.

ELVOCs have probably been a major SOA source in most previous chamber experiments conducted at atmospherically relevant  $\alpha$ -pinene loadings, though only the recent application of the CI-API-TOF has facilitated the detection of gas-phase ELVOCs, individually present at sub-parts-per-trillion mixing ratios. This capability allowed us to determine the ELVOC yield, and by adding inorganic seed particles, convert more of this potential SOA into actual SOA mass. In our experiments, the apparent SOA mass yield increased from ~1% with no seed particles to ~10% at the highest seed particle concentrations, which were still not high enough to fully overcome ELVOC losses to walls (see Methods). With much higher amounts of reacted  $\alpha$ -pinene than in our experiments, equilibrium partitioning<sup>15</sup> and reactive uptake<sup>21</sup> of SVOCs become more important sources of SOA mass, thus masking the specific contribution of ELVOCs, though in most cases ELVOCs still probably provide an initial organic medium required for such processes. Although outside the scope of this study, once in the condensed phase, molecules with multiple hydroperoxide moieties will probably participate in accretion reactions<sup>2,21</sup>, further decreasing the volatility of the reactants. Such reactions, and possible thermal decomposition on heating<sup>22</sup>, make it challenging, if not impossible, to detect the same ELVOCs that had condensed from the gas-phase by analysing the SOA<sup>2</sup>. Future efforts should focus on determining the exact structures of gas-phase ELVOCs, and the atmospheric evolution of the SOA formed through ELVOC condensation.

The finding of irreversibly condensing  $\alpha$ -pinene ozonolysis products formed at 14–19% mass yield at the low reactant concentrations in our chamber (Fig. 2a) has significant consequences for the SOA yield estimated from this reaction in the atmosphere. Our results suggest ELVOCs alone can drive the SOA mass yield from  $\alpha$ -pinene ozonolysis beyond 10% above the forest canopy where the condensational sink is the dominant loss for low-volatility vapours. However, existing  $\alpha$ -pinene ozonolysis parameterizations<sup>2</sup> predict that less than 5% of the products have vapour pressures below  $1 \mu\text{g m}^{-3}$ . Applying such yield parameterizations to the atmosphere would thus underestimate SOA, a feature common to current models<sup>2</sup>. Other ELVOC losses (for example, deposition, photolysis or OH oxidation) and shifts in the monomer to dimer ratio (see Methods) may somewhat lower the SOA mass formation potential of ELVOCs, but their contribution to  $\alpha$ -pinene ozonolysis SOA will almost certainly remain important, as we further illustrate below.

As ELVOCs form at significant mass yield and condense irreversibly onto surfaces, they should also contribute to the growth of newly formed particles. We found that concentrations of particles larger than ~3 nm in our chamber depend on both sulphuric acid vapour (H<sub>2</sub>SO<sub>4</sub>) and ELVOC concentrations, scaling approximately linearly with [ELVOC]<sup>2</sup> × [H<sub>2</sub>SO<sub>4</sub>] (Fig. 2d, Extended Data Fig. 4f–i). Thus, although H<sub>2</sub>SO<sub>4</sub> is important in the initial formation of growing clusters smaller than a few nanometres, as earlier studies have shown<sup>4,23</sup>, the formation rate of 3-nm particles is already more strongly driven by ELVOCs under these experimental conditions (see Extended Data Fig. 6d). We therefore propose that the ELVOCs we detect from monoterpene oxidation help explain the appearance and subsequent rapid growth of new particles observed in forested regions<sup>4,5</sup>. Indeed, we find that ELVOC dimers are large enough to act as nano-condensation nuclei<sup>24</sup> (Extended Data Fig. 4a–e). Importantly, using recent direct measurements of ELVOCs during new particle formation and growth events in the Hyytiälä forest, we show that ELVOCs are abundant enough to explain the observed particle growth rates in the 5–50 nm range (Fig. 3).

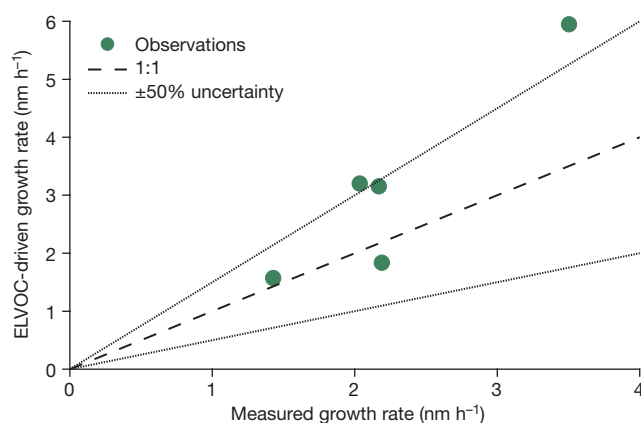


**Figure 3 | Comparison of measured particle growth rates with those predicted from measured ELVOC concentrations in Hyytiälä forest.** Measured growth rates are over the range 5–50 nm; details are given in Methods. The dashed line shows the 1:1 ratio, and the dotted lines correspond to 0.5:1 and 1:1.5, that is, a 50% uncertainty. The ELVOC concentrations are clearly in the right concentration range to be able to explain the majority of the growth of newly formed particles in the boreal forest. We thus have detected and quantified the nearly non-volatile organic compounds required to explain atmospheric particle growth rates, as predicted by previous studies<sup>4,5</sup>.

We have provided the first molecular elucidation and quantification of a direct and ubiquitous source of ELVOCs produced in the gas phase from oxidation of monoterpenes and other VOCs. This source is capable of explaining nanoparticle growth in boreal regions and a significant fraction of low-volatility SOA currently missing, or poorly described, in atmospheric models<sup>1,2,4,5</sup>. A schematic illustration of the atmospheric roles of ELVOCs is presented in Fig. 4. Some atmospheric models can replicate monoterpene SOA by assuming irreversible condensation of unspecified first-generation oxidation products<sup>25</sup>, an approach now validated and clarified by our results. We have also demonstrated mechanisms whereby anthropogenic emissions (SO<sub>2</sub>, NO) can affect the contribution of biogenic VOCs to aerosol particle formation and growth

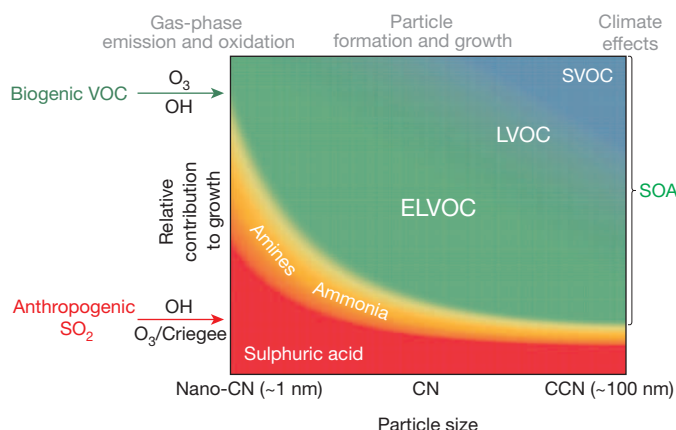


**Figure 4 | The importance of precursor vapours for aerosol growth at different sizes.** This schematic overview depicts the path from emissions of volatile compounds, via aerosol particles, to their climate effects (grey labels at top). Our findings suggest that ELVOCs are major contributors to condensational growth at all sizes, ranging from newly formed particles (nano-condensation nuclei, nano-CN) through to cloud condensation nuclei (CCN). The relative roles of different vapours, described by corresponding colours (H<sub>2</sub>SO<sub>4</sub>, red; bases, orange; organics, varying shades of green), will vary depending on location and prevailing meteorological conditions, but this figure provides an estimate of the average contribution of the most important precursor vapours to particle growth in boreal forest-type environments. Both biogenic VOCs (green arrow on vertical axis) and anthropogenic SO<sub>2</sub> emissions (red arrow on vertical axis) can enhance the formation and growth of particles to climate-relevant sizes.

by interacting with ELVOCs directly (for example,  $\text{H}_2\text{SO}_4$ ) or altering their formation pathways (for example, NO, see Methods).

Our results clearly demonstrate that current oxidation mechanisms underestimate the role of ozone and  $\text{RO}_2$  isomerization chemistry in producing highly oxygenated low-volatility compounds. This underlines the importance of accurately predicting oxidant levels and biogenic VOC emissions. Past or future changes in the ozone/OH ratio<sup>26,27</sup> may represent an additional anthropogenic influence on climate via ELVOC formation and thus concentrations of SOA and cloud condensation nuclei. Moreover, regional and global climate change influences VOC emissions by terrestrial vegetation<sup>28,29</sup>. Our new insights into ELVOC formation may help to more accurately quantify the effects of changes in biogenic VOC emissions—specifically, the effects on new particle formation, abundance of cloud condensation nuclei, and possible related climate feedbacks<sup>6–8</sup>.

## METHODS SUMMARY

The majority of the presented measurements were performed at the Jülich Plant Atmosphere Chamber facility (JPAC<sup>9</sup>). Contrary to many other chamber studies where a batch of VOCs is oxidized over a certain period of time, the JPAC measurements were mainly carried out in a continuously stirred tank reactor under steady-state conditions. This means that a constant flow of reactants and oxidants were added to the chamber until the chamber air (including VOCs, ELVOCs and particles) reached steady-state. The average residence time in the chamber was ~45 min. All ambient data presented in this work were measured at the Station for Measuring Ecosystem-Atmosphere Relations (SMEAR II) in Hyytiälä, Southern Finland.

The efficient ELVOC detection was made possible by the use of nitrate ion clustering at atmospheric pressure, using the CI-API-TOF<sup>11</sup>. This instrument is optimal for ELVOC detection, as its high sample flow rate and nearly wall-less inlet design minimizes losses of low-volatility vapours. The mass spectrometer has a high throughput of sampled ions, and high mass resolution allowing elemental composition determination up to masses where ELVOCs are detected (Fig. 1). Additionally, the selectivity of nitrate chemical ionization keeps the spectrum clean from many background contaminants, as well as more abundant, less oxidized compounds.

**Online Content** Any additional Methods, Extended Data display items and Source Data are available in the online version of the paper; references unique to these sections appear only in the online paper.

**Received 7 August 2013; accepted 14 January 2014.**

- Jimenez, J. L. *et al.* Evolution of organic aerosols in the atmosphere. *Science* **326**, 1525–1529 (2009).
- Hallquist, M. *et al.* The formation, properties and impact of secondary organic aerosol: current and emerging issues. *Atmos. Chem. Phys.* **9**, 5155–5236 (2009).
- Solomon, S. *et al.* (eds) *Climate Change 2007: The Physical Science Basis* (Cambridge Univ. Press, 2007).
- Kulmala, M. *et al.* Direct observations of atmospheric aerosol nucleation. *Science* **339**, 943–946 (2013).
- Riipinen, I. *et al.* Organic condensation: a vital link connecting aerosol formation to cloud condensation nuclei (CCN) concentrations. *Atmos. Chem. Phys.* **11**, 3865–3878 (2011).
- Paasonen, P. *et al.* Warming-induced increase in aerosol number concentration likely to moderate climate change. *Nature Geosci.* **6**, 438–442 (2013).
- Carlsaw, K. S. *et al.* A review of natural aerosol interactions and feedbacks within the Earth system. *Atmos. Chem. Phys.* **10**, 1701–1737 (2010).
- Spracklen, D. V., Bonn, B. & Carlsaw, K. S. Boreal forests, aerosols and the impacts on clouds and climate. *Phil. Trans. R. Soc. A* **366**, 4613–4626 (2008).
- Mentel, T. F. *et al.* Photochemical production of aerosols from real plant emissions. *Atmos. Chem. Phys.* **9**, 4387–4406 (2009).
- Pathak, R. K., Stanier, C. O., Donahue, N. M. & Pandis, S. N. Ozonolysis of  $\alpha$ -pinene at atmospherically relevant concentrations: temperature dependence of aerosol mass fractions (yields). *J. Geophys. Res.* **D 112**, D03201 (2007).
- Jokinen, T. *et al.* Atmospheric sulphuric acid and neutral cluster measurements using CI-API-TOF. *Atmos. Chem. Phys.* **12**, 4117–4125 (2012).
- Donahue, N. M., Kroll, J. H., Pandis, S. N. & Robinson, A. L. A two-dimensional volatility basis set – Part 2: diagnostics of organic-aerosol evolution. *Atmos. Chem. Phys.* **12**, 615–634 (2012).
- Capouet, M. & Muller, J. F. A group contribution method for estimating the vapour pressures of  $\alpha$ -pinene oxidation products. *Atmos. Chem. Phys.* **6**, 1455–1467 (2006).
- Grieshop, A. P., Donahue, N. M. & Robinson, A. L. Is the gas-particle partitioning in  $\alpha$ -pinene secondary organic aerosol reversible? *Geophys. Res. Lett.* **34**, L14810 (2007).
- Pankow, J. F. Gas/particle partitioning of neutral and ionizing compounds to single and multiple-phase aerosol particles. 1. Unified modeling framework. *Atmos. Environ.* **37**, 3323–3333 (2003).
- Shilling, J. E. *et al.* Particle mass yield in secondary organic aerosol formed by the dark ozonolysis of  $\alpha$ -pinene. *Atmos. Chem. Phys.* **8**, 2073–2088 (2008).
- Virtanen, A. *et al.* An amorphous solid state of biogenic secondary organic aerosol particles. *Nature* **467**, 824–827 (2010).
- Vaden, T. D., Imre, D., Beránek, J., Shrivastava, M. & Zelenyuk, A. Evaporation kinetics and phase of laboratory and ambient secondary organic aerosol. *Proc. Natl Acad. Sci. USA* **108**, 2190–2195 (2011).
- Vereecken, L., Muller, J. F. & Peeters, J. Low-volatility poly-oxygenates in the OH-initiated atmospheric oxidation of  $\alpha$ -pinene: impact of non-traditional peroxy radical chemistry. *Phys. Chem. Chem. Phys.* **9**, 5241–5248 (2007).
- Crounse, J. D., Nielsen, L. B., Jørgensen, S., Kjaergaard, H. G. & Wennberg, P. O. Autooxidation of organic compounds in the atmosphere. *J. Phys. Chem. Lett.* **4**, 3513–3520 (2013).
- Shiraiwa, M. *et al.* Size distribution dynamics reveal particle-phase chemistry in organic aerosol formation. *Proc. Natl Acad. Sci. USA* **110**, 11746–11750 (2013).
- Hall, W. A. & Johnston, M. V. The thermal-stability of oligomers in alpha-pinene secondary organic aerosol. *Aerosol Sci. Technol.* **46**, 983–989 (2012).
- Sipilä, M. *et al.* The role of sulfuric acid in atmospheric nucleation. *Science* **327**, 1243–1246 (2010).
- McMurry, P. H., Kulmala, M. & Worsnop, D. R. Special issue on aerosol measurements in the 1 nm range. *Aerosol Sci. Technol.* **45**, i (2011).
- Spracklen, D. V. *et al.* Aerosol mass spectrometer constraint on the global secondary organic aerosol budget. *Atmos. Chem. Phys.* **11**, 12109–12136 (2011).
- Naik, V. *et al.* Preindustrial to present-day changes in tropospheric hydroxyl radical and methane lifetime from the Atmospheric Chemistry and Climate Model Intercomparison Project (ACCMIP). *Atmos. Chem. Phys.* **13**, 5277–5298 (2013).
- Parrish, D. D. *et al.* Long-term changes in lower tropospheric baseline ozone concentrations at northern mid-latitudes. *Atmos. Chem. Phys.* **12**, 11485–11504 (2012).
- Guenther, A. *et al.* A model of natural volatile organic compound emissions. *J. Geophys. Res.* **100**, 8873–8892 (1995).
- Young, P. J., Arneth, A., Schurgers, G., Zeng, G. & Pyle, J. A. The  $\text{CO}_2$  inhibition of terrestrial isoprene emission significantly affects future ozone projections. *Atmos. Chem. Phys.* **9**, 2793–2803 (2009).
- Ehn, M. *et al.* Gas phase formation of extremely oxidized pinene reaction products in chamber and ambient air. *Atmos. Chem. Phys.* **12**, 5113–5127 (2012).

**Acknowledgements** M.E. was supported by the Emil Aaltonen foundation; J.A.T. was supported by the US Department of Energy, Office of Science (DE-SC0006867). This work was supported by the ERC Advanced Grant EU-FP7-ATMNUCLE (project no. 227463), the EU-FP7 project PEGASOS (project no. 265148), the Academy of Finland (project no. 251427 and 266388) and by the Academy of Finland Center of Excellence programme (project no. 1118615). We thank M. Kajos, S. Schallhart and T. Ruuskanen for measurement support, O. Kupiainen for collision rate calculations, and the tofTools team for analysis tools for mass spectra.

**Author Contributions** M.E., J.A.T., E.K., I.P., M. Springer, F.R., R.T., B.L., F.L.-H., S.A., I.-H.A., M.R., T.J., J. Kangasluoma, T.B. and J.W. conducted the data collection and analysis. H.J. and M.C. provided data analysis tools. J. Kontkanen and T.N. analysed the ambient data. M.E., J.A.T., T.K., L.B.N., S.J., H.G.K. and T.F.M. provided model calculations and developed the formation mechanism. M.E. and J.A.T. wrote the manuscript. M. Sipilä, M.D.M., T.P., A.W., V.-M.K., M.K., D.W. and T.F.M. did data interpretation and editing of the manuscript. All authors discussed the results and commented on the paper.

**Author Information** Reprints and permissions information is available at [www.nature.com/reprints](http://www.nature.com/reprints). The authors declare no competing financial interests. Readers are welcome to comment on the online version of the paper. Correspondence and requests for materials should be addressed to M.E. (mikael.ehn@helsinki.fi).

# Rapid remobilization of magmatic crystals kept in cold storage

Kari M. Cooper<sup>1</sup> & Adam J. R. Kent<sup>2</sup>

The processes involved in the formation and storage of magma within the Earth's upper crust are of fundamental importance to volcanology. Many volcanic eruptions, including some of the largest, result from the eruption of components stored for tens to hundreds of thousands of years before eruption<sup>1–3</sup>. Although the physical conditions of magma storage and remobilization are of paramount importance for understanding volcanic processes, they remain relatively poorly known<sup>4,5</sup>. Eruptions of crystal-rich magma are often suggested to require the mobilization of magma stored at near-solidus conditions<sup>6–8</sup>; however, accumulation of significant eruptible magma volumes has also been argued to require extended storage of magma at higher temperatures<sup>7–9</sup>. What has been lacking in this debate is clear observational evidence linking the thermal (and therefore physical) conditions within a magma reservoir to timescales of storage—that is, thermal histories. Here we present a method of constraining such thermal histories by combining timescales derived from uranium-series disequilibria, crystal sizes and trace-element zoning in crystals. At Mount Hood (Oregon, USA), only a small fraction of the total magma storage duration (at most 12 per cent and probably much less than 1 per cent) has been spent at temperatures above the critical crystallinity (40–50 per cent) at which magma is easily mobilized. Partial data sets for other volcanoes also suggest that similar conditions of magma storage are widespread and therefore that rapid mobilization of magmas stored at near-solidus temperatures is common. Magma storage at low temperatures indicates that, although thermobarometry calculations based on mineral compositions may record the conditions of crystallization, they are unlikely to reflect the conditions of most of the time that the magma is stored. Our results also suggest that largely liquid magma bodies that can be imaged geophysically will be ephemeral features and therefore their detection could indicate imminent eruption.

The thermal histories of magma bodies stored within the Earth's crust exert an important influence over the processes that lead to volcanic eruptions, but are poorly constrained by current observational data sets. Many volcanic eruptions involve magmatic components that have been stored within the Earth's crust for extended periods (tens to hundreds of thousands of years)<sup>1–3</sup>, and an understanding of the processes that lead to mobilization and eruption of these components is an important research goal, particularly where these can be linked to precursory phenomena that can be observed geophysically or by other remote means. One major area of uncertainty and a source of current debate are the thermal conditions under which magmas are stored within the crust<sup>3,4,6–8,10–13</sup>. Numerical models of magma remobilization and storage have shown that the viscosity of the stored magma (or crystal-rich magmatic 'mush') has a key role in the initiation of eruptions, the volume of magma that may be erupted from a reservoir, and the degree to which magmas are well mixed versus heterogeneous<sup>4,7,8</sup>. In turn, the viscosity of magma depends on temperature both directly and indirectly through variables such as crystallinity, dissolved water content and bubble content.

Therefore, the pre-eruptive thermal history is a critical factor in understanding magma behaviour. Of particular importance is constraining

the proportion of time that a magma body spends as a mechanically locked network as opposed to a relatively low-viscosity, eruptible body of magma<sup>7</sup>. Numerical models can delimit the thermal conditions necessary to maintain magma in a certain physical state for a given duration but cannot uniquely determine the total amount of time that magma is stored within the crust<sup>4,8,10,13</sup>. To further our understanding of magma storage and eruption mechanisms we need a method of independently constraining the total duration of storage and linking that storage time to the thermal state of the magma body.

Our approach to constraining thermal histories during crustal magma storage makes use of the varied information archived in crystal records. We use the U-series age of crystals to provide an absolute timescale for crystal residence and use temperature-dependent processes (diffusion of trace elements and crystal growth) to place constraints on how much of that history can have been spent at high temperature and therefore at low viscosity.

A compilation of crystal residence timescales (Fig. 1) documents a global pattern in which <sup>238</sup>U–<sup>230</sup>Th crystallization ages are typically older than <sup>230</sup>Th–<sup>226</sup>Ra crystallization ages, which are one to two orders of magnitude older than crystal residence ages based on diffusion or crystal size distributions. This observation has been noted before, and reflects the difference between an absolute age determined radiometrically (which, in turn, is averaged differently by the two parent–daughter pairs<sup>1,14</sup>; see Methods and Extended Data Fig. 1) and an elapsed time at high temperature constrained by diffusion<sup>15</sup> or crystal growth<sup>16</sup>. However, a previously unrecognized aspect of this difference in apparent ages is that we can use it to quantify the proportion of residence time spent at high temperature (Fig. 2). Radiometric ages, such as the U-series systems we use here, are largely unaffected by the thermal history and provide a means of gauging the absolute time that crystals have existed (Fig. 2). In contrast, the preservation of disequilibrium trace-element concentrations coupled with diffusion modelling limits the time spent at or above temperatures at which diffusion is sufficiently rapid to allow equilibration. Finally, the maximum crystal size or the crystal size distribution, in conjunction with estimates of crystal growth rates, reflects the duration of residence of these crystals at temperatures between the liquidus and solidus, where crystal growth can occur (Fig. 2). Petrological modelling (for example, R-MELTS modelling<sup>17</sup>) can be used to link these thermal constraints to the crystallinity and therefore to the effective viscosity of the magma in question (Fig. 3; Methods).

We apply this method to data for samples of the two most recent eruptions at Mount Hood, Oregon, occurring at approximately 1,500 years ago (Timberline) and 220 years ago (Old Maid)<sup>18</sup>. We have previously documented abundant evidence that injection of ascending mafic magma into a rhyodacitic to rhyolitic magma body stored at shallow crustal levels produces the monotonous andesites erupted throughout the volcano's history<sup>19,20</sup>. Crystal size distributions of plagioclase from erupted andesites show a kinked pattern, consistent with mixing of small, mafic-magma-derived crystals with larger crystals derived from the stored silicic magma<sup>19</sup>. We focus here on the population derived from the silicic magma because that is representative of the storage conditions within the upper

<sup>1</sup>Department of Earth and Planetary Sciences, University of California, Davis, One Shields Avenue, Davis, California 95616, USA. <sup>2</sup>College of Earth, Ocean and Atmospheric Sciences, 104 Ocean Administration, Oregon State University, Corvallis, Oregon 97331, USA.



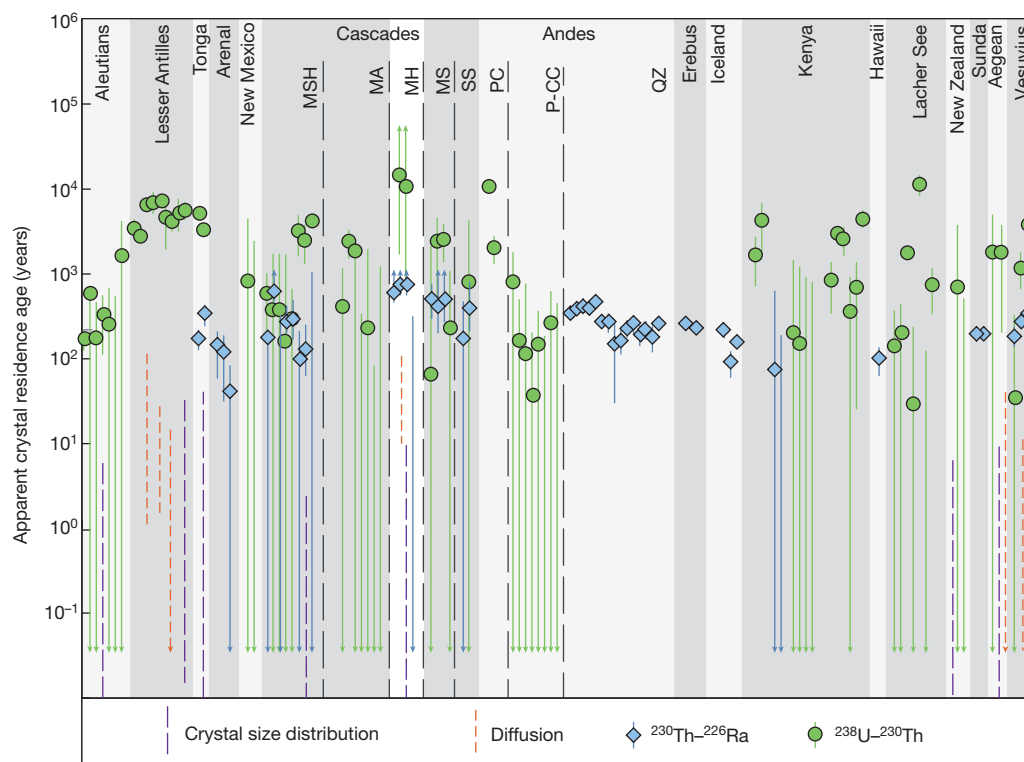


**Figure 1 | Global compilation of crystal residence ages.** Global compilation of all available data for  $^{238}\text{U}$ – $^{230}\text{Th}$ – $^{226}\text{Ra}$  crystal residence ages of major phases, and available crystal residence ages derived from CSD and from diffusion of trace elements in samples from the same volcanic systems. Regions are labelled, and individual volcanic centres within each region are abbreviated as follows: MSH, Mount St Helens; MA, Mount Adams; MH, Mount Hood; MS, Mount Shasta; SS, South Sister; PC, Parícut; P-CC, Puyehue-Cordon Caulle; QZ, Quizapu. Error bars for U-series crystal residence ages indicate maximum and minimum residence ages calculated by combining the  $2\sigma$  uncertainty on the crystal age with the  $2\sigma$  uncertainty on the eruption age (where both are given in the original reference; see Methods for details).

Arrows on error bars indicate samples with ages within error of eruption age (downward-pointing arrows) or indeterminate age maxima (see Methods). Mean or best-estimate ages are shown by green filled circles ( $^{238}\text{U}$ – $^{230}\text{Th}$  ages) or blue filled diamonds ( $^{230}\text{Th}$ – $^{226}\text{Ra}$  ages); lines without symbols indicate samples for which only a maximum and minimum age estimate were available. The lengths of lines representing crystal residence ages from CSD and diffusion indicate the uncertainties in crystal growth rates and temperature, respectively (see Methods). Data are from references cited in ref. 1, and additional references published subsequently (full reference list given in Methods; source data available as an Excel table online).

crust, and because the larger plagioclase from each of the two most recent eruptions appear identical in major- and trace-element composition and in age<sup>19,21</sup>. Mineral geobarometry also shows that these crystals were formed within the shallow crust at pressures of 100–200 MPa (4–8 km)<sup>20,22</sup>.  $^{238}\text{U}$ – $^{230}\text{Th}$  ages of the same crystals are older than  $^{230}\text{Th}$ – $^{226}\text{Ra}$  ages (minimum age for the bulk mineral separate of 17,000 years and mean age of 126,000 years, compared to average  $^{230}\text{Th}$ – $^{226}\text{Ra}$  ages of less than 10,000 years; ref. 21), indicating that there were at least two stages of crystal growth<sup>21</sup>. Assuming a simple two-stage growth history where the younger growth episode occurred immediately before eruption (consistent with petrographic observations and with post-mixing Mg diffusion timescales in rims<sup>19</sup>) yields a minimum age for the older crystallization episode of 21,000 years (ref. 21). Collectively, these data suggest that the same silicic magma body has been stored within the shallow crust for tens or hundreds of thousands of years, and has been resampled repeatedly by interaction with successive batches of mafic magma—which were not themselves stored for long periods of time at upper-crustal conditions<sup>19,21</sup>.

The distribution of Sr within plagioclase crystals derived from the shallow silicic magma also provides constraints on the thermal conditions of crystal residence. Measured Sr profiles across these crystals show significant disequilibria relative to profiles expected to be in equilibrium with a fixed melt Sr content (Methods, Extended Data Figs 2–4). In conjunction with forward models of Sr diffusion we can use this observation to constrain the maximum residence time for each plagioclase crystal at a given storage temperature. The results are summarized in Fig. 3 and Extended Data Figs 5–7 and Extended Data Table 1 and give

maximum residence times ranging from a few decades at temperatures over 900 °C, up to 140–2,800 years at 750 °C. Thus, during the >21,000-year history of these crystals, they spent, at most, less than 12% of this time at temperatures of 750 °C or above. In addition, the residence estimates based on Sr diffusion are maximum values (see Methods) and these calculations are based on the minimum U–Th age of 21,000 years. If the mean U–Th age of 126,000 years is more representative of the age of the old cores (that is, all but the outermost 50–100 µm) of these crystals (which also preserve Sr disequilibrium), the total residence time at above 750 °C is likely to be much less than 1% of the total age of the crystals.

These conclusions are supported by an independent estimate of crystal residence times derived from crystal size data. One approach to constraining the total crystal growth time is simply to combine the maximum observed crystal size with estimates of growth rates to obtain the growth duration. The largest observed plagioclase crystals in our Mount Hood samples are about 3 mm in maximum dimension. Using typical plagioclase growth rates from the literature<sup>23–27</sup> of  $10^{-8}$  to  $10^{-10}$  cm s<sup>-1</sup>, such a crystal would have taken approximately 1–100 years to grow (Methods; Extended Data Fig. 8). This represents the time spent between the plagioclase liquidus and the magma solidus (about 930–700 °C; Fig. 3), again corresponding to a fraction of a per cent up to about 1% of the 21,000-year minimum total time. Even if average growth rates were  $10^{-11}$  cm s<sup>-1</sup> (the lower end of well-constrained plagioclase growth rates) the growth time would be only around 1,000 years, about 5% of the minimum total time. The slope of the crystal size distributions (CSD) gives another estimate of the mean crystal residence age (assuming an

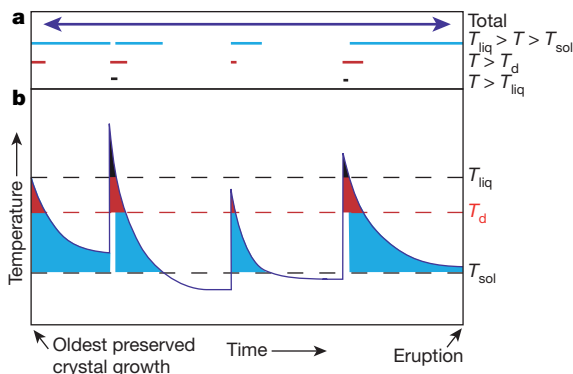


**Figure 2 | Schematic diagram illustrating our approach to constraining thermal histories.** **a**, Summary of durations of crystal residence in different temperature intervals, as derived from schematic temperature–time history within a magma reservoir (dark blue line) over the interval between the onset of crystallization to eruption (**b**). Black dashed lines indicate the solidus and liquidus temperatures ( $T_{\text{sol}}$  and  $T_{\text{liq}}$ , respectively). Coloured regions in **b** and lines in **a** indicate the various crystal residence times as follows. The dark blue line represents the total time represented by the crystal record for crystals sampled, constrained by the U-series crystal ages. Light blue line segments and regions represent the duration of crystal growth within the temperature interval between liquidus and solidus, constrained by the total crystal growth time from crystal size or CSD slope. Red line segments and regions represent the maximum duration at or above a given temperature ( $T_d$ ; red dashed line) constrained by diffusion modelling of trace-element profiles, and black line segments and regions indicate the duration of temperatures higher than  $T_{\text{liq}}$ , at which crystals would be rapidly dissolving, constrained by crystal dissolution rates and diffusion.

open, steady-state system<sup>16</sup>; see Methods) of less than 100 years, using a range of growth rates from  $10^{-8}$  to  $10^{-11}$  cm s<sup>-1</sup> (Extended Data Fig. 8 and Extended Data Table 2). Even if some growth had been erased by dissolution, the diffusion data suggest that this was a relatively minor effect (Methods). Thus, the crystal size data again indicate that the existing crystals could have spent only a small fraction of their time at conditions that allow plagioclase growth.

These data collectively place important constraints on the thermal state of the magma reservoir where the Mount Hood plagioclase crystals were stored: that is, that the magma most probably spent >99% (and at least 88%) of the past 21,000 years (and probably longer) at temperatures below about 750 °C. Rhyolite-MELTS<sup>17</sup> calculations indicate that the rheological transition between an eruptible (less than about 40% crystals<sup>7</sup>), low-viscosity magma capable of convection and a rigid mush for this composition occurs at about 750 °C (Fig. 3). Therefore, the Mount Hood shallow magma reservoir is not maintained at higher temperatures (that is, in an easily eruptible state) by periodic recharge of hotter magma<sup>9</sup> but rather is remobilized from a cold and rigid state via recharge events and erupted almost immediately. On the basis of chemical and age data<sup>19,21</sup>, the silicic population of crystals sampled in different eruptions is identical. Therefore, the region from which these silicic crystals are derived is not simply a quiescent body of magma at the periphery of the Mount Hood reservoir, but is part of the active magma reservoir. The implications of these observations are that the time between reheating and remobilization of the silicic magma body and eruption is short (consistent with other arguments based on Mg diffusion<sup>19</sup>), and that the system was relatively cool when reactivated. This conclusion is also consistent with the general lack of geophysical evidence for high-melt-fraction magma bodies beneath most volcanoes.

The combination of U-series crystal ages, diffusion data and textural information applied to a single volcano is rare, and the combination of data where all analyses apply to the same samples is so far unique to Mount Hood; therefore the extent to which our conclusions apply to other systems requires further investigation. However, partial data sets or combinations of data from different eruptions within the same system (Fig. 1) show that the general pattern of order-of-magnitude difference

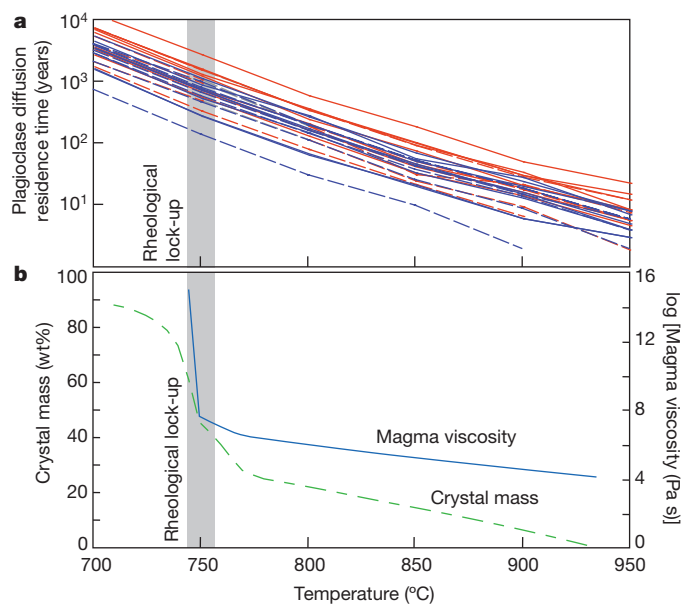


**Figure 3 | Results of diffusion and R-MELTS modelling.** **a**, Calculated plagioclase diffusion residence times as a function of temperature constrained by finite difference modelling. Results are shown for the two methods of estimating the initial Sr distribution: (1) using a best fit to the observed Sr versus anorthite distribution (blue lines), and (2) using the R-MELTS package to estimate the liquid line of descent (red lines). Dashed and solid lines indicate results for individual crystal traverses from samples MH-09-11 and MH-09-05, respectively. **b**, Crystal mass (green dashed line) and magma viscosity (blue line) as a function of temperature calculated by R-MELTS using the estimated silicic magma composition for Mount Hood from ref. 19. In each panel, grey boxes indicate the temperature interval where the magma reaches the critical crystallinity of 40%–60%, where rheological lock-up occurs. See Methods for additional details.

between CSD and diffusion ages versus U-series ages holds in many other arc systems, suggesting that many volcanic systems erupt magma that spends the majority of pre-eruptive storage under relatively cool, viscous and uneruptible conditions. Whether this behaviour is ubiquitous remains to be seen; some magma systems have been argued to be maintained at high temperatures over longer times<sup>7,9</sup>, and, as with the Mount Hood mafic component, mafic magmas appear to have much shorter transit and storage times<sup>28,29</sup>. However, the pattern we see at Mount Hood and at other systems (as implied by our data compilation) suggests that eruption of many silicic magma bodies occurs via rapid mobilization or ‘defrosting’ of crystal-rich mush stored at cooler and rheologically locked conditions<sup>4,13</sup> instead of a long crustal residence of magmas maintained at elevated temperatures, within a so-called ‘eruptible’ zone<sup>7,9</sup>.

Application of the techniques outlined here to a range of other volcanic systems provides a means of testing these ideas, to determine whether fundamentally different modes of magma storage exist, and to further constrain the variables controlling the thermal and therefore physical conditions of magmas within the crust. Even without complete data sets for other volcanoes, the implications of these findings for Mount Hood and for other similar systems are profound. Although mineral thermobarometry is commonly used to constrain conditions of magma storage immediately before eruption, our results indicate that although the temperature conditions determined by thermometry record that of mineral growth, they are unlikely to be representative of the magma during long-term crustal storage. The remarkable similarity in crystal residence times derived from diffusion and size data also suggests that the majority of plagioclase growth took place at temperatures above 750 °C rather than at near-solidus conditions. Finally, in terms of volcanic hazards, if long-term storage of magma generally occurs at high crystallinity as our data suggest, the geophysical detection of a largely liquid magma body may imply imminent eruption.

## METHODS SUMMARY

The CSD were measured and crystal residence ages calculated for plagioclase from eight lava samples from Mount Hood following the procedures outlined in ref. 19, and references therein, using a range of crystal growth rates from  $10^{-8}$ – $10^{-11}$  cm s $^{-1}$ . Residence ages for selected plagioclase crystals were also constrained using Sr concentrations measured by laser ablation inductively coupled plasma mass spectrometry along profiles in individual plagioclase crystals, combined with the results of one-dimensional forward modelling of Sr diffusion using a finite difference method<sup>15,30</sup>.

**Online Content** Any additional Methods, Extended Data display items and Source Data are available in the online version of the paper; references unique to these sections appear only in the online paper.

**Received 22 August; accepted 11 December 2013.**

**Published online 16 February 2014.**

- Cooper, K. M. & Reid, M. R. Uranium-series crystal ages. *Rev. Mineral. Geochem.* **69**, 479–544 (2008).
- Reid, M. R. How long does it take to supersize an eruption? *Elements* **4**, 23–28 (2008).
- Schmitt, A. K. Uranium series accessory crystal dating of magmatic processes. *Annu. Rev. Earth Planet. Sci.* **39**, 321–349 (2011).
- Burgisser, A. & Bergantz, G. W. A rapid mechanism to remobilize and homogenize highly crystalline magma bodies. *Nature* **471**, 212–215 (2011).
- Druitt, T. H., Costa, F., Deloule, E., Dungan, M. & Scaillet, B. Decadal to monthly timescales of magma transfer and reservoir growth at a caldera volcano. *Nature* **482**, 77–80 (2012).
- Bachmann, O. & Bergantz, G. W. Rhyolites and their source mushes across tectonic settings. *J. Petrol.* **49**, 2277–2285 (2008).
- Gelman, S. E., Gutierrez, F. J. & Bachmann, O. On the longevity of large upper crustal silicic magma reservoirs. *Geology* **41**, 759–762 (2013).
- Huber, C., Bachmann, O. & Dufek, J. Crystal-poor versus crystal-rich ignimbrites: a competition between stirring and reactivation. *Geology* **40**, 115–118 (2012).
- Annen, C., Pichavant, M., Bachmann, O. & Burgisser, A. Conditions for the growth of a long-lived shallow crustal magma chamber below Mount Pelee volcano (Martinique, Lesser Antilles Arc). *J. Geophys. Res.* **113**, B07209, <http://dx.doi.org/10.1029/2007JB005049> (2008).
- Annen, C. From plutons to magma chambers: thermal constraints on the accumulation of eruptible silicic magma in the upper crust. *Earth Planet. Sci. Lett.* **284**, 409–416 (2009).
- Bachmann, O., Miller, C. F. & de Silva, S. L. The volcanic-plutonic connection as a stage for understanding crustal magmatism. *J. Volcanol. Geotherm. Res.* **167**, 1–23 (2007).
- Davis, J. W., Coleman, D. S., Gracely, J. T., Gaschnig, R. & Stearns, M. Magma accumulation rates and thermal histories of plutons of the Sierra Nevada batholith, CA. *Contrib. Mineral. Petrol.* **163**, 449–465 (2012).
- Karlstrom, L., Rudolph, M. L. & Manga, M. Caldera size modulated by the yield stress within a crystal-rich magma reservoir. *Nature Geosci.* **5**, 402–405 (2012).
- Cooper, K. M. & Reid, M. R. Re-examination of crystal ages in recent Mount St. Helens lavas: implications for magma reservoir processes. *Earth Planet. Sci. Lett.* **213**, 149–167 (2003).
- Costa, F., Dohmen, R. & Chakraborty, S. Time scales of magmatic processes from modeling the zoning patterns of crystals. *Rev. Mineral. Geochem.* **69**, 545–594 (2008).
- Marsh, B. D. On the interpretation of crystal size distributions in magmatic systems. *J. Petrol.* **39**, 553–599 (1998).
- Gualda, G. A. R., Ghiorso, M. S., Lemons, R. V. & Carley, T. L. Rhyolite-MELTS: a modified calibration of MELTS optimized for silica-rich, fluid-bearing magmatic systems. *J. Petrol.* **53**, 875–890 (2012).
- Scott, W. E. *et al.* *Geologic History of Mount Hood Volcano, Oregon: A Field Trip Guidebook* 1–38 (USGS Open File Report 97-263, 1997).
- Kent, A. J. R., Darr, C., Koleszar, A. M., Salisbury, M. J. & Cooper, K. M. Preferential eruption of andesitic magmas through recharge filtering. *Nature Geosci.* **3**, 631–636 (2010).
- Koleszar, A. M. *Control on Eruption Style and Magma Compositions at Mount Hood, Oregon*. PhD thesis, Oregon State Univ. (2011).
- Eppich, G. R., Cooper, K. M., Kent, A. J. R. & Koleszar, A. Constraints on crystal storage timescales in mixed magmas: uranium-series disequilibria in plagioclase from Holocene magmas at Mount Hood, Oregon. *Earth Planet. Sci. Lett.* **317**, 317–318 (2012).
- Koleszar, A. M., Kent, A. J. R., Wallace, P. J. & Scott, W. E. Controls on long-term low explosivity at andesitic arc volcanoes: insights from Mount Hood, Oregon. *J. Volcanol. Geotherm. Res.* **219–220**, 1–14 (2012).
- Armienti, P. Decryption of igneous rock textures: crystal size distribution tools. *Rev. Mineral. Geochem.* **69**, 623–649 (2008).
- Cashman, K. V. Relationship between plagioclase crystallization and cooling rate in basaltic melts. *Contrib. Mineral. Petrol.* **113**, 126–142 (1993).
- Larsen, J. F. Experimental study of plagioclase rim growth around anorthite seed crystals in rhyodacitic melt. *Am. Mineral.* **90**, 417–427 (2005).
- Pupier, E., Duchene, S. & Toplis, M. J. Experimental quantification of plagioclase crystal size distribution during cooling of a basaltic liquid. *Contrib. Mineral. Petrol.* **155**, 555–570 (2008).
- Ruprecht, P., Bergantz, G. W. & Dufek, J. Modeling of gas-driven magmatic overturn: Tracking of phenocryst dispersal and gathering during magma mixing. *Geochim. Geophys. Res.* **9**, Q07017, <http://dx.doi.org/10.1029/2008GC002022> (2008).
- Rubin, K. H., van der Zander, I., Smith, M. C. & Bergmanis, E. C. Minimum speed limit for ocean ridge magmatism from  $^{210}\text{Pb}$ – $^{226}\text{Ra}$ – $^{230}\text{Th}$  disequilibria. *Nature* **437**, 534–538 (2005).
- Ruprecht, P. & Plank, T. Feeding andesitic eruptions with a high-speed connection from the mantle. *Nature* **500**, 68–72 (2013).
- Costa, F., Chakraborty, S. & Dohmen, R. Diffusion coupling between trace and major elements and a model for calculation of magma residence times using plagioclase. *Geochim. Cosmochim. Acta* **67**, 2189–2200 (2003).

**Acknowledgements** Funding for this project was provided by the US NSF (EAR-0838389 to KMC; EAR-0838421 to AJRK). We thank W. Bohron for assistance with R-MELTS and measurement of CSD. F. Costa also provided assistance with diffusion modelling. We thank T. Plank for comments that improved the clarity and content of the manuscript.

**Author Contributions** The authors jointly conceived the project, obtained funding, and developed the interpretations presented in the manuscript. K.M.C. was primarily responsible for the U-series age compilation and interpretations, and A.J.R.K. was primarily responsible for the CSD and diffusion modelling. K.M.C. took the lead on writing the manuscript, with substantial input by A.J.R.K.

**Author Information** Reprints and permissions information is available at [www.nature.com/reprints](http://www.nature.com/reprints). The authors declare no competing financial interests. Readers are welcome to comment on the online version of the paper. Correspondence and requests for materials should be addressed to K.M.C. ([kmcooper@ucdavis.edu](mailto:kmcooper@ucdavis.edu)).



# Skin pigmentation provides evidence of convergent melanism in extinct marine reptiles

Johan Lindgren<sup>1</sup>, Peter Sjövall<sup>2</sup>, Ryan M. Carney<sup>3</sup>, Per Uvdal<sup>4,5</sup>, Johan A. Gren<sup>1</sup>, Gareth Dyke<sup>6,7</sup>, Bo Pagh Schultz<sup>8</sup>, Matthew D. Shawkey<sup>9</sup>, Kenneth R. Barnes<sup>10</sup> & Michael J. Polcyn<sup>11</sup>

Throughout the animal kingdom, adaptive colouration serves critical functions ranging from inconspicuous camouflage to ostentatious sexual display, and can provide important information about the environment and biology of a particular organism<sup>1,2</sup>. The most ubiquitous and abundant pigment, melanin, also has a diverse range of non-visual roles, including thermoregulation in ectotherms<sup>3,4</sup>. However, little is known about the functional evolution of this important biochrome through deep time, owing to our limited ability to unambiguously identify traces of it in the fossil record<sup>2</sup>. Here we present direct chemical evidence of pigmentation in fossilized skin, from three distantly related marine reptiles: a leatherback turtle<sup>5</sup>, a mosasaur<sup>6</sup> and an ichthyosaur<sup>7</sup>. We demonstrate that dark traces of soft tissue in these fossils are dominated by molecularly preserved eumelanin, in intimate association with fossilized melanosomes. In addition, we suggest that contrary to the countershading of many pelagic animals<sup>8,9</sup>, at least some ichthyosaurs were uniformly dark-coloured in life. Our analyses expand current knowledge of pigmentation in fossil integument beyond that of feathers<sup>2,10</sup>, allowing for the reconstruction of colour over much greater ranges of extinct taxa and anatomy. In turn, our results provide evidence of convergent melanism in three disparate lineages of secondarily aquatic tetrapods. Based on extant marine analogues, we propose that the benefits of thermoregulation and/or crypsis are likely to have contributed to this melanisation, with the former having implications for the ability of each group to exploit cold environments.

On rare occasions, the fossil record reveals examples of exceptional preservation, in which decay-prone tissues, such as skin, are preserved as 'an organic film'<sup>11</sup> with a high degree of morphological fidelity. These specimens provide information crucial to our understanding of ancient anatomy and evolutionary patterns. For example, the discovery of a dark-coloured 'halo' surrounding the skeleton of extraordinarily preserved ichthyosaurs (an extinct group of ocean-going reptiles<sup>7</sup>) in the 1890s drastically changed the prevailing image of these animals, revealing their remarkably derived, piscine body plan. Likewise, the preservation of carbonised scales in mosasaurs (another lineage of Mesozoic-era marine reptiles<sup>6</sup>) has greatly improved our understanding of how these ancient lizards evolved from land dwellers to pelagic cruisers<sup>12</sup>.

Although such fossils have advanced our knowledge of the body plans of these animals, the origin and composition of the dark matter that forms preserved surface structures have yet to be resolved. Previous studies have shown that carbonised fossil 'skin' is rich in micrometre-sized spherical to rod-shaped bodies<sup>13</sup>. Morphologically, these structures resemble melanosomes (lysosome-related pigment organelles) but also microbes, and thus there has been debate over whether they represent fossilized remains of endogenous organelles<sup>10,14</sup> or bacteria<sup>7,13</sup>.

Therefore, to elucidate the molecular composition of putative fossilized skin, we analysed samples from three phylogenetically diverse marine reptiles—a 55-Myr-old leatherback turtle (FUM-N-1450; MUSERUM),

an 86-Myr-old mosasaur (SMU 76532; Shuler Museum of Paleontology) and a 196–190-Myr-old ichthyosaur (YORYM 1993.338; Yorkshire Museum) (Figs 1–4; see Supplementary Information)—using time-of-flight secondary ion mass spectrometry (ToF-SIMS) and scanning electron microscopy (SEM). ToF-SIMS provides detailed information on the composition and spatial distribution of surface molecules and chemical structures<sup>15,16</sup>. In the three specimens, soft tissue anatomy associated with the skeletal elements is preserved as macroscopically amorphous, matt black material; however, SEM reveals masses of ovoid bodies, with long and short axes of approximately  $0.8 \times 0.5 \mu\text{m}$  (turtle; Fig. 2b, c),  $0.5 \times 0.3 \mu\text{m}$  (mosasaur; Fig. 3b, c) and  $0.8 \times 0.5 \mu\text{m}$  (ichthyosaur; Fig. 4b, c) (Supplementary Information). These dimensions are consistent with those of melanosomes from extant lizards<sup>17</sup> and bird feathers<sup>10</sup>. Energy-dispersive X-ray (EDX) microanalysis shows that carbon in these specimens is associated with the 'skin' but not the adjacent sedimentary matrix, suggesting that the former represents organic residues (Extended Data Fig. 1).

ToF-SIMS analysis produced negative-ion mass spectra from specific sample regions that closely match the spectrum obtained from natural eumelanin (Figs 2d, 3d and 4d and Extended Data Figs 2 and 3), indicating the presence of considerable amounts of this black to brown biochrome on the sampled surfaces. All relevant features of the standard

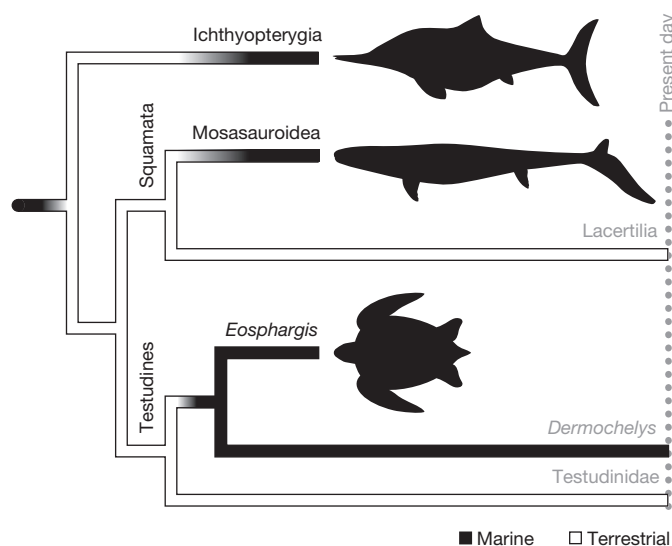


**Figure 1 | Phylogenetic relationships of the three fossil marine reptiles examined in this study.** Note that each lineage independently became secondarily aquatic (black branches, marine; white branches, terrestrial). Phylogeny is based on ref. 26; branch lengths and body sizes are not to respective scale.

<sup>1</sup>Department of Geology, Lund University, SE-223 62 Lund, Sweden. <sup>2</sup>SP Technical Research Institute of Sweden, Chemistry, Materials and Surfaces, SE-501 15 Borås, Sweden. <sup>3</sup>Department of Ecology and Evolutionary Biology, Brown University, Providence, Rhode Island 02906, USA. <sup>4</sup>MAX-IV laboratory, Lund University, SE-221 00 Lund, Sweden. <sup>5</sup>Chemical Physics, Department of Chemistry, Lund University, SE-221 00 Lund, Sweden. <sup>6</sup>Ocean and Earth Sciences, University of Southampton, Southampton SO14 3ZH, UK. <sup>7</sup>Institute for Life Sciences, University of Southampton, Southampton SO14 3ZH, UK. <sup>8</sup>MUSERUM, Natural History Division, Havnevej 14, 7800 Skive, Denmark. <sup>9</sup>Integrated Bioscience Program, University of Akron, Akron, Ohio 44325, USA. <sup>10</sup>Mosasaur Ranch Museum, Lajitas, Texas 79852, USA. <sup>11</sup>Roy M. Huffington Department of Earth Sciences, Southern Methodist University, Dallas, Texas 75275, USA.

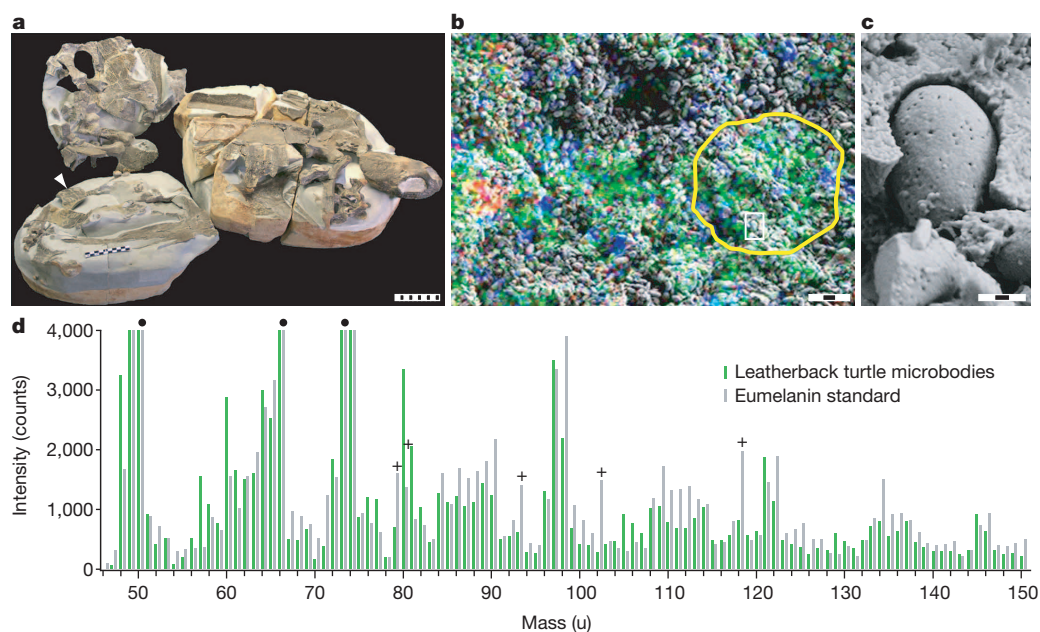


**Figure 2 | SEM and ToF-SIMS data of fossil leatherback turtle FUM-N-1450.** **a**, Photograph of specimen. Sampled skin structures are marked with an arrowhead. Scale bar, 10 cm. **b**, A semi-transparent ion image showing the spatial distribution of peaks characteristic of eumelanin (green; see Methods), silicon oxide (blue) and sulphate (red) superimposed onto a SEM image of the 'skin'. Scale bar, 3  $\mu$ m. **c**, Enlargement of the demarcated area in **b** (white box) showing a melanosome-like microbody. Scale bar, 300 nm. **d**, Negative-ion

ToF-SIMS spectra from the area demarcated by a yellow line in **b** ('Leatherback turtle microbodies') and natural eumelanin. Filled circles (above grey bars) indicate peaks used to produce the eumelanin ion image in **b**, and plus symbols (above grey bars) indicate peaks from inorganic ions that are not part of the eumelanin structure (see Methods for further discussion). u, unified atomic mass unit.

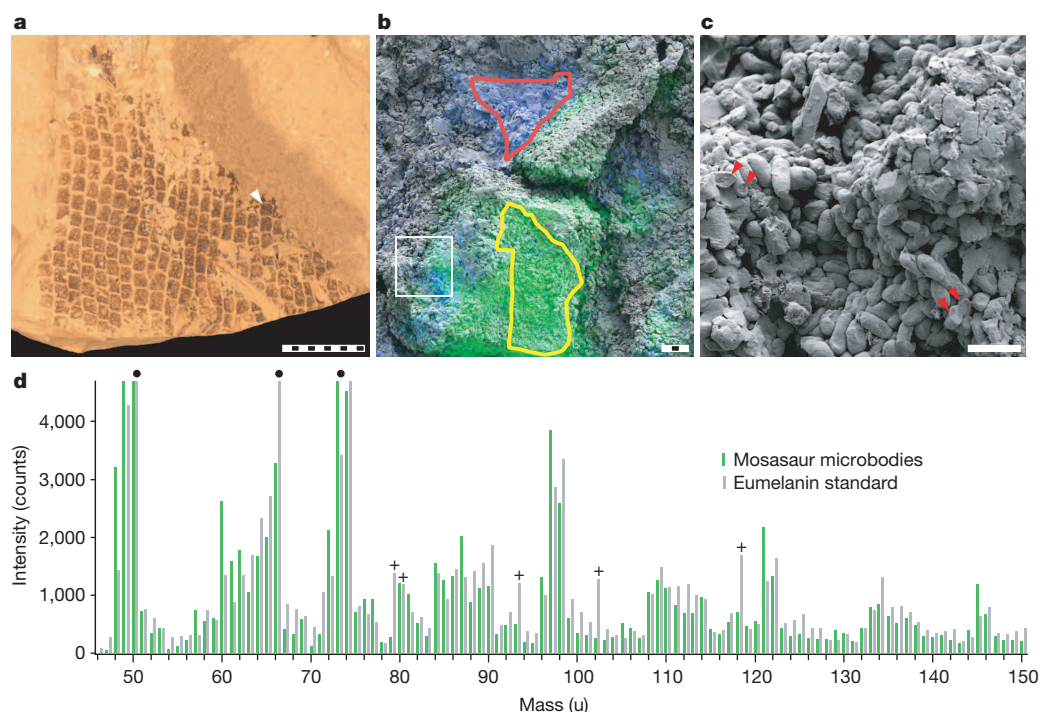


**Figure 3 | SEM and ToF-SIMS data of mosasaur SMU 76532.** **a**, Photograph of section with 'scales'. Arrowhead indicates analysed area. Scale bar, 10 mm. **b**, A semi-transparent ion image showing the spatial distribution of peaks characteristic of eumelanin (green; see Methods) and silicon oxide (blue) superimposed onto a SEM image of the 'scales'. The yellow line demarcates the area from which the spectrum presented in **d** ('Mosasaur microbodies') was collected, whereas the red line demarcates the area from which the upper spectrum in Extended Data Fig. 3 was collected. Scale bar, 3  $\mu$ m. **c**, Enlargement

of the demarcated area in **b** (white box) showing melanosome-like microbodies (arrowheads indicate solid interior; see Supplementary Information). Scale bar, 1  $\mu$ m. **d**, Negative-ion ToF-SIMS spectra from the area demarcated by a yellow line in **b** and natural eumelanin. Filled circles (above grey bars) indicate peaks used to produce the eumelanin ion image in **b**, and plus symbols (above grey bars) indicate peaks from inorganic ions that are not part of the eumelanin structure (see Methods for further discussion).

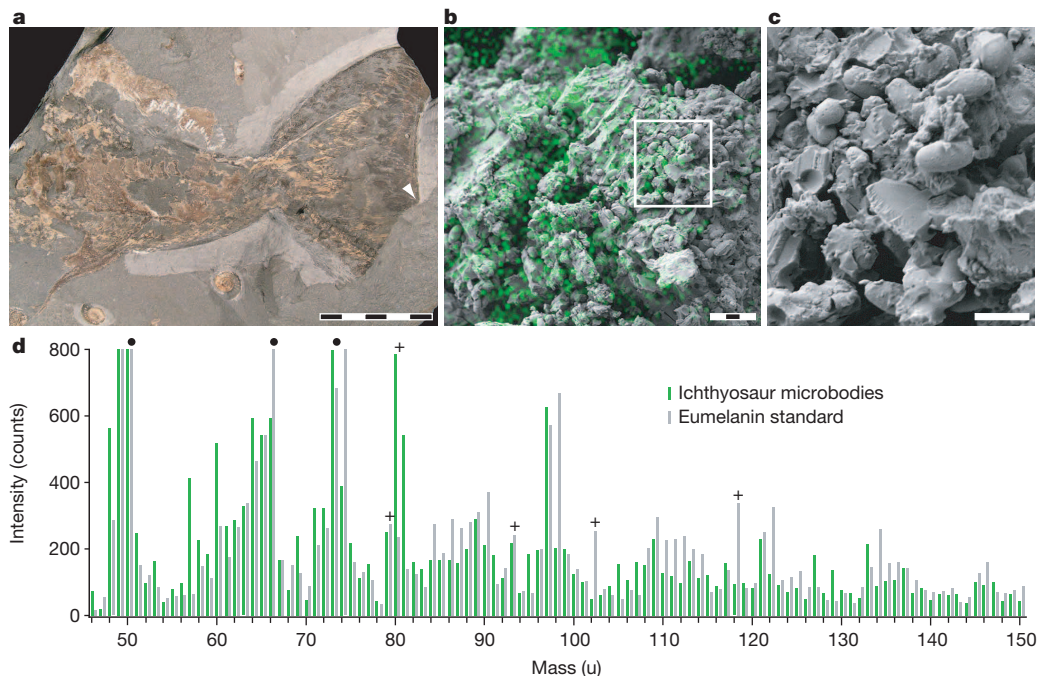


**Figure 4 | SEM and ToF-SIMS data of ichthyosaur YORYM 1993.338.**

**a**, Photograph of specimen (caudal region and tail fin). The analysed area is indicated by an arrowhead. Scale bar, 5 cm. **b**, A semi-transparent ion image showing the spatial distribution of peaks characteristic of eumelanin (green; see Methods) superimposed onto a SEM image of the 'skin'. Scale bar, 3  $\mu\text{m}$ . **c**, Enlargement of the demarcated area in **b** (white box) showing

melanosome-like microbodies. Scale bar, 1  $\mu\text{m}$ . **d**, Negative-ion ToF-SIMS spectra of the 'skin' and natural eumelanin. Filled circles (above grey bars) indicate peaks used to produce the ion image in **b**, and plus symbols (above grey bars) indicate peaks from inorganic ions that are not part of the eumelanin structure (see Methods for further discussion).

spectrum are reproduced in the fossil spectra, including relative intensity distributions and precise peak positions (measured at 'high' mass resolution; see Extended Data Table 1) of all major peaks occurring at 49, 50, 66, 73, 74, 97, 98, 121, 122, 145, and 146 u (unified atomic mass unit), as well as several less intense peaks in the entire mass range up to 175 u. Moreover, all main eumelanin peaks show the same spatial distribution, demonstrating that they originate from the same molecular species (Extended Data Fig. 4). Importantly, superimposition of these data onto SEM micrographs shows that the eumelanin peaks from all three fossil specimens consistently appear in intimate association with melanosome-like microbodies (Figs 2b, 3b and 4b). Additional peaks representing other molecular structures, including silica (60, 76 and 77 u) and sulphate (80 u), display distinctly different spatial distributions not associated with melanin or the microbodies (Figs 2b and 3b and Extended Data Fig. 4).

The other main class of melanin pigment is phaeomelanin, which imparts red to yellow colours<sup>18</sup>. For a long time phaeomelanin was thought to be absent outside of mammals and birds, but it has recently been identified in Testudines<sup>18</sup>; phaeomelanosomes have also been found to fossilize<sup>10</sup>. However, the spectra from our three specimens do not indicate large amounts of phaeomelanin (Extended Data Fig. 5), and the ovoid microbodies are inconsistent with the spherical morphology of phaeomelanosomes<sup>10</sup>. Although minor contributions from compounds, such as phaeomelanin, cannot be excluded given the presence of sulphur (Extended Data Figs 4 and 6), the latter is likely to be diagenetic in origin (Supplementary Information). Ultimately, our molecular and imaging analyses provide compelling evidence that the organic content of the structures forming the 'skin' in all three specimens is dominated by eumelanin, and that the structures themselves represent fossilized melanosomes (see also Supplementary Information).

The fossil spectra are also inconsistent with those taken from three microbial mat samples<sup>16</sup>, as well as from nine molecular standards consisting of two compounds that are structurally similar to melanin, three porphyrin pigments, and four compounds that comprise the three other types of colour-producing cells (chromatophores) found in reptilian

integument: erythrophores, iridophores and xanthophores (Extended Data Figs 5 and 6; Supplementary Information)<sup>17</sup>. However, given that the relative preservation potential of non-melanic pigments and structural colour-producing chromatophores is believed to be relatively low<sup>2</sup>, their absence may not necessarily indicate lack of original presence. Nevertheless, a relationship exists between melanin density and skin darkness<sup>3,17,19</sup>, and the soft tissues in the fossil specimens are composed entirely of tightly packed melanosomes. Therefore, we conclude that the bodies of the three marine reptiles represented by these fossils originally had, at least partially, eumelanin colouration similar to the extant leatherback turtle, *Dermochelys coriacea* (Extended Data Fig. 7)<sup>5</sup>.

Given that animal pigmentation is subject to natural selection<sup>1</sup>, the integumental melanisation we report was likely to have been advantageous to these organisms in life. One well-known modern example is thermal melanism, which provides faster heating and higher equilibrium temperatures through increased absorption of solar radiation due to lower albedo<sup>3,4</sup>. This adaptation has been found to increase the fitness of various organisms in cold climates, including reptiles<sup>3,4</sup>. Among extant reptiles, the leatherback turtle has the largest geographical and temperature ranges, including near-freezing waters in the Arctic Circle<sup>5,20</sup>. The leatherback's ability to maintain a high core body temperature is generally attributed to an integrated suite of physiological and behavioural adaptations, including extremely large body size (gigantothermy)<sup>5,20</sup>. It has also been suggested that the dark dorsal colouring of leatherbacks, coupled with their routinely observed, apparent basking behaviour, maximizes absorption of solar radiation<sup>21</sup>, and studies of leatherbacks foraging at high latitudes have revealed that these turtles surface for extended periods of time during daylight hours (peaking at around midday)<sup>5,21</sup>. Furthermore, experimental results demonstrate that the black dorsal colouration of hatchlings of the related green sea turtle, *Chelonia mydas*, has an important role in elevating body temperature; this in turn is believed to increase growth rates during this vulnerable life history stage<sup>22</sup>. Thus, such thermal melanism presumably also has a role in leatherback turtles, particularly given that they inhabit colder environments (at



least as sub-adults and adults<sup>5</sup>) and exhibit the fastest growth rates of any living turtle<sup>23</sup>. Adult leatherbacks also retain this black colouration—unlike adult green sea turtles<sup>22</sup> and despite lower growth rates compared to their juvenile stage<sup>23</sup>—which may be due in part to thermal selective pressure throughout ontogeny. In addition, results from physical and theoretical modelling predict more advantageous thermal melanism in larger organisms<sup>3</sup>.

It is therefore feasible that selective pressures for fast growth, large size and/or homeothermy also selected for melanisation in extant (and fossil) leatherbacks. It is interesting to note that Eocene-epoch leatherback turtles also ranged into cold, high-latitude climates<sup>24</sup>, and thus presumably possessed thermoregulatory adaptations comparable to those found in extant *Dermochelys*. Similar selective pressures are likely to have acted on mosasaurs and ichthyosaurs as well, both of which were fast-growing, large and homeothermic<sup>25,26</sup>. This homeothermy, which is likely to have been augmented by the thermal advantages of melanised skin during the sea-surfacing behaviours of these obligate air-breathers, allowed exploitation of ecological niches near the Arctic and Antarctic<sup>24,25,27</sup>.

Pigmentation is often a multi-functional trait<sup>1,2</sup>, and thus may have performed other non-mutually-exclusive roles, such as camouflage. For example, in addition to thermoregulation, the black colouration of green sea turtle hatchlings provides countershading (a dark dorsum and light ventrum), a simple but effective form of concealment against predators above, and below, the water surface<sup>22</sup>. Many other living aquatic organisms are countershaded<sup>9,22</sup>, including *Dermochelys*<sup>5</sup>, and this is occasionally also observed in exceptionally preserved fossils<sup>8</sup>. However, assuming that the black body outlines of ichthyosaur fossils with a full 'skin' envelope (Extended Data Fig. 8) represent endogenous pigments and/or organelles as reported here in YORYM 1993.338, we infer that these animals were uniformly dark-coloured in life. Some extant marine animals, including the deep diving sperm whale, *Physeter macrocephalus*, have a uniform dark colouration, and it has been suggested that this colour scheme acts as background matching in low light environments<sup>9</sup>. Although this is not a statistically supported association among cetaceans<sup>9</sup>, such a function in ichthyosaurs would nonetheless be consistent with their inferred deep diving habits<sup>7</sup>. The particular distribution of dark and light pigments in mosasaurs is unknown; however, the keeled scales present in some forms would have reduced shininess and provided a non-reflective appearance<sup>12</sup>. Similarly, we reason that both cryptic and thermal melanism in marine reptiles would tend to select against other types of chromatophores and structural colouration, which by their nature serve to reflect light. This is consistent with the matt black appearance of extant leatherback skin, which is also smooth in adults due to a lack of scales<sup>5</sup>, a feature believed to be shared by at least some derived ichthyosaurs<sup>7,11</sup>. More speculative functions for the melanisation observed in these three fossil taxa include photoprotection from the continuous exposure to ultraviolet radiation while at the sea surface<sup>28</sup>, and mechanical strengthening of the integumentary tissue<sup>29</sup>; gene(s) responsible for the melanisation may also have had pleiotropic effects on other physiological or behavioural traits, such as increased aggressiveness<sup>30</sup>.

Ultimately, our molecular approach provides an unprecedented level of confidence for the detection and characterization of pigment in fossilized integument. Furthermore, the ability to reconstruct colour in skin has great potential for a phylogenetically diverse range of fossil animals. Our results suggest that dark colouration in extinct marine reptiles may be common, as it is in extant marine amniotes<sup>5,9</sup>; such convergence reflects the important evolutionary role that melanin played after each of these ancient reptile lineages returned to the sea.

## METHODS SUMMARY

**Preparation of samples.** Small tissue samples were removed from each specimen using a sterile scalpel and rinsed multiple times in 96% ethanol and 'ultrapure' (Milli-Q) water, dried under a hood, and wrapped in aluminium foil until examination. Prior to ToF-SIMS analysis, the surface of each sample was partially removed

using a sterile scalpel, and the collected material was deposited on double-sided cellophane tape. Aluminium foil was used to cover all work areas, and surgical gloves were used in all handling of the 'skin' samples. Treatment of modern reference samples was identical to that of the fossil structures for all analyses.

**Scanning electron microscopy.** Initial screening was performed using a Hitachi S-3400N SEM on uncoated samples under low vacuum, and the elemental composition was determined via elemental mapping using EDX analysis (1,900 s scanning time at 15 keV, 62.0  $\mu$ A and a working distance of 10 mm). After ToF-SIMS analysis, the samples were sputter-coated with gold and re-examined using a Zeiss Supra 40VP scanning electron microscope (2 keV, working distance 3–5 mm, Everhart-Thornley secondary electron detector).

**Time-of-flight secondary ion mass spectrometry.** ToF-SIMS analyses in the static SIMS mode were performed in a ToF-SIMS IV instrument (IONTOF GmbH) using 25 keV  $\text{Bi}_3^+$  primary ions and low energy electron flooding for charge compensation. High mass resolution data ( $m/\Delta m \sim 5,000$ ) were acquired at a spatial resolution of  $\sim 3\text{--}4\text{ }\mu\text{m}$ , whereas high image resolution data (spatial resolution  $\sim 0.2\text{--}0.5\text{ }\mu\text{m}$ ) were obtained at a mass resolution of  $m/\Delta m \sim 300$ ; in both cases at  $256 \times 256$  pixels. Because the positive-ion spectra were found to show strong interference with the signal from the sedimentary matrix, only negative-ion data are presented here.

**Online Content** Any additional Methods, Extended Data display items and Source Data are available in the online version of the paper; references unique to these sections appear only in the online paper.

**Received 9 October; accepted 22 November 2013.**

**Published online 8 January 2014.**

- Hubbard, J. K., Uy, J. A. C., Hauber, M. E., Hoekstra, H. E. & Safran, R. J. Vertebrate pigmentation: from underlying genes to adaptive function. *Trends Genet.* **26**, 231–239 (2010).
- McNamara, M. E. The taphonomy of colour in fossil insects and feathers. *Palaeontology* **56**, 557–575 (2013).
- Clusella Trullas, S., van Wyk, J. H. & Spotila, J. R. Thermal melanism in ectotherms. *J. Therm. Biol.* **32**, 235–245 (2007).
- Clusella Trullas, S., van Wyk, J. H. & Spotila, J. R. Thermal benefits of melanism in cordylid lizards: a theoretical and field test. *Ecology* **90**, 2297–2312 (2009).
- Eckert, K. L., Wallace, B. P., Frazier, J. G., Eckert, S. A. & Pritchard, P. C. H. *Synopsis of the Biological Data on the Leatherback Sea Turtle (Dermochelys coriacea)* (US Department of Interior, Fish and Wildlife Service, 2012).
- Lindgren, J., Kaddumi, H. F. & Polcyn, M. J. Soft tissue preservation in a fossil marine lizard with a bilobed tail fin. *Nature Commun.* **4**, 2423 (2013).
- Motani, R. Evolution of fish-shaped reptiles (Reptilia: Ichthyopterygia) in their physical environments and constraints. *Annu. Rev. Earth Planet. Sci.* **33**, 395–420 (2005).
- Gottfried, M. D. Earliest fossil evidence for protective pigmentation in an actinopterygian fish. *Hist. Biol.* **3**, 79–83 (1989).
- Caro, T., Beeman, K., Stankowich, T. & Whitehead, H. The functional significance of colouration in cetaceans. *Evol. Ecol.* **25**, 1231–1245 (2011).
- Li, Q. *et al.* Plumage color patterns of an extinct dinosaur. *Science* **327**, 1369–1372 (2010).
- Martill, D. M. An ichthyosaur with preserved soft tissue from the Sinemurian of southern England. *Palaeontology* **38**, 897–903 (1995).
- Lindgren, J., Alwmark, C., Caldwell, M. W. & Fiorillo, A. R. Skin of the Cretaceous mosasaur *Platysuchus*: implications for aquatic adaptations in giant marine reptiles. *Biol. Lett.* **5**, 528–531 (2009).
- Martill, D. M. Prokaryote mats replacing soft tissues in Mesozoic marine reptiles. *Mod. Geol.* **11**, 265–269 (1987).
- Whitear, M. On the colour of an ichthyosaur. *Ann. Mag. Nat. Hist.* **9**, 742–744 (1956).
- Thiel, V. & Sjövall, P. Using time-of-flight secondary ion mass spectrometry to study biomarkers. *Annu. Rev. Earth Planet. Sci.* **39**, 125–156 (2011).
- Lindgren, J. *et al.* Molecular preservation of the pigment melanin in fossil melanosomes. *Nature Commun.* **3**, 824 (2012).
- Kuriyama, T., Miyaji, K., Sugimoto, M. & Hasegawa, M. Ultrastructure of the dermal chromatophores in a lizard (Scincidae: *Plestiodon latiscutatus*) with conspicuous body and tail coloration. *Zoolog. Sci.* **23**, 793–799 (2006).
- Roulin, A., Mafli, A. & Wakamatsu, K. Reptiles produce pheomelanin: evidence in the eastern Hermann's tortoise (*Testudo boettgeri*). *J. Herpetol.* **47**, 258–261 (2013).
- Rosenblum, E. B., Hoekstra, H. E. & Nachman, M. W. Adaptive reptile color variation and the evolution of the *Mc1r* gene. *Evolution* **58**, 1794–1808 (2004).
- Bostrom, B. L., Jones, T. T., Hastings, M. & Jones, D. R. Behaviour and physiology: the thermal strategy of leatherback turtles. *PLoS ONE* **5**, e13925 (2010).
- James, M. C., Myers, R. A. & Ottensmeyer, C. A. Behaviour of leatherback sea turtles, *Dermochelys coriacea*, during the migratory cycle. *Proc. R. Soc. Lond. B* **272**, 1547–1555 (2005).
- Bustard, H. R. The adaptive significance of coloration in hatchling green sea turtles. *Herpetologica* **26**, 224–227 (1970).

23. Zug, G. R. & Parham, J. F. Age and growth in leatherback turtles, *Dermochelys coriacea* (Testudines: Dermochelyidae): a skeletochronological analysis. *Chelonian Conserv. Biol.* **2**, 244–249 (1996).
24. Albright, L. B., Woodburne, M. O., Case, J. A. & Chaney, D. S. A leatherback sea turtle from the Eocene of Antarctica: implications for antiquity of gigantothermy in Dermochelyidae. *J. Vertebr. Paleontol.* **23**, 945–949 (2003).
25. Bernard, A. *et al.* Regulation of body temperature by some Mesozoic marine reptiles. *Science* **328**, 1379–1382 (2010).
26. Houssaye, A. Bone histology of aquatic reptiles: what does it tell us about secondary adaptation to an aquatic life? *Biol. J. Linn. Soc.* **108**, 3–21 (2013).
27. Rich, T. H., Vickers-Rich, P. & Gangloff, R. A. Polar dinosaurs. *Science* **295**, 979–980 (2002).
28. Martinez-Levasseur, L. M. *et al.* Whales use distinct strategies to counteract solar ultraviolet radiation. *Sci. Rep.* **3**, 2386 (2013).
29. McGraw, K. J. in *Bird Coloration* Vol. 1 (eds Hill, G. E. & McGraw, K. J.) 243–294 (Harvard Univ. Press, 2006).
30. Ducrest, A.-L., Keller, L. & Roulin, A. Pleiotropy in the melanocortin system, coloration and behavioural syndromes. *Trends Ecol. Evol.* **23**, 502–510 (2008).

**Supplementary Information** is available in the online version of the paper.

**Acknowledgements** We thank I. Gladstone, S. King and the Yorkshire Museum for permission to sample YORYM 1993.338, as well as J. Wyneken, P. Weston and L. Alibardi for providing and sectioning the extant leatherback turtle skin samples, respectively. B. P. Kear took the photograph of PMU R435 (Extended Data Fig. 8). This research was supported by grants from the Swedish Research Council, the Crafoord Foundation, the Royal Swedish Academy of Sciences (J.L.), VINNOVA Swedish Governmental Agency for Innovation Systems (P.S.), the National Geographic Society/Waite Foundation (R.M.C.), the National Science Foundation, Human Frontiers Science Program, and Air Force Office of Scientific Research (M.D.S.).

**Author Contributions** J.L. designed the project. J.L., P.S., R.M.C. and G.D. wrote the manuscript. J.L., P.S., R.M.C., J.A.G. and P.U. prepared the images. G.D., B.P.S., M.D.S., K.R.B. and M.J.P. provided materials, observations and scientific interpretations. All authors discussed the results and provided input on the manuscript.

**Author Information** Reprints and permissions information is available at [www.nature.com/reprints](http://www.nature.com/reprints). The authors declare no competing financial interests. Readers are welcome to comment on the online version of the paper. Correspondence and requests for materials should be addressed to J.L. ([johan.lindgren@geol.lu.se](mailto:johan.lindgren@geol.lu.se)).

# Sequential evolution of bacterial morphology by co-option of a developmental regulator

Chao Jiang<sup>1</sup>, Pamela J. B. Brown<sup>1†</sup>, Adrien Ducret<sup>1</sup> & Yves V. Brun<sup>1</sup>

What mechanisms underlie the transitions responsible for the diverse shapes observed in the living world? Although bacteria exhibit a myriad of morphologies<sup>1</sup>, the mechanisms responsible for the evolution of bacterial cell shape are not understood. We investigated morphological diversity in a group of bacteria that synthesize an appendage-like extension of the cell envelope called the stalk<sup>2,3</sup>. The location and number of stalks varies among species, as exemplified by three distinct subcellular positions of stalks within a rod-shaped cell body: polar in the genus *Caulobacter* and subpolar or bilateral in the genus *Asticcacaulis*<sup>4</sup>. Here we show that a developmental regulator of *Caulobacter crescentus*, SpmX<sup>5</sup>, is co-opted in the genus *Asticcacaulis* to specify stalk synthesis either at the subpolar or bilateral positions. We also show that stepwise evolution of a specific region of SpmX led to the gain of a new function and localization of this protein, which drove the sequential transition in stalk positioning. Our results indicate that changes in protein function, co-option and modularity are key elements in the evolution of bacterial morphology. Therefore, similar evolutionary principles of morphological transitions apply to both single-celled prokaryotes and multicellular eukaryotes.

Stalks are a common feature in aquatic bacterial species living in oligotrophic environments<sup>3,6</sup>. When these species are subjected to nutrient limitation, stalks elongate to increase the effective length and surface

area of the cells<sup>7</sup>, thereby increasing the rate of nutrient uptake<sup>2,8</sup>. The thin cylindrical stalk is composed of inner and outer membranes separated by peptidoglycan<sup>6</sup>, and compartmentalized by proteinaceous structures called 'cross-bands'<sup>9,10</sup> (Fig. 1a). In the *Caulobacteraceae* family, stalk synthesis occurs at a specific stage of a dimorphic life cycle in which a non-replicating motile swarmer cell differentiates into a sessile stalked cell<sup>11</sup> (Fig. 1b). In *C. crescentus*, the stalk is positioned at a single cell pole; in *Asticcacaulis excentricus*, the stalk is synthesized at a subpolar position off-centre from a cell pole; and in *Asticcacaulis biprosthecum*, two stalks are positioned bilaterally on the cell body<sup>4</sup> (Fig. 1a).

The natural variation in stalk location provides an opportunity to study the mechanisms underlying the precise targeting of cell envelope growth zones to generate different morphologies. Stalks in *C. crescentus* are synthesized from their base<sup>12</sup> by insertion of peptidoglycan within a small area of the cell body<sup>13,14</sup>. To test whether this mechanism is conserved in the genus *Asticcacaulis*, we used pulse-chase labelling with Texas Red succinimidyl ester (TRSE)<sup>15,16</sup> to study cell envelope growth and a fluorescent D-amino acid to label regions of peptidoglycan synthesis<sup>13</sup>. The stalks of *A. excentricus* and *A. biprosthecum* are also synthesized by insertion of peptidoglycan at their base (Extended Data Fig. 1a, b), suggesting that all three species share the same stalk synthesis mechanism.

In light of the above results, we considered that if a conserved stalk morphogen exists, it must localize to the base of stalks. Because many

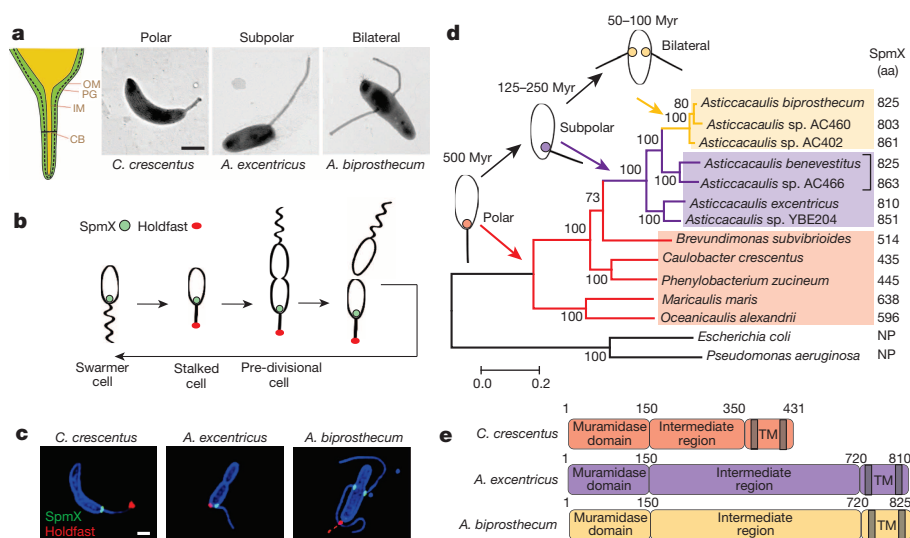


**Figure 1 | Natural variation and evolution of stalk positioning correlates with SpmX localization.** **a**, Left, schematic of the stalk. CB, cross-band; IM, inner membrane; OM, outer membrane; PG, peptidoglycan. Right, transmission electron micrographs of representative species. **b**, Dimorphic life cycle of *C. crescentus*. SpmX (green) and holdfast (red). **c**, Structured illumination microscopy images of cells with outer membrane protein stained with Pacific Blue succinimidyl ester (blue), SpmX-eGFP (green) and fluorescent-lectin-bound holdfast (red). Data are representative of three biological repetitions. Scale bars, 1  $\mu$ m. **d**, Phylogenetic tree and inferred

evolutionary trajectory of stalk positioning with the predicted origin of morphology calibrated by 16S rRNA identity<sup>26</sup>. Colours of shading, branches and SpmX (filled circles) denote the polar (red), subpolar (purple) and bilateral (yellow) stalk positioning, respectively. The size of SpmX is indicated in amino acids (aa). NP, orthologues not present. Bracket indicates subpolar stalked species that share the last common ancestor with the *A. biprosthecum* clade. Scale bar, number of substitutions per site. Myr, million years. **e**, Domain organization of SpmX; transmembrane domains (TM) are shown as grey bars.

<sup>1</sup>Department of Biology, Indiana University, Bloomington, Indiana 47405, USA. <sup>†</sup>Present address: Division of Biological Sciences, University of Missouri, Columbia, Missouri 65211, USA.



proteins localize at the pole in *C. crescentus*<sup>17</sup>, we took advantage of the non-polar localization of the stalks in *Asticcacaulis* to identify stalk morphogen candidates. We constructed fluorescent protein fusions to orthologues of the pole-localized proteins from *C. crescentus* DivJ, PleC, PopZ and SpmX and analysed their localization in *A. biprosthicum*. Strikingly, only the regulatory histidine kinase DivJ<sup>18</sup> (Extended Data Fig. 2a) and its localization and activation factor SpmX<sup>5</sup> (Fig. 1c) localized at the base of the stalks in *A. biprosthicum*. During the cell cycle, *A. biprosthicum* DivJ-enhanced green fluorescent protein (eGFP) localized at the base of stalks only after cytokinesis, during swarmer to stalked cell differentiation (Extended Data Fig. 2b). In stark contrast, SpmX-eGFP localized to bilateral positions in the incipient swarmer half of the pre-divisional cell before cytokinesis and subsequent stalk synthesis (Extended Data Fig. 1c, e). Therefore SpmX localization precedes both DivJ localization and stalk synthesis, potentially marking the future site of stalk synthesis.

Interestingly, although the *A. biprosthicum* *divJ*<sup>-</sup> mutant still synthesized bilateral stalks (Extended Data Fig. 2a), the *A. biprosthicum* *spmX*<sup>-</sup> mutant was stalkless (Fig. 2a). Moreover, although newly synthesized peptidoglycan material co-localized with SpmX-eGFP in wild-type cells, no bilateral foci of fluorescent D-amino acid staining were observed in the absence of SpmX (Extended Data Fig. 1h, j), demonstrating that SpmX is required for stalk peptidoglycan synthesis in *A. biprosthicum*. Finally, stalk elongation only occurred when SpmX was expressed (Extended Data Fig. 1f), suggesting that SpmX is required both for the initiation and the elongation of stalk synthesis in *A. biprosthicum*. Similar results were obtained for *A. excentricus* (Fig. 1c, middle; Extended Data Fig. 1d, e, g, i, k), suggesting that the role of SpmX is conserved in both *Asticcacaulis* species. Notably, SpmX is not required for stalk synthesis in *C. crescentus*<sup>5</sup>. Because the *Caulobacter* genus diverged earlier than *Asticcacaulis* (Fig. 1d), we conclude that SpmX has been co-opted for stalk synthesis in *Asticcacaulis*. However, despite its newly acquired

role in stalk synthesis, the ancestral function of SpmX in DivJ localization has been retained in *A. biprosthicum* (Extended Data Fig. 2c).

To test the hypothesis that SpmX has a pivotal role in the evolutionary transitions in stalk positioning, we performed cross-complementation experiments by expressing heterologous SpmX and SpmX fusions in wild-type or *spmX* mutant strains of the two *Asticcacaulis* species and quantitatively analysed SpmX localization. (Fig. 2 and Extended Data Figs 3–6). When we expressed SpmX-eGFP in either the homologous or heterologous wild-type backgrounds, SpmX both localized and drove stalk synthesis at its host-specific location, suggesting that the endogenous SpmX may be able to recruit the heterologous SpmX (Extended Data Fig. 4b, c, h, i). To test this possibility, we expressed heterologous SpmX in the absence of the native *spmX* gene. Strikingly, when SpmX from the subpolar stalked species *A. excentricus* (SpmX<sub>AE(S)</sub>-eGFP) was expressed in the bilateral stalked species *A. biprosthicum* *spmX*<sup>-</sup> mutant, it localized to and drove stalk synthesis at a subpolar position (Fig. 2c and Extended Data Fig. 7). (For simplicity throughout the paper, we use SpmX<sub>CC(P)</sub>, SpmX<sub>AE(S)</sub> and SpmX<sub>AB(L)</sub> to denote SpmX from *C. crescentus* (CC), *A. excentricus* (AE) and *A. biprosthicum* (AB), with the subscripts P, S and L indicating their native polar, subpolar and lateral positioning, respectively.) Therefore, *A. excentricus* SpmX can recruit the heterologous stalk synthesis machinery of *A. biprosthicum* to synthesize a stalk at an ectopic subpolar position. In contrast, when SpmX from the bilateral stalked species *A. biprosthicum* (SpmX<sub>AB(L)</sub>-eGFP) was expressed in the subpolar stalked species *A. excentricus* *spmX*<sup>-</sup> mutant, it localized mostly to poles where it induced stalk synthesis (Fig. 2d and Extended Data Fig. 7). These results indicate that although the subpolar positional information exists in *A. biprosthicum* and can be recognized by SpmX<sub>AE(S)</sub>, the specific bilateral positional information present in *A. biprosthicum* is absent or not recognizable in *A. excentricus*.

Remarkably, these observations also suggest that *A. excentricus* possesses the ability to synthesize polar stalks in the absence of its endogenous

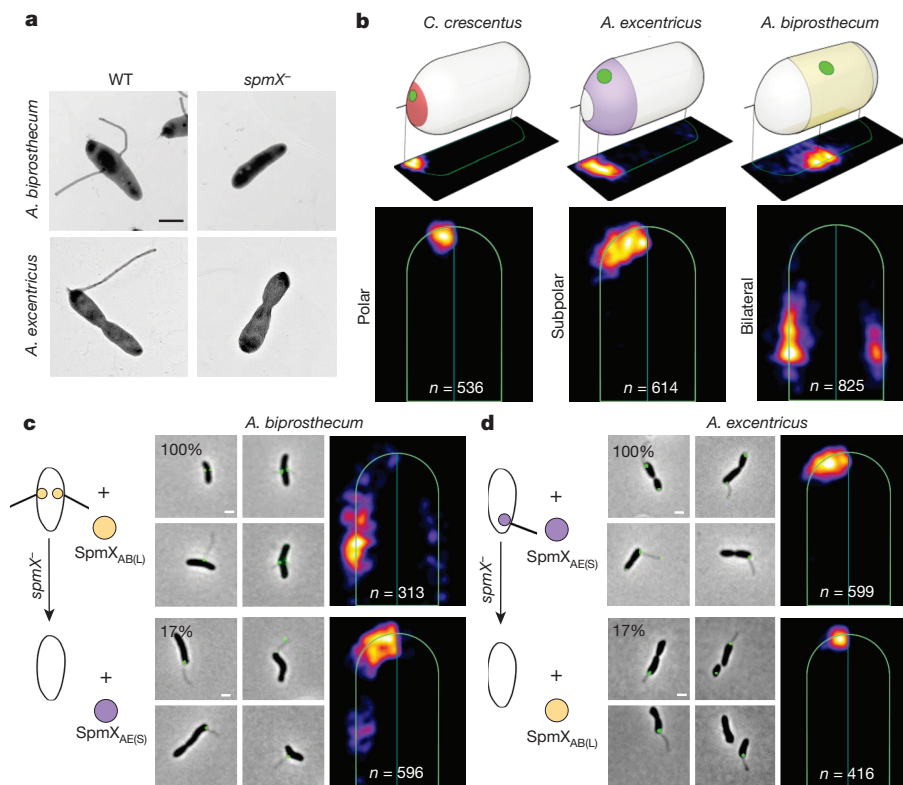


**Figure 2 | SpmX specifies the location of stalk synthesis in *Asticcacaulis*.**

**a**, SpmX is required for stalk synthesis in *Asticcacaulis*. Transmission electron microscopy images of *Asticcacaulis* species and their respective *spmX*<sup>-</sup> mutants. Data are representative of five biological repetitions. **b**, Heat maps of the localization patterns of SpmX-eGFP in three species with differentially

positioned stalks. The number (*n*) of foci quantified is shown at the bottom of each map. **c, d**, Microscopy images and heat maps of the *A. biprosthicum* and *A. excentricus* *spmX*<sup>-</sup> mutant expressing SpmX<sub>AB(L)</sub>-eGFP or SpmX<sub>AE(S)</sub>-eGFP. The percentage represents the stalk synthesis ability for each strain compared with the control *spmX*<sup>-</sup> mutant expressing native SpmX-eGFP.

SpmX. Indeed, phosphate starvation, which stimulates stalk synthesis in wild-type strains of all three species (Extended Data Fig. 2f, g), rescued stalk synthesis in *A. excentricus* *spmX*<sup>−</sup> cells, but stalks were located at the pole (Extended Data Fig. 2e, g, h). Using holdfast polysaccharide adhesin as a polar marker (Fig. 1c), we found that stalks from phosphate-starved *A. excentricus* *spmX*<sup>−</sup> cells were tipped by a holdfast (Extended Data Fig. 2e), confirming that they were synthesized polarly. We infer that *A. excentricus* possesses an alternative polar stalk synthesis mechanism that is normally masked by the endogenous SpmX-driven subpolar stalk synthesis mechanism (as detailed in Supplementary Information). In contrast, the *A. biprosthicum* *spmX*<sup>−</sup> mutant remained stalkless when starved for phosphate (Extended Data Fig. 2f), indicating that the *spmX*-independent pathway for stalk biosynthesis has been lost in *A. biprosthicum*, or is no longer regulated by phosphate starvation. We conclude that both *Asticcacaulis* species possess the ability to synthesize stalks at exogenous positions, which is masked by the effects of the endogenous SpmX in wild-type cells. We reasoned that the exogenous positions of stalk synthesis are phylogenetically ancestral, and we next sought to infer the evolutionary trajectory of stalk positioning.

To improve the phylogenetic resolution of stalk positioning, we sequenced the genomes of several extra *Asticcacaulis* strains (Extended Data Fig. 5f, g) and inferred their phylogeny (see Methods and Fig. 1d). Based on parsimony, the emergence of the polar stalk morphology occurred before the divergence between the Caulobacteraceae and Hyphomonadaceae families (*Maricaulis maris* and *Oceanicaulis alexandrii*)

(Fig. 1d). No known *Asticcacaulis* isolates synthesize polar stalks, implying that the transition in stalk positioning from polar to subpolar sites occurred very early. In addition, two subpolar stalked strains, *Asticcacaulis benevestitus* and *Asticcacaulis* sp. AC466 (Fig. 1d, bracket), diverged from the same ancestor that led to the sub-clade containing *A. biprosthicum*, indicating that subpolar stalk synthesis is ancestral to bilateral stalk synthesis. In conclusion, stalk positioning evolved from an ancestral single polar stalk to a single subpolar stalk, and subsequently to bilateral stalks.

We next sought to understand how SpmX has evolved at the protein level by testing the requirement of its main domains for localization and stalk synthesis (Fig. 1e and Extended Data Fig. 8). We constructed a set of truncated alleles removing various domains of *A. biprosthicum* SpmX, which failed to localize or rescue the stalkless phenotype of the *A. biprosthicum* *spmX*<sup>−</sup> mutant (Extended Data Fig. 7d, e). The muramidase domain and the carboxy (C)-terminal region (intermediate region and transmembrane domains) of SpmX are indispensable for its localization and function. To determine what region of SpmX evolved to specify the location of stalk synthesis, we constructed chimaeric SpmX proteins by mixing and matching the muramidase and the C-terminal regions of different SpmX proteins. In each case, the phenotype of the *spmX*<sup>−</sup> mutants expressing the various chimaeras correlated with the source of their C-terminal region (Fig. 3, Extended Data Fig. 4 and Supplementary Information). We conclude that mutations in the SpmX C-terminal region are responsible for the evolution of the ability of SpmX to drive stalk synthesis from polar to subpolar to bilateral positions.

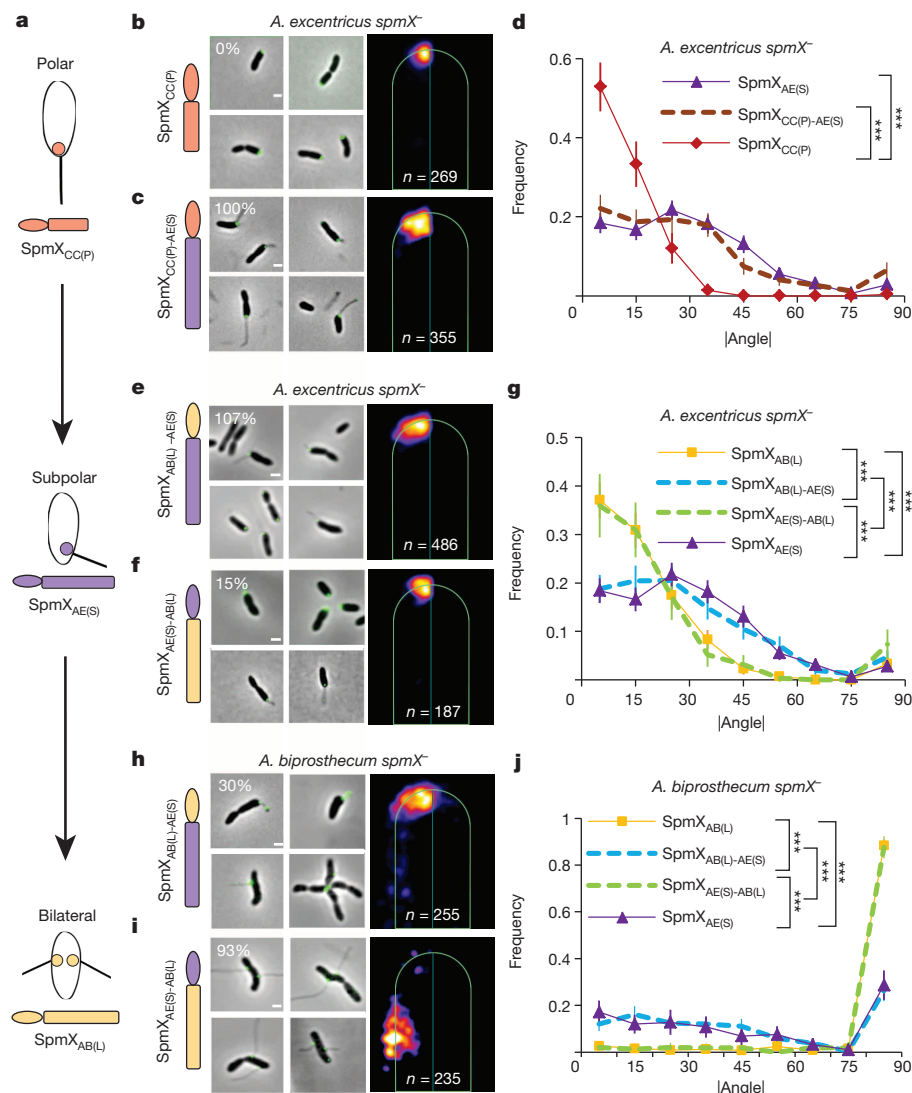


**Figure 3 | Evolution of the C-terminal region of SpmX drives the morphological transition in stalk positioning.** **a**, Schematic of inferred evolutionary trajectory of stalk positioning.

**b–g**, Microscopy images, heat maps and angle profile analysis for the *A. excentricus* *spmX*<sup>−</sup> mutant expressing SpmX<sub>CC(P)</sub> (**b**), the chimaera SpmX<sub>CC(P)-AE(S)</sub> (**c**), SpmX<sub>AB(L)-AE(S)</sub> (**e**) and SpmX<sub>AE(S)-AB(L)</sub> (**f**). **h–j**, Microscopy images, heat maps and angle profile analysis for the *A. biprosthicum* *spmX*<sup>−</sup> mutant expressing the chimaera SpmX<sub>AB(L)-AE(S)</sub> (**h**) and SpmX<sub>AE(S)-AB(L)</sub> (**i**). Percentages indicate stalk synthesis ability compared with the respective controls as in Fig. 2. Error bars in the angle profiles denote standard deviation of the sample evaluated by the Jackknifing method (see Methods). All profiles of absolute angles ( $|\theta|$ ) were generated by measuring the data points in associated heatmaps (same *n*) and were analysed by non-parametric statistical methods, as detailed in Supplementary Table 1 and Methods. \*\*\**P* < 0.001. Scale bars, 1  $\mu$ m.

Morphological transitions generate the diversity of biological forms. A few cases have been studied in eukaryotes, highlighting the importance both of changes in regulatory sequences and of functional protein evolution<sup>19–23</sup>. Our study has begun to unravel the elusive mechanisms of morphological transitions in bacteria by showing that evolution of the SpmX morphogen underlies the evolutionary trajectory of stalk positioning in the Caulobacteraceae family. Polar stalk synthesis arose from non-stalked species before the divergence of the Caulobacteraceae and Hyphomonadaceae families, but *C. crescentus* SpmX is not required for stalk synthesis, probably representing the ancestral state. Through differential protein evolution, changes in the SpmX C-terminal region led to stalk synthesis and positioning functions in the *Asticcacaulis* clade. Interestingly, the ancient polar targeting mechanism is conserved in *Asticcacaulis* because SpmX<sub>CC(P)</sub> can localize to the pole in both *A. excrucicus* and *A. biprosthecum* (Fig. 3b and Extended Data Figs 4a, g and 9f). Conversely, both SpmX<sub>AE(S)</sub> and SpmX<sub>AB(L)</sub> can still localize to the polar target in the *C. crescentus* strains, suggesting the lack of recognizable alternative targets (Extended Data Fig. 9). During the transition from polar to subpolar stalk positioning, the C-terminal region of SpmX evolved to position and coordinate the synthesis of stalks, coupled with its co-option at the subpolar target in *A. excrucicus* (Fig. 4). Further divergence of the C-terminal region of SpmX led to its ability to recognize new targets, combined with its co-option at the bilateral targets in *A. biprosthecum* (Fig. 4).

Our results highlight the modular nature of the positioning mechanism that directs the zonal peptidoglycan synthesis responsible for stalk synthesis. This modularity is evident in both *Asticcacaulis* species, because SpmX always localizes at the base of ectopically synthesized stalks in several genetically engineered strains (Figs 2 and 3 and Extended Data Fig. 2d). In addition, the fact that changes in the abundance of SpmX alone can alter the number of stalks in *A. excrucicus* (Extended Data Fig. 2d) suggests that simple changes in the regulation of SpmX expression could drive the evolution of a species with several subpolar stalks. Conceptually, to position the stalk around the cell body, the cells only need to evolve the ability to localize SpmX to a new subcellular position, where it recruits the stalk synthesis module. This morphogenetic

modularity could be exploited in synthetic biology to generate the optimal cell shape for a given process.

Finally, this study has demonstrated that functional evolution of a regulatory protein into a morphogenetic module made the evolution of stalk positioning possible, which in turn generated distinct cellular morphologies. Therefore, protein evolution, co-option and modularity can drive morphological transitions both in single-celled prokaryotes and in multicellular eukaryotes, contributing to the diversity of Darwin's 'endless forms most beautiful'<sup>24</sup> from the microscopic to the macroscopic world.

## METHODS SUMMARY

*C. crescentus*, *A. excrucicus* and *A. biprosthecum* strains were used in this study. Strains were grown in liquid peptone yeast extract (PYE) medium at 30 °C for *C. crescentus* and 26 °C for the *Asticcacaulis* strains. A detailed list of strains and plasmids and their methods of construction is provided in the Supplementary Information and Methods. For the quantitative analysis of fluorescent protein fusion localization, cells were incubated for 18 h in the presence of inducer, mounted on a 1% (w/v) agarose pad and imaged. Quantitative subcellular localization of fluorescent protein fusions was performed at sub-pixel resolution using a specifically developed plug-in for ImageJ<sup>25</sup>. For bioinformatics analysis, orthologues of SpmX were identified using the BLAST suite hosted by the National Center for Biotechnology Information (NCBI) and Integrated Microbial Genomes (IMG). Phylogenetic trees were generated using the maximum likelihood method, and a concatenation of the products of six housekeeping genes was used to infer the phylogeny of species involved. All procedures are detailed in Methods.

**Online Content** Any additional Methods, Extended Data display items and Source Data are available in the online version of the paper; references unique to these sections appear only in the online paper.

**Received 2 August; accepted 20 November 2013.**

**Published online 19 January; corrected online 26 February 2014 (see full-text HTML version for details).**

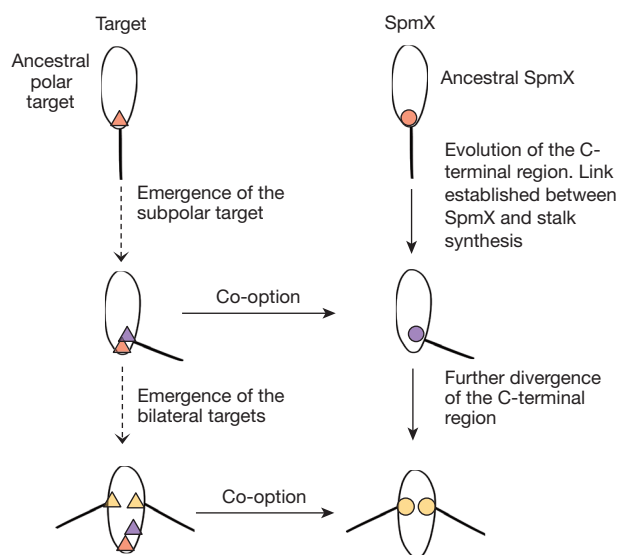


**Figure 4 | The co-option of SpmX in stalk synthesis leads to sequential morphological transitions.** From polar to subpolar stalk positioning, two events occurred: SpmX underwent an expansion of its C-terminal region and was co-opted for stalk synthesis, and the subpolar target emerged in *A. excrucicus*. Similarly, during the second transition of subpolar to bilateral positioning, SpmX evolved the ability to recognize the bilateral target and the bilateral targets emerged in *A. biprosthecum*. The exact order of events for each transition is unknown. Targets (triangles) and SpmXs (circles) are shown with respective colour-coding for the species.

- Young, K. D. The selective value of bacterial shape. *Microbiol. Mol. Biol. Rev.* **70**, 660–703 (2006).
- Wagner, J. K. & Brun, Y. V. Out on a limb: how the *Caulobacter* stalk can boost the study of bacterial cell shape. *Mol. Microbiol.* **64**, 28–33 (2007).
- Stove-POindexter, J. L. & Cohen-Bazire, G. The fine structure of stalked bacteria belonging to the family Caulobacteraceae. *J. Cell Biol.* **23**, 587–607 (1964).
- Pate, J. L. & Ordal, E. J. The fine structure of two unusual stalked bacteria. *J. Cell Biol.* **27**, 133–150 (1965).
- Radhakrishnan, S. K., Thanbichler, M. & Viollier, P. H. The dynamic interplay between a cell fate determinant and a lysozyme homolog drives the asymmetric division cycle of *Caulobacter crescentus*. *Genes Dev.* **22**, 212–225 (2008).
- POindexter, J. S. Biological properties and classification of the *Caulobacter* group. *Bacteriol. Rev.* **28**, 231–295 (1964).
- Gonin, M., Quardokus, E. M., O'Donnol, D., Maddock, J. & Brun, Y. V. Regulation of stalk elongation by phosphate in *Caulobacter crescentus*. *J. Bacteriol.* **182**, 337–347 (2000).
- Wagner, J. K., Setayeshgar, S., Sharon, L. A., Reilly, J. P. & Brun, Y. V. A nutrient uptake role for bacterial cell envelope extensions. *Proc. Natl Acad. Sci. USA* **103**, 11772–11777 (2006).
- Schlimpert, S. et al. General protein diffusion barriers create compartments within bacterial cells. *Cell* **151**, 1270–1282 (2012).
- Hughes, H. V. et al. Protein localization and dynamics within a bacterial organelle. *Proc. Natl Acad. Sci. USA* **107**, 5599–5604 (2010).
- Brown, P. J., Hardy, G. G., Trimble, M. J. & Brun, Y. V. Complex regulatory pathways coordinate cell-cycle progression and development in *Caulobacter crescentus*. *Adv. Microb. Physiol.* **54**, 1–101 (2009).
- Schmidt, J. M. & Stanier, R. Y. The development of cellular stalks in bacteria. *J. Cell Biol.* **28**, 423–436 (1966).
- Kuru, E. et al. In situ probing of newly synthesized peptidoglycan in live bacteria with fluorescent D-amino acids. *Angew. Chem. Int. Edn Engl.* **51**, 12519–12523 (2012).
- Aaron, M. et al. The tubulin homologue FtsZ contributes to cell elongation by guiding cell wall precursor synthesis in *Caulobacter crescentus*. *Mol. Microbiol.* **64**, 938–952 (2007).
- de Pedro, M. A., Grunfelder, C. G. & Schwarz, H. Restricted mobility of cell surface proteins in the polar regions of *Escherichia coli*. *J. Bacteriol.* **186**, 2594–2602 (2004).
- Brown, P. J. et al. Polar growth in the alphaproteobacterial order Rhizobiales. *Proc. Natl Acad. Sci. USA* **109**, 1697–1701 (2012).
- Curtis, P. D. & Brun, Y. V. Getting in the loop: regulation of development in *Caulobacter crescentus*. *Microbiol. Mol. Biol. Rev.* **74**, 13–41 (2010).
- Ohta, N., Lane, T., Ninfa, E. G., Sommer, J. M. & Newton, A. A histidine protein kinase homologue required for regulation of bacterial cell division and differentiation. *Proc. Natl Acad. Sci. USA* **89**, 10297–10301 (1992).
- Mallarino, R. et al. Two developmental modules establish 3D beak-shape variation in Darwin's finches. *Proc. Natl Acad. Sci. USA* **108**, 4057–4062 (2011).
- Loehlin, D. W. & Werren, J. H. Evolution of shape by multiple regulatory changes to a growth gene. *Science* **335**, 943–947 (2012).



21. Werner, T., Koshikawa, S., Williams, T. M. & Carroll, S. B. Generation of a novel wing colour pattern by the Wingless morphogen. *Nature* **464**, 1143–1148 (2010).
22. Chan, Y. F. *et al.* Adaptive evolution of pelvic reduction in sticklebacks by recurrent deletion of a Pitx1 enhancer. *Science* **327**, 302–305 (2010).
23. Ronshaugen, M., McGinnis, N. & McGinnis, W. Hox protein mutation and macroevolution of the insect body plan. *Nature* **415**, 914–917 (2002).
24. Darwin, C. *On the Origin of Species by Means of Natural Selection*, ix + 502 pp. (John Murray, 1859).
25. Collins, T. J. ImageJ for microscopy. *Biotechniques* **43**, 25–30 (2007).
26. Ochman, H., Elwyn, S. & Moran, N. A. Calibrating bacterial evolution. *Proc. Natl Acad. Sci. USA* **96**, 12638–12643 (1999).

**Supplementary Information** is available in the online version of the paper.

**Acknowledgements** We thank members of the Brun laboratory and C. Fuqua for comments on the manuscript. We thank D. Kysela, V. Hughes and V. Silvanose for help in environmental sampling and phylogenetic analysis, L. Zhuo and C. Huang for help in statistical analysis, S. Shaw for advice on quantitative image analysis, M. Hahn, M. Lynch and R. Raff for discussions on evolution, and the Center for Genomics and Bioinformatics at Indiana University for help in sequencing. We thank the Indiana University Light Microscopy Imaging Center for their help with OMX super-resolution microscopy, supported by National Institutes of Health grant S10RR028697-01, and the Indiana Molecular biology Institute electron microscopy facility at Indiana University for their help with electron microscopy. We thank M. Thanbichler, J. Poindexter, P. Caccamo and P. Viollier for providing us with *Caulobacter* strain and

plasmids, J. Poindexter, J. Peterson, J. Lindquist and A. Quinones for help in locating the strain collection of the late Jack Pate from which we obtained some of the *A. excentricus* and *A. biprosthecum* strains used in this study, and M. Wortinger, S. Green, E. Quardokus and J. (Wagner) Herman for early work with *Asticcacaulis* that helped set the stage for this study. This work was supported by National Institutes of Health grant GM051986, National Science Foundation grant MCB0731950 and by a grant from the Indiana University Metabolomics and Cytomics Initiative (METACyt) program, which was financed, in part, by a major endowment from the Lilly Foundation. P.J.B.B. was supported by National Institutes of Health National Research Service Award AI072992.

**Author Contributions** C.J., P.J.B.B. and Y.V.B. designed the experiments. C.J. performed the experiments and A.D. developed the automated image analysis tools. C.J., P.J.B.B., A.D. and Y.V.B. analysed and interpreted the data. C.J. and Y.V.B. wrote the paper. C.J., P.J.B.B., A.D. and Y.V.B. edited the paper.

**Author Information** Genomic data of strains sequenced in this study are deposited in GenBank/EMBL/DBJ under accession numbers AWGD000000000 (*Asticcacaulis* sp. AC460), AWGE000000000 (*Asticcacaulis* sp. AC466), AWGC000000000 (*Asticcacaulis* sp. AC402), AWGF000000000 (*Asticcacaulis* sp. YBE204) and AWGB000000000 (*Asticcacaulis benevestitus* DSM16100). Reprints and permissions information is available at [www.nature.com/reprints](http://www.nature.com/reprints). The authors declare no competing financial interests. Readers are welcome to comment on the online version of the paper. Correspondence and requests for materials should be addressed to Y.V.B. ([ybrun@indiana.edu](mailto:ybrun@indiana.edu)).

# Genetics of single-cell protein abundance variation in large yeast populations

Frank W. Albert<sup>1,2</sup>, Sebastian Treusch<sup>2</sup>, Arthur H. Shockley<sup>3</sup>, Joshua S. Bloom<sup>1,4</sup> & Leonid Kruglyak<sup>1,4,5</sup>

Variation among individuals arises in part from differences in DNA sequences, but the genetic basis for variation in most traits, including common diseases, remains only partly understood. Many DNA variants influence phenotypes by altering the expression level of one or several genes. The effects of such variants can be detected as expression quantitative trait loci (eQTL)<sup>1</sup>. Traditional eQTL mapping requires large-scale genotype and gene expression data for each individual in the study sample, which limits sample sizes to hundreds of individuals in both humans and model organisms and reduces statistical power<sup>2–6</sup>. Consequently, many eQTL are probably missed, especially those with smaller effects<sup>7</sup>. Furthermore, most studies use messenger RNA rather than protein abundance as the measure of gene expression. Studies that have used mass-spectrometry proteomics<sup>8–13</sup> reported unexpected differences between eQTL and protein QTL (pQTL) for the same genes<sup>9,10</sup>, but these studies have been even more limited in scope. Here we introduce a powerful method for identifying genetic loci that influence protein expression in the yeast *Saccharomyces cerevisiae*. We measure single-cell protein abundance through the use of green fluorescent protein tags in very large populations of genetically variable cells, and use pooled sequencing to compare allele frequencies across the genome in thousands of individuals with high versus low protein abundance. We applied this method to 160 genes and detected many more loci per gene than previous studies. We also observed closer correspondence between loci that influence protein abundance and loci that influence mRNA abundance of a given gene. Most loci that we detected were clustered in ‘hotspots’ that influence multiple proteins, and some hotspots were found to influence more than half of the proteins that we examined. The variants that underlie these hotspots have profound effects on the gene regulatory network and provide insights into genetic variation in cell physiology between yeast strains.

We developed a method for detecting genetic influences on protein levels in large populations of genetically distinct individual yeast cells (Extended Data Fig. 1). The method leverages extreme QTL mapping (X-QTL), a bulk segregant QTL mapping strategy with high statistical power<sup>14</sup>. We quantified protein abundance by measuring levels of green fluorescent protein (GFP) inserted in-frame downstream of a given gene of interest. The GFP tag allows protein abundance to be rapidly and accurately measured in millions of live, single cells by fluorescence-activated cell sorting (FACS). To apply the method to many genes, we took advantage of the yeast GFP collection<sup>15</sup>, in which over 4,000 strains each contain a different gene tagged with GFP in a common genetic background (BY). For each gene under study, we crossed the GFP strain to a genetically divergent vineyard strain (RM) and generated a large pool of haploid GFP-positive offspring (segregants) of the same mating type. Across the genome, each segregant inherits either the BY or the RM allele at each locus, some of which influence the given gene’s protein level. We took a starting population of over 500,000 segregants and used FACS to collect 10,000 cells each from the high and low tails of GFP levels (Extended Data Fig. 2a). Such selection of phenotypically

extreme individuals from a large population provides high power to detect loci with small effects<sup>14</sup>. We extracted DNA in bulk from these extreme populations, sequenced it to ~34-fold coverage, and used an analysis method that combines information across linked single nucleotide polymorphisms to accurately estimate allele frequencies from this depth of coverage<sup>16</sup>. We detected loci that influence protein abundance as genomic regions where the high and low GFP pools differ in the frequency of the parental alleles (Extended Data Fig. 3). We denote these loci ‘extreme protein QTL’ or X-pQTL.

We applied our method to 174 abundantly expressed genes, 140 of which were chosen based on previous eQTL and pQTL results, whereas 34 were selected at random. False discovery rates were determined using control experiments in which two cell populations were collected at random with respect to GFP level and compared as described above (Extended Data Fig. 2b). High-quality results were obtained for 160 genes (Supplementary Data 1 contains details on the genes, including exclusion criteria). Across these 160 genes, we identified 1,025 X-pQTL at a false discovery rate of 0.7%. The median genomic region spanned by these loci was 68 kilobases (Supplementary Data 2). The resulting X-pQTL were highly reproducible as gauged by biological and technical replicates (Supplementary Note 1, Supplementary Table 1 and Extended Data Fig. 4). The number of X-pQTL per gene ranged from 0 to 25, with a median of five. We compared these numbers to eQTL and pQTL results based on published mRNA and mass-spectrometry protein data on ~100 segregants from a cross between the same BY and RM isolates we study here<sup>2,12</sup>. Eighty-five genes were assayed in all three data sets; for these genes, we observed a mean of 1.2 eQTL, 0.6 pQTL and 7.2 X-pQTL (Fig. 1). Our method increased detection of loci that influence protein levels by an average of 1,100%, as compared to a 15% increase

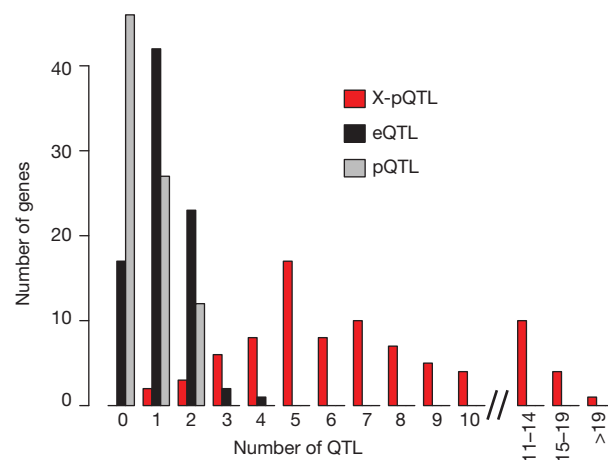


**Figure 1 | Multiple loci affect protein levels.** Histogram showing the number of loci per gene among 85 genes with X-pQTL, eQTL and pQTL data.

<sup>1</sup>Department of Human Genetics, University of California, Los Angeles, California 90095, USA. <sup>2</sup>Lewis Sigler Institute for Integrative Genomics, Princeton University, Princeton, New Jersey 08544, USA. <sup>3</sup>Synthetic Genomics, 11149 North Torrey Pines Road, La Jolla, California 92037, USA. <sup>4</sup>Howard Hughes Medical Institute, University of California, Los Angeles, California 90095, USA. <sup>5</sup>Department of Biological Chemistry, University of California, Los Angeles, California 90095, USA.

recently reported through improvements in mass spectrometry<sup>17</sup>. Interestingly, the distribution of detected loci per gene approaches that previously predicted to underlie gene expression variation in this yeast cross<sup>7</sup>, indicating that the higher power of the method enabled discovery of loci with small effects that escaped detection in previous studies. Our detection of multiple X-pQTL per gene directly demonstrates considerable genetic complexity in protein expression variation.

By design, all cells in the experiments described above inherit the GFP-tagged gene of interest, and the surrounding local region of the genome, from the BY strain. Therefore, the detected X-pQTL are distant from the gene of interest, and probably influence gene expression in *trans*. Previous studies have shown that mRNA levels of many genes are influenced by genetic variants in or near the gene itself (local eQTL), the majority of which influence gene expression in *cis*<sup>1</sup>. By contrast, local pQTL were reported to be rare on the basis of mass spectrometry data<sup>8,9</sup>. We investigated local X-pQTL by generating GFP-tagged strains for 41 genes in the RM genetic background, and repeating the crosses so that both parent strains carried GFP-tagged alleles, which then segregated among the progeny. We detected local X-pQTL at genome-wide significance for 20 genes (49%, Extended Data Fig. 5), and several additional genes would pass a more relaxed local significance threshold (Supplementary Table 2). Thus, local genetic variation affects protein levels for at least half of the genes we tested, in contrast to earlier observations<sup>8,9</sup> but in line with more recent work<sup>11,13</sup>.

The genetic basis of mRNA variation has previously been reported to be surprisingly different from that of protein variation<sup>8–10</sup>. For example, on the basis of published microarray<sup>7</sup> and mass-spectrometry data<sup>12</sup> for genes also present in our current study, only 23% of the eQTL had a corresponding pQTL. By contrast, we observed that 60% of the distant eQTL had a corresponding X-pQTL whereas only 5% were expected by chance (randomization test,  $P < 0.01$ ). The direction of QTL effect (that is, whether higher expression is associated with the BY or the RM allele) agreed for 92% of these shared loci (randomization test,  $P < 0.01$ ). The local eQTL showed similar concurrence (13 out of 21 local eQTL, or 62%, had a corresponding X-pQTL), with slightly lower directional agreement (77%). Thus, in line with recent results for strong local eQTL in yeast<sup>13</sup>, at least half of both local and distant loci with effects on mRNA levels also influence protein levels. The fraction of pQTL with a corresponding X-pQTL was similar to that for eQTL (46% versus 60%; chi-squared test:  $\chi^2 = 1.1$ ,  $P = 0.3$ ).

We next asked whether the many new X-pQTL discovered here (that is, those without a corresponding significant eQTL) are best explained by post-transcriptional effects or by mRNA differences that are too small to be detected at genome-wide significance thresholds. In support of the latter hypothesis, we found that X-pQTL that correspond to significant eQTL have larger effects than those that do not (Wilcoxon rank test,  $P = 6 \times 10^{-11}$ , Extended Data Fig. 6). Furthermore, at X-pQTL without a significant eQTL the direction of allelic effect nevertheless agreed with that in the mRNA data 66% of the time (randomization test,  $P < 0.01$ ). These results are consistent with the existence of many undetected weak-effect eQTL (Supplementary Note 2 and Extended Data Fig. 7), but larger studies of mRNA levels are needed to confirm this. We did observe some clear differences between X-pQTL and eQTL. For 21 out of 109 significant distant eQTL (19%), we saw no evidence for a corresponding X-pQTL, even at low statistical stringency (log odds ratio (lod)  $< 1$ ). Five genes with strong local eQTL also showed no evidence for a local X-pQTL; conversely, four genes with a local X-pQTL had no corresponding eQTL (Extended Data Table 1). These cases may represent influences of genetic variation on post-transcriptional processes.

Distant eQTL in yeast, as well as in other species, are not randomly distributed throughout the genome, but instead are clustered at 'hotspot' loci that influence the expression of many genes<sup>3,5,18</sup>. We observed such clustering of X-pQTL at 20 genome locations, each of which overlapped more X-pQTL ( $\geq 12$ ) than expected by chance (Extended Data Table 2). The majority of all detected distant X-pQTL (69%) fell within a hotspot.

Notably, these 20 X-pQTL hotspots captured nearly all of the mRNA hotspots identified in the eQTL data for the same cross<sup>2</sup> (Fig. 2 and Extended Data Table 2). By contrast, many eQTL hotspots did not correspond to a mass-spectrometry-based pQTL hotspot<sup>9,12</sup>.

The X-pQTL hotspots had widespread effects on protein levels. The median fraction of genes a hotspot affected was 27% of the 160 genes tested, and two of the hotspots each affected more than half of the genes (Extended Data Table 2). The magnitude and direction of expression changes differed considerably among the genes influenced by a given hotspot (Fig. 3a). Together, these observations are best explained by hotspots shaping the proteome in a hierarchical manner. Proteins with the largest abundance changes are likely to be closely related in biological function to the gene whose alleles underlie a hotspot. Abundance of more distantly connected proteins may be more weakly perturbed through mechanisms that influence the overall physiological state of the cell<sup>19</sup>. The consequences of some genetic differences may thus reverberate through much of the cell. We illustrate these ideas with a closer look at three of the hotspots.

The hotspot at ~239 kilobases on chromosome XII influences the expression of nearly half the genes in our set (Fig. 3b). It contains the gene *HAP1*, a transcriptional activator of genes involved in cellular respiration<sup>20</sup>. In BY, transcriptional activation by *HAP1* is reduced owing to a transposon insertion, whereas *HAP1* function is intact in RM<sup>18,21</sup>. Of the nine genes in our data set that are under direct transcriptional control by *HAP1* (ref. 22), seven were regulated by this hotspot (*YHB1*, *ACS2*, *CYC1*, *ERG10*, *OLE1*, *ADO1*, *PDR16*), more than expected by chance (Fisher's exact test,  $P = 0.02$ ). Further, these seven direct *HAP1* targets all had reduced expression in the presence of the BY allele of *HAP1*, and they were more strongly influenced by the hotspot than the other genes linking here (Wilcoxon test,  $P = 0.002$ , Fig. 3c). Similarly, the hotspot on chromosome XI contains the gene *HAP4*, which encodes a component of the Hap2/3/4/5 complex, an activator of respiratory gene expression with different target genes than *HAP1* (ref. 23). Direct transcriptional targets of this complex<sup>22</sup> are enriched among the genes influenced by this hotspot in our data (5 out of 6 genes,  $P = 0.0003$ ), and these target genes were more strongly affected than other genes (Wilcoxon test,  $P = 0.02$ ). Notably, the BY allele was associated with lower expression at all these *HAP4* targets (Fig. 3c). Thus, variation at both *HAP1* and *HAP4* regulates direct targets involved in cellular respiration. In both cases, the RM allele is associated with a more respiratory cellular state<sup>19</sup>, probably resulting in the weaker expression changes for the many other genes affected by these hotspots.

The hotspot on chromosome XV regulates the largest fraction of genes in our data set (Extended Data Table 2). We previously showed that variation in the gene *IRA2* underlies the corresponding eQTL hotspot<sup>2</sup>. *IRA2* is an inhibitor of the Ras/protein kinase A (PKA) signalling pathway, which regulates a wide variety of processes, including the cellular

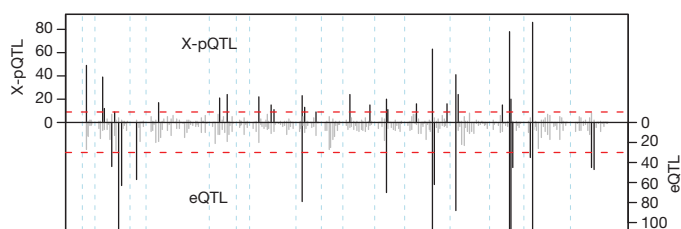


**Figure 2 | X-pQTL hotspots.** Number of X-pQTL (top) versus eQTL (bottom, inverted scale) in 20-cM bins along the genome. The red dashed lines correspond to the expectation if QTL were distributed randomly. Bins in which the QTL count exceeds this threshold are shown in black, others in grey. Note that the eQTL axis is truncated to permit easier visual comparison. The eQTL hotspot *glu1* (ref. 2) (Extended Data Table 2) narrowly failed the permutation threshold in our re-analysis. The eQTL hotspots on chromosomes II and III (*glu3*, *glu4*, *glu5*) correspond to polymorphisms that do not segregate in our strains.



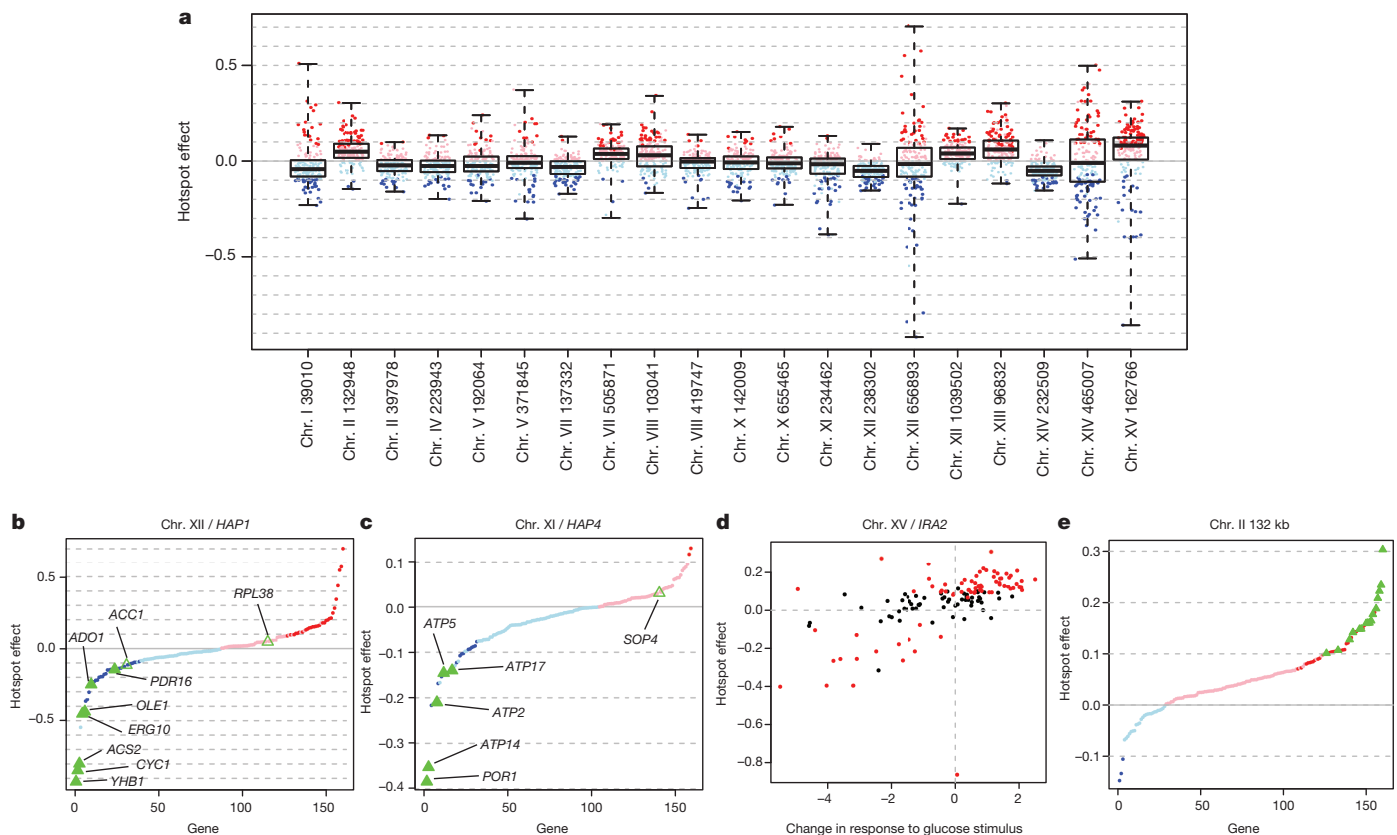


**Figure 3 | Hotspot effects.** **a**, Distribution of hotspot effects. Red (blue): higher (lower) expression associated with the BY allele. Darker dots: significant X-pQTL. Boxplots show the median (central line), central quartiles (boxes) and data extremes (whiskers). **b**, **c**, Effects of the *HAP1* (**b**) and *HAP4* (**c**) hotspots sorted by effect size. Green triangles: direct transcriptional targets of *HAP1* or

*HAP4*. Filled triangles: significant X-pQTL. **d**, Correlation of hotspot effects with expression changes triggered by glucose response. Red circles: genes significantly regulated by the hotspot. **e**, Effects of the chromosome II hotspot at position 132,948. Green triangles: genes with ribosomal and translation-related functions (Supplementary Table 3).

response to glucose<sup>24</sup>. Addition of glucose to yeast growing on non-fermentable carbon sources results in expression changes at >40% of all genes<sup>24</sup>, and most of these changes are mediated through the Ras/PKA pathway<sup>25</sup>. The BY allele of *IRA2* is less active than the RM allele<sup>2</sup>, and is therefore expected to be associated with higher Ras/PKA activity<sup>19</sup>. Indeed, the effects of this hotspot on protein levels are correlated with the mRNA expression changes induced by glucose addition<sup>25</sup> (Spearman rank correlation  $\rho = 0.68$ ,  $P < 2 \times 10^{-16}$ , Fig. 3d). The BY allele thus mimics stronger glucose signalling<sup>19</sup> even though glucose levels are constant and identical for all cells in our experiments. Interestingly, activation of respiratory genes by *HAP1* and *HAP4* is a branch of glucose signalling that is independent of Ras/PKA activity<sup>25</sup>. Thus, the BY laboratory strain differs from the wild RM strain in at least three key components of glucose sensing.

The hotspot effects often overlap for individual proteins. For example, the three hotspots described above jointly regulate a set of 11 genes in our data set (Extended Data Fig. 8). The three BY alleles all reduced expression of five of these proteins. Interestingly, these five genes (*ATP14*, *ATP17*, *ATP2*, *CIT1*, *MDH1*; Extended Data Fig. 8) are all involved in aerobic respiration, whereas the remaining six genes are not. The BY strain grows better than wild strains on glucose-rich media that favour fermentation over respiration<sup>26,27</sup>. Consistent direction of eQTL effects for genes in a pathway can be interpreted as evidence for adaptive evolution<sup>28</sup>. Thus, the *HAP1*, *HAP4* and *IRA2* hotspots may represent adaptations of BY to the glucose-rich culture conditions commonly used in the laboratory<sup>29</sup>.

Ten X-pQTL hotspots did not have corresponding eQTL hotspots. They may arise from eQTL with effects below the detection limit of the earlier studies, or from variants that influence protein levels via post-transcriptional mechanisms. For example, the locus centred at 132,948

base pairs on chromosome II regulated about one-third of genes in our data set; the largest fraction among the ten novel hotspots (Extended Data Table 2). The BY allele increased expression of multiple ribosomal proteins and translation factors, suggesting that this hotspot regulates the abundance of ribosomes (Fig. 3e and Supplementary Table 3). Interestingly, none of the ribosomal genes whose protein levels mapped to this hotspot had an eQTL at this locus, suggesting that it may influence ribosome abundance through post-transcriptional processes<sup>30</sup>.

We developed a powerful method to detect genetic variants affecting protein levels and used it to uncover substantial complexity in gene expression regulation. Our findings suggest that many more eQTL and pQTL will be discovered in studies with larger sample sizes in other species. Our approach can be readily extended to any situation in which segregating cells can be subjected to fluorescent labelling and sorting.

## METHODS SUMMARY

Full information can be found in the Methods section.

**Online Content** Any additional Methods, Extended Data display items and Source Data are available in the online version of the paper; references unique to these sections appear only in the online paper.

Received 25 July; accepted 19 November 2013.

Published online 8 January; corrected online 10 January 2014 (see full-text HTML version for details).

1. Rockman, M. V. & Kruglyak, L. Genetics of global gene expression. *Nature Rev. Genet.* **7**, 862–872 (2006).
2. Smith, E. N. & Kruglyak, L. Gene–environment interaction in yeast gene expression. *PLoS Biol.* **6**, e83 (2008).
3. Rockman, M. V., Skovranek, S. S. & Kruglyak, L. Selection at linked sites shapes heritable phenotypic variation in *C. elegans*. *Science* **330**, 372–376 (2010).

4. Huang, G. J. *et al.* High resolution mapping of expression QTLs in heterogeneous stock mice in multiple tissues. *Genome Res.* **19**, 1133–1140 (2009).
5. West, M. A. L. *et al.* Global eQTL mapping reveals the complex genetic architecture of transcript-level variation in *Arabidopsis*. *Genetics* **175**, 1441–1450 (2007).
6. Lappalainen, T. *et al.* Transcriptome and genome sequencing uncovers functional variation in humans. *Nature* **501**, 506–511 (2013).
7. Brem, R. B. & Kruglyak, L. The landscape of genetic complexity across 5,700 gene expression traits in yeast. *Proc. Natl Acad. Sci. USA* **102**, 1572–1577 (2005).
8. Foss, E. J. *et al.* Genetic basis of proteome variation in yeast. *Nature Genet.* **39**, 1369–1375 (2007).
9. Foss, E. J. *et al.* Genetic variation shapes protein networks mainly through non-transcriptional mechanisms. *PLoS Biol.* **9**, e1001144 (2011).
10. Ghazalpour, A. *et al.* Comparative analysis of proteome and transcriptome variation in mouse. *PLoS Genet.* **7**, e1001393 (2011).
11. Wu, L. *et al.* Variation and genetic control of protein abundance in humans. *Nature* **499**, 79–82 (2013).
12. Khan, Z., Bloom, J. S., Garcia, B. A., Singh, M. & Kruglyak, L. Protein quantification across hundreds of experimental conditions. *Proc. Natl Acad. Sci. USA* **106**, 15544–15548 (2009).
13. Skelly, D. A. *et al.* Integrative phenomics reveals insight into the structure of phenotypic diversity in budding yeast. *Genome Res.* **23**, 1496–1504 (2013).
14. Ehrenreich, I. M. *et al.* Dissection of genetically complex traits with extremely large pools of yeast segregants. *Nature* **464**, 1039–1042 (2010).
15. Huh, W.-K. *et al.* Global analysis of protein localization in budding yeast. *Nature* **425**, 686–691 (2003).
16. Edwards, M. D. & Gifford, D. K. High-resolution genetic mapping with pooled sequencing. *BMC Bioinformatics* **13**, S8 (2012).
17. Picotti, P. *et al.* A complete mass-spectrometric map of the yeast proteome applied to quantitative trait analysis. *Nature* **494**, 266–270 (2013).
18. Brem, R. B., Yvert, G., Clinton, R. & Kruglyak, L. Genetic dissection of transcriptional regulation in budding yeast. *Science* **296**, 752–755 (2002).
19. Litvin, O., Causton, H. C., Chen, B. J. & Pe'er, D. Modularity and interactions in the genetics of gene expression. *Proc. Natl Acad. Sci. USA* **106**, 6441–6446 (2009).
20. Zitomer, R. S. & Lowry, C. V. Regulation of gene expression by oxygen in *Saccharomyces cerevisiae*. *Microbiol. Rev.* **56**, 1–11 (1992).
21. Gaisne, M., Bécam, A. M., Verdier, J. & Herbert, C. J. A. A 'natural' mutation in *Saccharomyces cerevisiae* strains derived from S288c affects the complex regulatory gene HAP1 (CYP1). *Curr. Genet.* **36**, 195–200 (1999).
22. Harbison, C. T. *et al.* Transcriptional regulatory code of a eukaryotic genome. *Nature* **431**, 99–104 (2004).
23. Butler, G. Hypoxia and gene expression in eukaryotic microbes. *Annu. Rev. Microbiol.* **67**, 291–312 (2013).
24. Zaman, S., Lippman, S. I., Zhao, X. & Broach, J. R. How *Saccharomyces* responds to nutrients. *Annu. Rev. Genet.* **42**, 27–81 (2008).
25. Zaman, S., Lippman, S. I., Schnepfer, L., Slonim, N. & Broach, J. R. Glucose regulates transcription in yeast through a network of signaling pathways. *Mol. Syst. Biol.* **5**, 245 (2009).
26. Spor, A. *et al.* Niche-driven evolution of metabolic and life-history strategies in natural and domesticated populations of *Saccharomyces cerevisiae*. *BMC Evol. Biol.* **9**, 296 (2009).
27. Warringer, J. *et al.* Trait variation in yeast is defined by population history. *PLoS Genet.* **7**, e1002111 (2011).
28. Fraser, H. B., Moses, A. M. & Schadt, E. E. Evidence for widespread adaptive evolution of gene expression in budding yeast. *Proc. Natl Acad. Sci. USA* **107**, 2977–2982 (2010).
29. Lewis, J. A. & Gasch, A. P. Natural variation in the yeast glucose-signaling network reveals a new role for the Mig3p transcription factor. *G3 Gene Genomes Genetics* **2**, 1607–1612 (2012).
30. Henras, A. K. *et al.* The post-transcriptional steps of eukaryotic ribosome biogenesis. *Cell. Mol. Life Sci.* **65**, 2334–2359 (2008).

**Supplementary Information** is available in the online version of the paper.

**Acknowledgements** We are grateful to C. DeCoste at the Princeton Flow Cytometry Resource Facility for technical assistance and advice on the experiments. This work was supported by National Institutes of Health (NIH) grant R01 GM102308, a James S. McDonnell Centennial Fellowship, and the Howard Hughes Medical Institute (L.K.), German Science Foundation research fellowship AL 1525/1-1 (F.W.A.), a National Science Foundation fellowship (J.S.B.), and NIH postdoctoral fellowship F32 GM101857-02 (S.T.).

**Author Contributions** F.W.A. and L.K. conceived the project, designed research and wrote the paper. F.W.A. and A.H.S. performed experiments. F.W.A. analysed the data. S.T. provided advice on yeast strain construction, the initial experimental design and other experimental procedures. J.S.B. provided advice on experimental procedures and data analysis.

**Author Information** Reprints and permissions information is available at [www.nature.com/reprints](http://www.nature.com/reprints). The authors declare no competing financial interests. Readers are welcome to comment on the online version of the paper. Correspondence and requests for materials should be addressed to F.W.A. ([fabert@mednet.ucla.edu](mailto:fabert@mednet.ucla.edu)) or L.K. ([LKruglyak@mednet.ucla.edu](mailto:LKruglyak@mednet.ucla.edu)).

# A discrete genetic locus confers xyloglucan metabolism in select human gut Bacteroidetes

Johan Larsbrink<sup>1\*</sup>, Theresa E. Rogers<sup>2\*</sup>, Glyn R. Hemsworth<sup>3\*</sup>, Lauren S. McKee<sup>1,4</sup>, Alexandra S. Tauzin<sup>5</sup>, Oliver Spadiut<sup>1,4</sup>, Stefan Klinger<sup>1</sup>, Nicholas A. Pudlo<sup>2</sup>, Karthik Urs<sup>2</sup>, Nicole M. Koropatkin<sup>2</sup>, A. Louise Creagh<sup>6</sup>, Charles A. Haynes<sup>6</sup>, Amelia G. Kelly<sup>2</sup>, Stefan Nilsson Cederholm<sup>1</sup>, Gideon J. Davies<sup>3</sup>, Eric C. Martens<sup>2</sup> & Harry Brumer<sup>1,5</sup>

A well-balanced human diet includes a significant intake of non-starch polysaccharides, collectively termed 'dietary fibre', from the cell walls of diverse fruits and vegetables<sup>1</sup>. Owing to the paucity of alimentary enzymes encoded by the human genome<sup>2</sup>, our ability to derive energy from dietary fibre depends on the saccharification and fermentation of complex carbohydrates by the massive microbial community residing in our distal gut<sup>3,4</sup>. The xyloglucans (XyGs) are a ubiquitous family of highly branched plant cell wall polysaccharides<sup>5,6</sup> whose mechanism(s) of degradation in the human gut and consequent importance in nutrition have been unclear<sup>1,7,8</sup>. Here we demonstrate that a single, complex gene locus in *Bacteroides ovatus* confers XyG catabolism in this common colonic symbiont. Through targeted gene disruption, biochemical analysis of all predicted glycoside hydrolases and carbohydrate-binding proteins, and three-dimensional structural determination of the vanguard *endo*-xyloglucanase, we reveal the molecular mechanisms through which XyGs are hydrolysed to component monosaccharides for further metabolism. We also observe that orthologous XyG utilization loci (XyGULs) serve as genetic markers of XyG catabolism in Bacteroidetes, that XyGULs are restricted to a limited number of phylogenetically diverse strains, and that XyGULs are ubiquitous in surveyed human metagenomes. Our findings reveal that the metabolism of even highly abundant components of dietary fibre may be mediated by niche species, which has immediate fundamental and practical implications for gut symbiont population ecology in the context of human diet, nutrition and health<sup>9–12</sup>.

Despite our omnivory, a census of the glycoside hydrolases (GHs) encoded by the human genome indicates that our inherent ability to digest carbohydrates is restricted to starch and simple saccharides such as malto-oligosaccharides, sucrose and lactose<sup>2</sup>. Consequently, the human gut microbiota and its cohort of predicted carbohydrate-active enzymes are implicated in the conversion of otherwise indigestible plant polysaccharides to short-chain fatty acids<sup>2,7,13</sup>, which provide up to 10% of daily caloric intake in humans<sup>14,15</sup>, and are central to colonic health<sup>4,9,11,16</sup>. Despite an increasing body of (meta)genomic sequence data<sup>13,17–20</sup>, the enzymatic pathways by which the most common dietary polysaccharides are digested in the human gut have not been elucidated<sup>7,13</sup>.

XyGs are widespread in the vegetables we consume: dicot primary cell walls, for example those of lettuce, onions and tomatoes, may contain up to 25% XyG on a dry-weight basis<sup>15,6</sup>. The primary walls of commelinoid monocots, including the cereals, contain much lower (1–5%)—but still non-zero—amounts of XyGs<sup>1,6</sup>. Seed XyGs are also widely used as food-thickening agents and have been used as drug delivery matrices in the intestine<sup>21</sup>. This family of polysaccharides is typified by a  $\beta(1\rightarrow4)$ -glucan main chain that is heavily substituted with pendant  $\alpha(1\rightarrow6)$ -linked xylosyl units. Depending on the species and tissue of

origin, these branches may be further extended by additional monosaccharides, including galactose, fucose and/or arabinose<sup>5,22</sup> (Fig. 1). As such, complete saccharification in the gut necessarily requires a cadre of enzymes to address the monosaccharide and linkage diversity of these complex polysaccharides.

We recently identified a polysaccharide utilization locus (PUL) in the genome of a common human gut symbiont, *B. ovatus*—but not in the closely related model species *B. thetaiotaomicron*<sup>17</sup>—that was transcriptionally upregulated in response to growth on galactoxyloglucan<sup>7</sup>. By homology with the archetypal starch utilization system (Sus) of *B. thetaiotaomicron*, this PUL was predicted to encode an outer membrane sugar-binding protein (SusD-like), a TonB-dependent sugar receptor/transporter (SusC-like), and an inner membrane hybrid two-component sensor. Further analysis revealed that this PUL was also predicted to encode eight GHs from six enzyme families (Fig. 2), which tantalizingly suggested a collective role in XyG utilization by *B. ovatus*. To establish a direct causal link for growth on XyG<sup>7,8</sup> and outline a pathway for its degradation, we performed an in-depth molecular characterization of the PUL through reverse genetics, *in vitro* protein biochemistry and enzymology, and structural biology.

A mutant strain of *B. ovatus* harbouring a targeted deletion of the complete predicted XyGUL (Fig. 2) was indeed totally unable to grow

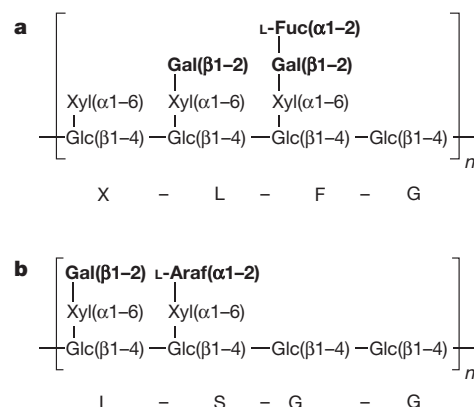


**Figure 1 | Representative structures of XXXG- and XXGG-type XyGs.**

**a**, XXXG-type XyGs, comprising a  $\text{Glc}_4\text{Xyl}_3$  repeating motif with variable branch extensions (bold residues). Tamarind seed XyG and primary cell wall XyGs (for example, from lettuce leaves) are distinguished by the absence of fucose in the former. **b**, XXGG-type XyGs, comprising a  $\text{Glc}_4\text{Xyl}_2$  repeating motif. These XyGs are common to solanaceous species (for example, tomato) and are typified by branches extended with arabinofuranosyl residues. Standard single-letter abbreviations<sup>5</sup> for designating backbone decorations are shown.

<sup>1</sup>Division of Glycoscience, School of Biotechnology, Royal Institute of Technology (KTH), AlbaNova University Centre, 106 91 Stockholm, Sweden. <sup>2</sup>Department of Microbiology and Immunology, University of Michigan Medical School, Ann Arbor, Michigan 48109, USA. <sup>3</sup>Structural Biology Laboratory, Department of Chemistry, University of York, York YO10 5DD, UK. <sup>4</sup>Wallenberg Wood Science Center, Royal Institute of Technology (KTH), Teknikringen 56-58, 100 44 Stockholm, Sweden. <sup>5</sup>Michael Smith Laboratories and Department of Chemistry, University of British Columbia, 2185 East Mall, Vancouver, British Columbia V6T 1Z4, Canada. <sup>6</sup>Michael Smith Laboratories and Department of Chemical and Biological Engineering, University of British Columbia, 2185 East Mall, Vancouver, British Columbia V6T 1Z4, Canada.

\*These authors contributed equally to this work.



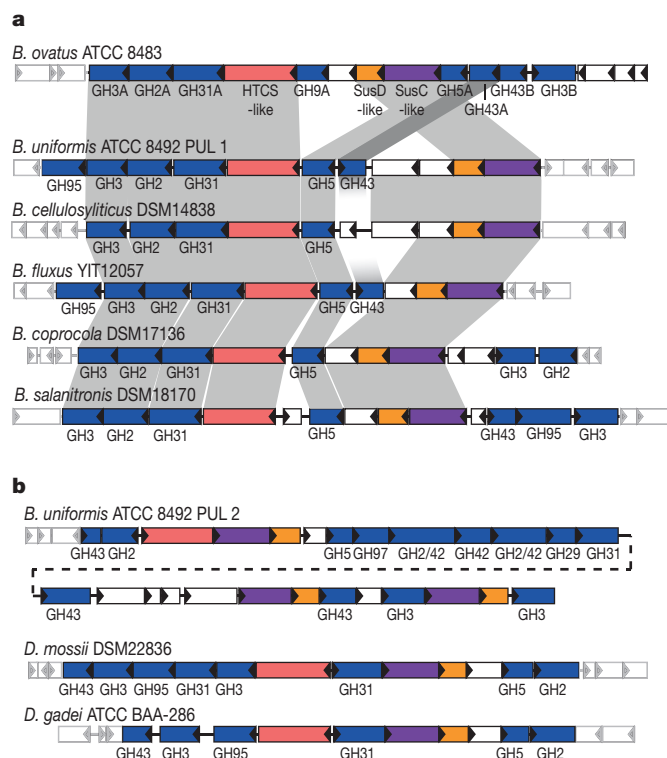


**Figure 2 | Structure of the *B. ovatus* XyGUL and evolution in the *Bacteroidetes* lineage.** **a**, PULs with partial homology and synteny; homologous genes are connected by grey bars and flanking genes lacking synteny are shown as semi-transparent. **b**, PULs with partial homology, but lacking overall synteny. Extended Data Fig. 2 provides transcriptional evidence that each of these gene clusters is responsive to growth on XyG.

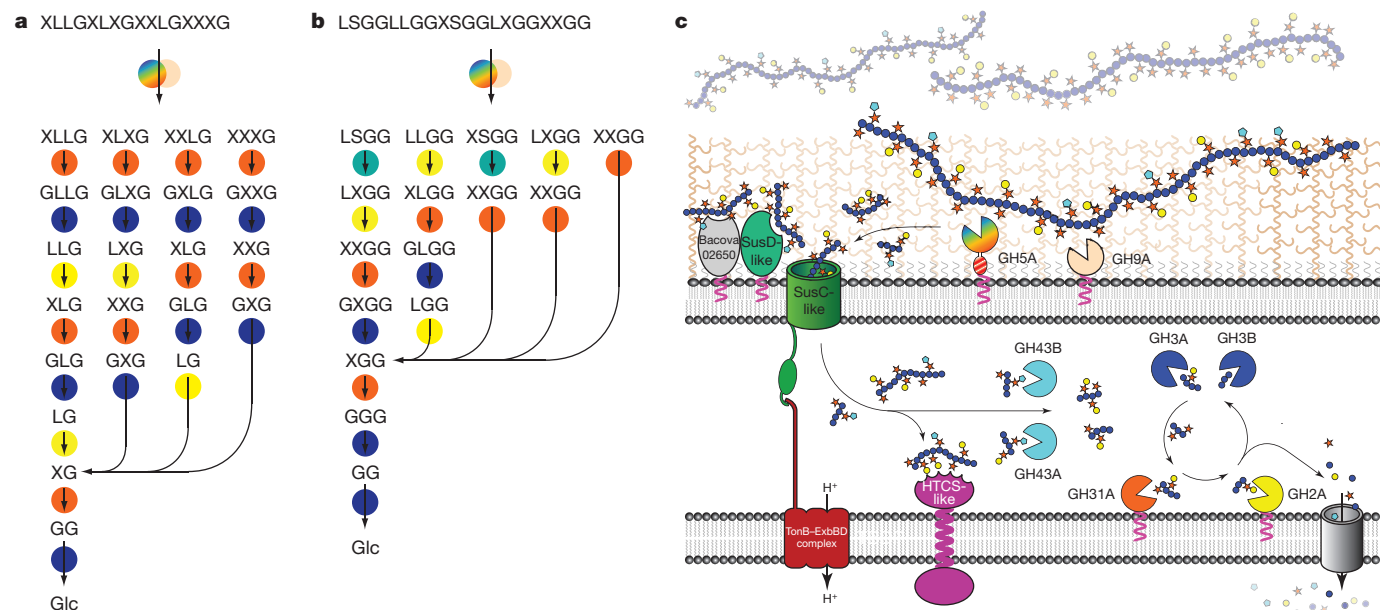
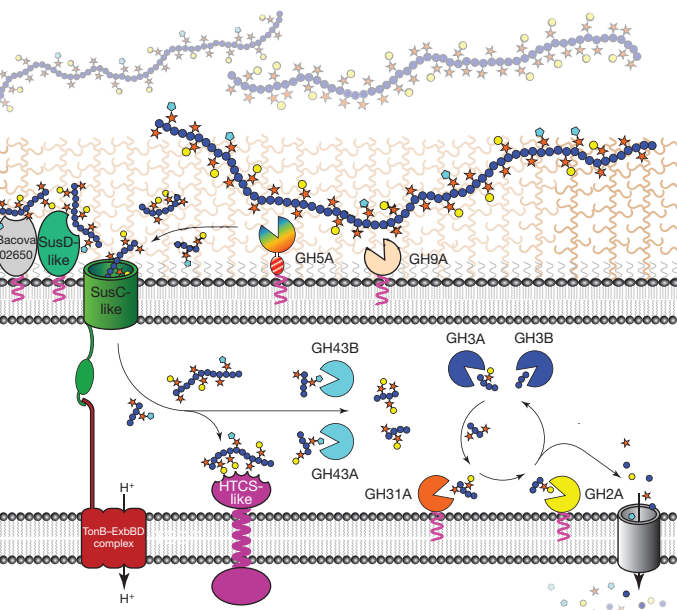


**Figure 3 | The concerted action of XyGUL gene products in the degradation of XyGs.** **a**, **b**, Most probable sequential pathways for the hydrolysis of galactoxyloglucan (**a**) and arabinogalactoxyloglucan (**b**) on the basis of enzyme kinetic data, product analysis and selected gene knockout studies (see Fig. 1 for XyG motif abbreviations). Enzymes are represented as circles, colour-coded as in panel **c**: rainbow, endo-xyloglucanase BoGH5A; tan,

on tamarind XyG as the sole carbon source, but was otherwise phenotypically identical to the wild-type strain (data not shown). This indicated an absolute requirement for one or more of the corresponding gene products in XyG catabolism. Subsequently, all eight predicted GHs were produced recombinantly in *Escherichia coli* and subjected to detailed enzymatic characterization to establish their substrate specificities and reaction products (Extended Data Table 1 and Supplementary Figs 1–20). All enzymes were maximally active in the pH range 6.0–7.0, which is consistent with function in the distal human gut (Supplementary Figs 1–6).

Reducing-sugar assays and mass spectrometry demonstrated that the recombinant *B. ovatus* (Bo)GH5A and BoGH9A enzymes were versatile endo-xyloglucanases, which cleaved the backbone of the three major types of natural XyGs, that is, seed galactoxyloglucan from tamarind kernel, dicot fucogalactoxyloglucan from lettuce leaves, and solanaceous arabinogalactoxyloglucan from tomato fruit, to produce XyG oligosaccharides (XyGOs) based on a Glc<sub>4</sub> backbone (Extended Data Table 1 and Supplementary Figs 7–10, compare with Fig. 1). Assays on chromogenic aryl β-glycosides and natural XyGOs, together with product analyses, revealed the following exo-specificities for the remaining XyGUL enzymes: BoGH2A, β-galactosidase; BoGH3A and BoGH3B, β-glucosidase; BoGH31A α-xylosidase; BoGH43A and BoGH43B, α-L-arabinofuranosidase (Extended Data Table 1 and Supplementary Figs 11–20). This profile of activities, together with phenotypic data from additional gene-specific knockout strains (Extended Data Table 2), allowed us to outline a complete model of XyG degradation by *B. ovatus* (Fig. 3).

Analogous to the endo-amylase SusG of the *B. thetaotaomicron* starch utilization system<sup>4</sup>, the vanguard role in XyG utilization by *B. ovatus* is performed by the versatile endo-xyloglucanase BoGH5A, which generates short XyGOs for uptake (Fig. 3). Indeed, a gene-specific knockout of *BoGH5A* rendered *B. ovatus* incapable of growth on XyG polysaccharide, but this phenotype could be directly rescued by the addition of XyGOs produced exogenously by recombinant BoGH5A (Extended



endo-xyloglucanase BoGH9A; orange, α-xylosidase BoGH31A; turquoise, α-L-arabinofuranosidase BoGH43A and/or BoGH43B; yellow, β-galactosidase BoGH2; dark blue, β-glucosidases BoGH3A and/or BoGH3B. **c**, Model of enzyme localization by analogy with the archetypal *sus* locus<sup>4</sup> and based on inference of N-terminal lipoprotein modification from protein sequence data.

Data Table 2, compare with Supplementary Fig. 8). By contrast, a gene-specific knockout of *BoGH9A* had no effect on growth (Extended Data Table 2), consistent with the observation that although this enzyme produced the same limit-digestion products from all XyGs as *BoGH5A*, *BoGH9A* was catalytically feeble with kinetics too slow to be quantified (Extended Data Table 1 and Supplementary Fig. 8–10). That a corresponding GH9 member is not found in orthologous XyGULs from other species, nor in a *B. ovatus* strain possessing a simpler XyGUL, which were all capable of growth on tamarind XyG (Fig. 2 and Extended Data Figs 1, 2), suggests that *BoGH9A* may be largely superfluous, or that it has a specialized role not revealed in our analysis.

A gene-specific knockout of *BoGH31A*, which encodes the  $\alpha$ -xylosidase, severely reduced *B. ovatus* growth on tamarind XyG and completely abolished growth on XyGOs (Extended Data Table 2). This is consistent with *BoGH31A* having an essential role in the removal of  $\alpha(1\rightarrow6)$ -xylosyl residues from the non-reducing-end of XyGOs (converting 'X' units to 'G' units), to allow subsequent hydrolysis by the  $\beta$ -glucosidases *BoGH3A* and *BoGH3B* (removing backbone 'G' units) and the  $\beta$ -galactosidase *BoGH2A* (or another  $\beta$ -galactosidase converting 'L' units to 'X' units; Fig. 3). The two  $\alpha$ -L-arabinofuranosidases *BoGH43A* and *BoGH43B* encoded by the XyGUL provide additional capacity to convert 'S' units to 'X' units, thereby enabling complete hydrolysis of solanaceous (for example, tomato, aubergine, pepper, and so on) arabinogalactoxyloglucan. It is presently unclear if the doubling of GH3- and GH43-encoding genes in the XyGUL has any biological importance; the similar specific activities of *BoGH3A* and *BoGH3B* towards XyGO  $\beta$ -glucosides suggests functional redundancy, whereas the apparent catalytic febleness of *BoGH43B* towards arabinofuranosides (Extended Data Table 1) may suggest simple loss-of-function or evolution of a currently unresolved, orthogonal activity contrasting with that of *BoGH43A*. Notably, the *B. ovatus* XyGUL does not encode an  $\alpha$ -fucosidase, as might be anticipated for the cleavage of the 'F' side chain in dicot fucogalactoxyloglucan (Fig. 1). This may reflect compensation by exogenous or endogenous  $\alpha(1\rightarrow2)$ -fucosidases<sup>2</sup> or strain specialization for XyGs from individual plant sources. Indeed, XyGULs from other *Bacteroides* species encode predicted  $\alpha$ -fucosidases from families GH29 and GH95 (Fig. 2).

To provide further insight into XyG recognition by the keystone enzyme, we solved the three-dimensional structure of *BoGH5A* in complex with the heptasaccharide XXXG by X-ray crystallography (Fig. 4 and Extended Data Table 3). The tertiary structure comprised a 96-residue bacteroidetes-associated carbohydrate-binding often N-terminal (BACON) domain<sup>23</sup> followed by a 372-residue C-terminal GH5 domain. The BACON domain comprised an eight-stranded, immunoglobulin-like  $\beta$ -sandwich fold and represents, to our knowledge, the first three-dimensional representative of this domain family. Notably, the two molecules in the asymmetric unit showed a large difference in the relative orientations of the BACON and GH5 domains (Fig. 4a). This suggested significant flexibility in the enzyme (Supplementary Video 1), which is anchored on the cell surface through N-terminal lipidation; mutation of the predicted lipidation site (Cys 1 $\rightarrow$ Ala) ablates surface localization and hampers growth on XyG (Extended Data Fig. 3). Notably, we were unable to find experimental evidence *in vitro* that the BACON domain functions in substrate binding (Extended Data Fig. 4), nor that it mediates interactions with other proteins of the XyGUL (native polyacrylamide gel electrophoresis (PAGE) data not shown). By contrast, the observation of strong XyG binding (Extended Data Fig. 4) by the SusD-like protein and neighbouring gene product (Fig. 2; locus tags Bacova\_02651 and Bacova\_02650, respectively) indicates that, as in the archetypal Sus system<sup>24</sup>, polysaccharide binding is mediated by independently encoded, non-catalytic proteins of the XyGUL. Thus, the broad designation of BACON domains as 'carbohydrate binding', as inferred by bioinformatics alone, may be actively misleading<sup>23,25</sup>. In light of current experimental data, the most parsimonious conclusion is that the primary function of the BACON domain in *BoGH5A* may be to distance the catalytic module from the cell surface and confer additional mobility to the catalytic domain for attack of the polysaccharide.

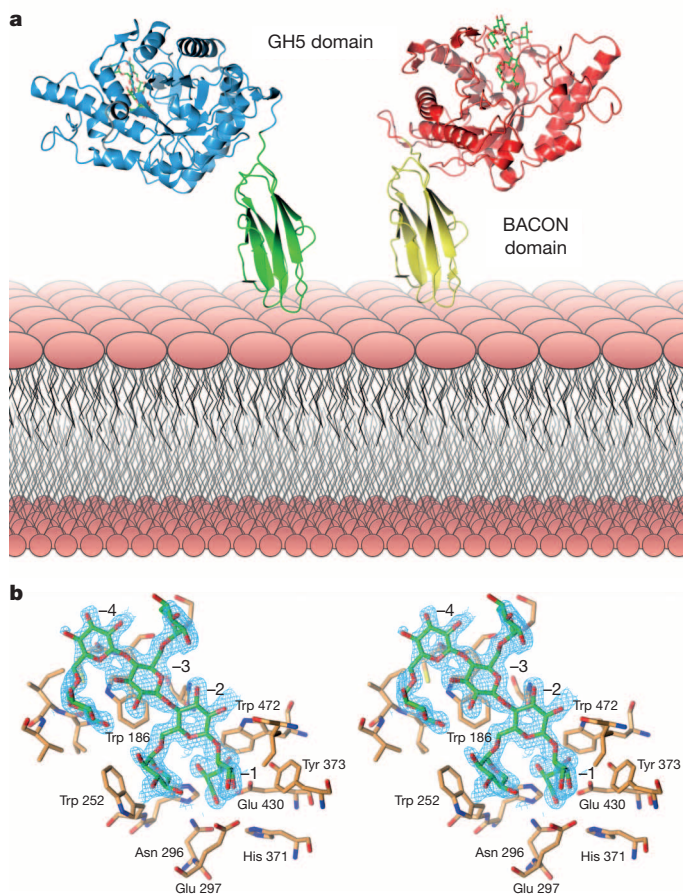


**Figure 4 | Structural biology of *BoGH5A*.** **a**, Tertiary structure; the two conformations observed *in crystallo* have been oriented relative to the N-terminal, membrane-anchored BACON domain (see also Supplementary Video 1). **b**, Divergent stereo view of the binding of XXXG in the  $-4$  to  $-1$  subsites (see also Supplementary Video 2). The wire frame represents an unbiased  $2F_o - F_c$  map (contoured at 0.3 electrons per  $\text{\AA}^3$ ) obtained using phases calculated from the best model prior to the incorporation of any ligand in refinement.

The catalytic domain has the prototypical  $(\alpha/\beta)_8$  fold typical of other GH5 members and is most similar to the *Paenibacillus pabuli* endo-xyloglucanase PpXG5 (Protein Data Bank (PDB) accession 2JEP; root mean squared deviation (r.m.s.d.) 1.47  $\text{\AA}$ , 330 C $\alpha$  atoms) and the *Clostridium cellulovorans* endo-glucanase EngD (PDB accession 3ICG; r.m.s.d. 1.45  $\text{\AA}$ , 345 C $\alpha$  atoms) of subfamily 4 (ref. 26). The heptasaccharide XXXG was observed to extend from subsites  $-4$  to  $-1$  in the active-site cleft in both molecules of the asymmetric unit, with binding mediated through sugar–aromatic-ring interactions and hydrogen bonds to both backbone and branching substrate moieties (Fig. 4b and Supplementary Video 2). The structure of this complex is well correlated with activity on chromogenic XyGO aryl  $\beta$ -glycoside substrates, which indicated that the enzyme productively harnesses the Xyl $\alpha(1\rightarrow6)$  side chains for catalysis (Extended Data Table 1). Detailed comparison with the PpXG5–GXLG complex structure (PDB accession 2JEQ)<sup>27</sup> revealed that binding of the  $\beta(1\rightarrow4)$ -glucan backbone is essentially identical in the two enzymes, although differences emerge in the subsites that accommodate the branching sugar residues (Supplementary Video 2). Regardless, it is clear that a broad active-site cleft engendering binding plasticity is the key feature allowing *BoGH5A* to accommodate a wide range of natural XyGs.

With a solid molecular understanding of the locus that confers *B. ovatus* with the ability to utilize XyG, we undertook a growth analysis of 292 individual *Bacteroides* strains isolated from the human gut, representing 29 different named species, to reveal the distribution of this trait



in nature. XyG catabolism was rare, confined to 70 strains belonging to just 6 individual, phylogenetically dispersed species (Fig. 5). Of the 25 *B. ovatus* strains tested, all but one grew on tamarind XyG. Interestingly, none of the 18 strains of the closely related *B. xylanisolvens* exhibited growth on XyG, which suggested that the XyGUL has been independently acquired by the *B. ovatus* lineage. This is supported by a comparative genomic analysis of the XyGUL and surrounding chromosomal region in these two species (Extended Data Fig. 1). All ten strains tested of the more distantly related *B. cellulosilyticus* grew very well on XyG, comparable with the less proficient *B. ovatus* strains. Representing a third phylogenetic clade, the single *B. fluxus* strain also grew to high density on XyG. Of 37 strains of *B. uniformis*, which is closely related to *B. fluxus* and among the most abundant organisms in the microbiota of Westerners<sup>18</sup>, 33 exhibited varying abilities to grow on XyG. Finally, two non-*Bacteroides* species, *Dysgonomonas gadei* and *D. mossii*, which are rarely observed in humans, but are abundant in termites, also possessed the capacity to degrade XyG, revealing that this phenotype has evolved in other lineages of Bacteroidetes.

A comparative analysis using genomic sequence data available for many of the strains tested showed a perfect concordance between the presence of an orthologous XyGUL and the ability to utilize XyG. Thus, we revealed putative XyGULs in *B. cellulosilyticus*, *B. uniformis*, *B. fluxus*, *D. mossii* and *D. gadei*, as well as in two sequenced species, *B. coprocola* and *B. salanitronis*, that were not available to test growth directly (Figs 2 and 5). These XyGULs were all activated during growth on XyG (Extended Data Fig. 2) and shared a similar overall organization with that of *B. ovatus*, but did not share similar flanking regions in their genomes, suggesting that they were acquired through separate events. In notable contrast with a recent report showing that conjugative transposons are capable

of mediating the horizontal transfer of new PULs into *Bacteroides* genomes<sup>28</sup>, there is no evidence of such a mechanism for XyGUL acquisition. Rather, the XyGUL seems to have been precisely inserted between two ancestral genes that are shared by all sequenced strains. For example, on the left side of XyGUL (Fig. 2 and Extended Data Fig. 1), there are only 108 base pairs (bp) between the 3' end of *BoGH3A* (Bacova\_02644) and the end of the adjacent shared region; on the right side there are only 640 bp between the end of *BoGH3B* (Bacova\_02659) and the second adjacent shared region.

To underscore the broad importance of dietary XyG metabolism, we surveyed public metagenomic data from 250 adult humans, revealing that 92% harbour at least one of five different *Bacteroides* XyGULs identified in this study (Extended Data Fig. 5). By contrast, the presence of a PUL involved in degrading the red algal polysaccharide porphyran (a component of the food product nori)<sup>29</sup> was exceptionally rare in the same population, and largely confined to a small cohort of Japanese subjects. To demonstrate that a metabolic advantage is associated with possessing a XyGUL, a competition experiment was performed using germ-free mice co-colonized with wild-type *B. ovatus* and an isogenic XyGUL deletion mutant. Both strains competed equally when glucose was presented as the sole dietary carbohydrate or when XyG was presented in a mixture of polysaccharides from natural vegetable sources (a diet comprising equal amounts of cooked bell pepper, aubergine, tomato fruit and lettuce). However, when this complex diet was removed and XyG was maintained as the only exogenous polysaccharide via the drinking water, the *B. ovatus* XyGUL mutant exhibited a significant fitness defect over a three-week period (Extended Data Fig. 6).

The prevalence of XyGs in the human diet suggests that the mechanism by which bacteria degrade these complex polysaccharides is highly important to human energy acquisition. Moreover, the rarity of XyG metabolism (Fig. 5, see also ref. 8) highlights the significance of *B. ovatus* and other proficient XyG-degrading Bacteroidetes as key members of the human gut microbial consortium<sup>10</sup>. Additional work will now be required to determine whether bacteria from other groups have evolved strategies to attack this ubiquitous plant cell wall polysaccharide in competition or synergy with members of the Bacteroidetes<sup>8,30</sup>. An unexpected finding is the specific adaptation of the GH complement of some XyGULs to XyGs from different plant sources; this theme may extend to other groups of plant polysaccharides and host mucosal glycans with similar or greater degrees of fine-structural variation. Following the example presented here, defining cohorts of enzymes and binding proteins that coordinate to target other complex dietary polysaccharides will be essential to elucidate fully the systems biology of gut microbial catabolism. Such a refined mechanistic understanding will be essential in designing rational intervention strategies, including prebiotics, probiotics or microbial community transplants, which aim to manipulate the membership, function and stability of this important ecosystem<sup>4,9–12</sup>.

## METHODS SUMMARY

Gene deletions in *B. ovatus* were conducted by allelic exchange in a  $\Delta tdk$  (thymidine kinase, Bacova\_03071) derivative strain of ATCC 8483 using the vector pExchange-*tdk*. Growth was measured spectrophotometrically in minimal media including XyG or XyGOs as appropriate. The Bacteroidetes species phylogeny was constructed by concatenating nucleotide sequences of six core genes, alignment with CLUSTAL-W, trimming of poorly aligned base pairs with Gblocks, and maximum parsimony tree building with MEGA5. Genes encoding the GHs of the XyGUL were cloned into pET21a vectors (predicted signal-peptide-encoding sequences were removed) and overexpressed in *E. coli* BL21(DE3) cells at 25 °C. Proteins were purified by immobilized nickel affinity and gel-filtration chromatography and expected molar masses were verified by mass spectrometry. Enzyme activities were determined against a range of aryl glycosides, polysaccharides and oligosaccharides using standard spectrophotometric, reducing-sugar and coupled enzyme assays; enzyme reaction products were analysed by high-performance anion exchange chromatography and matrix-assisted laser desorption ionization-time of flight (MALDI-TOF) mass spectrometry. Poly- and oligosaccharides were produced by extraction from natural sources and selective enzymatic hydrolysis using XyGUL and other enzymes as appropriate. X-ray diffraction data were collected at the

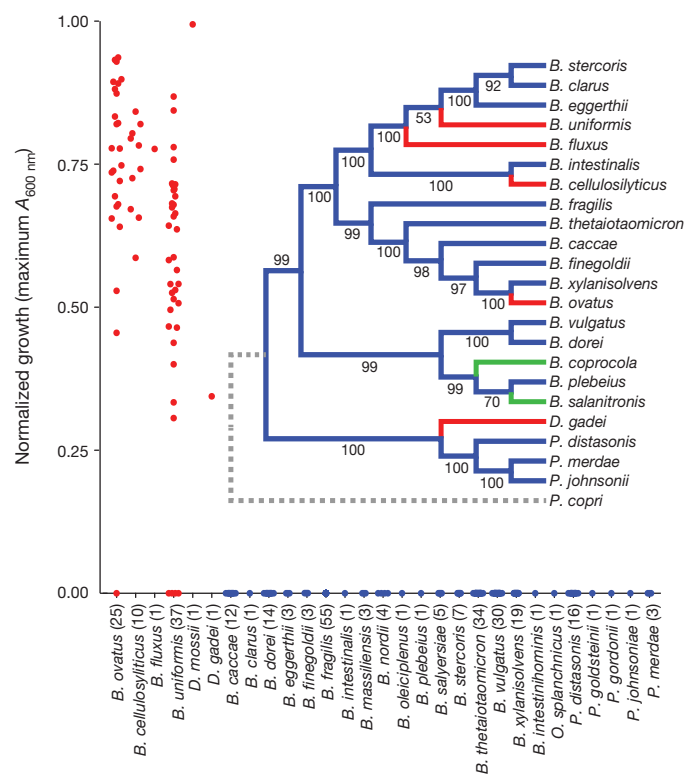


**Figure 5 | Growth of different human-gut-resident Bacteroidetes on XyG.** Each point represents the normalized maximum growth (absorbance at 600 nm,  $A_{600\text{ nm}}$ ) achieved by each strain after 4 days of growth in minimal medium with tamarind XyG as the sole carbon source (average of  $n = 2$  independent growth analyses per strain). The inset shows a phylogenetic tree constructed from fully sequenced strains of the species shown; those labelled in red have the ability to grow on XyG as the sole carbon source and those labelled in green have PULs similar to *B. ovatus* XyGUL but were not tested for growth on XyG. Bootstrap values based on 1,000 replicate trees are indicated.



Diamond Light Source synchrotron, station I03, and the structure was solved by molecular replacement using chain A of the *P. pabuli* GH5 (PDB accession 2JEP) as the search model.

**Online Content** Any additional Methods, Extended Data display items and Source Data are available in the online version of the paper; references unique to these sections appear only in the online paper.

**Received 20 February; accepted 22 November 2013.**

**Published online 19 January 2014.**

- McDougall, G. J., Morrison, I. M., Stewart, D. & Hillman, J. R. Plant cell walls as dietary fibre: range, structure, processing and function. *J. Sci. Food Agric.* **70**, 133–150 (1996).
- El Kaoutari, A., Armougom, F., Gordon, J. I., Raoult, D. & Henrissat, B. The abundance and variety of carbohydrate-active enzymes in the human gut microbiota. *Nature Rev. Microbiol.* **11**, 497–504 (2013).
- Flint, H. J., Scott, K. P., Duncan, S. H., Louis, P. & Forano, E. Microbial degradation of complex carbohydrates in the gut. *Gut Microbes* **3**, 289–306 (2012).
- Koropatkin, N. M., Cameron, E. A. & Martens, E. C. How glycan metabolism shapes the human gut microbiota. *Nature Rev. Microbiol.* **10**, 323–335 (2012).
- Hoffman, M. *et al.* Structural analysis of xyloglucans in the primary cell walls of plants in the subclass Asteridae. *Carbohydr. Res.* **340**, 1826–1840 (2005).
- Vogel, J. Unique aspects of the grass cell wall. *Curr. Opin. Plant Biol.* **11**, 301–307 (2008).
- Martens, E. C. *et al.* Recognition and degradation of plant cell wall polysaccharides by two human gut symbionts. *PLoS Biol.* **9**, e1001221 (2011).
- Hartemink, R., VanLaere, K. M. J., Mertens, A. K. C. & Rombouts, F. M. Fermentation of xyloglucan by intestinal bacteria. *Anaerobe* **2**, 223–230 (1996).
- Kootte, R. S. *et al.* The therapeutic potential of manipulating gut microbiota in obesity and type 2 diabetes mellitus. *Diabetes Obes. Metab.* **14**, 112–120 (2012).
- Ley, R. E., Peterson, D. A. & Gordon, J. I. Ecological and evolutionary forces shaping microbial diversity in the human intestine. *Cell* **124**, 837–848 (2006).
- van Nood, E. *et al.* Duodenal infusion of donor feces for recurrent *Clostridium difficile*. *N. Engl. J. Med.* **368**, 407–415 (2013).
- Petrof, E. *et al.* Stool substitute transplant therapy for the eradication of *Clostridium difficile* infection: ‘RePOOPulating’ the gut. *Microbiome* **1**, 3 (2013).
- Tasse, L. *et al.* Functional metagenomics to mine the human gut microbiome for dietary fiber catabolic enzymes. *Genome Res.* **20**, 1605–1612 (2010).
- Cummings, J. H. & Macfarlane, G. T. Role of intestinal bacteria in nutrient metabolism. *Clin. Nutr.* **16**, 3–11 (1997).
- McNeil, N. I. The contribution of the large-intestine to energy supplies in man. *Am. J. Clin. Nutr.* **39**, 338–342 (1984).
- Smith, M. I. *et al.* Gut microbiomes of Malawian twin pairs discordant for kwashiorkor. *Science* **339**, 548–554 (2013).
- Xu, J. *et al.* A genomic view of the human-*Bacteroides thetaiotaomicron* symbiosis. *Science* **299**, 2074–2076 (2003).
- Qin, J. *et al.* A human gut microbial gene catalogue established by metagenomic sequencing. *Nature* **464**, 59–65 (2010).
- Huttenhower, C. *et al.* Structure, function and diversity of the healthy human microbiome. *Nature* **486**, 207–214 (2012).
- Nelson, K. E. *et al.* A catalog of reference genomes from the human microbiome. *Science* **328**, 994–999 (2010).
- Yamatoya, K. & Shirakawa, M. Xyloglucan: structure, rheological properties, biological functions and enzymatic modification. *Curr. Trends Polym. Sci.* **8**, 27–72 (2003).
- Hsieh, Y. S. Y. & Harris, P. J. Xyloglucans of monocotyledons have diverse structures. *Mol. Plant* **2**, 943–965 (2009).
- Mello, L. V., Chen, X. & Rigden, D. J. Mining metagenomic data for novel domains: BACON, a new carbohydrate-binding module. *FEBS Lett.* **584**, 2421–2426 (2010).
- Cameron, E. A. *et al.* Multidomain carbohydrate-binding proteins involved in *Bacteroides thetaiotaomicron* starch metabolism. *J. Biol. Chem.* **287**, 34614–34625 (2012).
- Nakjang, S., Ndeh, D. A., Wipat, A., Bolam, D. N. & Hirt, R. P. A novel extracellular metalloproteinase domain shared by animal host-associated mutualistic and pathogenic microbes. *PLoS ONE* **7**, e30287 (2012).
- Aspeborg, H., Coutinho, P. M., Wang, Y., Brumer, H. & Henrissat, B. Evolution, substrate specificity and subfamily classification of glycoside hydrolase family 5 (GH5). *BMC Evol. Biol.* **12**, 186 (2012).
- Gloster, T. M. *et al.* Characterization and three-dimensional structures of two distinct bacterial xyloglucanases from families GH5 and GH12. *J. Biol. Chem.* **282**, 19177–19189 (2007).
- Hehemann, J. H., Kelly, A. G., Pudlo, N. A., Martens, E. C. & Boraston, A. B. Bacteria of the human gut microbiome catabolize red seaweed glycans with carbohydrate-active enzyme updates from extrinsic microbes. *Proc. Natl Acad. Sci. USA* **109**, 19786–19791 (2012).
- Hehemann, J. H. *et al.* Transfer of carbohydrate-active enzymes from marine bacteria to Japanese gut microbiota. *Nature* **464**, 908–912 (2010).
- Wegmann, U. *et al.* Complete genome of a new Firmicutes species belonging to the dominant human colonic microbiota (*Ruminococcus bicirculans*) reveals two chromosomes and a selective capacity to utilize plant glucans. *Environ. Microbiol.* <http://dx.doi.org/10.1111/1462-2920.12217> (2013).

**Supplementary Information** is available in the online version of the paper.

**Acknowledgements** We are grateful to the following colleagues for providing materials or experimental assistance: F. Vilaplana (neutral sugar analysis of XyG preparations), G. Sundqvist (protein mass spectrometry), F. Ibatullin (aryl glycoside syntheses), S. Prexler (protein production and purification), S. Tuomivaara and W. York (provision of acetylated tomato XyG samples), the staff at the University of Michigan Germfree Laboratory (technical assistance with gnotobiotic mouse experiments) and the staff at the Diamond Light Source (provision of data collection facilities). Work in Stockholm was supported by the Mizutani Foundation for Glycoscience, The Swedish Research Council Formas (via CarboMat—the KTH Advanced Carbohydrate Materials Centre), The Swedish Research Council (Vetenskapsrådet; salary support to H.B.), and the Wallenberg Wood Science Centre (salary support to O.S. and L.S.M.). Work in Vancouver was supported by faculty funding from the Michael Smith Laboratories, University of British Columbia; the Natural Sciences and Engineering Research Council of Canada (Discovery Grant); the Canada Foundation for Innovation and the British Columbia Knowledge Development Fund. Work in York was supported by the Biotechnology and Biological Sciences Research Council under reference BB/I014802/1. Work in Ann Arbor was supported by National Institutes of Health grants DK084214 and GM099513; T.E.R. was supported in part by the Global Probiotics Council Young Investigator Grant for Probiotics Research awarded to E.C.M.

**Author Contributions** J.L. performed gene cloning, recombinant production and biochemical/enzymatic characterization for all enzymes. T.E.R. constructed *B. ovatus* genetic mutants and tested mutant growth phenotypes. G.R.H. performed all protein X-ray crystallography. L.S.M. performed enzyme kinetic analyses and product analyses on select enzymes and substrates (BoGH3A and 3B, BoGH5A, BoGH9A, BoGH43A and 43B). A.S.T. performed all experiments and data analysis relating to the BACON domain and carbohydrate-binding proteins. O.S. and S.K. performed initial gene cloning and production of all enzymes, and enzymatic characterization of BoGH5A and BoGH2A. N.A.P. performed growth profiling of various *Bacteroides* strains, including *B. ovatus* deletion mutants ( $\Delta$ BoGH31A), on XyG oligo- and polysaccharides and analysed *in vivo* competition data by qPCR. K.U. analysed growth data from 292 *Bacteroides* isolates on XyG and other substrates, and assisted with metagenomic surveys. N.M.K. provided advice and assistance on XyGUL recombinant carbohydrate-binding protein production. A.L.C. and C.A.H. assisted with calorimetry and data analysis. A.G.K. assisted with comparative genomic locus identification and performed *Bacteroides* phylogenetic analysis. S.N.C. assisted with recombinant production of all enzymes and performed stability studies. E.C.M. constructed the *B. ovatus*  $\Delta$ tdk strain and the N-terminal lipidation mutant, performed corresponding cellular localization and growth studies, and performed comparative genomic analyses and metagenomic surveys. H.B., E.C.M. and G.J.D. conceived the study, directed research, analysed data, and wrote the article, including significant data analysis and writing input from J.L., T.E.R. and L.S.M.

**Author Information** Atomic coordinates and structure factors for the BoGH5A-XXXG complex structure have been deposited at the PDB under accession 3ZMR. Reprints and permissions information is available at [www.nature.com/reprints](http://www.nature.com/reprints). The authors declare no competing financial interests. Readers are welcome to comment on the online version of the paper. Correspondence and requests for materials should be addressed to H.B. ([brumer@msl.ubc.ca](mailto:brumer@msl.ubc.ca)), E.C.M. ([emartens@umich.edu](mailto:emartens@umich.edu)) or G.J.D. ([gideon.davies@york.ac.uk](mailto:gideon.davies@york.ac.uk)).

# Sessile alveolar macrophages communicate with alveolar epithelium to modulate immunity

Kristin Westphalen<sup>1</sup>, Galina A. Gusarova<sup>1</sup>, Mohammad N. Islam<sup>1</sup>, Manikandan Subramanian<sup>2</sup>, Taylor S. Cohen<sup>3</sup>, Alice S. Prince<sup>3</sup> & Jahar Bhattacharya<sup>1,4</sup>

**The tissue-resident macrophages of barrier organs constitute the first line of defence against pathogens at the systemic interface with the ambient environment. In the lung, resident alveolar macrophages (AMs) provide a sentinel function against inhaled pathogens<sup>1</sup>. Bacterial constituents ligate Toll-like receptors (TLRs) on AMs<sup>2</sup>, causing AMs to secrete proinflammatory cytokines<sup>3</sup> that activate alveolar epithelial receptors<sup>4</sup>, leading to recruitment of neutrophils that engulf pathogens<sup>5,6</sup>. Because the AM-induced response could itself cause tissue injury, it is unclear how AMs modulate the response to prevent injury. Here, using real-time alveolar imaging *in situ*, we show that a subset of AMs attached to the alveolar wall form connexin 43 (Cx43)-containing gap junction channels with the epithelium. During lipopolysaccharide-induced inflammation, the AMs remained sessile and attached to the alveoli, and they established intercommunication through synchronized  $\text{Ca}^{2+}$  waves, using the epithelium as the conducting pathway. The intercommunication was immunosuppressive, involving  $\text{Ca}^{2+}$ -dependent activation of Akt, because AM-specific knockout of Cx43 enhanced alveolar neutrophil recruitment and secretion of proinflammatory cytokines in the bronchoalveolar lavage. A picture emerges of a novel immunomodulatory process in which a subset of alveolus-attached AMs intercommunicates immunosuppressive signals to reduce endotoxin-induced lung inflammation.**

As most of our understanding of AMs is based on studies in which AMs were isolated by bronchoalveolar lavage (BAL) and studied *in vitro*, or in which they were depleted from the lungs<sup>5,7</sup>, we lack an understanding of the dynamic interactions between AMs and the alveolar epithelium that might critically modulate the lung's inflammatory response. To determine these interactions *in situ*, we took advantage of the fact that AMs express CD11c<sup>8</sup> and crossed *Cd11c-cre* mice<sup>9</sup> with *Rosa26-LSL-eYFP* mice<sup>10</sup> to obtain mice expressing enhanced yellow fluorescence protein (eYFP) in CD11c-expressing cells.

Live confocal microscopy of isolated, blood-perfused mouse lungs<sup>11</sup> derived from CD11c/eYFP mice revealed YFP<sup>+</sup> cells in the subpleural interstitium and the alveolar lumen (Fig. 1a). To distinguish AMs from lung dendritic cells that also express CD11c<sup>8,12</sup>, we gave mice intra-alveolar microinjections of the AM marker Siglec F (ref. 13) and an antibody for the major histocompatibility complex class II (MHC-II), which marks lung dendritic cells<sup>12</sup>. These microinjections revealed that luminal YFP<sup>+</sup> cells were AMs, because they stained strongly for Siglec F but weakly for MHC-II (Fig. 1b), whereas interstitial YFP<sup>+</sup> cells that we stained by topical antibody applications to the saponin-permeabilized pleura were MHC-II<sup>+</sup>/Siglec F<sup>-</sup> dendritic cells (Fig. 1b). The alveolar epithelium inhibits transepithelial transit of reagents injected in the alveolar lumen<sup>4</sup>. Hence, alveolar microinjections of dye resulted in fluorescence uptake in AMs, but not in dendritic cells (Fig. 1c), suggesting that dendritic cells did not communicate with the alveolar lumen. In further affirmation that luminal YFP<sup>+</sup> cells were AMs, YFP<sup>+</sup>-MHC-II<sup>low</sup> cells recovered in the BAL failed to induce T-cell proliferation in antigen-presentation assays (Extended Data Fig. 1a). Together, these

findings indicate that YFP<sup>+</sup> AMs localized to the alveolar lumen, whereas YFP<sup>+</sup> dendritic cells were compartmentalized in the perialveolar interstitium.

We detected a single AM for approximately every three alveoli (Extended Data Fig. 1b), suggesting that AMs carry out pathogen surveillance by patrolling the alveolar surface<sup>14</sup>. However, AMs remained stationary at fixed alveolar locations for the duration of our imaging studies, which lasted up to 4 h (Extended Data Fig. 1c). Our attempts to dislodge AMs by BAL or by direct alveolar microinjection of buffer were unsuccessful (Extended Data Fig. 1c). To determine whether AMs might be induced to migrate towards bacteria, we microinjected *Staphylococcus aureus* in the alveolar lumen. Although AMs rapidly ingested the *S. aureus* that lay within one AM diameter, they did not migrate towards the bacteria (Fig. 1d and Extended Data Fig. 1c). The alveolar liquid flow<sup>15</sup> appeared to wash bacteria towards the AMs (data not shown). Thus, contrary to expectations, our findings indicate that AMs were sessile.

Macrophages express Cx43 (ref. 16), potentially enabling AMs to form gap junction channels (GJCs) with the alveolar epithelium. To determine the presence of GJCs, we applied photolytic uncaging to induce cell-specific increases in cytosolic  $\text{Ca}^{2+}$  (ref. 17), and fluorescence recovery after photobleaching (FRAP) to quantify intercellular dye diffusion<sup>11</sup>. In 40% of AMs, uncaging-induced  $\text{Ca}^{2+}$  waves travelled from the epithelium to AMs (Fig. 1e) and in the opposite direction (data not shown). Cx43 expression in AMs correlated directly with FRAP (Fig. 1f). A 1 h treatment with GAP26 and 27, inhibitors of Cx43-based GJCs and hemichannels, blocked uncaging-induced  $\text{Ca}^{2+}$  waves (Fig. 1e) as well as FRAP (data not shown) between AMs and the epithelium. In CD11c<sup>high</sup> MHC-II<sup>low</sup> AMs, which we obtained by BAL and by extraction from lung tissue after BAL, respectively (Extended Data Fig. 1a, d), Cx43 protein and messenger RNA expression were higher in tissue than in BAL AMs (Fig. 1g), suggesting that Cx43 was higher in alveolus-adherent than alveolus-non-adherent AMs. In mice with CD11c-specific Cx43 knockout (CD11c Cx43<sup>-/-</sup>) (Extended Data Fig. 2a), AMs remained immobile even after alveolar microinjections of bacteria or PBS buffer (Extended Data Fig. 2b, c). Hence, Cx43 was not responsible for AM immobility. In lungs given intranasal *Escherichia coli*-derived lipopolysaccharide (LPS) instillation, neutrophils entered and migrated freely on the alveolar surface (Supplementary Fig. 1 and Supplementary Video 1), ruling out non-specific physical factors in causing AM immobility. Taken together, our findings reveal the presence of Cx43<sup>high</sup> and Cx43<sup>low</sup> AM populations in the lung, in which Cx43<sup>high</sup> AMs formed GJCs with the alveolar epithelium.

Next, we gave mice intranasal LPS to induce lung injury or PBS as a control. We removed lungs 1, 4 or 24 h after the instillations to establish isolated perfused lungs for imaging studies<sup>11</sup>. Instillation of fluorescent LPS confirmed LPS entry in AMs (Fig. 2a). Fluorescent LPS did not enter interstitial dendritic cells, indicating that in alveoli LPS ligated AMs, not dendritic cells. Fluorescent LPS uptake was markedly greater in BAL-derived dendritic cells than in those recovered from the tissue

<sup>1</sup>Lung Biology Laboratory, Department of Medicine, Division of Pulmonary, Allergy and Critical Care, Columbia University Medical Center, New York, New York 10032, USA. <sup>2</sup>Department of Medicine, Division of Molecular Medicine, Columbia University Medical Center, New York, New York 10032, USA. <sup>3</sup>Department of Pediatrics, Columbia University Medical Center, New York, New York 10032, USA. <sup>4</sup>Department of Physiology & Cellular Biophysics, College of Physicians and Surgeons, Columbia University Medical Center, New York, New York 10032, USA.

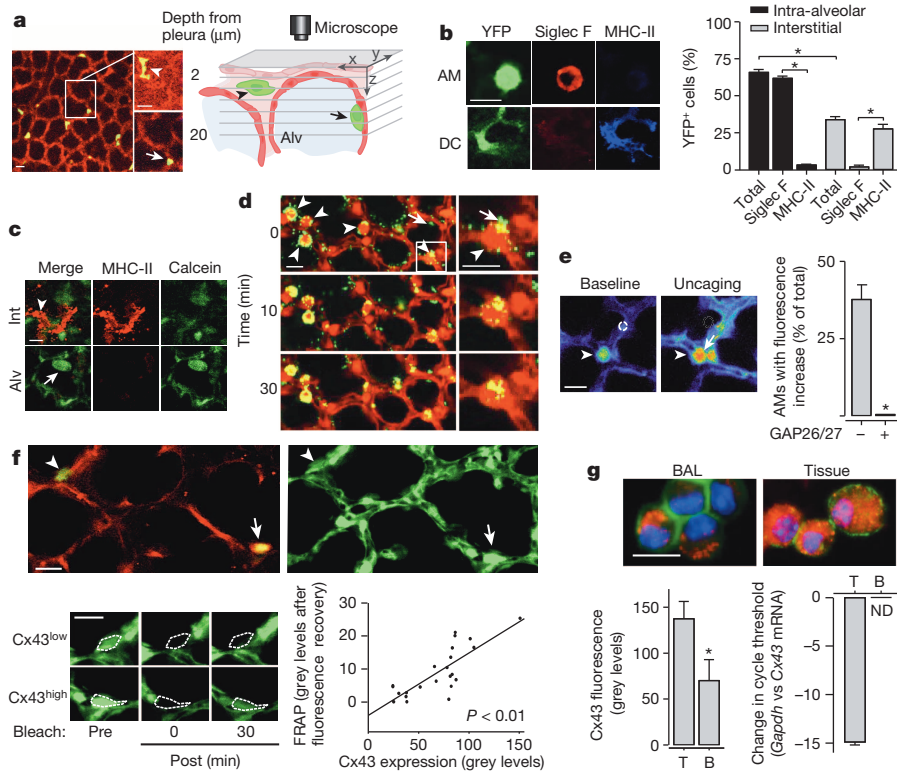


**Figure 1 | Live confocal microscopy of AMs *in situ*.** **a**, Interstitial (arrowhead) and luminal (arrow) YFP<sup>+</sup> cells (yellow/green) in autofluorescent alveoli (red) ( $n = 15$ ). Sketch of imaged field. **b**, Immunofluorescence and quantification of alveolar (top) and interstitial (bottom) YFP<sup>+</sup> cells ( $n = 4$  or  $5$ ). DC, dendritic cell. **c**, Dye (green) injection in alveolus (Alv). Interstitial (Int) MHC-II<sup>+</sup> dendritic cell (red, arrowhead) and luminal AM (arrow) ( $n = 3$ ). **d**, Merge of *S. aureus* (green, arrow in inset) with AMs (red; arrowhead in inset) ( $n = 4$ ). **e**,  $\text{Ca}^{2+}$  uncaging in epithelium (dotted circle) spreads  $\text{Ca}^{2+}$  (arrow) to AM (arrowhead) ( $n = 4$  or  $5$ ). Bars show GAP26/27 effect. **f**, Alveoli with Cx43 (red) and calcein (green) show Cx43<sup>low</sup> (arrowhead) and Cx43<sup>high</sup> AMs (arrow) expressing YFP (yellow/green). High-power images show calcein in AMs before (Pre) and after (Post) photobleaching. Line drawn by linear regression.  $n = 23$  AMs, four lungs. **g**, Cx43 (red), CD11c (green) and nuclei (blue) in AMs from BAL (B) or lung tissue (T) ( $n = 4$ ). Bars show protein (left) and mRNA (right) expressions in AMs. ND, not detected. Scale bars, 15  $\mu\text{m}$ . Data show mean  $\pm$  standard error of the mean (s.e.m.). \* $P < 0.05$ .

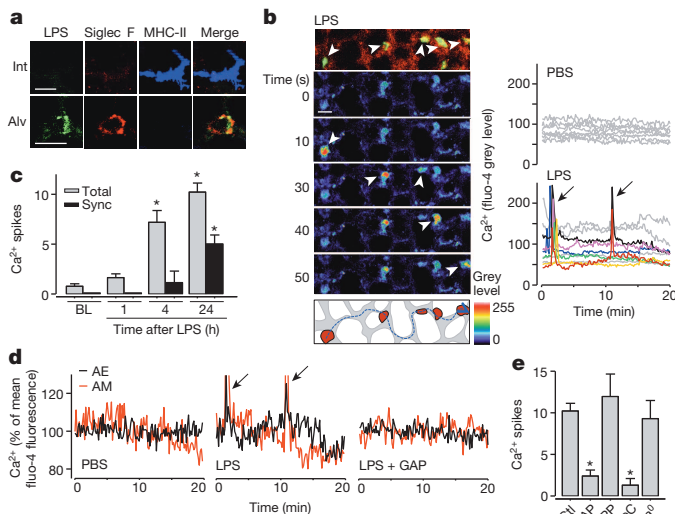
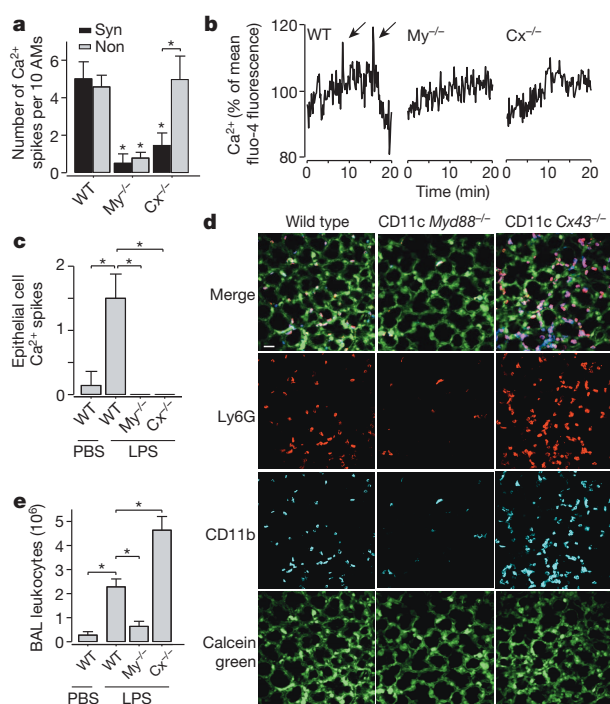


**Figure 2 | Communicating  $\text{Ca}^{2+}$  spikes in AMs.** **a**, Fluorescent LPS (green), AM (red) and dendritic cell (blue) in interstitium (Int) and alveolar lumen (Alv) ( $n = 3$ ). **b**, YFP-expressing AMs (yellow; top), pseudocoloured sequential images show increased fluo-4 fluorescence (arrowheads) 24 h after LPS ( $n = 4$ ). Dashed sketch spike path between AMs. Tracings show synchronous AM responses (arrows). **c**,  $\text{Ca}^{2+}$  spikes normalized for ten AMs per imaging field. Sync, synchronous spikes; Total, all spikes; BL, baseline ( $n = 8$ ); 1 h,  $n = 6$ ; 4 h,  $n = 4$ ; 24 h,  $n = 12$ . **d**,  $\text{Ca}^{2+}$  oscillations and spikes (arrows) in AMs and adjoining alveolar epithelium (AE) 24 h after LPS or PBS ( $n = 4$ ). GAP, GAP26/27. **e**,  $\text{Ca}^{2+}$  spikes are 24 h after LPS, normalized for ten AMs per imaging field. Ctl, LPS alone ( $n = 12$ ); PP, PPADS ( $n = 4$ ); XeC, xestospingon C ( $n = 4$ );  $\text{Ca}^{2+}$  depletion ( $n = 3$ ). GAP,  $n = 5$ . Scale bars, 20  $\mu\text{m}$ . Bars, mean  $\pm$  s.e.m. \* $P < 0.05$  versus LPS alone or corresponding baseline.

of post-lavage lungs, suggesting that access to the airway lumen may be greater for BAL- than tissue-derived dendritic cells (Extended Data Fig. 3).

By contrast with PBS-treated lungs, in which there were no notable effects, the AMs of LPS-treated lungs showed synchronous  $\text{Ca}^{2+}$  spikes, all of which occurred within 1 min of one another in AM clusters. Spikes lasted 10–15 s, appearing every 10–20 min (Fig. 2b and Supplementary Video 2). They began 4 h after LPS and increased over 24 h (Fig. 2c). Concomitant  $\text{Ca}^{2+}$  spikes occurred in the adjoining epithelium (Fig. 2d). The spikes travelled between different AMs, often separated by several alveoli, across the intervening epithelium (Fig. 2b and Extended Data Fig. 4a). We did not identify a specific, ‘pacemaker’ AM that initiated synchronous spiking. Intra-alveolar microinjection of GAP26/27 blocked synchronous epithelial and AM spikes (Fig. 2d, e), suggesting that there was interdependence between these responses. GAP26/27 did not block non-synchronous spikes (data not shown). Connexin hemichannels are implicated in some forms of ATP-dependent purinergic signalling<sup>18</sup>. However, after LPS treatment, cytosolic dyes (fluo-4, calcein) that can transit connexin channels did not leak from AMs or the epithelium (Extended Data Fig. 4b, c). The ATP receptor inhibitor pyridoxal phosphate-6-azo(benzene-2,4-disulphonic acid) tetrasodium salt hydrate (PPADS) did not modify spike formation (Fig. 2e). These findings rule out a role for connexin hemichannels in inducing spike intercommunication. Alveolar microinfusion of the inositol-(1,4,5)-trisphosphate (Ins(1,4,5) $\text{P}_3$ ) receptor inhibitor xestospingon C, but not depletion of extracellular  $\text{Ca}^{2+}$ , blocked the  $\text{Ca}^{2+}$  spikes (Fig. 2e), indicating that the spikes resulted from  $\text{Ca}^{2+}$  release from intracellular stores. Depletion of alveolar neutrophils, which we identified as CD11b<sup>+</sup> cells of 6–8- $\mu\text{m}$  diameter, did not diminish spike formation (Extended Data Fig. 4d). The numbers of AMs per imaging field were identical at all time points (Extended Data Fig. 4e). Together, these findings indicate that LPS induced intercommunicated  $\text{Ca}^{2+}$  spikes between AMs lying in different alveoli and that the communication occurred through the epithelium. LPS ligation of TLR4 induces signalling through the adaptor proteins myeloid differentiation factor 88 (MyD88) and TIR-domain-containing





adaptor-inducing interferon- $\beta$  (TRIF; also known as Ticam-1)<sup>19</sup>. MyD88 and TRIF are implicated in lung injury<sup>20,21</sup>. We generated mice (CD11c *Myd88*<sup>-/-</sup>) lacking MyD88 in CD11c-expressing cells<sup>22</sup>. In CD11c *Myd88*<sup>-/-</sup>, but not wild-type mice, LPS-induced  $\text{Ca}^{2+}$  spikes in AMs (Fig. 3a) and the epithelium (Fig. 3b, c) were lacking, and alveolar neutrophil entry at 24 h was diminished (Fig. 3d, e), although both mice had similar Cx43 expression in AMs (Extended Data Fig. 4f).

**Figure 3 | AM MyD88 in inflammatory signalling.** a–c, Synchronized (Syn) and non-synchronized (Non)  $\text{Ca}^{2+}$  spikes (arrows) and oscillations in wild-type (WT,  $n = 12$ ), CD11c *Myd88*<sup>-/-</sup> (*Myd88*<sup>-/-</sup>,  $n = 5$ ) and CD11c *Cx43*<sup>-/-</sup> (*Cx43*<sup>-/-</sup>,  $n = 5$ ) mice. d, Alveoli (green), and Ly6G<sup>+</sup> (red) and CD11b<sup>+</sup> neutrophils (blue) 24 h after LPS ( $n = 4$ ). Scale bar, 30  $\mu\text{m}$ . e, Responses are 24 h after treatments. LPS wild type,  $n = 9$ ; others,  $n = 4$ . Bars, mean  $\pm$  s.e.m. \* $P < 0.05$ .

We conclude that MyD88-dependent signalling was responsible for the LPS-induced spike formation and lung inflammation, and that AMs initiated the signalling.

Synchronous spikes in AMs and the epithelium were inhibited in CD11c *Cx43*<sup>-/-</sup> mice (Fig. 3a–c), although non-synchronous  $\text{Ca}^{2+}$  spikes in AMs were similar to those of wild-type mice (Fig. 3a). Lung inflammation was markedly greater in CD11c *Cx43*<sup>-/-</sup> than wild-type mice, as indicated by increased LPS- or *E. coli*-induced alveolar neutrophil recruitment and BAL leukocyte counts (Fig. 3d, e and Extended Data Fig. 5). As compared with *Cx43*<sup>flx/flx</sup> mice (littermate controls), BAL from CD11c *Cx43*<sup>-/-</sup> mice contained more proinflammatory cytokines (Fig. 4a). Cx43 knockdown in bone-marrow-derived macrophages did not alter cytokine secretion (Extended Data Fig. 6), ruling out Cx43 depletion as a determinant of the response. LPS-induced mortality was higher in CD11c *Cx43*<sup>-/-</sup> mice than in littermate controls (Fig. 4b). In CD11c *Cx43*<sup>-/-</sup> mice, LPS caused greater degradation of I- $\kappa$ B $\alpha$  (Fig. 4c) and increased nuclear translocation of NF- $\kappa$ B (Extended Data Fig. 7a). AM numbers did not differ between wild-type and CD11c *Cx43*<sup>-/-</sup> mice (Extended Data Fig. 7b). Together, these findings indicate that Cx43 knockout in AMs augmented LPS-induced inflammation and lung injury, indicating that AM-epithelium GJCs were protective.

An increase in intracellular  $\text{Ca}^{2+}$  activates the  $\text{Ca}^{2+}$ /calmodulin-dependent kinase kinase (CAMKK) and its downstream target, the pro-survival kinase Akt<sup>23,24</sup>. As these CAMKK-induced mechanisms are undetermined for lung inflammation, we immunoprecipitated CAMKK $\alpha$  or Akt from wild-type lungs. In each case, LPS enhanced

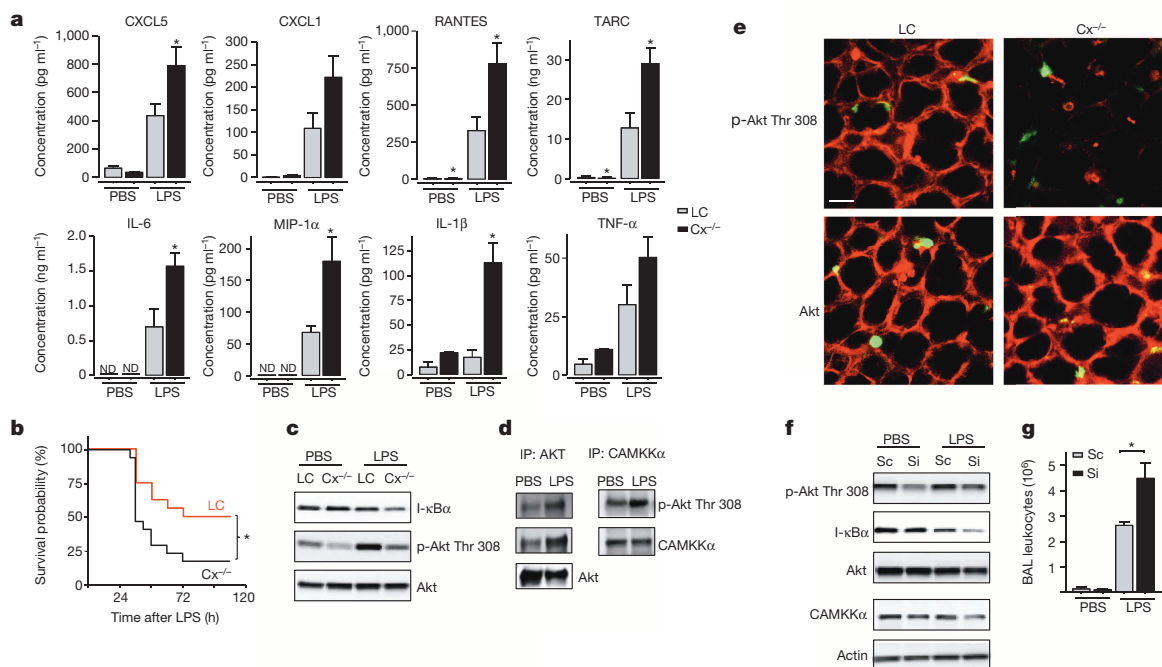


**Figure 4 | AM-epithelial signalling.** a, BAL cytokine enzyme-linked immunosorbent assay (ELISA) in CD11c *Cx43*<sup>-/-</sup> (*Cx43*<sup>-/-</sup>) and littermate control (LC) mice ( $n = 3$  or 4). ND, not detectable. b, Kaplan–Meier plots.  $n = 16$  littermate control mice, 17 CD11c *Cx43*<sup>-/-</sup> mice. c, d, Data are from 24 h after treatment ( $n = 4$ ). IP, immunoprecipitation; p, phospho. e, *In situ* immunofluorescence (red) of the alveolar epithelium and YFP<sup>+</sup> AMs

(yellow/green) 24 h after LPS ( $n = 4$ ). Scale bar, 20  $\mu\text{m}$ . f, g, Lung lysate western blots and BAL leukocyte counts 24 h after LPS in lungs given scrambled (Sc) or CAMKK $\alpha$ -specific (Si) siRNA.  $n = 4$  for PBS plus siRNA;  $n = 5$  for LPS plus siRNA;  $n = 6$  for other conditions. All blots are from the same sample set ( $n = 3$ ). CAMKK $\alpha$  and actin were processed on different gels. Bars, mean  $\pm$  s.e.m. \* $P < 0.05$  versus littermate control or scrambled RNA.

pull-down of the corresponding binding partner (Fig. 4d), and it enhanced Akt phosphorylation in wild-type, but not in CD11c *Cx43*<sup>-/-</sup> mice (Fig. 4c). Imaging indicated that the alveolar epithelium was the site of the LPS-induced enhancement of phospho-Akt expression (Fig. 4e). This effect was inhibited in CD11c *Cx43*<sup>-/-</sup> mice (Fig. 4e) and by treatment with the intracellular Ca<sup>2+</sup> chelator BAPTA-AM (Extended Data Fig. 8a). Short interfering RNA (siRNA)-induced knockdown of CAMKK $\alpha$  decreased Akt phosphorylation, whereas it increased I- $\kappa$ B $\alpha$  degradation and BAL leukocyte counts (Fig. 4f, g). We generated SPC *Cx43*<sup>-/-</sup> mice lacking *Cx43* in the alveolar epithelium<sup>25</sup>. In SPC *Cx43*<sup>-/-</sup> mice, LPS-induced responses were similar to those of CD11c *Cx43*<sup>-/-</sup> mice, in that Akt phosphorylation decreased and BAL leukocyte counts increased (Extended Data Fig. 8b). Thus, loss of *Cx43* on either face of AM-epithelial GJCs induced similar effects. These findings indicate that *Cx43*-based AM GJCs suppressed inflammation through CAMKK $\alpha$ -induced phosphorylation of epithelial Akt.

Our studies highlight the importance of intercellular connectivity in lung immunity. AMs critically elicit lung inflammation. However, concomitantly, sets of alveolus-attached AMs intercommunicate immunosuppressive signals. *Cx43* deletion in AMs increased the secretion of cytokines that were likely to be predominantly of AM (MIP-1 $\alpha$ ) and of epithelial (CXCL1 and 5) origin, suggesting the possibility that AMs and the epithelium might mutually suppress cytokine release. Previous lung studies implicated syncytial connectivity in the endothelium and epithelium in surfactant secretion<sup>17</sup>, leukocyte recruitment<sup>26</sup> and hypoxic vasoconstriction<sup>27</sup>. Here we show that *Cx43*<sup>high</sup> AMs co-opt syncytial communication to subvert lung inflammation. This communication might play a part in other forms of lung inflammation, such as those involving tolerogenic responses to antigen. Although future studies are needed to elucidate further the roles of Ca<sup>2+</sup>-regulatory mechanisms in this process, especially regarding second messengers such as Ins(1,4,5)P<sub>3</sub> that can diffuse through GJCs<sup>28</sup>, we propose that *Cx43* expression in AMs might provide a drug-delivery focus for new therapeutics for inflammatory lung disease.

## METHODS SUMMARY

All animal experiments were approved by the Institutional Animal Care and Use Committee of Columbia University Medical Center. We imaged isolated, blood-perfused lungs by laser scanning microscopy (LSM 510 META; Zeiss)<sup>11</sup>. Alveoli were imaged to a depth of 40  $\mu$ m from the pleura. We loaded alveolar cells with dyes and reagents by alveolar micropuncture<sup>11</sup>. LPS concentrations were 1 mg kg body weight<sup>-1</sup> for all experiments, and 25 mg kg<sup>-1</sup> for survival studies. We infused calcein-stained *S. aureus* (1  $\times$  10<sup>8</sup> bacteria ml<sup>-1</sup>) by alveolar micropuncture. For Ca<sup>2+</sup> imaging (one image every 5 or 10 s), we microinfused alveoli with fluo-4. For photolytic Ca<sup>2+</sup> uncaging<sup>17</sup>, we targeted single cells co-loaded with fluo-4 and the ultraviolet-radiation-sensitive Ca<sup>2+</sup> cage, *o*-Nitrophenyl EGTA, with high-intensity ultraviolet illumination (~320 nm, 10 pulses s<sup>-1</sup>) in 2- $\mu$ m-diameter spots. *In situ* *Cx43*, NF- $\kappa$ B and Akt staining was carried out after fixation and permeabilization of the alveolus. We quantified *Cx43* mRNA by qPCR in AMs sorted from BAL and lung tissue samples (Influx Cell Sorter; BD Biosciences). BAL and cell culture supernatant cytokines were analysed by ELISA. Western blot analyses and co-immunoprecipitations were performed as previously described<sup>29</sup>. siRNA was complexed with freshly extruded liposomes and intranasally instilled.

**Online Content** Any additional Methods, Extended Data display items and Source Data are available in the online version of the paper; references unique to these sections appear only in the online paper.

Received 8 April; accepted 20 November 2013.

Published online 19 January 2014.

1. Laskin, D. L., Sunil, V. R., Gardner, C. R. & Laskin, J. D. Macrophages and tissue injury: agents of defense or destruction? *Annu. Rev. Pharmacol. Toxicol.* **51**, 267–288 (2011).
2. Medzhitov, R. Toll-like receptors and innate immunity. *Nature Rev. Immunol.* **1**, 135–145 (2001).
3. Thorley, A. J. et al. Differential regulation of cytokine release and leukocyte migration by lipopolysaccharide-stimulated primary human lung alveolar type II epithelial cells and macrophages. *J. Immunol.* **178**, 463–473 (2007).

4. Kuebler, W. M., Parthasarathi, K., Wang, P. M. & Bhattacharya, J. A novel signaling mechanism between gas and blood compartments of the lung. *J. Clin. Invest.* **105**, 905–913 (2000).
5. Maus, U. A. et al. Role of resident alveolar macrophages in leukocyte traffic into the alveolar air space of intact mice. *Am. J. Physiol. Lung Cell. Mol. Physiol.* **282**, L1245–L1252 (2002).
6. Zhang, P., Summer, W. R., Bagby, G. J. & Nelson, S. Innate immunity and pulmonary host defense. *Immunol. Rev.* **173**, 39–51 (2000).
7. Cohen, T. S. & Prince, A. S. Activation of inflammasome signaling mediates pathology of acute *P. aeruginosa* pneumonia. *J. Clin. Invest.* **123**, 1630–1637 (2013).
8. Guth, A. M. et al. Lung environment determines unique phenotype of alveolar macrophages. *Am. J. Physiol. Lung Cell. Mol. Physiol.* **296**, L936–L946 (2009).
9. Caton, M. L., Smith-Raska, M. R. & Reizis, B. Notch-RBP-J signaling controls the homeostasis of CD8<sup>+</sup> dendritic cells in the spleen. *J. Exp. Med.* **204**, 1653–1664 (2007).
10. Srinivas, S. et al. Cre reporter strains produced by targeted insertion of EYFP and ECFP into the ROSA26 locus. *BMC Dev. Biol.* **1**, 4 (2001).
11. Islam, M. N. et al. Mitochondrial transfer from bone-marrow-derived stromal cells to pulmonary alveoli protects against acute lung injury. *Nature Med.* **18**, 759–765 (2012).
12. Miller, J. C. et al. Deciphering the transcriptional network of the dendritic cell lineage. *Nature Immunol.* **13**, 888–899 (2012).
13. Thornton, E. E. et al. Spatiotemporally separated antigen uptake by alveolar dendritic cells and airway presentation to T cells in the lung. *J. Exp. Med.* **209**, 1183–1199 (2012).
14. Kirby, A. C., Coles, M. C. & Kaye, P. M. Alveolar macrophages transport pathogens to lung draining lymph nodes. *J. Immunol.* **183**, 1983–1989 (2009).
15. Lindert, J., Perlman, C. E., Parthasarathi, K. & Bhattacharya, J. Chloride-dependent secretion of alveolar wall liquid determined by optical-sectioning microscopy. *Am. J. Respir. Cell Mol. Biol.* **36**, 688–696 (2007).
16. Pfenniger, A., Chanson, M. & Kwak, B. R. Connexins in atherosclerosis. *Biochim. Biophys. Acta* **1828**, 157–166 (2013).
17. Ichimura, H., Parthasarathi, K., Lindert, J. & Bhattacharya, J. Lung surfactant secretion by interalveolar Ca<sup>2+</sup> signaling. *Am. J. Physiol. Lung Cell. Mol. Physiol.* **291**, L596–L601 (2006).
18. Wong, C. W. et al. Connexin37 protects against atherosclerosis by regulating monocyte adhesion. *Nature Med.* **12**, 950–954 (2006).
19. Akira, S. & Takeda, K. Toll-like receptor signalling. *Nature Rev. Immunol.* **4**, 499–511 (2004).
20. Li, H. et al. Toll-like receptor 4-myeloid differentiation factor 88 signaling contributes to ventilator-induced lung injury in mice. *Anesthesiology* **113**, 619–629 (2010).
21. Imai, Y. et al. Identification of oxidative stress and Toll-like receptor 4 signaling as a key pathway of acute lung injury. *Cell* **133**, 235–249 (2008).
22. Subramanian, M., Thorp, E., Hansson, G. K. & Tabas, I. T<sub>reg</sub>-mediated suppression of atherosclerosis requires MYD88 signaling in DCs. *J. Clin. Invest.* **123**, 179–188 (2013).
23. Yano, S., Tokumitsu, H. & Soderling, T. R. Calcium promotes cell survival through CaM-K kinase activation of the protein-kinase-B pathway. *Nature* **396**, 584–587 (1998).
24. Chen, B. C., Wu, W. T., Ho, F. M. & Lin, W. W. Inhibition of interleukin-1 $\beta$ -induced NF- $\kappa$ B activation by calcium/calmodulin-dependent protein kinase kinase occurs through Akt activation associated with interleukin-1 receptor-associated kinase phosphorylation and uncoupling of MyD88. *J. Biol. Chem.* **277**, 24169–24179 (2002).
25. Perl, A. K., Wert, S. E., Nagy, A., Lobe, C. G. & Whitsett, J. A. Early restriction of peripheral and proximal cell lineages during formation of the lung. *Proc. Natl Acad. Sci. USA* **99**, 10482–10487 (2002).
26. Parthasarathi, K. et al. Connexin 43 mediates spread of Ca<sup>2+</sup>-dependent proinflammatory responses in lung capillaries. *J. Clin. Invest.* **116**, 2193–2200 (2006).
27. Wang, L. et al. Hypoxic pulmonary vasoconstriction requires connexin 40-mediated endothelial signal conduction. *J. Clin. Invest.* **122**, 4218–4230 (2012).
28. Decrock, E. et al. IP<sub>3</sub>, a small molecule with a powerful message. *Biochim. Biophys. Acta* **1833**, 1772–1786 (2013).
29. Huang, B. X. & Kim, H. Y. Effective identification of Akt interacting proteins by two-step chemical crosslinking, co-immunoprecipitation and mass spectrometry. *PLoS ONE* **8**, e61430 (2013).

**Supplementary Information** is available in the online version of the paper.

**Acknowledgements** We thank B. Reizis for providing the *Cd11c-cre* mice and J. Whitsett for providing the *Spc-cre* mice. We thank I. Tabas for discussions. This study was supported by US National Institutes of Health grants HL78645, HL57556 and HL64896 to J.B., HL73989 to A.S.P., and Parker B. Francis Fellowships to T.S.C. and M.N.I.

**Author Contributions** K.W. designed and carried out the experiments, prepared the figures and wrote the initial manuscript. G.A.G. contributed to western blot, immunoprecipitation and FRAP experiments. M.N.I. carried out the NF- $\kappa$ B *in situ* stainings, and contributed to BAL cell counting and survival studies. M.S. performed the antigen-presentation assay and provided the *CD11c Myd88*<sup>-/-</sup> mice. T.S.C. provided *S. aureus* and contributed to ELISA studies. A.S.P. contributed to the experimental design. J.B. was responsible for the overall project, designed the experiments and wrote the initial manuscript. All authors edited the manuscript.

**Author Information** Reprints and permissions information is available at [www.nature.com/reprints](http://www.nature.com/reprints). The authors declare no competing financial interests. Readers are welcome to comment on the online version of the paper. Correspondence and requests for materials should be addressed to J.B. (jb39@columbia.edu).

# A new metabolic cell-wall labelling method reveals peptidoglycan in *Chlamydia trachomatis*

G. W. Liechti<sup>1\*</sup>, E. Kuru<sup>2\*</sup>, E. Hall<sup>3</sup>, A. Kalinda<sup>3</sup>, Y. V. Brun<sup>4</sup>, M. VanNieuwenhze<sup>3</sup> & A. T. Maurelli<sup>1</sup>

**Peptidoglycan (PG), an essential structure in the cell walls of the vast majority of bacteria, is critical for division and maintaining cell shape and hydrostatic pressure<sup>1</sup>. Bacteria comprising the Chlamydiales were thought to be one of the few exceptions. *Chlamydia* harbour genes for PG biosynthesis<sup>2–7</sup> and exhibit susceptibility to ‘anti-PG’ antibiotics<sup>8,9</sup>, yet attempts to detect PG in any chlamydial species have proven unsuccessful (the ‘chlamydial anomaly’<sup>10</sup>). We used a novel approach to metabolically label chlamydial PG using D-amino acid dipeptide probes and click chemistry. Replicating *Chlamydia trachomatis* were labelled with these probes throughout their biphasic developmental life cycle, and the results of differential probe incorporation experiments conducted in the presence of ampicillin are consistent with the presence of chlamydial PG-modifying enzymes. These findings culminate 50 years of speculation and debate concerning the chlamydial anomaly and are the strongest evidence so far that chlamydial species possess functional PG.**

*Chlamydia trachomatis* is the leading cause of infectious blindness and sexually transmitted bacterial infection worldwide. It is a member of the Chlamydiae, a phylum consisting of obligate, intracellular, bacteria that cause a wide variety of infectious diseases in humans and animals. Their obligate intracellular nature and dimorphic life cycle has made studying *Chlamydia* a challenge and questions remain about even the basic processes of cell division and cell envelope maintenance in these pathogens. The infectious form of the organism, the elementary body (EB), is small (~0.3 µm) and essentially metabolically inert<sup>11</sup>. After attachment to and infection of a host cell, the EB undergoes a transition to the metabolically active reticulate body (RB), which replicates via binary fission but is incapable of attaching to or infecting new host cells. Thus, RBs must differentiate back to the EB form to complete the developmental cycle. Infected cells then lyse, releasing infectious EBs that infect new host cells.

Peptidoglycan (PG) is a sugar amino acid polymer that forms a mesh-like sheet surrounding the cytoplasmic membrane of bacterial cells. In the vast majority of free-living bacteria, PG aids in cell division<sup>1</sup>, maintenance of osmotic pressure, and provides a stable anchor for transmembrane complexes and integral membrane proteins<sup>12</sup>. Bacteria maintain their cell shape largely due to the presence of this rigid yet modifiable cell wall. A single PG subunit consists of a disaccharide backbone coupled to a pentapeptide chain (Fig. 1a). During cell-wall synthesis, disaccharide pentapeptide monomers are linked together at their corresponding sugars, creating a sugar polymer with polypeptide stems, which are crosslinked by transpeptidation. The pentapeptide chain is assembled sequentially by a series of ligases that specifically incorporate both L- and D-amino acids (D-glutamic acid and D-alanine) (Fig. 1a). These two D-amino acids are unique to bacteria and they are not used by mammalian cells. Thus, the enzymes involved in their synthesis and incorporation into PG are excellent targets for antibiotics such as β-lactams and D-cycloserine.

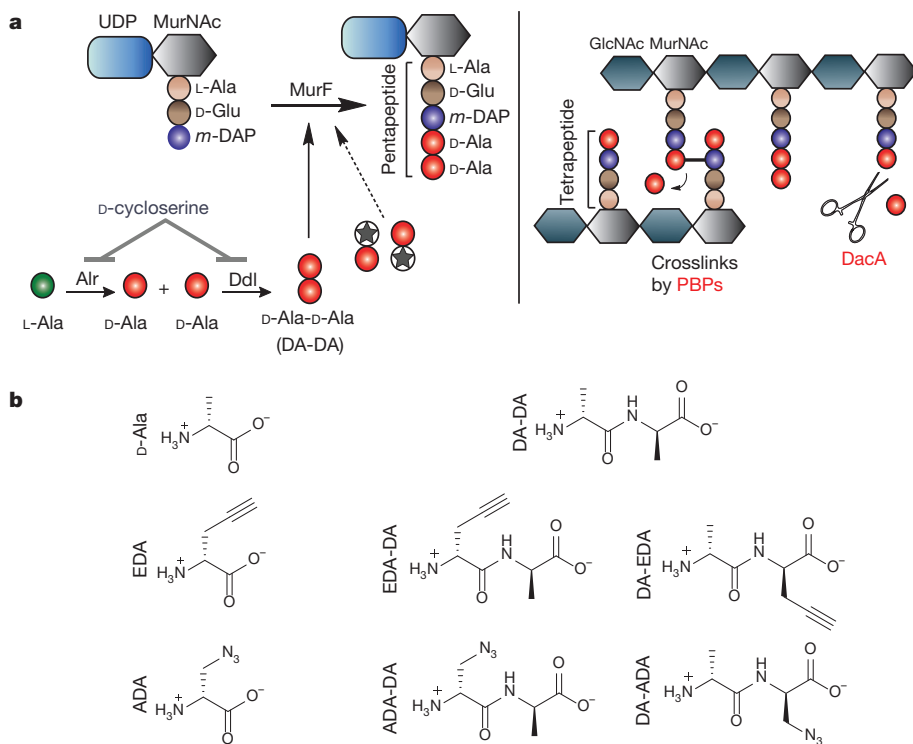
The existence of PG in *Chlamydia* has long been debated. Whereas genetic analysis and antibiotic susceptibility indicate that chlamydial PG exists<sup>8,9,13</sup>, all attempts to detect or purify PG in *Chlamydia* have been unsuccessful<sup>10,14–17</sup>, resulting in the ‘chlamydial anomaly’<sup>10</sup>. It has been established that the cytosolic receptor for PG, Nod1, is triggered upon infection by various chlamydial species<sup>18</sup>. Chlamydial homologues of PG biosynthetic enzymes have been extensively studied<sup>2–7</sup> and a growing body of literature supports the functionality of a complete biosynthesis pathway. A functional chlamydial UDP-N-acetylglucosamine enolpyruvyl transferase (MurA) has been described<sup>2</sup>. The product of the MurA reaction is specifically used for the synthesis of UDP-N-acetylmuramic acid (the sugar unique to the PG disaccharide backbone), suggesting the presence of the sugar component of PG in *Chlamydia*. During PG biosynthesis in most bacteria, D-alanine-D-alanine (DA-DA) generated by D-alanine-D-alanine ligase (Ddl) is incorporated directly into growing PG peptide chains through the MurF enzyme (Fig. 1a). Characterization of Ddl<sup>4</sup> and MurF<sup>6</sup> enzymes in *Chlamydia* coupled with recent advances in the chemical modification of PG through the incorporation of single D-amino acids<sup>19,20</sup> present an opportunity to covalently label the PG of actively growing *Chlamydia*.

*C. trachomatis* can take up both D-alanine and DA-DA dipeptide<sup>4,8</sup>; however, efforts to successfully label *Chlamydia* using previously characterized D-amino acid probes<sup>19,20</sup> were unsuccessful (Extended Data Fig. 1). We reasoned that this result was due to the inability of the chlamydial PG synthesis machinery to incorporate the modified single D-amino acids. Thus, we developed a novel and broadly applicable PG-labelling approach that bypassed the bacterial Ddl enzyme and used DA-DA dipeptide analogues modified with alkyne or azide functional groups (Fig. 1). Initial studies in *Escherichia coli* and *Bacillus subtilis* established that the alkyne and azide analogues of DA-DA (EDA-DA, DA-EDA, ADA-DA and DA-ADA, respectively, where ADA, azido-D-alanine; EDA, ethynyl-D-alanine) are capable of rescuing the growth of bacteria with depleted DA-DA dipeptide pools, whereas an alkyne analogue of the enantiomer L-alanine-L-alanine (LA-LA) is not capable of rescuing growth (Extended Data Table 1). In rich medium, bacterial growth is unaffected by the presence of DA-DA analogues (Extended Data Fig. 2). Once incorporated into a macromolecule such as PG, the functional groups of these dipeptides can be selectively captured via a click-chemistry reaction<sup>20,21</sup>. Labelling studies using DA-DA analogues in conjunction with clickable, modified Alexa Fluor dyes confirmed D-enantiomer-specific incorporation of the modified dipeptides in diverse bacterial species (Extended Data Figs 2 and 3). Polarly growing *Streptomyces venezuelae* was grown in the presence of the previously characterized, fluorescent D-amino acid HADA (7-hydroxycoumarin-3-carboxylic acid-3-amino-D-alanine, see ref. 19) for a few generations, and upon addition of EDA-DA for a brief period, subsequent polar-labelling confirmed that these dipeptides specifically label areas of new PG synthesis (Extended Data Fig. 3e). The labelling of *E. coli* and *B. subtilis* was covalent and cell-wall-specific (Extended Data

<sup>1</sup>Department of Microbiology and Immunology, F. Edward Hébert School of Medicine, Uniformed Services University of the Health Sciences, 4301 Jones Bridge Road, Bethesda, Maryland 20814-4799, USA. <sup>2</sup>Interdisciplinary Biochemistry Program, Indiana University, Bloomington, Indiana 47405, USA. <sup>3</sup>Department of Chemistry, Indiana University, Bloomington, Indiana 47405, USA. <sup>4</sup>Department of Biology, Indiana University, Bloomington, Indiana 47405, USA.

\*These authors contributed equally to this work.





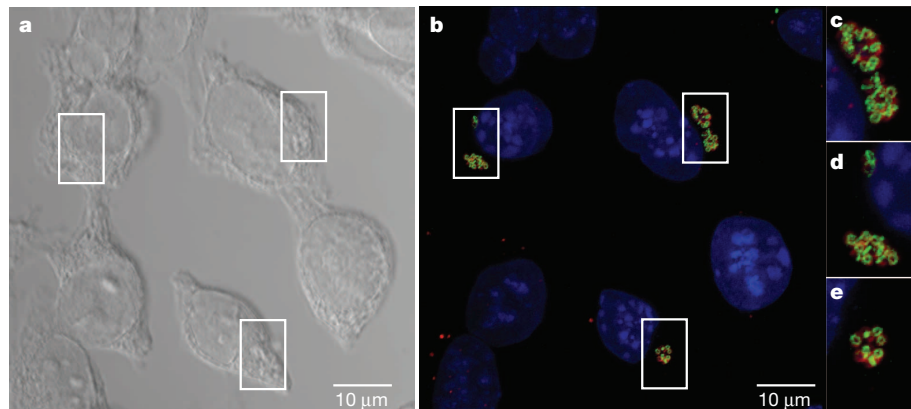
**Figure 1 | Novel dipeptide PG labelling strategy.** **a**, Biosynthesis of the terminal PG stem peptide of Gram-negative bacteria. Two D-alanines are first ligated together by D-alanine-D-alanine ligase and the dipeptide is subsequently added to the stem tripeptide by MurF, resulting in a pentapeptide. The labelling strategy relies on the inherent tolerance of the PG machinery to accept DA-DA analogues. Subsequent crosslinking between neighbouring peptide stems is carried out by a series of transpeptidases (penicillin-binding proteins). Upon transpeptidation, a proximal *m*-DAP from a neighbouring peptide stem attacks the carbonyl group between the penultimate and terminal D-alanines of the PG stem. The terminal D-alanine is thus cleaved from the stem peptide, which results in a tetrapeptide. Another pathway for the loss of terminal D-alanine is D,D-carboxypeptidation catalysed by enzymes such as DacA. **b**, Chemical structures of D-Ala, DA-DA, and their derivatives carrying bio-orthogonal handles used in this study. ADA, azido-D-alanine; ADA-DA, azido-D-alanyl-D-alanine; D-Ala, D-alanine; L-Ala, L-alanine; Alr, alanine racemase; DA-DA, D-alanyl-D-alanine; *m*-DAP, *meso*-diaminopimelic acid; Ddl, D-alanine-D-alanine ligase; EDA, ethynyl-D-alanine; EDA-DA, ethynyl-D-alanyl-D-alanine; DacA, D-alanyl-D-alanine carboxypeptidase A; GlcNAc, *N*-acetylglucosamine; D-Glu, D-Glutamic Acid; MurF, UDP-*N*-acetylmuramoyl-tripeptide-D-alanyl-D-alanine ligase; MurNac, *N*-acetylmuramic acid; PBPs, penicillin-binding proteins.

Fig. 4a), and *B. subtilis* label could be removed by treatment with the PG-digesting enzyme, lysozyme (Extended Data Fig. 4b), indicating that the probes were incorporated in the PG.

We next attempted to measure dipeptide probe uptake and incorporation in intracellular *Chlamydia*. L2 mouse fibroblast cells were infected for 18 h with *C. trachomatis* serovar L2 strain 434/Bu in the presence of 1 mM EDA-DA. Cells were then fixed and permeabilized, and click chemistry was used to attach an Alexa fluorophore modified with a terminal azide group to the alkyne group present on the EDA-DA probe. The probe localized within chlamydial inclusions with individual bacteria clearly discernible (Fig. 2). When co-labelled with antibody to the chlamydial major outer membrane protein (MOMP), EDA-DA labelling appeared as either a ring or a single line bisecting MOMP-labelled RBs (Extended Data Fig. 5). The labelling was arranged in a distinct, ring-like shape, consistent with a cellular division plane and the labelling bore a striking resemblance to images previously obtained for intracellular *C. trachomatis* stained with antibody generated with Ribi adjuvant<sup>22</sup>. Labelling was only present in *Chlamydia*-infected cells and only in the presence of probe (Extended Data Fig. 6a–c). This result indicates that the majority of labelled chlamydial PG is localized to the

septum of dividing RBs. However, we cannot rule out the possibility that low levels of PG exist elsewhere on the bacterium and are simply below the detection limit of fluorescence microscopy. Similar to our results with *B. subtilis*, we found that incubation with lysozyme for two hours was sufficient to remove EDA-DA labelling within chlamydial inclusions (Extended Data Fig. 6d, e), supporting our conclusion that the dipeptide probes are incorporating into chlamydial PG.

To further confirm that the modified probes were being taken up and incorporated into chlamydial PG, we performed plaque assays<sup>23</sup> that allow quantification of intracellular bacterial growth and infectivity. D-cycloserine (DCS) is an inhibitor of cell-wall biosynthesis that targets bacterial alanine racemase and D-alanine-D-alanine ligase<sup>24</sup> and previous studies have shown that *Chlamydia* growth is inhibited by DCS at millimolar concentrations<sup>4,8,25</sup>. Growth inhibition is overcome by supplementation with exogenous D-alanine or DA-DA dipeptide<sup>4</sup>, most likely owing to the exogenous single D-amino acids outcompeting DCS for the binding sites of the chlamydial ligase or, in the case of DA-DA, bypassing the need for the ligase altogether. Various D-amino acids, dipeptides and their corresponding alkyne-modified probes were tested to determine the level of DCS rescue they conferred upon



**Figure 2 | Fluorescent labelling of intracellular *C. trachomatis* PG.** **a–e**, Differential interference contrast (DIC) (**a**) and fluorescent (**b–e**) microscopy of L2 cells infected for 18 h with *C. trachomatis* in the presence of the dipeptide probe EDA-DA (1 mM). Subsequent binding of the probe to an azide modified Alexa Fluor 488 (green) was achieved via click chemistry. Antibody to MOMP (red) was used to label chlamydial EBs and RBs. DAPI (blue) was used for nuclear staining. **b–e** show a merge of all three fluorescent channels. Boxes indicate location of chlamydial inclusions, and magnification of the boxes is provided in **c–e**. Fluorescent images are maximum intensity projections of deconvoluted z-stacks. Three-dimensional renderings are provided in Supplementary Videos 1 and 2.

**Table 1 | DCS *Chlamydia trachomatis* plaque assay in the presence of natural and modified D-amino acids**

DCS ( $\mu$ M)	Amino acid, amino acid to DCS ratio	Plaque formation
0	—	++++
294	No amino acid	—
	Dipeptides	
	DA-DA, 1:1	++
	DA-DA, 10:1	+++
	DA-EDA, 1:1	—
	DA-EDA, 10:1	+++
	EDA-DA, 1:1	—
	EDA-DA, 10:1	++
	Single amino acids	
	D-Ala, 1:1	++++
	D-Ala, 1:10	+++
	EDA, 1:1	—
	EDA, 10:1	—

*C. trachomatis* serovar L2 strain 434/Bu was grown in the plaque assay as previously described<sup>4</sup> in the presence of D-cycloserine (DCS) and varying molar equivalent concentrations of D-alanine (D-Ala), D-alanine-D-alanine (DA-DA), EDA, DA-EDA, and EDA-DA. +++++, complete infection, bacterial growth and lysis of the monolayer; +++, numerous large plaques but less than complete lysis of the monolayer; ++, numerous small plaques; +, few (~10–20) small plaques; —, no plaque formation (no bacterial growth). Data represent the average of three biological replicates and each experiment was conducted with technical duplicates.

growing *C. trachomatis*. We found that DA-DA dipeptide and the corresponding modified dipeptides (EDA-DA and DA-EDA) were both capable of rescuing chlamydial plaquing (Table 1), indicating their successful uptake and incorporation by *Chlamydia*. However, whereas unmodified D-alanine was capable of overcoming the growth inhibitory effects of DCS, the corresponding chemically modified, single D-alanine probe (EDA) was not. These results were consistent with our inability to detect fluorescent labelling of *C. trachomatis* through single EDA probes (Extended Data Fig. 1).

Despite rescue of chlamydial growth by both EDA-DA and DA-EDA in the DCS plaque assay, we initially were not able to label chlamydial PG with DA-EDA (Extended Data Fig. 7). Similarly, we were unable to obtain labelling with DA-EDA in *E. coli* (Extended Data Fig. 2). We reasoned that the inability to label *Chlamydia* with DA-EDA was due to the removal of the terminal, modified EDA amino acid from the PG pentapeptide stem during either transpeptidation or carboxypeptidation (Fig. 1a). To test this hypothesis and to further validate that our probes were incorporated into *C. trachomatis* PG, we conducted EDA-DA and DA-EDA labelling studies in the presence of two antibiotics that block PG biosynthesis: DCS, a competitive inhibitor of both alanine racemase and D-alanine-D-alanine ligase, and ampicillin, an inhibitor of PG transpeptidases/carboxypeptidases. When grown for 18 h in

the presence of either antibiotic, inclusions contained enlarged, aberrant RBs. The presence of fewer bacteria per inclusion is indicative of a pre-division block, due to the absence of transpeptidation, and is consistent with the literature<sup>26</sup>. In the presence of DCS and 1 mM EDA-DA, fluorescent PG was discernible within aberrant RBs (Fig. 3a). This result indicates that EDA-DA was capable of partly substituting for DA-DA after depletion of the bacterium's natural dipeptide pool and confirms the DCS plaquing assay results. EDA-DA labelling intensity seemed unaffected by inhibition of PG transpeptidation/carboxypeptidation with ampicillin (Extended Data Fig. 7), indicating that probe incorporation is not dependent on transpeptidation and does not occur in the periplasm in *Chlamydia*. When imaged by epifluorescence, labelling of aberrant bodies grown in the presence of ampicillin often appeared punctate, owing to the enlarged PG ring structures that no longer exist within a single focal plane (see Extended Data Fig. 8). z-stacks taken of the ampicillin-treated aberrant RBs clearly revealed labelled PG sequestered to an equatorial region where the bacterial division plane would normally form (Fig. 3b). Fluorescence labelling of *Chlamydia* with DA-EDA was only observed when transpeptidation/carboxypeptidation was inhibited with ampicillin (Extended Data Fig. 7). DA-EDA labelling of a *B. subtilis* D,D-carboxypeptidase mutant ( $\Delta dacA$ ) confirmed this finding; labelling was greatly increased compared to the parental, wild-type strain and was not significantly turned over as the labelled cells were allowed to grow (Extended Data Fig. 3). These observations indicate that PG modifications (through transpeptidation and/or carboxypeptidation) occur *in vivo* in *Chlamydia*, as inhibition of these modifications would preserve the terminal D-alanine in the stem peptide, thus allowing for labelling of PG with DA-EDA.

Several investigators have examined the transcriptional profile of PG biosynthesis genes throughout the chlamydial life cycle<sup>11,27–30</sup>. The current consensus is that PG biosynthesis genes are upregulated during the transition phase between EB and RB<sup>27</sup>, indicating the need for PG before cell division. These results fit well with the knowledge that PG is closely involved in bacterial growth and cytokinesis<sup>1</sup>. To correlate these findings with actual PG production as measured via the incorporation of dipeptide probes into actively forming chlamydial PG, we conducted a time-course study to determine the earliest time at which dipeptide incorporation occurs. We detected EDA-DA-labelled *C. trachomatis* as early as 8 h post infection (Extended Data Fig. 9), and labelled bacteria were always seen in the context of developing chlamydial inclusions. Pre-incubating L2 cells with EDA-DA for 8 h before infection with *C. trachomatis* did not result in probe incorporation at earlier time points (data not shown). This suggests that probe incorporation and

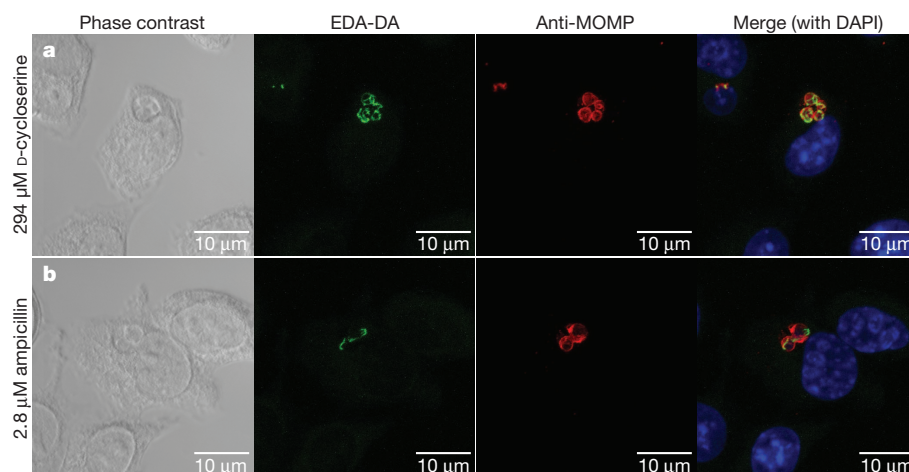


**Figure 3 | Labelling in the presence of PG synthesis inhibitors.** a, b, DIC and fluorescent microscopy of infected L2 cells 18 h post infection in the presence of 1 mM EDA-DA and either D-cycloserine (DCS) (a) or ampicillin (AMP) (b). Labelling was conducted as described in the Fig. 2 legend. A merge of all three

fluorescent channels is presented in the panels on the right. Fluorescent images are maximum intensity projections of z-stacks and three-dimensional renderings are provided in Supplementary Videos 3 and 4.

new PG synthesis occur during the early stages of EB to RB transition, consistent with transcriptome data<sup>27</sup>.

In conclusion, we have successfully labelled the peptidoglycan of intracellular *Chlamydia trachomatis* using modified dipeptide probes. The development and characterization of this versatile, general and non-toxic method for metabolically labelling peptidoglycan provides a unique and powerful technique for studying bacterial peptidoglycan biosynthetic pathways in a myriad of bacterial species. The strength of the click chemistry approach used in this work is in its specificity, but future studies will also exploit its versatility. These probes can be selectively captured by molecules other than conventional dyes, such as specified fluorophores for use in super-resolution microscopy, modified gold nanoparticles for use in electron microscopy, or agarose resins for use in peptidoglycan enrichment and chemical characterization. Although this technique has opened the door to a wide range of studies in *Chlamydia*, it is readily adaptable to other model systems, thus providing a powerful investigative tool for use in the examination of bacterial peptidoglycan biosynthesis, modification and degradation pathways.

## METHODS SUMMARY

EDA was purchased from BoaoPharma and dipeptide probes EDA-DA, DA-EDA, ADA-DA, and DA-ADA were synthesized (detailed in the Supplementary Methods section). Click chemistry was carried out with a 'clickable' Alexa Fluor 488 and Click-iT Cell Reaction Buffer Kit, which were purchased from Invitrogen. Wild-type *Escherichia coli* strain MG1655 and mutants, *Bacillus subtilis* strain PY79, *Streptomyces venezuelae* and *Streptococcus pneumoniae* strain IU1945 were all grown as previously described<sup>19</sup>. L2 mouse fibroblasts and *C. trachomatis* serovar L2 strain 434/Bu were grown, bacterial and antibiotic titres calculated, and infections/plaque assays were conducted as previously described<sup>4,23</sup>. For counter-labelling of *C. trachomatis*, either monoclonal anti-MOMP antibody (LifeSpan Biosciences) or anti-IncA antibody (D. Rockey) was used. Detailed protocols for PG labelling of all bacteria described in this work are provided in the Methods section, along with lysozyme treatment protocols, plating assays and details concerning image acquisition and analysis for all microscopy.

**Online Content** Any additional Methods, Extended Data display items and Source Data are available in the online version of the paper; references unique to these sections appear only in the online paper.

**Received 3 September; accepted 21 November 2013.**

**Published online 11 December 2013.**

- Egan, A. J. & Vollmer, W. The physiology of bacterial cell division. *Ann. NY Acad. Sci.* **1277**, 8–28 (2013).
- McCoy, A. J., Sandlin, R. C. & Maurelli, A. T. *In vitro* and *in vivo* functional activity of *Chlamydia* MurA, a UDP-N-acetylglucosamine enolpyruvyl transferase involved in peptidoglycan synthesis and fosfomycin resistance. *J. Bacteriol.* **185**, 1218–1228 (2003).
- Hesse, L. *et al.* Functional and biochemical analysis of *Chlamydia trachomatis* MurC, an enzyme displaying UDP-N-acetylmuramate:amino acid ligase activity. *J. Bacteriol.* **185**, 6507–6512 (2003).
- McCoy, A. J. & Maurelli, A. T. Characterization of *Chlamydia* MurC-Ddl, a fusion protein exhibiting D-alanyl-D-alanine ligase activity involved in peptidoglycan synthesis and D-cycloserine sensitivity. *Mol. Microbiol.* **57**, 41–52 (2005).
- Patin, D., Bostock, J., Blano, D., Mengin-Lecreulx, D. & Chopra, I. Functional and biochemical analysis of the *Chlamydia trachomatis* ligase MurE. *J. Bacteriol.* **191**, 7430–7435 (2009).
- Patin, D., Bostock, J., Chopra, I., Mengin-Lecreulx, D. & Blano, D. Biochemical characterisation of the chlamydial MurF ligase, and possible sequence of the chlamydial peptidoglycan pentapeptide stem. *Arch. Microbiol.* **194**, 505–512 (2012).
- McCoy, A. J. *et al.* L-L-diaminopimelate aminotransferase, a trans-kingdom enzyme shared by *Chlamydia* and plants for synthesis of diaminopimelate/lysine. *Proc. Natl Acad. Sci. USA* **103**, 17909–17914 (2006).
- Moulder, J. W., Novosel, D. L. & Officer, J. E. Inhibition of the growth of agents of the psittacosis group by D-cycloserine and its specific reversal by D-alanine. *J. Bacteriol.* **85**, 707–711 (1963).

- Tamura, A. & Manire, G. P. Effect of penicillin on the multiplication of meningopneumonitis organisms (*Chlamydia psittaci*). *J. Bacteriol.* **96**, 875–880 (1968).
- Moulder, J. W. Why is *Chlamydia* sensitive to penicillin in the absence of peptidoglycan? *Infect. Agents Dis.* **2**, 87–99 (1993).
- Ormsland, A., Sager, J., Nair, V., Sturdevant, D. E. & Hackstadt, T. Developmental stage-specific metabolic and transcriptional activity of *Chlamydia trachomatis* in an axenic medium. *Proc. Natl Acad. Sci. USA* **109**, 19781–19785 (2012).
- Mattei, P.-J., Neves, D. & Dessen, A. Bridging cell wall biosynthesis and bacterial morphogenesis. *Curr. Opin. Struct. Biol.* **20**, 749–755 (2010).
- Stephens, R. S. *et al.* Genome sequence of an obligate intracellular pathogen of humans: *Chlamydia trachomatis*. *Science* **282**, 754–759 (1998).
- Fox, A. *et al.* Muramic acid is not detectable in *Chlamydia psittaci* or *Chlamydia trachomatis* by gas chromatography-mass spectrometry. *Infect. Immun.* **58**, 835–837 (1990).
- Hatch, T. P. Disulfide cross-linked envelope proteins: the functional equivalent of peptidoglycan in chlamydiae? *J. Bacteriol.* **178**, 1–5 (1996).
- Chopra, I., Storey, C., Falla, T. J. & Pearce, J. H. Antibiotics, peptidoglycan synthesis and genomics: the chlamydial anomaly revisited. *Microbiology* **144**, 2673–2678 (1998).
- Barbour, A. G., Amano, K., Hackstadt, T., Perry, L. & Caldwell, H. D. *Chlamydia trachomatis* has penicillin-binding proteins but not detectable muramic acid. *J. Bacteriol.* **151**, 420–428 (1982).
- Welter-Stahl, L. *et al.* Stimulation of the cytosolic receptor for peptidoglycan, Nod1, by infection with *Chlamydia trachomatis* or *Chlamydia muridarum*. *Cell. Microbiol.* **8**, 1047–1057 (2006).
- Kuru, E. *et al.* In situ probing of newly synthesized peptidoglycan in live bacteria with fluorescent D-acids. *Angew. Chem.* **51**, 12519–12523 (2012).
- Siegrist, M. S. *et al.* D-amino acid chemical reporters reveal peptidoglycan dynamics of an intracellular pathogen. *ACS Chem. Biol.* **8**, 500–505 (2013).
- Breinbauer, R. & Kohn, M. Azide-alkyne coupling: a powerful reaction for bioconjugate chemistry. *ChemBioChem* **4**, 1147–1149 (2003).
- Brown, W. J. & Rockey, D. D. Identification of an antigen localized to an apparent septum within dividing chlamydiae. *Infect. Immun.* **68**, 708–715 (2000).
- Binet, R. & Maurelli, A. T. Frequency of spontaneous mutations that confer antibiotic resistance in *Chlamydia* spp. *Antimicrob. Agents Chemother.* **49**, 2865–2873 (2005).
- Neuhaus, F. C. & Hammes, W. P. Inhibition of cell wall biosynthesis by analogues and alanine. *Pharmacol. Ther.* **14**, 265–319 (1981).
- Gordon, F. B. & Quan, A. L. Susceptibility of *Chlamydia* to antibacterial drugs: test in cell cultures. *Antimicrob. Agents Chemother.* **2**, 242–244 (1972).
- Skilton, R. J. *et al.* Penicillin induced persistence in *Chlamydia trachomatis*: high quality time lapse video analysis of the developmental cycle. *PLoS ONE* **4**, e7723 (2009).
- Belland, R. J. *et al.* Genomic transcriptional profiling of the developmental cycle of *Chlamydia trachomatis*. *Proc. Natl Acad. Sci. USA* **100**, 8478–8483 (2003).
- Albrecht, M., Sharma, C. M., Reinhardt, R., Vogel, J. & Rudel, T. Deep sequencing-based discovery of the *Chlamydia trachomatis* transcriptome. *Nucleic Acids Res.* **38**, 868–877 (2010).
- Albrecht, M. *et al.* The transcriptional landscape of *Chlamydia pneumoniae*. *Genome Biol.* **12**, R98 (2011).
- Shaw, E. I. *et al.* Three temporal classes of gene expression during the *Chlamydia trachomatis* developmental cycle. *Mol. Microbiol.* **37**, 913–925 (2000).

**Supplementary Information** is available in the online version of the paper.

**Acknowledgements** This work was supported by NIH grants to A.T.M. (AI044033) and Y.V.B. (GM51986). We would like to thank D. McDaniel and M. Murgai for their help with image acquisition and presentation, P. Foster and D. Kearns for help in early stages of the project, R. Calvo for help with strain construction, and M. Winkler for providing strains and advice.

**Author Contributions** G.W.L. conducted all labelling, imaging, intracellular growth-rescue, and probe characterization studies in *C. trachomatis*. E.K. developed the dipeptide labelling strategy, conducted all labelling, imaging and probe characterization studies for *E. coli*, *B. subtilis*, *S. pneumoniae* and *S. venezuelae*, purification and imaging of labelled bacterial PG, and *E. coli* and *B. subtilis* growth rescue experiments. E.H. and A.K. were involved in the synthesis of probes. M.V.N., Y.V.B. and A.T.M. were all involved in study design. G.W.L. and E.K. designed the study, analysed the data and wrote the manuscript. G.W.L. and E.K. contributed equally to this work. All authors discussed the results and commented on the manuscript. The opinions or assertions contained herein are ours and are not to be construed as official or as reflecting the views of the Department of Defense or the Uniformed Services University.

**Author Information** Reprints and permissions information is available at [www.nature.com/reprints](http://www.nature.com/reprints). The authors declare no competing financial interests. Readers are welcome to comment on the online version of the paper. Correspondence and requests for materials should be addressed to A.T.M. (anthony.maurelli@usuhs.edu) or to M.V.N. (mvannieu@indiana.edu). Requests for materials should be addressed to M.V.N. (mvannieu@indiana.edu).



# Broadly permissive intestinal chromatin underlies lateral inhibition and cell plasticity

Tae-Hee Kim<sup>1,2</sup>, Fugen Li<sup>1</sup>, Isabel Ferreiro-Neira<sup>1,2</sup>, Li-Lun Ho<sup>1,2</sup>, Annouck Luyten<sup>1,2</sup>, Kodandaramireddy Nalapareddy<sup>1,2</sup>, Henry Long<sup>1</sup>, Michael Verzi<sup>1,2</sup> & Ramesh A. Shivdasani<sup>1,2</sup>

Cells differentiate when transcription factors bind accessible *cis*-regulatory elements to establish specific gene expression programs. In differentiating embryonic stem cells, chromatin at lineage-restricted genes becomes sequentially accessible<sup>1–4</sup>, probably by means of ‘pioneer’ transcription factor activity<sup>5</sup>, but tissues may use other strategies *in vivo*. Lateral inhibition is a pervasive process in which one cell forces a different identity on its neighbours<sup>6</sup>, and it is unclear how chromatin in equipotent progenitors undergoing lateral inhibition quickly enables distinct, transiently reversible cell fates. Here we report the chromatin and transcriptional underpinnings of differentiation in mouse small intestine crypts, where notch signalling mediates lateral inhibition to assign progenitor cells into absorptive or secretory lineages<sup>7–9</sup>. Transcript profiles in isolated LGR5<sup>+</sup> intestinal stem cells<sup>10</sup> and secretory and absorptive progenitors indicated that each cell population was distinct and the progenitors specified. Nevertheless, secretory and absorptive progenitors showed comparable levels of H3K4me2 and H3K27ac histone marks and DNase I hypersensitivity—signifying accessible, permissive chromatin—at most of the same *cis*-elements. Enhancers acting uniquely in progenitors were well demarcated in LGR5<sup>+</sup> intestinal stem cells, revealing early priming of chromatin for divergent transcriptional programs, and retained active marks well after lineages were specified. On this chromatin background, ATOH1, a secretory-specific transcription

factor, controls lateral inhibition through delta-like notch ligand genes and also drives the expression of numerous secretory lineage genes. Depletion of ATOH1 from specified secretory cells converted them into functional enterocytes, indicating prolonged responsiveness of marked enhancers to the presence or absence of a key transcription factor. Thus, lateral inhibition and intestinal crypt lineage plasticity involve interaction of a lineage-restricted transcription factor with broadly permissive chromatin established in multipotent stem cells.

Intestinal crypts produce enterocyte and secretory (enteroendocrine, goblet, or Paneth) lineages after bipotential progenitors start to express ATOH1 and delta-like ligands, which activate Notch receptors on adjacent cells<sup>8,9</sup>. Notch signalling silences *Atoh1* expression in recipient cells and within 6 h ATOH1<sup>+</sup> cells adopt the secretory fate, whereas ATOH1<sup>−</sup> cells become enterocytes<sup>9,11,12</sup> (Extended Data Fig. 1a); forced ATOH1 expression in mouse fetal intestines promotes secretory differentiation<sup>13</sup>. To investigate the chromatin basis for the deterministic activity of ATOH1 in lateral inhibition, we purified LGR5<sup>+</sup> intestinal stem cells from *Lgr5*<sup>GFP-cre</sup> mouse crypts<sup>10</sup> (Extended Data Fig. 1b, c). Exploiting a total absence of secretory cells in *Atoh1*<sup>−/−</sup> intestines<sup>11,12,14</sup> (Extended Data Fig. 1d, e), we also collected mature villus enterocytes (Fig. 1f) and their crypt progenitors (hereafter termed Ent-Pro, Fig. 1l) from villin-*cre*<sup>ER</sup>; *Atoh1*<sup>fl/fl</sup> mice (Extended Data Table 1). To expand secretory cell

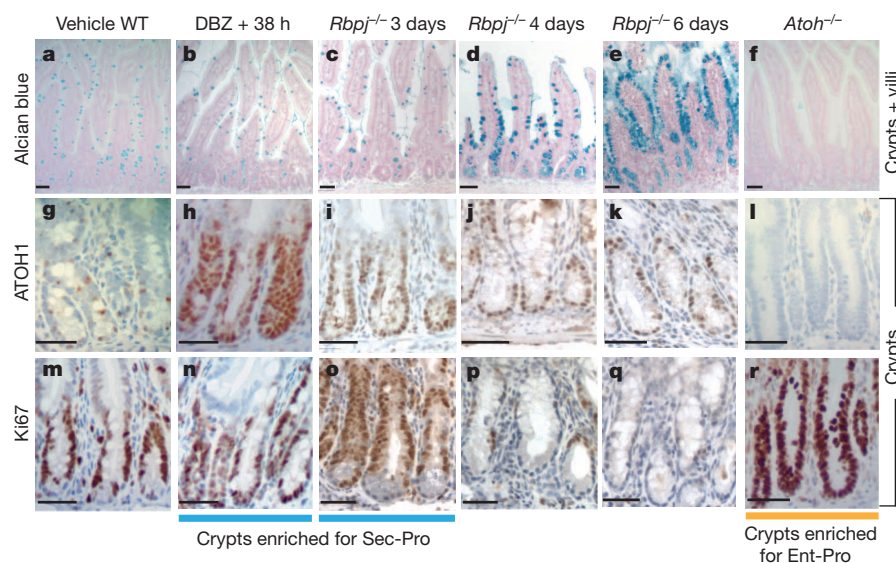


**Figure 1 | Enrichment of Sec-Pro and Ent-Pro cells.** **a, g, m,** Control intestines. **b, c, h, i, n, o,** Approximately 38 h (DBZ treatment) or 3 days (*Rbpj* loss) after notch inhibition, crypt cells remain proliferative (**n, o**) but express ATOH1 (**h, i**) and fail to stain with Alcian blue (**b, c**), indicating immaturity. **d, e, j, k, p, q,** By 4 days after *Rbpj* deletion, crypt cells cease replication (**p**), retain ATOH1 (**j**), and show weak Alcian blue staining (**d**); 2 days later,

their goblet cell progeny occupy short villi (**e, k, q**). **f, l, r,** *Atoh1*<sup>−/−</sup> intestines lack secretory cells, carrying only enterocytes on villi (**f**) and replicating ATOH1<sup>−</sup> Ent-Pro in crypts (**l, r**). Scale bars, 50 μm. Duplicate samples were examined from three (*Rbpj*<sup>−/−</sup> and wild type (WT)) or seven (DBZ + 38 h and *Atoh1*<sup>−/−</sup>) mice.

<sup>1</sup>Department of Medical Oncology and Center for Functional Cancer Epigenetics, Dana-Farber Cancer Institute, Boston, Massachusetts 02215, USA. <sup>2</sup>Department of Medicine, Brigham and Women's Hospital and Harvard Medical School, Boston, Massachusetts 02215, USA.

progenitors (Sec-Pro cells), we separately depleted transcription factor RBPJ, which mediates notch responses<sup>6,7</sup>, or disrupted notch signalling with the  $\gamma$ -secretase inhibitor dibenzazepine (DBZ)<sup>7,15</sup>. Both approaches induced replication arrest and an excess of all secretory cell types<sup>12,16</sup> (Fig. 1e, q and Extended Data Figs 1f and 2). Four days after induced *Rbpj* deletion or 72 h after administration of DBZ, secretory cells appeared in all crypts, but not yet on villi (Fig. 1d and Extended Data Fig. 2), revealing their origins in Sec-Pro cells. Accordingly, 1 day (*Rbpj*<sup>-/-</sup>) or 1.5 days (DBZ) earlier, crypts uniformly showed high ATOH1 expression, ongoing cell replication, and negligible avidity for the goblet cell stain Alcian blue (Fig. 1b, c, h, i, n, o). Confirming that these ATOH1<sup>+</sup> cells are bona fide Sec-Pro cells, they robustly expressed known secretory genes<sup>17</sup> (for example, *Neurog3*, *Gfi1*, *Spdef*); moreover, Sec-Pro cells produced in different ways had similar expression profiles, distinct from characteristic transcripts enriched in other cell populations (Extended Data Fig. 3 and Supplementary Information Table 1). Although LGR5<sup>+</sup> intestinal stem cells, Sec-Pro and Ent-Pro cells share many transcripts, the divergent cell sources and expression profiles indicate that they represent discrete, specified crypt populations.

We used chromatin immunoprecipitation with deep sequencing (ChIP-seq) to first identify sites carrying H3K4me2, a robust mark of functional *cis*-element activity<sup>18,19</sup>. As mammalian genes are controlled mainly through distant enhancers<sup>20</sup>, where tissue-restricted transcription

factors bind DNA<sup>21</sup>, we concentrated on regions  $\geq 2$  kilobases (kb) upstream or  $\geq 1$  kb downstream of transcription start sites (TSSs). Highly concordant enhancer profiles in independent Ent-Pro replicates and in Sec-Pro obtained after genetic or chemical notch inhibition (Fig. 2a, b and Extended Data Fig. 4) gave confidence in epigenome analysis of primary cells. As prevailing concepts predict, villus cells clustered farthest in aggregate analysis of H3K4me2-marked enhancers (Fig. 2b) because many enhancers were marked in mature enterocytes and goblet cells, but not in their progenitors (group 2 in Fig. 2a and Extended Data Fig. 5a); these enhancers, delineated only in mature cells, showed significant transcription factor motif enrichment (Supplementary Information Table 2). To our surprise, not only were many enhancers prominently marked in progenitor cells, but H3K4me2 showed markedly similar distributions in Sec-Pro and Ent-Pro cells (group 1 in Fig. 2a and Extended Data Fig. 5b). Marks were evident at these sites even in LGR5<sup>+</sup> intestinal stem cells, distinct from the group 2 profile, and aggregate analysis verified significant overlap of H3K4me2 enhancers among crypt populations (Fig. 2b). Sites that seemed superficially better marked in DBZ-derived Sec-Pro cells (group 1b) lacked transcription factor motif enrichment or other distinguishing features, and Sec-Pro-restricted genes were not enriched near these sites but distributed among enhancers marked in all three crypt populations (Fig. 2a and Supplementary Information Tables 1 and 2).

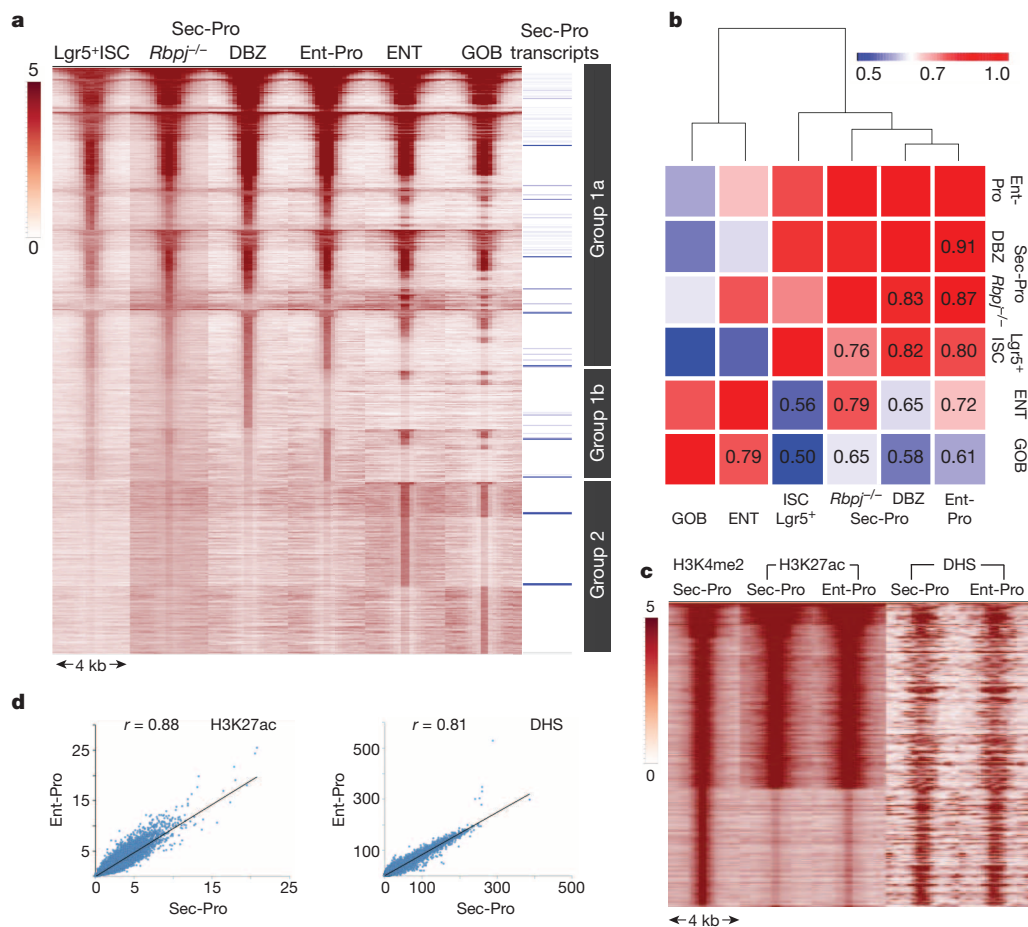


**Figure 2 | Broadly permissive chromatin in intestinal crypt progenitors.** **a**, H3K4me2 levels at 57,481 sites ( $\geq 2$  kb upstream or  $\geq 1$  kb downstream of any TSS) are similar in Sec-Pro, Ent-Pro and LGR5<sup>+</sup> intestinal stem cells (ISC); Sec-Pro-selective genes are usually marked as strongly in other cells as in Sec-Pro. Groups 1a and 2 denote strongly marked and unmarked enhancers, respectively, in Sec-Pro. Group 1b denotes enhancers with superficially stronger marking in one or other progenitor. GOB, goblet cells; ENT, enterocytes. **b**, Hierarchical clustering and Spearman's correlation coefficients for normalized H3K4me2 signals in crypt and villus enhancers. Crypt and villus

cells show expected differences, but crypt progenitors and intestinal stem cells are highly similar. **c**, H3K27ac and DHS levels at 21,354 enhancers with robust H3K4me2 in *Rbpj*<sup>-/-</sup> Sec-Pro cells. Many sites show high H3K27ac and DHS, both similar in Sec-Pro and Ent-Pro. **d**, High concordance, shown with Spearman's correlation coefficients, between all sites with H3K27ac (33,257 sites) or DHS (116,325 sites) in Sec-Pro and Ent-Pro cells. Coloured scale bars in **a** and **c** represent a range of normalized values for reads per million tags; coloured scale bar in **b** shows the colour range for Spearman's correlation coefficient values.

As H3K4 is methylated at both poised and active *cis*-elements in embryonic stem (ES) cells<sup>1</sup>, the striking overlap in progenitor cell marks might reflect enhancer potential, distinct from enhancer activity; H3K27ac is thought to mark active enhancers specifically<sup>22,23</sup>. Although many H3K4me2-marked enhancers lacked H3K27ac, global and local distributions of the latter were remarkably similar in Sec-Pro and Ent-Pro cells (Fig. 2c, d). DNase I hypersensitivity (DHS, an independent, direct measure of chromatin access)<sup>24</sup> was evident at most H3K4me2 sites and its distribution was also highly similar in Sec-Pro and Ent-Pro cells (Fig. 2c, d), distinct from DHS in other mouse tissues (Extended Data Fig. 5c). Thus, thousands of enhancers for lineage-restricted genes show comparable histone activation and tissue-specific chromatin access in distinct, specified crypt progenitors, and most such sites carry H3K4me2 in intestinal stem cells. This early, indiscriminate delineation of enhancers offers a compelling explanation for crypt cell equipotency, a key feature of lateral inhibition, and reveals that intestinal lineage separation does not require differential chromatin priming in daughter cells and may instead rely principally on transcription factor activity.

ATOH1, a Sec-Pro-specific transcription factor, is an ideal candidate to confer selectivity (Extended Data Fig. 6a). Flag ChIP-seq in Sec-Pro cells isolated from *Atoh1*<sup>Flag</sup> mice<sup>25</sup> identified thousands of binding sites, most of them in highly conserved, distant enhancers carrying ATOH1 consensus motifs (Extended Data Figs 4b and 6b) and different from ATOH1 binding sites in cerebellar neurons<sup>25</sup> (Fig. 3a). Intestinal and neuronal binding sites coincided with tissue-specific H3K4 methylation (Extended Data Fig. 6c), attesting to the regulatory significance of this histone modification. Lateral inhibition requires *Atoh1* repression in prospective Ent-Pro cells and ATOH1 activity in Sec-Pro cells<sup>12,14</sup>, and the rapidity of ATOH1-induced lineage divergence<sup>9</sup> suggests that it may directly regulate genes driving lateral inhibition. Indeed, ATOH1 bound strongly to its own locus and those for notch ligands *Dll1* and *Dll4* (Fig. 3b), but not Ent-Pro-specific loci such as *Bcl2l15* (Extended Data Fig. 6d). These findings support a cell-intrinsic,

ATOH1-dependent mechanism for lateral inhibition and a simple, direct means for feed-forward maintenance of this bistable system<sup>26</sup>. ATOH1 also bound numerous loci implicated in secretory differentiation, including determinants of each sub-lineage, and the corresponding transcripts are low or absent in *Atoh1*<sup>-/-</sup> crypts (Fig. 3b and Extended Data Fig. 6e, f). Strong, specific association of ATOH1 binding with Sec-Pro-restricted transcripts further indicates that ATOH1 activates secretory genes without binding or directly repressing enterocyte genes (Extended Data Fig. 6g).

H3K4me2, H3K27ac and DHS signals at ATOH1-bound enhancers were, on average, equally strong in ATOH1<sup>+</sup> Sec-Pro and Ent-Pro cells, which categorically lack ATOH1 (Fig. 3c). A few secretory loci showed modestly stronger features in Sec-Pro or goblet cells (Extended Data Fig. 5d), but most profiles were similar in LGR5<sup>+</sup> intestinal stem cells and both progenitors (Fig. 3d). Although in villus cells ATOH1 preferred sites marked only in goblet cells over those marked only in enterocytes, in crypts ATOH1 overwhelmingly favoured enhancers bearing H3K4me2 in all populations (Extended Data Fig. 7). The pervasive demarcation of ATOH1-bound enhancers in *Atoh1*<sup>-/-</sup> Ent-Pro cells reveals that this transcription factor does not initiate or maintain chromatin access in crypt cells.

The extreme overlap of Sec-Pro and Ent-Pro enhancer profiles indicates persistence of *cis*-element marks after lineage specification. Intestinal lineages might therefore remain plastic beyond the period of lateral inhibition, and sustained chromatin access might explain why some differentiated crypt cells readily assume stem-cell properties<sup>17,27,28</sup>. Our findings indicate that chromatin in specified cells may stay responsive to the presence or absence of ATOH1. In *Atoh1*-null fetal intestines, an *Atoh1*<sup>lacZ</sup> allele is expressed in enterocytes<sup>14</sup>, but this finding could represent a non-cell-autonomous effect of abortive lateral inhibition. We postulated prolonged, cell-autonomous ATOH1 control of lineage identity in specified cells.

To test this hypothesis, we suppressed notch in *Atoh1*<sup>fl/fl</sup>;villin-cre<sup>ER</sup> mice and waited past the period of widespread Sec-Pro differentiation

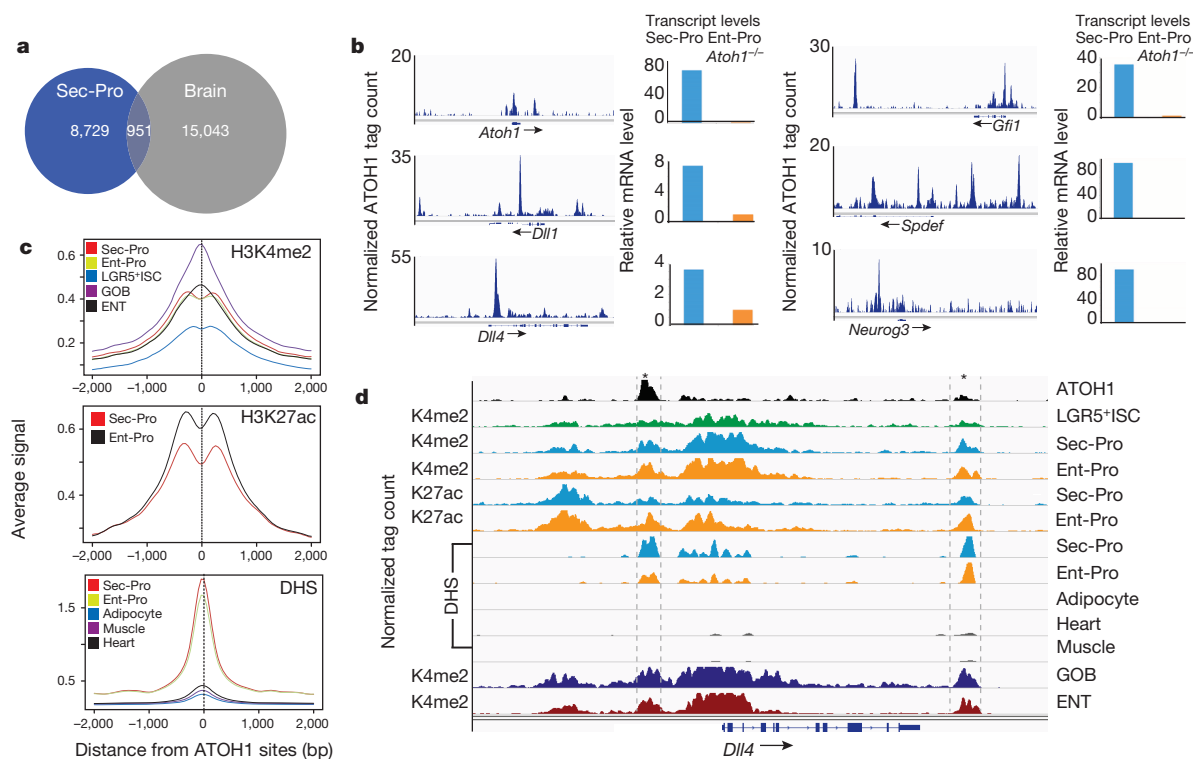


**Figure 3 | ATOH1 binding and chromatin interactions.** **a**, Low overlap of ATOH1 binding sites in mouse Sec-Pro and brain. **b**, ChIP-seq data showing multiple strong ATOH1 binding sites at Sec-Pro-selective *Atoh1*, *Dll1* and *Dll4* genes (left) and at crucial transcription factor genes expressed specifically in Sec-Pro cells (right). **c**, Average H3K4me2, H3K27ac and DHS signals at

ATOH1-bound enhancers are comparable in intestinal crypt cell populations, including *Atoh1*-null Ent-Pro cells. Intestinal DHS sites differ from those in other tissues. **d**, Data at a representative secretory locus show similar H3K4me2, H3K27ac and DHS levels in all crypt populations, including at ATOH1-bound enhancers (asterisks and dotted lines).



before administering tamoxifen to induce *Atoh1* deletion; we also injected bromodeoxyuridine (BrdU) to monitor cell replication and turnover (Fig. 4a). Crypts and villus bases in control *Atoh1*<sup>fl/fl</sup>;Cre<sup>-</sup> mice became filled with non-replicating goblet cells 3 days after notch inhibition, as expected (Fig. 4b–d), whereas ATOH1-depleted crypts showed substantial proliferation and many fewer Alcian-blue-avid cells (Fig. 4e–g). To demonstrate that this marked difference from control mice did not represent rescue by a few intestinal stem cells that might have eluded notch inhibition, but rather was due to secretory cell conversion to enterocytes, we followed cells for three additional days (Fig. 4a). By this time notch-inhibited control *Atoh1*<sup>fl/fl</sup>;Cre<sup>-</sup> mice became moribund and had short villi containing only goblet cells that showed no BrdU labelling (Fig. 4h–k). Meanwhile, in the absence of notch suppression, BrdU tracer in wild-type or *Atoh1*<sup>-/-</sup> intestines had moved from crypts into villus tips (Extended Data Fig. 8a–d), as expected.

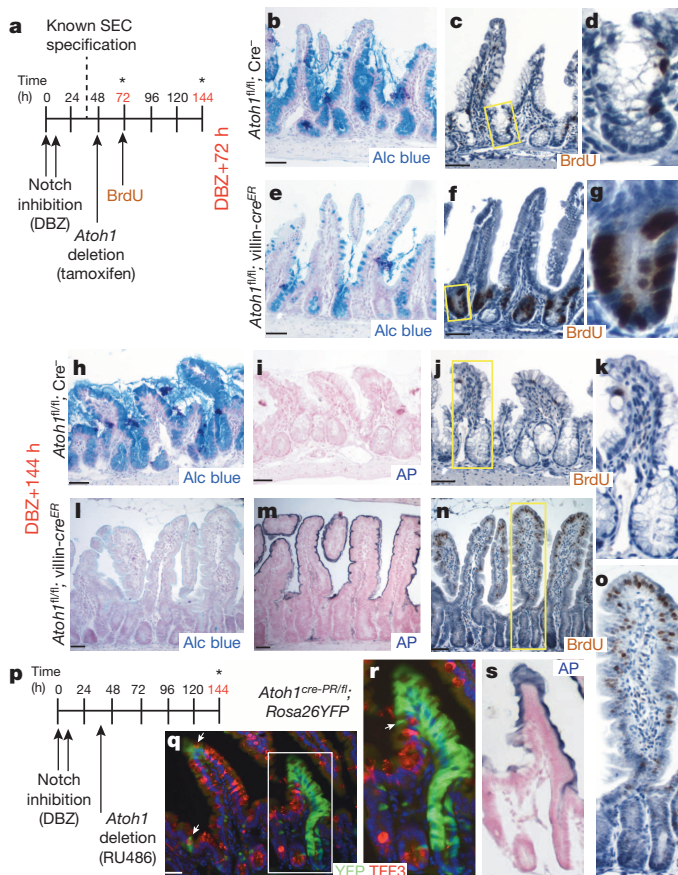


**Figure 4 | Conversion of specified secretory cells to enterocytes.** **a**, Notch inhibition (DBZ, two doses 6 h apart) and ATOH1 depletion schema in *Atoh1*<sup>fl/fl</sup>;villin-cre<sup>ER</sup> mice, with BrdU tracing. **b–g**, Three days after notch inhibition (1 h after BrdU), most ATOH1-depleted crypt cells showed BrdU and little Alcian blue staining; Cre<sup>-</sup> crypt cells had largely stopped replicating and started to mature into goblet cells. **h, i, l, m**, Six days after notch inhibition (3 days after BrdU), ATOH1-depleted cells had converted globally to enterocytes, showing alkaline phosphatase (AP) but not Alcian blue staining; ATOH1<sup>+</sup> control intestines showed profound goblet cell metaplasia. **j, k, n, o**, BrdU, absent in *Atoh1*<sup>fl/fl</sup>;Cre<sup>-</sup> intestines, appeared at villus tips in *Atoh1*<sup>fl/fl</sup>;villin-cre<sup>ER</sup> intestines. Boxes in **c** and **f** are magnified 370% and boxes in **j** and **n** are magnified 200% in adjacent panels. **p**, Notch inhibition and Sec-Pro-selective *Atoh1* deletion strategy in *Atoh1*<sup>cre-PR/β</sup>;Rosa26<sup>YFP</sup> mice. **q–s**, Ribbons of crypt cells originally specified as secretory (YFP<sup>+</sup>) and then rendered *Atoh1*-null expressed alkaline phosphatase but not goblet cell marker TFF3. The box in **q** is magnified in **r** and **s**; arrows point to rare YFP<sup>+</sup>TFF3<sup>+</sup> cells. All scale bars, 50 μm except in **q** (30 μm). Duplicate samples were examined from three (Cre<sup>-</sup>: DBZ+72 h, DBZ+144 h), nine (villin-cre, DBZ+72 h), six (villin-cre, DBZ+144 h), or four (*Atoh1*<sup>cre-PR/β</sup>) mice.

*Atoh1*<sup>fl/fl</sup>;villin-cre<sup>ER</sup> mice remained fit and carried only alkaline-phosphatase-expressing enterocytes on tall villi with abundant BrdU signal at the tips (Fig. 4l–o). Thus, loss of ATOH1 results in cells that overcome secretory fate and replication arrest more than 2 days after notch inhibition to become Ent-Pro cells that proliferate and mature into functional enterocytes.

To verify cell-autonomous fate conversion, we used progesterone/RU486-responsive *Atoh1*<sup>cre-PR</sup> mice<sup>29</sup>. After RU486 injection, YFP signals in control *Atoh1*<sup>cre-PR/+</sup>;Rosa26<sup>YFP</sup> mice were confined to a few goblet and enteroendocrine cells, indicating weak but restricted Cre activity; four independent mice showed no labelling of enterocytes or cell stripes, crucially confirming absence of leaky Cre activity in intestinal stem cells or multipotent progenitors (Extended Data Fig. 8e, f). We suppressed notch in *Atoh1*<sup>cre-PR/β</sup>;Rosa26<sup>YFP</sup> mice, then activated Cre selectively in ATOH1<sup>+</sup> secretory cells, thus deleting the floxed *Atoh1* allele and simultaneously activating a fluorescent lineage tracer (Fig. 4p). Four days later, stripes of YFP<sup>+</sup> cells emanated from crypts and 95 ± 4.1% (s.d.) of YFP<sup>+</sup> ATOH1-depleted cells (*n* = 1,200 cells; 4 mice) in these ribbons lacked the goblet cell marker TFF3 but expressed alkaline phosphatase (Fig. 4q–s and Extended Data Fig. 8g), confirming bona fide conversion of secretory cells to enterocytes. Thus, specified secretory cells are not irrevocably committed and their switched identity upon ATOH1 withdrawal mirrors the broadly permissive chromatin in crypt cells.

Mathematical modelling indicates that bifurcating valleys in Waddington's epigenetic landscape best represent reversible nodes, a hallmark of lateral inhibition<sup>26</sup>. The broad priming of intestinal stem cell and progenitor cell enhancers offers a satisfying explanation for this property in intestinal crypts and accounts for ATOH1 activity in both lateral inhibition and secretory differentiation. ATOH1 reinforces its own expression and directly regulates *Dll1* and *Dll4*, thus enabling notch-dependent *Atoh1* repression in neighbouring cells; its subsequent activity at primed *cis*-elements triggers numerous secretory genes. Sustained enhancer priming allows ATOH1 activity or its absence, which respectively promotes or represses secretory differentiation<sup>13</sup>, to affect the fate of specified cells, and DNA methylation also barely changes as intestinal stem cells differentiate<sup>30</sup>. True lineage commitment thus occurs late, if ever, in the intestinal epithelium. Indeed, various stimuli revert differentiated cells into intestinal stem cells with surprising ease<sup>17,27,28</sup>, indicating that the environment, and not some cell-intrinsic feature, determines crypt cell potential. Broadly delineated enhancers probably underlie this remarkable plasticity.

## METHODS SUMMARY

Mouse strains were received as gifts or purchased from The Jackson Laboratory, as referenced in Extended Data Table 1. We characterized epigenomes in cells isolated from the first half of small intestines isolated from 2–6-month-old male and female C57BL/6 mice. Detailed protocols to isolate crypt and villus cell populations are described in the Methods. Chromatin sheared by sonication was precipitated with H3K4me2 (Millipore 07-030), H3K27ac (Abcam ab4729), or Flag (Sigma F3165) antibodies; precipitated DNA was amplified using ThruPLEX-FD kits (Rubicon Genomics). For DNase I hypersensitive (DHS)-seq, nuclei were treated with 25 U, 40 U or 50 U DNase I (Roche), followed by procedures described in the Methods. ChIP and DHS libraries were sequenced using Hi-seq 2000 (Illumina).

**Online Content** Any additional Methods, Extended Data display items and Source Data are available in the online version of the paper; references unique to these sections appear only in the online paper.

Received 15 May; accepted 19 November 2013.

Published online 12 January 2014.

- Bernstein, B. E. *et al.* A bivalent chromatin structure marks key developmental genes in embryonic stem cells. *Cell* **125**, 315–326 (2006).
- Wamstad, J. A. *et al.* Dynamic and coordinated epigenetic regulation of developmental transitions in the cardiac lineage. *Cell* **151**, 206–220 (2012).
- Rada-Iglesias, A. *et al.* Epigenomic annotation of enhancers predicts transcriptional regulators of human neural crest. *Cell Stem Cell* **11**, 633–648 (2012).

4. Xie, W. *et al.* Epigenomic analysis of multilineage differentiation of human embryonic stem cells. *Cell* **153**, 1134–1148 (2013).
5. Zaret, K. S. & Carroll, J. S. Pioneer transcription factors: establishing competence for gene expression. *Genes Dev.* **25**, 2227–2241 (2011).
6. Artavanis-Tsakonas, S., Rand, M. D. & Lake, R. J. Notch signaling: cell fate control and signal integration in development. *Science* **284**, 770–776 (1999).
7. van Es, J. H. *et al.* Notch/ $\gamma$ -secretase inhibition turns proliferative cells in intestinal crypts and adenomas into goblet cells. *Nature* **435**, 959–963 (2005).
8. Pellegrinet, L. *et al.* Dll1- and dll4-mediated notch signaling are required for homeostasis of intestinal stem cells. *Gastroenterology* **140**, 1230–1240 (2011).
9. Stamatakis, D. *et al.* Delta1 expression, cell cycle exit, and commitment to a specific secretory fate coincide within a few hours in the mouse intestinal stem cell system. *PLoS ONE* **6**, e24484 (2011).
10. Barker, N. *et al.* Identification of stem cells in small intestine and colon by marker gene *Lgr5*. *Nature* **449**, 1003–1007 (2007).
11. Yang, Q., Bermingham, N. A., Finegold, M. J. & Zoghbi, H. Y. Requirement of Math1 for secretory cell lineage commitment in the mouse intestine. *Science* **294**, 2155–2158 (2001).
12. Kim, T. H. & Shivdasani, R. A. Genetic evidence that intestinal Notch functions vary regionally and operate through a common mechanism of Math1 repression. *J. Biol. Chem.* **286**, 11427–11433 (2011).
13. VanDussen, K. L. & Samuelson, L. C. Mouse atonal homolog 1 directs intestinal progenitors to secretory cell rather than absorptive cell fate. *Dev. Biol.* **346**, 215–223 (2010).
14. Shroyer, N. F. *et al.* Intestine-specific ablation of mouse atonal homolog 1 (Math1) reveals a role in cellular homeostasis. *Gastroenterology* **132**, 2478–2488 (2007).
15. Milano, J. *et al.* Modulation of notch processing by  $\gamma$ -secretase inhibitors causes intestinal goblet cell metaplasia and induction of genes known to specify gut secretory lineage differentiation. *Toxicol. Sci.* **82**, 341–358 (2004).
16. Kazanjian, A., Noah, T., Brown, D., Burkart, J. & Shroyer, N. F. Atonal homolog 1 is required for growth and differentiation effects of notch/ $\gamma$ -secretase inhibitors on normal and cancerous intestinal epithelial cells. *Gastroenterology* **139**, 918–928 (2010).
17. van Es, J. H. *et al.* Dll1<sup>+</sup> secretory progenitor cells revert to stem cells upon crypt damage. *Nature Cell Biol.* **14**, 1099–1104 (2012).
18. Barski, A. *et al.* High-resolution profiling of histone methylations in the human genome. *Cell* **129**, 823–837 (2007).
19. Verzi, M. P. *et al.* Differentiation-specific histone modifications reveal dynamic chromatin interactions and partners for the intestinal transcription factor CDX2. *Dev. Cell* **19**, 713–726 (2010).
20. Heintzman, N. D. *et al.* Distinct and predictive chromatin signatures of transcriptional promoters and enhancers in the human genome. *Nature Genet.* **39**, 311–318 (2007).
21. Gerstein, M. B. *et al.* Architecture of the human regulatory network derived from ENCODE data. *Nature* **489**, 91–100 (2012).
22. Rada-Iglesias, A. *et al.* A unique chromatin signature uncovers early developmental enhancers in humans. *Nature* **470**, 279–283 (2011).
23. Creighton, M. P. *et al.* Histone H3K27ac separates active from poised enhancers and predicts developmental state. *Proc. Natl Acad. Sci. USA* **107**, 21931–21936 (2010).
24. Boyle, A. P. *et al.* High-resolution mapping and characterization of open chromatin across the genome. *Cell* **132**, 311–322 (2008).
25. Klisch, T. J. *et al.* In vivo Atoh1 targetome reveals how a proneural transcription factor regulates cerebellar development. *Proc. Natl Acad. Sci. USA* **108**, 3288–3293 (2011).
26. Ferrell, J. E. Jr. Bistability, bifurcations, and Waddington's epigenetic landscape. *Curr. Biol.* **22**, R458–R466 (2012).
27. Schwitala, S. *et al.* Intestinal tumorigenesis initiated by dedifferentiation and acquisition of stem-cell-like properties. *Cell* **152**, 25–38 (2013).
28. Buczacki, S. J. *et al.* Intestinal label-retaining cells are secretory precursors expressing *Lgr5*. *Nature* **495**, 65–69 (2013).
29. Rose, M. F., Ahmad, K. A., Thaller, C. & Zoghbi, H. Y. Excitatory neurons of the proprioceptive, interoceptive, and arousal hindbrain networks share a developmental requirement for Math1. *Proc. Natl Acad. Sci. USA* **106**, 22462–22467 (2009).
30. Kaaij, L. T. *et al.* DNA methylation dynamics during intestinal stem cell differentiation reveals enhancers driving gene expression in the villus. *Genome Biol.* **14**, R50 (2013).

**Supplementary Information** is available in the online version of the paper.

**Acknowledgements** This work was supported by NIH grants R01DK082889 and R01DK081113 (R.A.S.), K99DK095983 (T.-H.K.), K01DK088868 (M.V.), and P50CA127003; a North American Neuroendocrine Tumor Society fellowship (T.-H.K.); and the Caring For Carcinoid Foundation (R.A.S.). We thank S. Robine for villin-Cre<sup>ER-T2</sup> mice; T. Honjo and S. Artavanis-Tsakonas for *Rbpj*<sup>fl</sup> mice; J. Johnson for ATOH1 antibody; D. Podolsky for TFF3 antibody; and M. Brown and P. Cejas for discussions.

**Author Contributions** T.-H.K. conceived and designed experiments, collected and analysed data, and drafted the manuscript; F.L. performed computational analyses; I.F.-N. performed some mouse experiments; L.-L.H., A.L., K.N. and M.V. prepared some ChIP-seq libraries; H.L. supervised computational analyses; R.A.S. conceived and supervised the study, analysed data and wrote the manuscript.

**Author Information** Data are deposited in the Gene Expression Omnibus under accession number GSE51464. Reprints and permissions information is available at [www.nature.com/reprints](http://www.nature.com/reprints). The authors declare no competing financial interests. Readers are welcome to comment on the online version of the paper. Correspondence and requests for materials should be addressed to R.A.S. ([ramesh\\_shivdasani@dfci.harvard.edu](mailto:ramesh_shivdasani@dfci.harvard.edu)).

## ERRATUM

doi:10.1038/nature13040

### **Erratum: Asymmetric synthesis from terminal alkenes by cascades of diboration and cross-coupling**

Scott N. Mlynarski, Christopher H. Schuster & James P. Morken

*Nature* **505**, 386–390 (2014); doi:10.1038/nature12781

In Fig. 2b of this Letter, the structure of RuPhos should be depicted with a PCy<sub>2</sub> (not PCy<sub>3</sub>) substituent. The correct structure for RuPhos is 2-dicyclohexylphosphino-2',6'-diisopropoxybiphenyl (CAS number 787618-22-8). Also, the first step of Fig. 6d should read 1% Pt(dba)<sub>3</sub>, 1.2% (*R,R*)-**L1**. These errors have been corrected in the online versions of the paper.



## RETRACTION

doi:10.1038/nature12897

### **Retraction: The NAD-dependent deacetylase SIRT2 is required for programmed necrosis**

Nisha Narayan, In Hye Lee, Ronen Borenstein, Junhui Sun, Renee Wong, Guang Tong, Maria M. Fergusson, Jie Liu, Ilsa I. Rovira, Hwei-Ling Cheng, Guanghui Wang, Marjan Gucek, David Lombard, Fredrick W. Alt, Michael N. Sack, Elizabeth Murphy, Liu Cao & Toren Finkel

*Nature* **492**, 199–204 (2012); doi:10.1038/nature11700

We retract this Article because some of the data, specifically the data reported in Fig. 2 demonstrating an *in vitro* requirement for Sirt2 in TNF- $\alpha$ -mediated necroptosis, appears to be irreproducible. We and others have confirmed that Sirt2 and RIP3 interact, and we continue to believe that the absence of Sirt2 protects against ischaemic myocardial damage. Nonetheless, our inability to reproduce the data in Fig. 2 involving TNF- $\alpha$ -mediated necroptosis undermines our confidence in the scientific conclusions reported and the proposed mechanism. Although the matter is currently under further review, we wish to retract the Article in its entirety, and regret any adverse consequences that may have resulted from the paper's publication.

## ADDENDUM

doi:10.1038/nature13075

### Addendum: Enterotypes of the human gut microbiome

Manimozhiyan Arumugam, Jeroen Raes, Eric Pelletier, Denis Le Paslier, Takuji Yamada, Daniel R. Mende, Gabriel R. Fernandes, Julien Tap, Thomas Bruls, Jean-Michel Batto, Marcelo Bertalan, Natalia Borrueal, Francesc Casellas, Leyden Fernandez, Laurent Gautier, Torben Hansen, Masahira Hattori, Tetsuya Hayashi, Michiel Kleerebezem, Ken Kurokawa, Marion Leclerc, Florence Levenez, Chaysavanh Manichanh, H. Bjørn Nielsen, Trine Nielsen, Nicolas Pons, Julie Poulain, Junjie Qin, Thomas Sicheritz-Ponten, Sebastian Tims, David Torrents, Edgardo Ugarte, Erwin G. Zoetendal, Jun Wang, Francisco Guarner, Oluf Pedersen, Willem M. de Vos, Søren Brunak, Joel Doré, MetaHIT Consortium, Jean Weissenbach, S. Dusko Ehrlich & Peer Bork

*Nature* **473**, 174–180 (2011); doi:10.1038/nature09944 and corrigendum **474**, 666 (2011); doi:10.1038/nature10187

It has been drawn to our attention that the methods described in the main text and the Supplementary Information of this Article have been considered by some researchers to be insufficient to enable them to identify enterotypes in their own data sets. Enterotypes were originally defined in this Article (page 177) as “densely populated areas in a multi-dimensional space of community composition” and should not be seen as discrete clusters, but as a way of stratifying samples to reduce complexity. Additionally, the Fig. 2 legend should not imply that between-class analysis is simply a method of visualizing principal component analysis (PCA); rather, it is a supervised rather than an unsupervised analysis of data because it incorporates the outcome of clustering of data. To simplify enterotype identification in the original and other data sets, we have developed a comprehensive tutorial at <http://enterotype.embl.de>—which is a website on enterotypes that will be updated as methods improve. We thank Ivica Letunic and Paul Costea from EMBL for setting up the tutorial.

# CAREERS

**MINORITY SUPPORT** University consortium to boost diversity using NSF funds **p.519**

**DISCRIMINATION** Race found to be a barrier in the behavioural sciences **p.519**

**NATUREJOBS** For the latest career listings and advice [www.naturejobs.com](http://www.naturejobs.com)



## COMPUTER SCIENCE

# Hacking into the cyberworld

*Scientists are well placed to enter the growing, under-supplied cybersecurity workforce.*

BY BRYN NELSON

In mid-November 2013, shadowy saboteurs attacked and crippled multiple sections of the electric grid in the United States. The previous day, assailants sponsored by a rogue government had struck at the heart of London's investment-banking industry, four months after a similarly brazen assault on New York's Wall Street firms.

Fortunately, the mayhem unleashed was only simulated. The three independently planned 'war games', respectively code-named GridEx II, Waking Shark II and Quantum Dawn 2, were designed by financial and government officials to test defences and responses

to the growing threat of cyberattacks. GridEx II alone involved more than 1,800 participants from 200 government and utility organizations in the United States, Canada and Mexico, part of a major emergency drill aimed at improving the agencies' crisis action plans.

Why go to such lengths? The magnitude of the cybersecurity problem is massive. In the United States, President Barack Obama called it "one of the most serious economic and national security challenges we face as a nation". The threat is growing as crucial infrastructure — everything from energy and security to transportation and telecommunications — becomes increasingly reliant on the Internet.

"One thing is clear: the attacks are increasing in number, frequency, sophistication and damage," says Abdou Youssef, chairman of the computer-science department at George Washington University (GWU) in Washington DC.

Accompanying the growing risk is a huge demand for cybersecurity expertise, creating an unprecedented opportunity for physicists, computer scientists, mathematicians and other researchers with the right skills who are looking for a hands-on career option. Good candidates are finding jobs in government, academia and industry, says Jennifer Havermann, an engineering manager for international defence contractor Raytheon in Waltham, Massachusetts. From identifying vulnerabilities and designing firewalls to investigating security breaches, she says, the sector offers career paths that cater to backgrounds as varied as physics and behavioural psychology. "I think there's enough diversity in the field that there should be something for everyone," she says. "We need more of everything" (see 'Women and young people needed').

Irrespective of speciality, employers say that some traits are universally appreciated, such as an ability to analyse large data sets, think critically and see the big picture. Attention to detail, composure under pressure and a willingness and ability to adapt and continuously learn also help job candidates to stand out, says Youssef, who initially trained in maths at The Lebanese University in Beirut.

## WIDESPREAD DEMAND

Cybersecurity essentially means defending a computer or group of computers from attempts to break into or hack a system or network and steal, change or destroy information. These cyberattacks originate from hard-to-trace sources and often consist of software known as viruses, worms, bots or Trojan horses, depending on how they infect, proliferate and inflict damage.

The cybersecurity field is frequently likened to chess, soccer or other games that reward a well-executed strategy and the ability to anticipate opponents' next moves. "I want to figure out how people can beat me — and stop it before it happens," says Markus Jakobsson, a cybersecurity expert in the San Francisco Bay Area and formerly the principal scientist at PayPal. The best cybersecurity professionals, he says, are curious, sneaky, smart and passionate about solving hard problems.

Around the world, multinational corporations such as Northrop Grumman and General Dynamics in the United States, BAE ►



► Systems in the United Kingdom, Trend Micro in Japan and Thales Group in France are snapping up cybersecurity specialists. “Big companies are fighting for good security people,” says Jakobsson. “There are more open positions than there are available experts.”

### RAPID EXPANSION

The same is true for the rapidly expanding roster of cybersecurity start-ups. When Michael Geppi founded Integrata Security in Baltimore, Maryland, in October 2012, he was the firm's sole employee. Now there are eight, including several with master's degrees in engineering. Geppi, the chief executive, hopes to add at least 20 more employees within the next 18 months.

He sees a huge demand for college graduates with degrees in engineering, computer science or maths. The extensive use of mathematical algorithms in detecting signals that might indicate criminal activity, and in designing security-minded computer software and hardware, also plays to the strengths of physicists, he says. “An advanced degree is not required,” he adds, “but with more tenure under your belt, it makes you very marketable” (see ‘Boot camps and degrees’).

Tasks vary. Some defence specialists try to outmanoeuvre criminals by developing anti-virus software and other tools to prevent an attack. Penetration testers, or ethical hackers, instead play the part of attacker and try to breach a company's computer network to identify weak points and recommend how to beef

up security. Experts known as intrusion-detection specialists identify unusual patterns or signals that might point to a real cyber break-in. And some specialists develop codes to protect information or break codes to help identify and dismantle malicious software (malware).

Experts are also keeping a wary eye on attacks that allow criminals to breach wireless networks and infiltrate smartphones, tablets and other portable devices. But perhaps the biggest emerging danger is what the field calls an advanced persistent threat (APT). Instead of a lone hacker, well-funded groups sponsored by criminal organizations or governments often carry out these sophisticated attacks. “This is falling into the realm of cyberwarfare or cyberterrorism or cyber-organized crime, and that really ups the stakes,” says Marcus Rogers, head of the Cyber Forensics Program at Purdue University in West Lafayette, Indiana.

One recent high-profile incident illustrated the havoc that can be wrought by



**“An advanced degree is not required, but with more tenure under your belt, it makes you very marketable.”**

Michael Geppi

well-organized criminals. In December 2013, cybercriminals used malware to steal personal or financial information from an estimated 110 million customers of the Target store chain in the United States. The retailer has not disclosed many details of the data breach — one of the largest ever reported — or how it is now beefing up security. Experts say, however, that an effective response generally requires the services of forensic specialists, who can determine how the criminals gained access, how to contain the damage and how to prevent a repeat occurrence. Cybersecurity expert and blogger Brian Krebs in Annandale, Virginia has suggested that a “malware-laced” phishing e-mail sent to employees of an independent Target contractor might have allowed criminals to swipe credit-card data from cash registers in retail stores. By scrutinizing this type of malware, investigators might be able to determine how it infected the computer system and where it originated.

### CYBERSCIENTIST

Rogers, who trained as a forensic psychologist and once worked as a detective, says that it can be “surprisingly easy” for scientists to make the transition to cybersecurity, even if they do not have a strong background in computer science. “A strong foundation in science itself — the scientific method, hypothesis testing — and even a rudimentary amount of statistics allows you to transition to this area very quickly,” he says. “The technology area of what we’re dealing with isn’t really the hard part. It’s trying to figure out what’s coming next.”

At Purdue University, students can obtain PhDs in interdisciplinary information security from the university's Center for Education and Research in Information Assurance and Security — and the centre boasts a 100% placement rate for its graduates, Rogers says. The roughly ten students enrolled at any given time come with backgrounds ranging from criminology and psychology to physics and maths, and pursue projects sponsored by a dozen academic departments. “Most of the students are offered two or three different jobs and internships,” Rogers says. Potential employers, he adds, are “almost getting into bidding wars”.

Graduate students who are pursuing other degrees can take cybersecurity classes on the side to explore the potential security applications of their research. During his PhD coursework in computer science at GWU, Moroccan native Anasse Bari also completed a graduate certificate programme in Computer Security and Information Assurance, a common academic discipline in the cybersecurity field. His classes, including one on computer security and another on information policy, helped him to realize that his research on a data-mining algorithm — inspired by flocking birds and called Flock by Leader — had a strong security tie-in.

Now a visiting assistant professor of computer science at GWU, Bari uses the physics of how birds fly in formation to detect ‘flocking’

## UNTAPPED POTENTIAL

### Women and young people needed

Cybersecurity may be a growing field — but not everyone is aware of the job potential. A 2013 survey commissioned by international aerospace and defence contractor Raytheon in Waltham, Massachusetts, revealed a lag in enthusiasm for the field among 18- to 26-year-olds in the United States. Fewer than one in four said they were interested in a career as a cybersecurity professional, near the bottom of 14 options ranging from an entertainer (the most popular) to a Wall Street analyst (the least popular). The results also highlighted the field's significant gender gap: 35% of young men but only 14% of young women showed an interest in the career.

Lisa Foreman, a freelance information-security consultant based in the Washington DC area, founded the Women's Society of Cyberjutsu in 2012 to encourage more girls and women to consider the career choice. “I wanted to create a community where women can come together and learn in a comfortable learning environment,” she says, “and have a place to go and really geek

out without feeling intimidated.”

The society sponsors monthly workshops that offer hands-on experience for women who want to learn more about particular cybersecurity tools or topics such as web app security, digital forensics and ethical hacking. It also fields teams in fast-paced ‘capture the flag’ challenges that test participants' cybersecurity skills by requiring them to defend their own systems from an attack while trying to hack into those of other teams. The Women's Security Society has a similar role in encouraging the advancement of women in the profession in the United Kingdom.

“I think it's especially important that women who are in the career field share their stories,” says Jennifer Havermann, an engineering manager at Raytheon. During a trip in October 2013 to talk to students at a cybersecurity fair hosted by California State Polytechnic University in Pomona, she was inundated by questions about the field and her own career trajectory. “I'm really encouraged,” she says. **B.N.**

## E-SKILLS

*Boot camps and degrees*

For job applicants with the right core skills, companies and government agencies often provide the training for specialized tasks. But how can job seekers acquire the skills that will get them noticed?

Among degree-granting cybersecurity institutions, Carnegie Mellon University's CyLab in Pittsburgh, Pennsylvania, the Lincoln Laboratory at the Massachusetts Institute of Technology in Lexington and the Maryland Cybersecurity Center at the University of Maryland in College Park are some of the best-known US programmes. In the United Kingdom, the University of Oxford and Royal Holloway, University of London received £7.5 million (US\$12.5 million) in government and research-council funding in 2013 to offer multidisciplinary PhD degrees in support of national cybersecurity interests.

Beyond a degree, most job

seekers must also earn some form of professional certification. One of the field's most important is the CISSP (Certified Information Systems Security Professional), which is commonly required for government work. Another is the CEH (Certified Ethical Hacker), which applies to professionals who help clients to bolster their defences through simulated attacks, or penetration testing.

Institutions often provide certification training for their own workers or students. Other individuals can study at university-sponsored or corporate training centres that host intensive one-week boot camps costing US\$2,000 to \$4,600 or more. With names such as Intense School and SecureNinja, these programmes run students through a rigorous regimen of drills and reviews to prepare for the certification's final examination. **B.N.**

patterns that can be applied to groupings of similar people, tweets, Facebook data, documents and other information. As a security tool, the work might help to identify leaders and followers in online communities and use that knowledge to predict criminal activity or to detect fraud.

A strong background in maths, meanwhile, might provide an advantage for cryptography, a subspecialty that involves writing or breaking secret codes that are designed to protect data or channels of communication. Peter Ryan, professor of applied security at the University of Luxembourg, had been fascinated by codes since childhood, but began exploring cybersecurity only after receiving his PhD in mathematical physics from the University of London. He later found a job in cryptography at the UK intelligence agency Government Communications Headquarters.

At the University of Luxembourg, Ryan uses some of the same maths-based methods to make touch-screen and other electronic voting systems less vulnerable to tampering. "We try to imagine how an attacker might attack these and, as best we can, develop techniques to foil all of the attacks we can come up with," he says.

Other specialists have found a niche in quickly neutralizing potential cybersecurity threats. Krysta Cox, an analyst for ManTech International Corporation based in Washington DC, describes her job as an emergency medical technician for computer networks — "you're the first responder when an incident happens", she says. If an employee at one of her corporate clients receives a suspicious e-mail that asks the reader to follow

a link and reset a password, Cox sequesters the message within a secure system that is isolated from the rest of the computer network. Then she clicks on the link to see where it leads. If the destination spells trouble, she can capture the information and instruct the computer network to automatically flag similar e-mails to prevent future risks.

Anyone wanting to enter the cybersecurity job market should be aware that irrespective of speciality, stringent background checks are routine, especially for a government agency or a private contractor working closely with one. "You need to expect investigators to go over every single aspect of your life," says Integrata's Geppi. Ill-advised Facebook posts, tweets and other social-media messages can come back to haunt potential job applicants.

And in many countries, positions within government or with government contractors may require proof of citizenship or long-term residency. Foreign students may have more success pursuing a job in academia, or with multinational companies.

Beyond these caveats, experts say that motivated individuals with strong scientific skills should be well positioned for a successful cybersecurity career. "Security is always a cat-and-mouse kind of game, and often the attackers are a bit ahead," Ryan says. "In a way, it's slightly depressing that it's like that, but in another sense it's actually quite fun. And it means that there's probably not going to be any shortage of jobs for people for a long time to come." ■

**Bryn Nelson** is a freelance writer based in Seattle, Washington.

## EQUAL OPPORTUNITIES

**Minority support**

A consortium of four US universities aims to boost diversity in maths, engineering and physical and computer sciences with the help of a US\$2.2 million grant from the US National Science Foundation. The California Alliance for Graduate Education and the Professoriate is being led by the University of California (UC), Berkeley, and includes UC Los Angeles, the California Institute of Technology in Pasadena and Stanford University. The universities aim to create a community of minority PhD students, postdocs and faculty members by providing training and funding travel between institutions. "We want to create an environment that's more welcoming," says Mark Richards, executive dean of the College of Letters and Science at UC Berkeley.

## FELLOWSHIPS

**Canada needs managers**

The Canadian federal government is investing Can\$8 million (US\$7.3 million) over two years to tackle the country's shortage of research and development managers. Mitacs, a nonprofit organization in Vancouver, will run a fellowship programme to support 125 to 150 postdocs in industrial research, providing training in skills such as management and leadership. Researchers who have received a PhD from a Canadian university within the past five years can join the scheme. The employment rate is high for those who have finished the pilot programme, says Arvind Gupta, Mitacs chief executive and scientific director. "Researchers come out of the programme with the skills to manage a company's research portfolio," he says.

## DISCRIMINATION

**Race obstacle**

One-fifth of workplace barriers faced by minority researchers in behavioural science are related to race, a study says (R. R. Kameny *et al. J. Career Dev.* **41**, 43–61; 2014). In addition to barriers such as a lack of mentors, early- to mid-career US minority researchers identified race-related hurdles such as colleagues' low expectations of performance and a lack of support for studies on minority groups. Minority researchers must seek help from faculty members who are capable of changing the department culture, says co-author Rebecca Kameny, a psychologist at the research company 3C Institute in Cary, North Carolina.

# NO FURY LIKE A WOMAN COLD-CALLED

*A degree of foresight.*

BY JEREMY R. BUTLER

"Hello?"

"Hello, Mrs Cooper?"

"Yes?"

"This is Flip Figglesworth with Cassandra Mutual."

"Sorry, we are long-time customers of —"

"Dutch Consolidated. But did you know that Cassandra is not your ordinary insurance firm? We employ the world's most accurate precognitive actuaries — bypassing the unnecessary risk-taking that plagues the average insurer lets us pass the savings on to you."

"Precognitive actuaries. Seers?"

"Yes, ma'am. Best in the world."

"Isn't that illegal?"

"Not with the passage of Bill 413. Perhaps we could set up a time to sit down with your husband and discuss —"

"Tony's far too busy for that."

"Then might I interest you in flood protection at 35% of what you're currently paying?"

"Um, maybe."

"What about fire protection at 40% off?"

"That's good! How about car insurance?"

"For you or your husband?"

"For me."

"I can save you \$100 a month."

"And my husband?"

"Well, there are other factors than price that you should consider. For instance —"

"Just tell me the price."

"I'm afraid it would be more expensive."

"How much more expensive?"

"Considerably."

"Why is that?"

"Under Bill 413 I cannot disclose —"

"You're saying he'll have another accident, aren't you? A bad one?"

"I'm afraid I —"

"Oh no. What about life insurance for him?"

"No problem there. Just a fraction of what you're currently paying."

"Phew, that's great. For a moment there, I thought ... I thought he might die."

"Well, we all do. Just please remember to read the fine print in all the policies."

"What are you saying?"

"Nothing. It's just you should read our policies closely to ensure they meet your needs."

"Any fine print in particular?"

"Well ... denial of payment to beneficiaries in cases of domestic homicide, for example."

"I'm sorry, did you say homicide?"

"No, well, yes, but no. That's just an example. Read the fine print, that's all I'm saying."

"What the ..."

"How about travel insurance? Kazakhstan is host to many infectious diseases. Our hospitalization and repatriation policies —"

"Kazakhstan? I don't travel anywhere we don't have an embassy."

"No, of course not. My mistake. Can I interest you in —"

"Wait."

"— dental —"

"Are you saying what I think you're saying?"

"That there's no bad time for dental?"

"No. That my husband will be killed, intentionally, in his car? By me?"

"Under Bill 413, I can neither confirm nor deny —"

"Why would I do that? That's not like me. I do yoga. I mean, I've thought about it, who hasn't? But running away to a country I know nothing about? That sounds ... reckless."

"I hear it has great food."

"Really?"

"If you like spicy."

"I love spicy. Regardless, I'm not going to kill my husband."

"I'm glad to hear that. Maybe there's a time when the three of us could sit down. What about tomorrow night?"

"No, he's at a meeting."

"Thursday?"

"Charity benefit."

"Next week?"

"Conference."

"Oh."

"Tony's a busy man."

"I see."

"I'm sure you do."

"I'm just a salesman, ma'am. I only know what the computer tells me, like his frequent travel policies with a Ms Tanya Riggins."

"His secretary."

"I see."

"Stop that."

"Oh, no, I didn't mean to suggest ... I'm sorry if I —"

"Don't be sorry, Mr Figglesworth. You've helped me immensely. I've been in denial

about long-term planning. I'm going to revamp our entire portfolio. Not only that, I'm going to

spread the word to my friends and family and give them your name."

"Fantastic! I would greatly appreciate that. To be honest, I haven't been meeting my targets and the boss says —"

"When I'm done you'll ride the leader board for the rest of the year. I just need a few more quotes."

"Certainly!"

"A life-insurance policy for Tanya Riggins, payable to her husband, Jim. Would that be more or less expensive than her current one?"

"Considerably more, I'm afraid."

"Uh huh. I thought so. Anyone else that I shouldn't recommend to you?"

"Like acquaintances whose rates would go up significantly?"

"Right, I wouldn't want to drown out the praises everyone will be singing ..."

"Good idea. Sally Forthright."

"Sally! OK, I'll just scratch her off."

"Connie Gardner."

"Gotcha. She's gone."

"Patty St James."

"My maid of honour!?"

"Yes. And please, don't mention fire coverage to her."

"Fire. Understood. Anyone else?"

"Oh, quite a few more. At least two dozen."

"Aaaargh!"

"I mean, no, under Bill 413 I can neither —"

"OK, I just need one last quote."

"Fine."

"A life-insurance policy for me."

"Beneficiary?"

"You."

"Me? We haven't even —"

"How much?"

"Well, it's quite unusual, but not unethical, I suppose. The premiums would be quite low."

"That's fantastic. I'm so glad. Thank you."

"You're welcome. I will print up the policies and perhaps I could come by this evening for your signature?"

"..."

"Hello? Mrs Cooper? Hello? Oh, Figglesworth, you idiot! Not again." ■

Jeremy R. Butler is a psychiatrist, part-time improviser and father to two energetic girls.

JACEY



➔ **NATURE.COM**  
Follow Futures:  
@NatureFutures  
go.nature.com/mtoodm